

# SCATTEROMETRY

CIP-GEGEVENS KONINKLIJKE BIBLIOTHEEK, DEN HAAG

Stoffelen, Ad

Scatterometry

Ad Stoffelen

Proefschrift Universiteit Utrecht. -Met lit. opg.-

Met samenvatting in het Nederlands.

ISBN 90-393-1708-9

Trefw.: meteorologie, satellietwaarnemingen

# SCATTEROMETRY

## DE SCATTEROMETER

(Met een samenvatting in het Nederlands)

### **Proefschrift**

ter verkrijging van de graad van doctor aan de Universiteit Utrecht op gezag van de Rector  
Magnificus Prof. Dr. H. O. Voorma, ingevolge het besluit van het College voor Promoties in  
het openbaar te verdedigen op maandag 26 oktober 1998 des namiddags te 4.15 uur

door

**Adrianus Cornelis Maria Stoffelen**

geboren op 25 februari 1962, te Alphen (N.Br.)

Promotoren: Prof. Dr. Bert Holtslag, Universiteit Utrecht  
Prof. Dr. David Anderson, University of Oxford  
Prof. Dr. Ir. Arnold Heemink, Technische Universiteit Delft

The research described in this thesis has been carried out at the European Centre for Medium-range Weather Forecasts (ECMWF) and the Royal Netherlands Meteorological Institute (KNMI) with financial support from the European Space Agency (ESA) and the Netherlands Remote Sensing Board (BCRS).

*Winds at sea,  
As wild as they can be,  
Imagine the light,  
That sees them bright.*

*Aan Karin,  
Kees, Elma, Leon, en Rian*

# CONTENTS

## SAMENVATTING

<i>De Scatterometer</i> .....	<i>vii</i>
<i>Overzicht</i> .....	<i>viii</i>

## CHAPTER I INTRODUCTION TO SCATTEROMETRY

<i>1. The Need for Wind Data</i> .....	<i>I-1</i>
1.1. Atmospheric Flow .....	<i>I-1</i>
1.2. Global Observing System .....	<i>I-4</i>
1.3. Data Assimilation .....	<i>I-7</i>
1.4. Weather and Wave Prediction .....	<i>I-9</i>
1.5. Climate .....	<i>I-10</i>
1.6. Ocean Modeling .....	<i>I-10</i>
<i>2. Scatterometer Instruments</i> .....	<i>I-12</i>
2.1. Normalized Radar Cross Section .....	<i>I-12</i>
2.2. SeaSat, NSCAT and SeaWinds .....	<i>I-15</i>
2.3. ERS Scatterometers and ASCAT .....	<i>I-18</i>
<i>3. The Physics Behind Scatterometry</i> .....	<i>I-19</i>
3.1. Electromagnetic Interaction of Microwaves With the Ocean Surface .....	<i>I-20</i>
3.2. The Ocean Topography .....	<i>I-21</i>
3.3. From Capillary Waves to Winds .....	<i>I-23</i>
<i>4. Aim and Overview of the Thesis</i> .....	<i>I-26</i>
<i>References</i> .....	<i>I-29</i>

## CHAPTER II MEASUREMENT SPACE AND INVERSION

<i>Abstract</i>	<b>II-1</b>
<b>1. Introduction</b>	<b>II-2</b>
<b>2. Visualization in Measurement Space</b>	<b>II-4</b>
<b>2.1. Visualization of Anisotropy</b>	<b>II-6</b>
2.1.1. Validation of the Existence of a Solution Surface	II-8
2.1.2. Estimation of $B_2$	II-9
2.1.3. The Need for Higher Harmonics	II-12
<b>2.2. Visualization of the Triplet Distribution Along the Cone</b>	<b>II-13</b>
2.2.1. Upwind-Downwind Effect	II-14
<b>2.3. Wind Speed Dependence</b>	<b>II-16</b>
<b>2.4. Other Geophysical Dependencies</b>	<b>II-16</b>
<b>3. Inversion</b>	<b>II-18</b>
<b>3.1. Measurement Space Transformation</b>	<b>II-19</b>
<b>3.2. Quality Tests in the Transformed Space</b>	<b>II-22</b>
<b>4. Summary and Conclusions</b>	<b>II-23</b>
<i>Appendix A: The Prelaunch Transfer Function CMOD2</i>	<b>II-25</b>
<i>Appendix B: Assumptions for <math>B_1</math> Estimation</i>	<b>II-26</b>
<i>Appendix C: Theoretical Derivation of the Inversion Procedure</i>	<b>II-27</b>
<i>Appendix D: Estimation of the Triplet Scatter</i>	<b>II-28</b>
<i>Acknowledgements</i>	<b>II-28</b>
<i>References</i>	<b>II-29</b>

CHAPTER III ESTIMATION AND VALIDATION OF THE TRANSFER FUNCTION CMOD4

<i>Abstract</i>	<i>III-1</i>
<b>1. Introduction</b>	<b>III-1</b>
<b>2. Estimation of the Transfer Function: Simulation Studies</b>	<b>III-2</b>
<b>2.1. Example 1: Tuning Simulations using Wind Components rather than Speed and Direction</b>	<b>III-6</b>
<b>2.2. Example 2 :Tuning Simulations in Logarithmic Space</b>	<b>III-7</b>
<b>3. Estimation of the Transfer Function: Real Data</b>	<b>III-8</b>
<b>3.1. Data Selection</b>	<b>III-8</b>
<b>3.2. Estimation</b>	<b>III-10</b>
<b>4. Validation Procedure</b>	<b>III-12</b>
<b>4.1. Interpretation of <math>\sigma^0</math> Differences</b>	<b>III-12</b>
<b>4.2. Simulation of the Effect of Noise on the Validation</b>	<b>III-12</b>
<b>5. A Posteriori Verification</b>	<b>III-13</b>
<b>5.1. Validation in <math>\sigma^0</math> Space</b>	<b>III-13</b>
<b>5.2. Validation against Winds</b>	<b>III-14</b>
<b>5.3. High Speed Comparisons</b>	<b>III-19</b>
<b>5.4. Wind Error Correlation</b>	<b>III-22</b>
<b>6. Summary and Conclusions</b>	<b>III-24</b>
<i>Appendix A: Analytic Illustration of Curve-Fitting Complications</i>	<i>III-27</i>
<b>A1. Example 1: Nonlinearity in the Transfer Function</b>	<b>III-27</b>
<b>A2. Example 2: Bias Resulting from Proportional Errors</b>	<b>III-29</b>
<i>Appendix B: The CMOD4 Model Formulation and Coefficients</i>	<i>III-30</i>
<i>Acknowledgements</i>	<i>III-31</i>
<i>References</i>	<i>III-32</i>

CHAPTER IV ERROR MODELING AND CALIBRATION USING TRIPLE COLLOCATION



<i>Abstract</i>	<i>IV-1</i>
<i>1. Introduction</i>	<i>IV-2</i>
<i>2. Observation Errors and Error Domain</i>	<i>IV-3</i>
<i>3. Error Modeling and Calibration With Two Systems</i>	<i>IV-8</i>
<i>4. Error Modeling and Calibration With Three Systems</i>	<i>IV-9</i>
<i>5. Higher-Order Calibration</i>	<i>IV-10</i>
<i>6. Calibration and Error Model Results</i>	<i>IV-11</i>
<i>6.1. First-Order Calibration</i>	<i>IV-12</i>
<i>6.2. Higher-Order Calibration</i>	<i>IV-16</i>
<i>7. Conclusions</i>	<i>IV-18</i>
<i>7.1. Résumé</i>	<i>IV-18</i>
<i>7.2. Application</i>	<i>IV-19</i>
<i>Appendix A: Necessity of Error Modeling Before Calibration or Validation</i>	<i>IV-20</i>
<i>A1. Scatter Plots and Regression</i>	<i>IV-20</i>
<i>A2. Necessity of Error Modeling Before Calibration</i>	<i>IV-21</i>
<i>Appendix B: Pseudobias Through Nonlinear Transformation</i>	<i>IV-23</i>
<i>Acknowledgements</i>	<i>IV-23</i>
<i>References</i>	<i>IV-23</i>

<i>Abstract</i>	V-1
<b>1. Introduction</b>	V-2
<b>2. Ambiguity Removal</b>	V-4
<b>2.1. Description of the Ambiguity Removal Procedure</b>	V-4
<b>2.2. Examples of Ambiguity Removal Using PRESCAT</b>	V-7
<b>3. Optimum Interpolation (OI) Assimilation</b>	V-12
<b>3.1. The Analysis System</b>	V-12
<b>3.2. Analysis and Short-Range Impact</b>	V-15
<b>3.3. Medium-Range Forecast Impact</b>	V-20
<b>3.4. Validation of the OI Data Assimilation System</b>	V-24
<b>4. Variational Methods</b>	V-26
<b>5. Summary and Conclusions</b>	V-29
<i>Acknowledgements</i>	V-32
<i>References</i>	V-32

## CHAPTER VI    OUTLOOK

<b>1. Empirical Methodology</b>	VI-1
<b>1.1. Using NWP fields</b>	VI-1
<b>1.2. Uncertainty and Non-linearity</b>	VI-3
<b>1.3. Backscatter Measurement Space</b>	VI-4
<b>2. Physics of Scatterometry</b>	VI-6
<b>3. Impact of Scatterometers</b>	VI-10
<i>References</i>	VI-11

## APPENDIX

<b><i>A Simple Method for Calibration of a Scatterometer over the Ocean</i></b>	<b><i>A-1</i></b>
<b>Abstract</b>	<b>A-1</b>
<b>1. Introduction</b>	<b>A-1</b>
<b>2. Method</b>	<b>A-4</b>
<b>3. Results</b>	<b>A-8</b>
3.1. Ocean Calibration	A-8
3.2. Antenna Gain Variations	A-10
3.3. Application	A-12
<b>4. Conclusions</b>	<b>A-14</b>
<b>References</b>	<b>A-17</b>
<b><i>Acronyms</i></b>	<b><i>A-19</i></b>
<b><i>Acknowledgments</i></b>	<b><i>A-21</i></b>
<b><i>Curriculum Vitae</i></b>	<b><i>A-23</i></b>

## SAMENVATTING

### **De Scatterometer**

Een veelheid aan meteorologische metingen is dagelijks beschikbaar. De meeste van deze waarnemingen bevinden zich echter boven land, en met name windwaarnemingen boven de (Noord Atlantische) oceaan zijn schaars. Bij een westelijke luchtstroming is dit een duidelijke beperking voor de weers- en golfverwachtingen ten behoeve van Nederland. Juist dan is het gevaar voor bijvoorbeeld storm of overstroming het grootst. Ook in het aardse klimaatsysteem speelt de wind aan het oppervlak een grote rol en is de belangrijkste factor voor de aandrijving van de oceaancirculatie. De oceaancirculatie op zijn beurt is cruciaal voor de verschijnselen die samenhangen met bijvoorbeeld El Niño. Dit proefschrift gaat over het scatterometer instrument dat vanuit de ruimte, zelfs onder een wolkendeck, nauwkeurige en betrouwbare informatie geeft over de wind aan het oceaanooppervlak met een hoge mate van ruimtelijke consistentie.

Tijdens de tweede wereldoorlog werden radars aan boord van schepen veelvuldig gebruikt voor de opsporing van vijandige vaartuigen. Hierbij werd vastgesteld dat de detectie slechter werd naarmate de wind aan het zeeoppervlak groter was. Proefondervindelijk was hiermee het principe van een wind scatterometer aangetoond. Al snel ontwikkelde zich dan ook de idee de wind aan het zeeoppervlak te meten met behulp van radar. Vanuit een vliegtuig of een satelliet wordt dan een microgolfbundel onder een schuine hoek naar het zeeoppervlak gestuurd. De microgolfstraling, met gewoonlijk een golflengte van enkele centimeters, wordt verstrooid aan het ruwe oppervlak, en een klein gedeelte van de uitgezonden puls keert terug naar het detectorgedeelte van de scatterometer.

Het fysische fenomeen van belang voor de werking van de scatterometer is de aanwezigheid van zogeheten capillaire gavitatiegolven op het zeeoppervlak. Deze golven hebben een golflengte van enkele centimeters en reageren vrijwel instantaan op de sterkte van de wind. De verstrooiing van microgolven is op zijn beurt weer sterk afhankelijk van de amplitude van de capillaire golven. Bovendien blijken de capillaire golfjes over het algemeen gericht in lijn met de windrichting. Aldus bestaat er een verband tussen de hoeveelheid teruggestrooide energie en de windsterkte en -richting op enige hoogte. Een scatterometer instrument wordt zo ontworpen dat uit diverse metingen van het teruggestrooide vermogen, windsterkte en -richting afgeleid kunnen worden. Deze metingen kunnen dan eenvoudig vergeleken worden met bestaande windgegevens van boeien, schepen en weermodellen ter calibratie en validatie.

## Overzicht

In de loop der jaren zijn scatterometer instrumenten aan boord van verscheidene satellieten gelanceerd. De scatterometers op de ERS-1 en ERS-2 (“European Remote-sensing Satellite”) hebben de langste staat van dienst en zijn sinds 1991 operationeel. Deze scatterometers (die identiek zijn) hebben ieder drie antennes, waarmee het oceaanooppervlak in drie verschillende richtingen bemeten wordt. Een punt op het aardoppervlak wordt eerst door de naar voren gerichte bundel belicht, dan door de naar opzij gerichte bundel, en als laatste door de naar achteren gerichte bundel. De drie metingen, verder kortweg aangeduid als trits, kunnen tegen elkaar worden uitgezet, hetgeen resulteert in een ruimtelijk (3D) plaatje. Door uitgekende doorsneden te maken van deze ruimte kan de samenhang van de drie metingen kwalitatief worden bestudeerd. De drie metingen blijken dan inderdaad een sterke samenhang te vertonen die verklaard kan worden uit twee geofysische parameters. De drie metingen liggen namelijk in het algemeen dichtbij een hoornvormig (2D) oppervlak. De lengterichting van de hoorn blijkt voornamelijk te corresponderen met een variërende windsterkte (of ruwheid van de zee), en de kortste omtrek van de hoorn met een variërende windrichting (ofwel oriëntatie van de capillaire golfjes). De karakterisatie en modellering van dit oppervlak heeft geleid tot een aanzienlijke verbetering in de interpretatie van de scatterometer, zoals beschreven is in dit proefschrift.

Hierboven is een uiterst simplistisch beeld gegeven van de fysica die van belang is bij de interpretatie van de scatterometer. Het eerste hoofdstuk van dit proefschrift beschrijft in meer detail de fysische modellering van belang bij de interpretatie van de scatterometer metingen. Ten eerste, de topografie van het zeeoppervlak is uitermate gecompliceerd en niet nauwkeurig te beschrijven met eenvoudige wiskundige vergelijkingen. De capillaire golven hebben een andere fasesnelheid dan de langere golven en beide hebben hiermee een ingewikkelde dynamische interactie. Bij hogere windsnelheid breken de golven en ontstaan er schuimkoppen, hetgeen de fysische beschrijving verder compliceert. Ten tweede, de interactie van een schuin invallende microgolfbundel met dit gecompliceerde oppervlak is evenmin nauwkeurig te beschrijven. Zowel verstrooiing als reflectie kunnen een rol spelen. Ten derde, over de relatie tussen de amplitude van de capillaire golven en de wind op enige hoogte, laten we veronderstellen 10 m, is in de literatuur niet de overeenstemming tot in het gewenste detail. Bij lage windsnelheid zouden de oppervlaktespanning of variaties in de wind variabiliteit een rol kunnen spelen.

Gezien de fysische complexiteit, is het niet verwonderlijk dat voor de interpretatie van scatterometer metingen statistische methoden hun opgang gevonden hebben. Dit proefschrift gaat met name in op deze methoden, en geeft, aan de hand van vijf wetenschappelijke publicaties, een tamelijk volledig beeld van de “state-of-the-art”, zoals die bereikt is met de

ERS scatterometers (ERS-1 vanaf 17 juli 1991 en later ERS-2 vanaf 22 november 1995).

Het derde hoofdstuk behandelt de visualisatie van de gemeten tritsen in de 3D meetruimte, de bepaling van de spreiding van de metingen rond het hoornvormige oppervlak, en de schatting van de meest waarschijnlijke “werkelijke” (of ruisvrije) trits bij het hoornvormige oppervlak gegeven de metingen en hun nauwkeurigheid (inversie). De perceptie dat de metingen met grote waarschijnlijkheid dichtbij een hoornvormig oppervlak liggen, vormt essentiële a priori informatie van belang voor de inversie. Een inversieprocedure gestoeld op waarschijnlijkheidstheorie is afgeleid. Verder worden aan de hand van de structuur van het hoornvormige oppervlak indicatoren bepaald, van belang voor de kwaliteitscontrole, instrumentbewaking, en de verdere verwerking van de gegevens.

In de appendix wordt een methode besproken die beschrijft hoe, aan de hand van geselecteerde windgegevens en een goed wind-microgolf verband, ofwel transfer functie, de scatterometer verstrooiingsmetingen gecalibreerd kunnen worden boven de oceaan. Het blijkt dat deze calibratie, die per antenne wordt uitgevoerd, uiterst nauwkeurig is, en, wanneer toegepast, in de 3D meetruimte de verdeling van gemeten tritsen gemiddeld dichterbij de door de transfer functie gemodelleerde hoorn brengt. Dit levert een verbeterd scatterometer wind product op. De methode was met name van groot belang voor de validatie en calibratie van de ERS-2 scatterometer, voordat de instrumentele calibratie was voltooid.

Met behulp van een set windgegevens uit een weermodel en hun geschatte nauwkeurigheden, passend in locatie en tijd bij een set van scatterometer metingen en hun geschatte nauwkeurigheden, kan met quasi-lineaire schattingstheorie (“Maximum Likelihood Estimation”) de meest waarschijnlijke wind-microgolf transfer functie worden afgeleid. De niet-lineariteit en onnauwkeurige formulering van de transfer functie, een niet-uniforme verdeling van invoergegevens, en een inaccurate formulering van de geschatte nauwkeurigheid kunnen hier een goed resultaat in de weg staan. Een nieuwe functie, genoemd CMOD4, wordt afgeleid in hoofdstuk IV. Een eerste eis die gesteld wordt aan een transfer functie, is dat het in de 3D meetruimte nauwkeurig bij de gemeten tritsen past. Wanneer de “fit” optimaal is zal het gecombineerde effect van meetonnauwkeurigheid en inversiefout kleiner zijn dan  $0.5 \text{ m s}^{-1}$  in de wind vector. CMOD4 blijkt binnen deze fout bij de metingen te passen. Een tweede eis is, dat voor een onafhankelijke gegevensset, het verschil tussen de geïnverteerde scatterometer wind en de bijpassende wind van bijvoorbeeld een weermodel zo klein mogelijk is. In de praktijk blijkt dat deze tweede eis impliciet volgt uit de eerste, maar ook dat de onnauwkeurigheid van de scatterometer wind met name wordt bepaald door de associatie van een locatie op de hoorn met een wind vector. De onnauwkeurigheid in de scatterometer wind kan dan ook goed beschreven worden in het wind domein.

In hoofdstuk V wordt dit laatste verder uitgewerkt, en wordt gestreefd naar een gedetailleerde wind calibratie met behulp van *in situ* gegevens. Windgegevens bevatten doorgaans een relatief grote onnauwkeurigheid. Het wordt aangetoond dat ijking of regressie van zulke gegevens niet mogelijk is in een vergelijking van twee meetsystemen, tenzij de nauwkeurigheid van één van de twee meetsystemen bekend is. In de praktijk is dit meestal niet zo. Voor deze gevallen wordt een methode voorgesteld die uitgaat van de simultane vergelijking van drie meetsystemen. In dit geval kan zowel de ijking als een foutenmodel voor de drie meetsystemen worden opgelost. Toepassing van de methode laat zien dat de scatterometer wind afgeleid met behulp van CMOD4 ruwweg 5 % te laag is, en de oppervlaktewind van het gebruikte weermodel ongeveer 5 % te hoog.

Het hoornvormige oppervlak blijkt te bestaan uit twee nauw samenvallende laagjes. Wanneer de wind een component heeft in de kijkrichting van de middelste microgolfbundel wordt de ene hoorn beschreven, en wanneer de wind een component heeft tegengesteld hieraan, de andere. Uit een trits metingen (met ruis) kan dus in het algemeen niet een unieke windvector worden bepaald. Twee ongeveer tegengestelde oplossingen resulteren. Deze dubbelzinnigheid in de windrichting kan in de praktijk worden opgelost door die oplossing te kiezen die het dichtst bij een korte termijn weervoorspelling ligt. Daarna kunnen eisen worden gesteld aan de ruimtelijke consistentie van het gevonden windvector veld. Zoals beschreven in hoofdstuk V levert zo'n methode de goede oplossing in meer dan 99 % van de gevallen. Zo kan een in het algemeen kwalitatief goed windproduct worden afgeleid uit de ERS scatterometermetingen.

In het tweede gedeelte van hoofdstuk V wordt ingegaan op de assimilatie van scatterometergegevens in weermodellen. Voor variationele gegevensassimilatie wordt een methode voorgesteld, waarbij de dubbelzinnige scatterometerwinden worden geassimileerd, en niet direct de terugstrooiingsmetingen. Dit vanwege het feit dat de onzekerheid in de interpretatie van de scatterometer, het best is uit te drukken als een fout in de wind. De projectie van deze fout op de microgolfmetingen is niet-lineair, en daarmee tamelijk moeilijk te verwerken binnen de context van meteorologische variationele gegevensassimilatie. Assimilatie van de dubbelzinnige wind daarentegen is tamelijk recht toe recht aan.

De scatterometermetingen leiden tot een duidelijk betere analyse en korte-termijn voorspelling van het windveld boven zee. De bedekking is echter zodanig dat andere windwaarnemingen nog lang een zeer welkome aanvulling zullen zijn. Nieuwe Amerikaanse scatterometers met een grotere bedekking zijn in ontwikkeling (met name QuikSCAT en SeaWinds). Vanwege hun andere geometrie en golflengte is echter eerst ontwikkelwerk nodig om tot een gedegen interpretatie te komen. De in dit proefschrift beschreven methodologie kan een belangrijke rol spelen in de interpretatie van de gegevens van deze scatterometers. De volgende generatie Europese scatterometers (ASCAT genoemd) heeft een

grote bedekking en de microgolflengte en meetgeometrie van de ERS scatterometers. Hiermee zijn we op termijn verzekerd van een goed scatterometer wind product.



## CHAPTER I

### Introduction to Scatterometry

The scatterometer is an instrument that provides information on the wind over the ocean near the surface, and scatterometry is the knowledge of extracting this information from the instrument's output. This thesis consists of a number of scientific publications on scatterometry, and aims to provide a contemporary overview of the subject. Space-based scatterometry has become of great benefit to meteorology and climate in the past years, and the scientific work laid down here has contributed to this. This introductory chapter explains the background of scatterometry and the structure of the thesis.

The first section of this chapter addresses atmospheric flow and the need for wind observations for weather and wave prediction, and climate and ocean modeling. An evaluation is given of the existing global meteorological observing system and data assimilation capabilities in order to clarify the potential benefits of scatterometry. Next section discusses past and future space-based scatterometers. Section 3 deals with the complex physics of scatterometry and section 4 with how this is related to the empirical approach that was followed for most studies in this thesis. An overview of the thesis concludes this chapter.

#### **1. The Need for Wind Data**

##### **1.1. Atmospheric Flow**

In order to obtain the requirements for the meteorological observing system, knowledge of atmospheric dynamics is essential. *Phillips* [1990] discusses in detail the atmospheric flow in relation to the atmospheric analysis and forecasting problem. Atmospheric dispersion processes make that small-scale uncertainties in the analysis amplify and grow during a subsequent forecast. With the current meteorological observing system the largest scales of atmospheric motion are well resolved. This results in a basic weather prediction skill. Over the last decades improvements in data assimilation methodology and observation processing (*Lorenc* [1986], *Daley* [1991], or *Rabier et al* [1997]) have lead to a better analysis of the atmospheric flow and in improved weather forecasts. Scales down to ~250 km are reasonably well analyzed. This threshold is largely determined by the density of the current meteorological global observing system, as pointed

out in next section. Satellite data provide the potential to analyze yet smaller scales and further improve weather and wave forecast skill, or climate and ocean modeling. The atmospheric flow is determined by the wind field, but also by the mass or atmospheric density field. It is shown below that wind observations are in particular useful on all scales in the tropics, and elsewhere, to define the required smaller scales of atmospheric motion.

The atmosphere may be regarded as an oscillating system. Just like a piano string, it has its own (eigen) oscillations. Each oscillation is associated with a particular frequency, the eigen-frequency, and is often referred to as a “mode”. Such a mode describes a three-dimensional structure of the mass and wind field. Usually, these modes are discussed as perturbations to a resting basic atmospheric state (for a review see *Phillips* [1990]). Here we focus on the so-called Rossby modes that describe the flow component that is most relevant to the problem of atmospheric data analysis (*Daley* [1991], section 6.6). Rossby modes describe the relatively stationary component of the atmospheric flow, whereas inertia-gravity waves propagate fast and disappear quickly.

Rossby modes have low frequencies and obey a characteristic relationship between the wind and the atmospheric density or mass field. Outside the tropics, this mass-wind balance can be well approximated by the quasi-geostrophic relationship in which the pressure gradient force is closely balanced by the Coriolis force (see, e.g., *Holton* [1992]). The Rossby radius of deformation,  $R$ , can help to identify the conditions for exciting a Rossby mode, and may be defined as

$$R = \frac{\sqrt{gH}}{2\Omega\sin\Phi} \quad (1)$$

where  $g$  is the acceleration due to gravity,  $H$  the equivalent depth of the atmosphere,  $\Omega$  the angular velocity of the Earth and  $\Phi$  is latitude.  $R$  can be thought of as the horizontal length scale for which the mass and wind fields contribute equally in exciting the Rossby mode (*Holton* [1992], and *ESA* [1996]). *Gill* [1992] shows that geostrophic flow with a length scale of  $L > R$  contains mostly potential energy, whereas that with  $L < R$  is dominated by kinetic energy. In line with this, for  $L > R$ , mass field information is most relevant and the wind field adjusts to it, whereas for  $L < R$ , wind information is dominant and the mass field adjusts to it. One and another is depicted in Figure 1.

*Okland* [1970] found that Rossby modes are also relevant in a vertically stratified atmosphere. In such a case multiple equivalent vertical depths may be defined for each of which a Rossby radius applies. Note from equation (1) that vertically uniform or barotropic structures with an equivalent depth of  $10^4$  m are more sensitive to wind data than the vertically varying or baroclinic structures with a typical vertical depth of  $10^3$  m. In figure 1 their corresponding Rossby radii are respectively 3000 and 1000 km. Wind data are thus

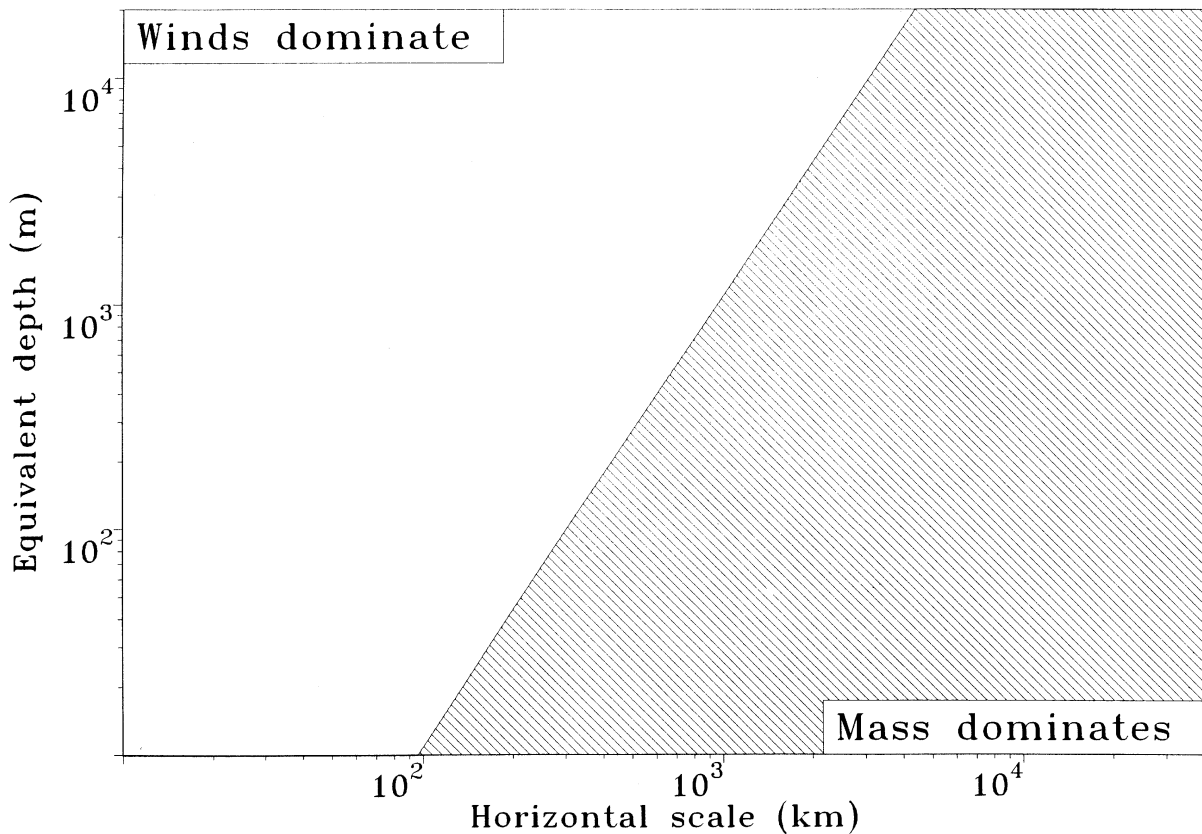


**Figure 1.** Rossby radius of deformation for a latitude of  $45^\circ$  as a function of horizontal scale and equivalent depth. Along both axes some typical atmospheric phenomena are indicated. Open areas denote the parameter range where the wind field dominates and in the gray area the mass field dominates ((c) ESA, 1996). Wind data is particularly relevant at the smaller horizontal scales.

relevant to determine the subsynoptic horizontal scales for particularly the larger vertical depths, whereas mass data are important to define the larger synoptic scales.

To investigate the effect of small-scale wind information versus the effect of small-scale mass information, *Daley* [1991] compares the geostrophic adjustment of a 8.5-km deep midlatitude mass perturbation to the adjustment of a nondivergent wind perturbation of similar energy and spatial scale. Almost all of the energy in the 400-km-scale mass perturbation is carried away by inertia-gravity waves in a time frame of 6 hours, whereas, over the same period, the similar-scale wind perturbation remains largely unchanged and is quickly accompanied by a balanced mass field. This confirms that small-scale wind information is most effective for analyzing the relevant component of the flow.

Figure 1 shows  $R$  for a latitude of  $45^\circ$ , and from equation (1) we note that  $R$  is latitude dependent. With decreasing latitude, wind data will gain importance for the exciting of the Rossby modes. As such, in the tropics the wind field will be the all-dominating factor for the atmospheric flow [*Gill*, 1982].

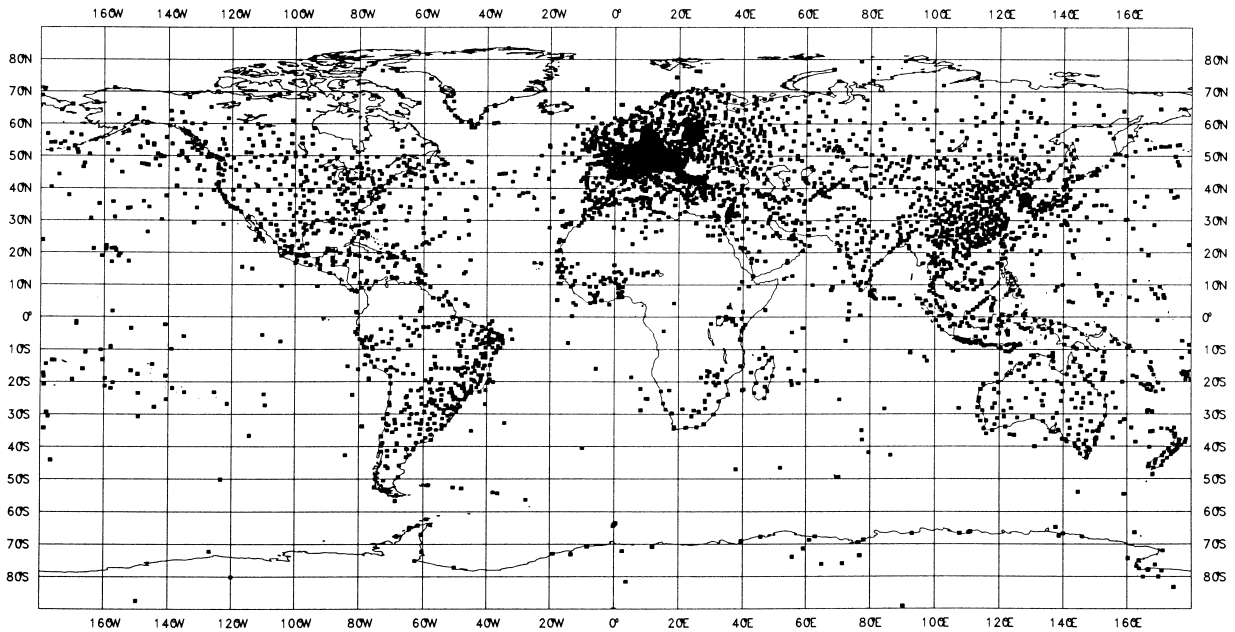


**Figure 2.** Above, the coverage of (a) stations measuring near surface variables (SYNOPS), and, on the right, (b) stations releasing balloon radiosondes for atmospheric profiling, and (c) aircraft observations. Large data sparse areas remain.

The above analysis of the atmospheric dynamics is relevant to define the observation requirements for wind measurements. It turns out that outside the tropics the large-scale component of the wind field may be derived from the atmospheric pressure and temperature fields, but that elsewhere pressure or temperature observations alone are not sufficient to describe the atmospheric flow. Wind measurements are necessary to define the circulation on the subsynoptic scales and in the tropics.

## 1.2. Global Observing System

Since the beginning of weather prediction it has been recognized that a sound meteorological observation network is a prerequisite to the success of such a system. The Global Telecommunication System, GTS, has been set up to distribute observations of relevant meteorological parameters in a timely manner. Conventionally, world-wide surface-based observations of pressure, temperature, humidity, wind and other weather parameters were communicated over the GTS, including balloon radiosondes that make vertical profiles of temperature, humidity and wind, while ascending in the atmosphere. Latter observations are an essential component of the Global Observing System, GOS (e.g., *Kelly* [1997]). Later on, aircraft measurement systems were included. However, these conventional observation types are not adequate to describe the atmospheric circulation in sufficient detail (see, e.g., *ESA* [1996], or *Stoffelen* [1993]). In Figure 2 a typical data coverage plot is shown for the near-surface meteorological observations and the radiosondes. Over land, these observations

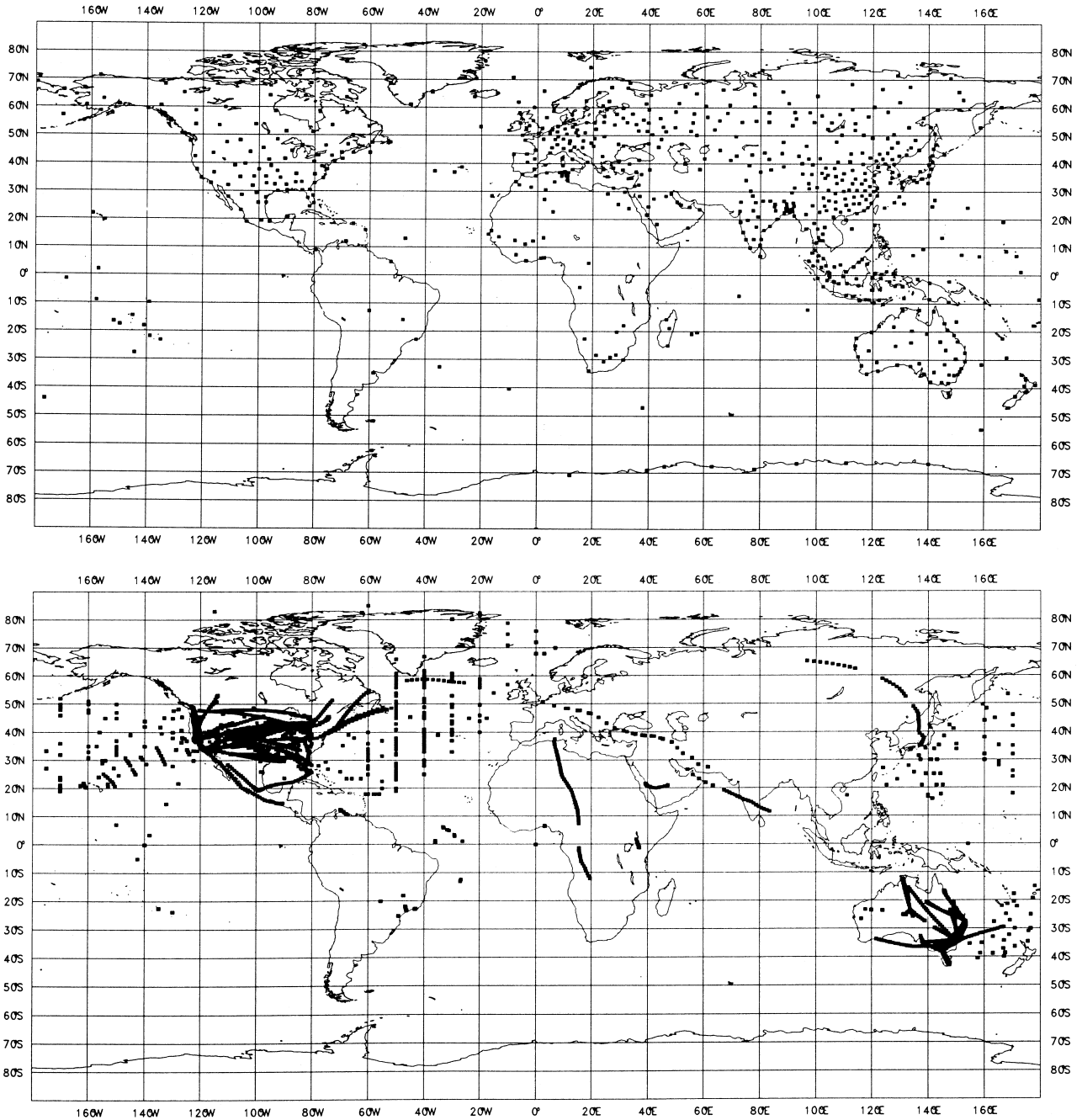


**Figure 2.** Continued.

are mainly available over the densely populated and more developed areas. Over the oceans much less observations are present, and those present, are close to the busiest sea and air traffic routes. Especially over the oceans, extended data sparse regions remain. Therefore, over the last two decades substantial effort has been devoted to the development of complementary space-borne systems that provide meteorological information in these otherwise data sparse regions.

The, in principle, simplest way to obtain information about the earth's atmosphere from Remote Sensing, RS, is by using so-called passive instruments. In this case the

instrument on board the spacecraft will measure the microwave, infrared, visual or ultraviolet electromagnetic (e.m.) radiation received from the Earth and its surrounding atmosphere. Since the atmospheric transmission is temperature and humidity content dependent, these so-called top-of-the-atmosphere radiances from sounding and imaging instruments can provide, among other things, information on the three-dimensional temperature and humidity structure of the troposphere and stratosphere. However, in section 1.1 it was argued that wind information is needed to describe the atmospheric flow in sufficient detail.

By tracking cloud features or humidity structures on subsequent images taken by passive instruments on geostationary satellites, one can get information on the atmospheric flow. Geostationary satellites have fixed positions above the equator and as such currently provide useful winds between latitudes of  $50^\circ$  south and north. However, it is often difficult to accurately assign a height to the structures tracked. Alternatively, one can estimate the wind speed over the ocean from passive microwave imagery. The emission of microwave radiation from the ocean surface depends on the surface roughness, which in turn depends on the near surface wind speed (see section 3.3). A drawback is that current wind algorithms lack accuracy in cloudy areas and do not provide wind direction. So, although some wind information may be obtained from passive instruments, their value for the analysis of the atmospheric flow also has some limitations.

Active instruments emit e.m. radiation towards the Earth, and after absorption, reflection or scattering by the Earth or its atmosphere, receive a small fraction of the emitted power back. Since only a very small fraction of the emitted power is returned, active sensing usually requires a powerful source and very sensitive detectors. An example of a potentially very useful active instrument that would help resolve atmospheric dynamics, is a space-borne Doppler Wind Lidar, DWL, [ESA, 1996]. In Figure 3 a sketch is given of a DWL. A DWL emits a laser pulse towards the Earth which is scattered in all directions by aerosol particles in the atmosphere. A very small part of the aerosol scattered radiation will be returned in the direction of the satellite and fall onto the DWL receiver. The movement of the aerosol particles with respect to the laser in the direction along the laser beam, called line of sight (LOS), will result in a so-called Doppler frequency shift, i.e., the frequency difference between the emitted and backscattered radiation is proportional to this movement. If one assumes that the particles move with the wind, then from the detection of the Doppler shift one may infer the wind along the LOS. Since aerosol particles are abundant in the troposphere and lower stratosphere, a DWL would be able to provide vertical profiles of the wind vector. A DWL requires a powerful laser source and a very sensitive detector. Nevertheless, well advanced programs exist for a DWL in space at ESA (ESA [1996]) and NASA.

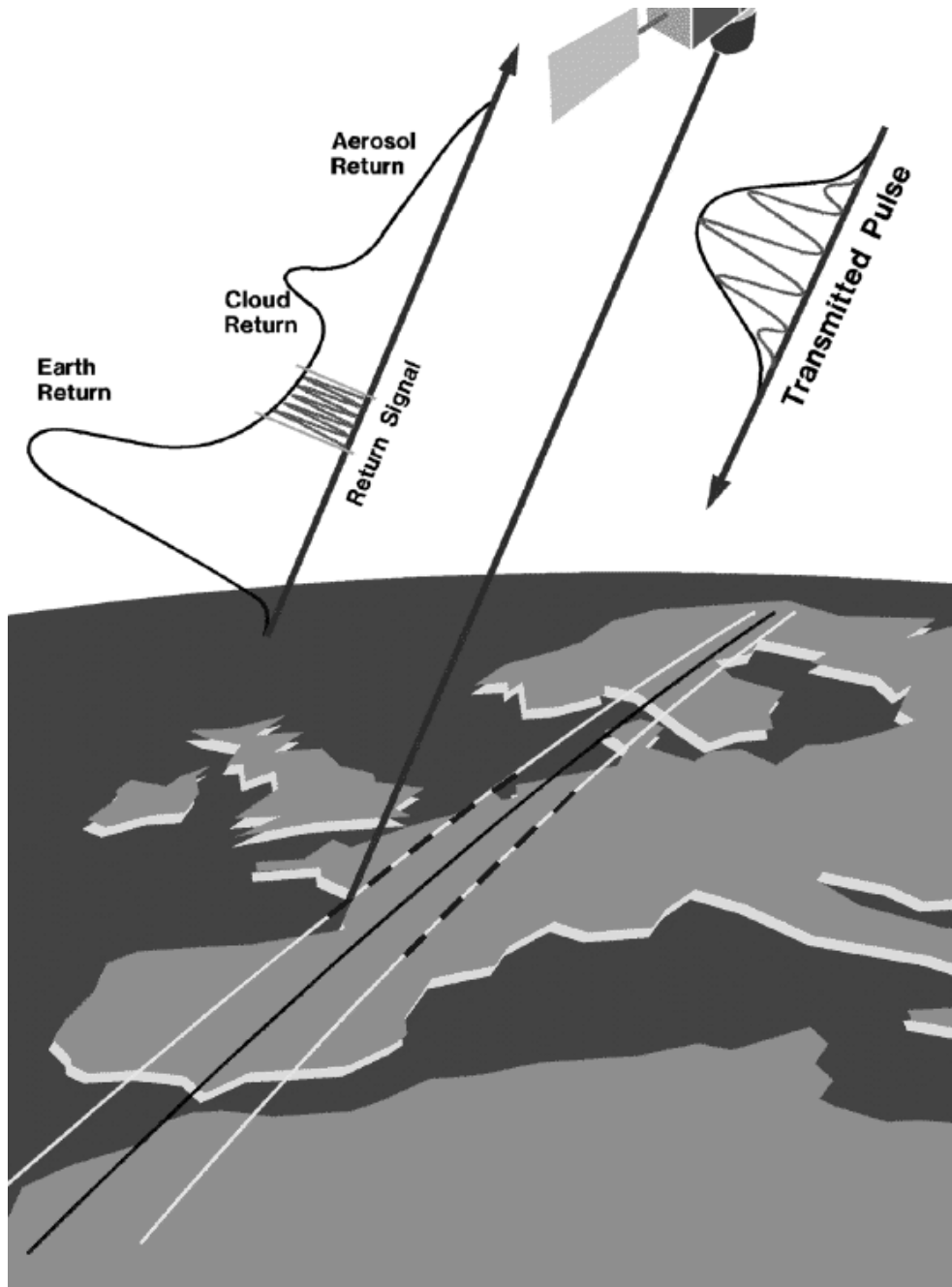


**Figure 3.** Sketch of the principle of a Doppler Wind Lidar useful for atmospheric dynamics (© ESA, 1996).

### 1.3. Data Assimilation

It is a challenging task to analyze the atmospheric state in a temporally and spatially consistent way from the broad range of available meteorological observations. This task is called data assimilation and depicted in Figure 4. In meteorological models the atmospheric

state is determined by typically  $10^7$  variables, but only of the order of  $10^4$  observed variables are present in a 6-hour assimilation window, i.e., data assimilation is an under-determined initial-value problem. To overcome this problem several solutions are offered. Firstly, knowledge on the time evolution of the atmospheric state is used by projecting information from past observations forward in time. This is done in the so-called forecast step, which results in a first guess for the next analysis. Secondly, statistical knowledge is used about the spatial coherence of the first guess error. This spatial coherence structure is then used to project the new observational information onto the model state vector. Thirdly, first guess errors in the temperature and pressure field are correlated with the errors in the wind field, since these fields are coupled (see also section 1.1). This correlation between the meteorological variables causes a pressure observation to modify the wind field and a wind observation to modify the pressure field in the analysis.

The data assimilation system has the following components:

- observation quality control,
- analysis step, and
- forecast step.

In the forecast step, using the previous analysis as initial conditions, a forecast model is run, which provides background information, the first guess, on the expected atmospheric state for the new observations in the next assimilation time window. The new observations will generally not perfectly agree with the background information, and in the analysis step both need to be compromised. If the accuracy of the observation is estimated to be poor, then the analysis will be close to the first guess. Conversely, when the observation is estimated to be very accurate as compared to the first guess, then the analysis will be close to the observation. The accuracies of the observations and the first guess are estimated on the basis of the monitoring of the differences between the first guess and the different observation types and parameters. In Chapter V, we explain in more detail the process of data assimilation.

Most observation types are not fully reliable. For instance, there may be a risk of instrument malfunction, a possibility that the measurement platform (satellite, ship, etc.) attitude or motion is incorrectly accounted for, a problem with the geophysical interpretation in certain extreme conditions, or hick-ups in the transmission of the data. All of these may cause the meteorological information content of the observations to be lost, and if such data are used in the data assimilation process, they may cause severe damage to the quality of the meteorological analysis. As such, it may be no surprise that an important aspect of the operational use of observations is their quality control and quality assurance.



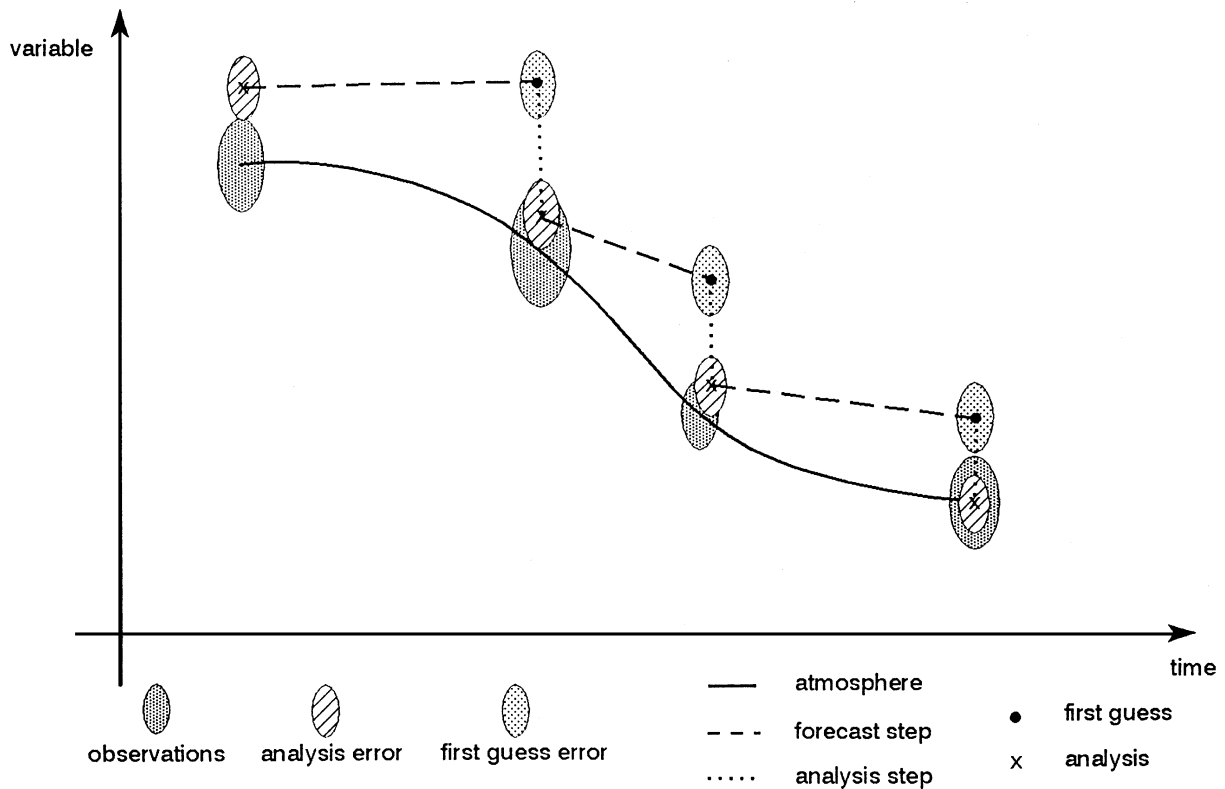


**Figure 4.** Schematic of data assimilation. The vertical axis represents the atmospheric state and the horizontal represents time.

#### 1.4. Weather and Wave Prediction

The real-time analysis and forecast of the wind is relevant for various applications. For example, ship and aircraft traffic may profit from wind information by saving fuel, and off-shore activities by assessing and reducing risks. Moreover, a skillful forecast of extreme wind events, usually associated with extreme waves and storm surges, is critical for these activities, as well as for, for example, tourism or indeed sometimes for the population in a broader sense (e.g., in case of severe storms or tropical cyclones). For the detection of subsynoptic scale phenomena, such as polar lows, the required spatial and temporal coverage is very large.

The availability of faster and more advanced computer systems, contributed to the fact that Numerical Weather Prediction, NWP, has considerably improved its skill over the last few decades. Naturally, improvements in the use of conventional observations, the use of satellite data, and improvements in the forecast model, have also contributed to the skill increase. The vastly expanding computer resources are spent to a large extent to improve the meteorological analysis, but also to increase the sampling of the analysis and forecast fields.

An immediate effect of this increased sampling is that the surface topography is better resolved, and thus the flow around mountains. Also other well-defined small scale forcing, e.g. due to the land-sea mask, may result in a better forecast of the flow.

However, in more general terms, the resolution of a short range wind forecast is determined by the density of the observational network, and is currently typically 250 km. In the absence of a denser meteorological observation network, there is thus little scope to better define the meso-scale flow. As such, scatterometer data are useful to fill in the data sparse areas.

For the validation of NWP model parameterizations it is further useful to have high resolution data for special cases, such as land-sea breezes or catabatic flow (e.g., mistral).

### **1.5. Climate**

Near surface wind in the tropics is an essential variable of the climate system but which is poorly defined. It determines momentum, heat, humidity, and carbondioxide gas fluxes at the interface of the atmosphere and the ocean. Moreover, the tropical atmospheric circulation (Hadley circulation) is of essential importance for predicting climate and climate change. There are several indications (see, e.g., *ESA* [1996] or *Kallberg* [1997]) that the Hadley circulation is ill-defined. Widely available and accurate near surface wind observations would improve the situation to a substantial degree.

### **1.6. Ocean Modeling**

The ocean is driven by atmospheric wind and heat exchange, and thus the output of an ocean model is strongly related to the quality of the forcing input. Most important in this respect are the air-sea momentum and latent heat fluxes that strongly depend on the wind in the surface (air) layer. Ocean circulation models play an important role in the earth climate system, and in the tropics for the seasonal forecasting of the El Niño southern oscillation. Ocean wave models are most sensitive to the accurate definition of the air-sea momentum flux.

For ocean modeling studies, NWP analyses may be used. As a refinement to these, re-analyses can be made over longer periods in the past, where all available measurements are used in the best possible way. This means that the observation requirements for NWP generally cover those for climate or ocean circulation and wave prediction.

A currently available active instrument that is most useful to help analyze the atmospheric flow is the scatterometer.

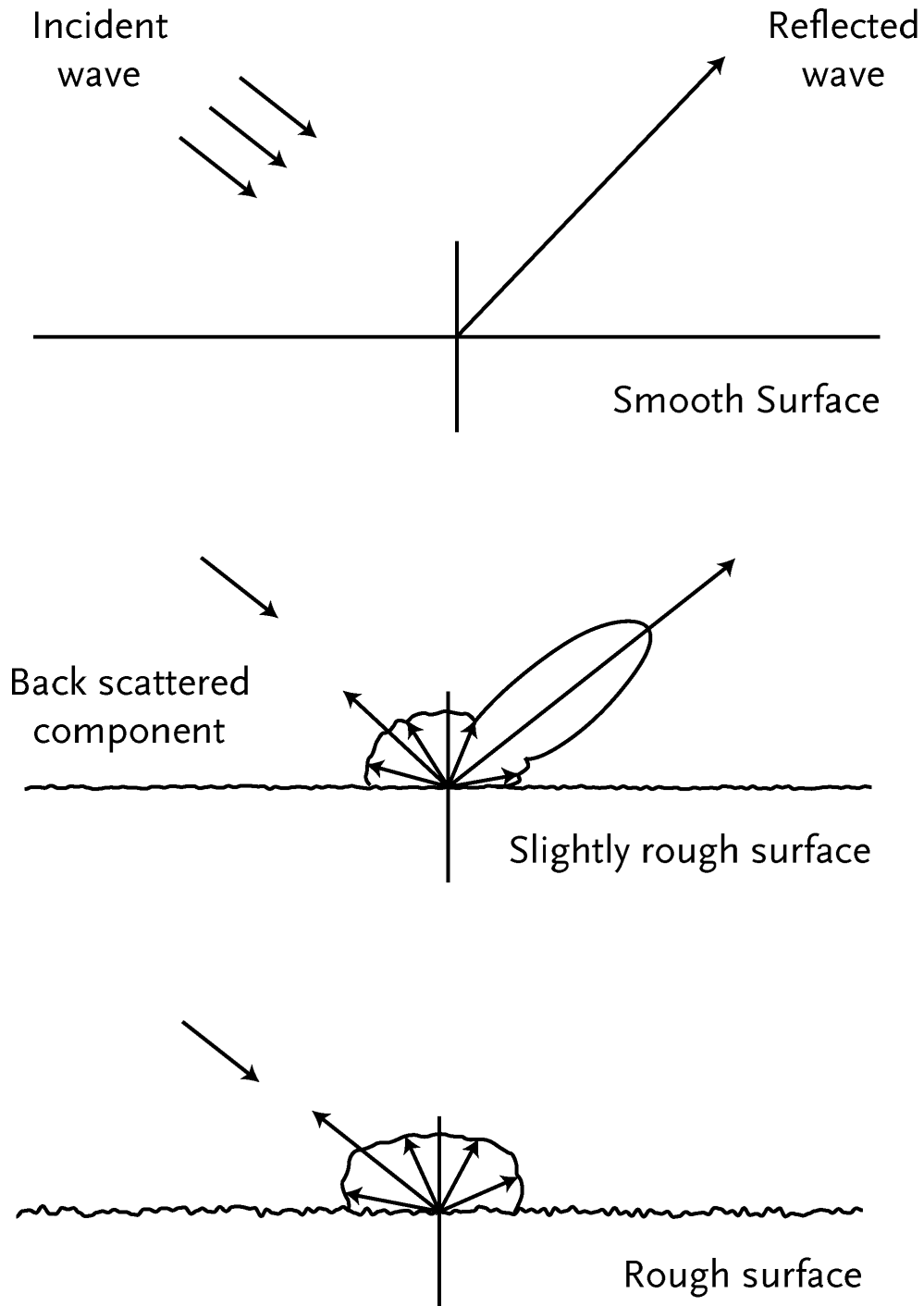


**Figure 5.** Schematic representation of microwave scattering and reflection at a smooth (a), rough (b) and very rough (c) ocean surface. As the roughness increases more microwave power is returned towards the direction of the microwave source.

## 2. Scatterometer Instruments

During the second world war, radar was much in use to detect and track hostile vessels. It was noted that this detection was more and more hampered with increasing wind speed. Naturally, the idea of measuring wind near the sea surface by using microwaves, i.e., scatterometry (e.g., *Moore and Pierson [1967]*), developed not much later. From an aircraft or satellite a microwave beam is emitted to the ocean surface under an angle, as depicted in Figure 5. This radiation, with a wavelength of some centimeters, will be scattered and reflected on the rough ocean surface and a small part of the power emitted will be returned to the detector of the scatterometer instrument.

### 2.1. Normalized Radar Cross Section

Suppose a point source emits a microwave pulse of power  $P_T$  uniformly in all directions in space. The power flux  $\Phi_T$  at a distance  $R$  from the source will then be  $\Phi_T = P_T / (4\pi R^2)$ . The antenna gain is defined as  $G = 4\pi / \Omega$ , where  $\Omega$  is the beam width in steradians in which the emitted power is contained. For an emission uniform in all directions  $G = 1$ , whereas for a narrow radar beam  $G \gg 1$ , and the power flux becomes  $\Phi_T = G P_T / (4\pi R^2)$ . Figure 6 depicts radar backscattering.

Now suppose that microwave radiation hits a scatterer. Then the radar cross section is defined as

$$\mathbf{s} = \frac{P_S}{\Phi_T} \quad (2)$$

where  $P_S$  is the backscattered power by the target. The radar cross section depends on the geometry of the target with respect to the incident microwaves and the dielectric constant of the material of the scatterer. The power detected by the receiving antenna, let's suppose it is identical to the source antenna and of size  $A$ , is then  $P_R = P_S A / (4\pi R^2) = G P_T \mathbf{s} A / (4\pi R^2)^2$ . For a narrow beam rectangular antenna, i.e.,  $L_X$  by  $L_Y$ , and a system without losses, a relationship exists between the gain  $G$  and the antenna surface area  $A$  since  $\Omega = (1/L_X)(1/L_Y) = 1^2/A$ . Thus  $A = 1^2 G / 4\pi$ .

A scatterometer has a footprint,  $F$ , of several tens of kilometers in diameter with generally a large number of scattering elements in it. For such a distributed target one may define a dimensionless microwave cross section per unit surface, often denoted "Normalized Radar Cross Section" or NRCS and by convention written as  $\mathbf{s}^0$ . We can now write:

$$P_R = \frac{1^2}{(4\pi)^3} \int_F \frac{P_T \mathbf{s}^0 G^2}{R^4} dF \quad (3)$$

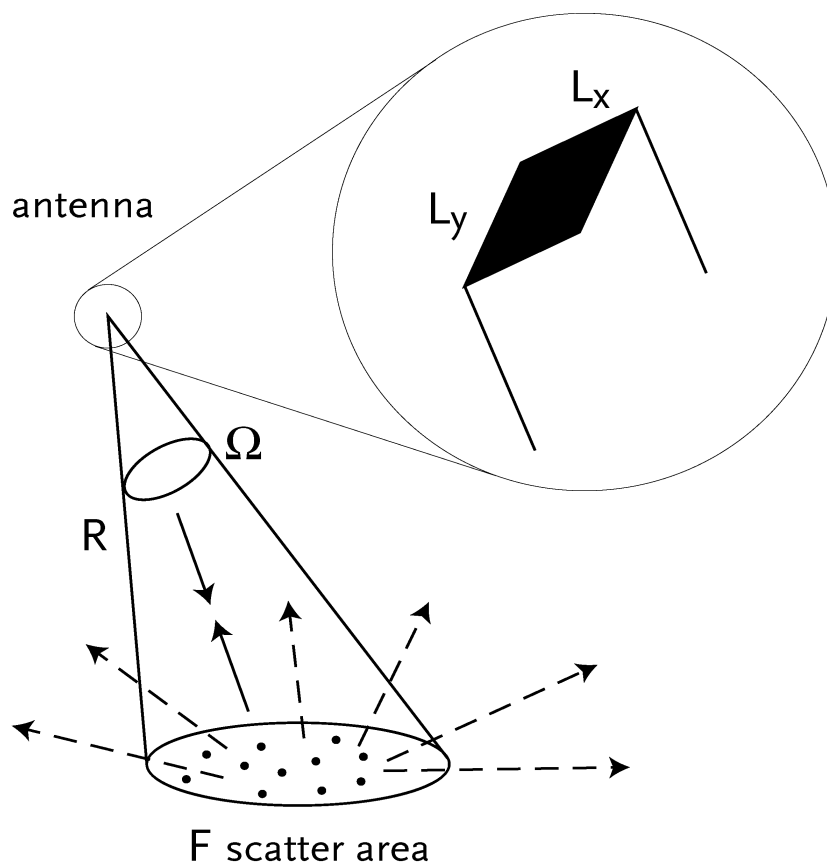


**Figure 6.** Microwave scattering.

In order to solve this integral one usually assumes that  $\mathbf{s}^0$  does not vary over the area of interest such that:

$$\mathbf{s}^0 = \frac{(4\mathbf{p})^3 R^4}{I^2 G^2 F} \frac{P_R}{P_T} \quad (4)$$

However, in reality the roughness elements on the ocean surface will largely depend on the local wind condition, which in turn exhibits large variability over a scatterometer footprint. As the scattering mechanism does not linearly depend on the geophysical condition, the geophysical variability within the footprint will contribute to  $\mathbf{s}^0$ . This will be particularly acute at low winds.

$\mathbf{s}^0$  is generally expressed in dB, i.e., as the value of  $10 \log(\mathbf{s}^0)$ .

The backscattered power turns out to be well correlated with the ocean near-surface wind conditions, and empirical relationships exist that describe this correlation (see, e.g., Chapter III or *Wentz* [1984]). Scatterometer retrieved winds may be validated against winds measured at conventional platforms (see, e.g., Chapter IV). The widely available and validated scatterometer winds provide, even below cloud, accurate and spatially consistent information on the near-surface atmospheric flow, and have as such become a relevant

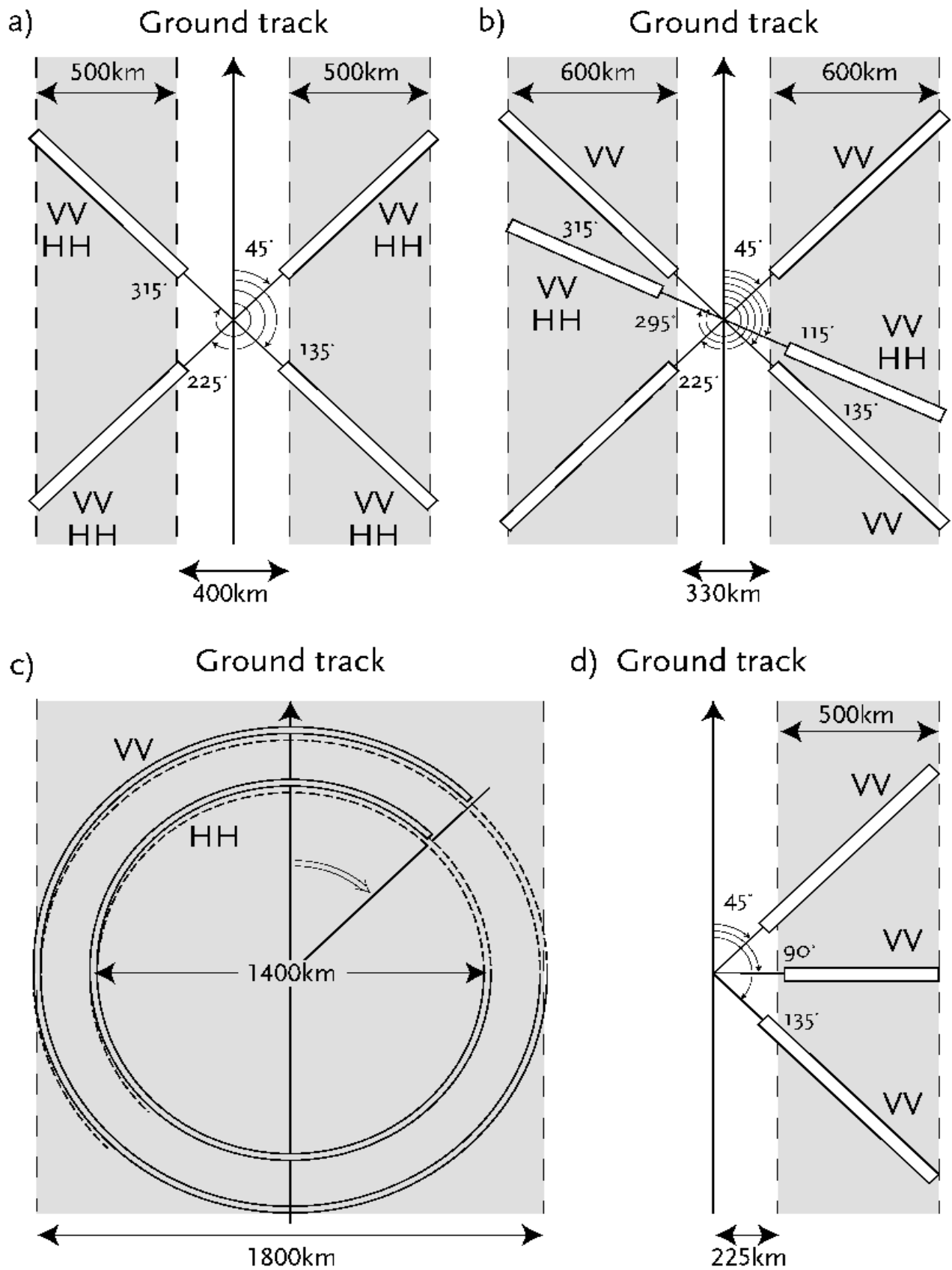
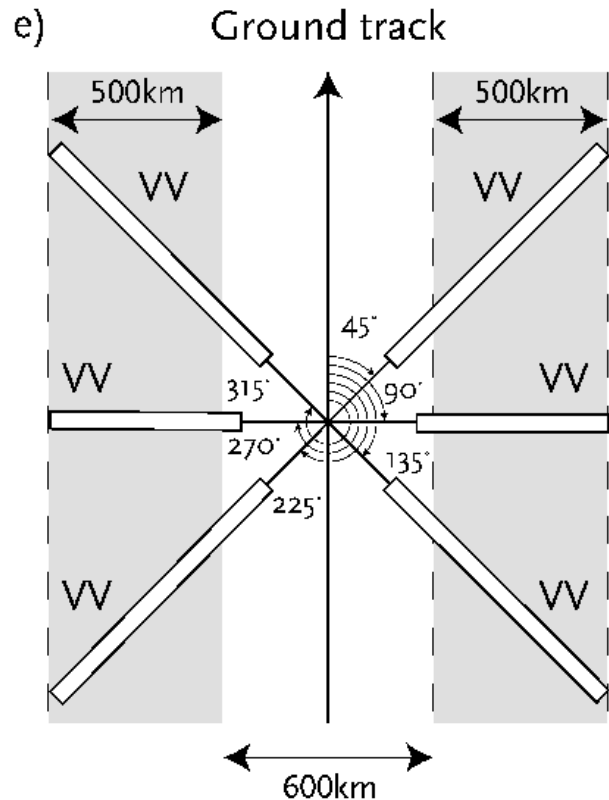


Figure 7. See at right page.

**Figure 7.** On the left, sketch of the microwave illumination pattern of a) SASS, b) NSCAT, c) SeaWinds, and d) SCAT, and, right, e) ASCAT on the earth's surface. The gray areas denote the swath and the arrow the direction of the ground track. All beams pass a particular location in the swath within  $\sim 7$  minutes. The ERS SCAT has a swath only at one side of the spacecraft and has therefore a smaller area coverage than the other scatterometers shown here. See text for further explanation.



component of the Global Observing System.

Given the evidence of the speed and direction sensitivity of ocean microwave returns, several concepts have been tested from ground, aircraft and space-borne platforms, that exploit this relationship. Focusing on space-borne efforts, we could distinguish the concepts used by NASA and those employed in Europe. These will be addressed respectively in the next two sections.

## 2.2. SeaSat, NSCAT and SeaWinds

The first scatterometer in space was the NASA SeaSat-A Scatterometer System, SASS, that flew in 1978 for amply three months. SASS had four antennae, two on both sides of the satellite, as depicted in Figure 7. Each set of two antennae covered a swath; one to the right of the subsatellite (ground) track and one to the left. In the horizontal plane, the fore and aft beams were pointing at respectively  $45^\circ$  and  $135^\circ$  with respect to the ground track. A location in the swath was first hit by the fore beam, and a few minutes later by the aft beam. Thus, each node in the swath revealed two backscatter measurements obtained with a  $90^\circ$  difference in azimuth. Figure 8 illustrates the analysis of two such measurements. For each measurement it shows the wind speed solution as a function of all possible wind directions. Given the basic harmonic wind direction dependency of the backscatter signal, four solutions exist in this general case. This ambiguity poses a strong limitation to the usefulness of the SASS wind data, and extended manual ambiguity removal efforts were

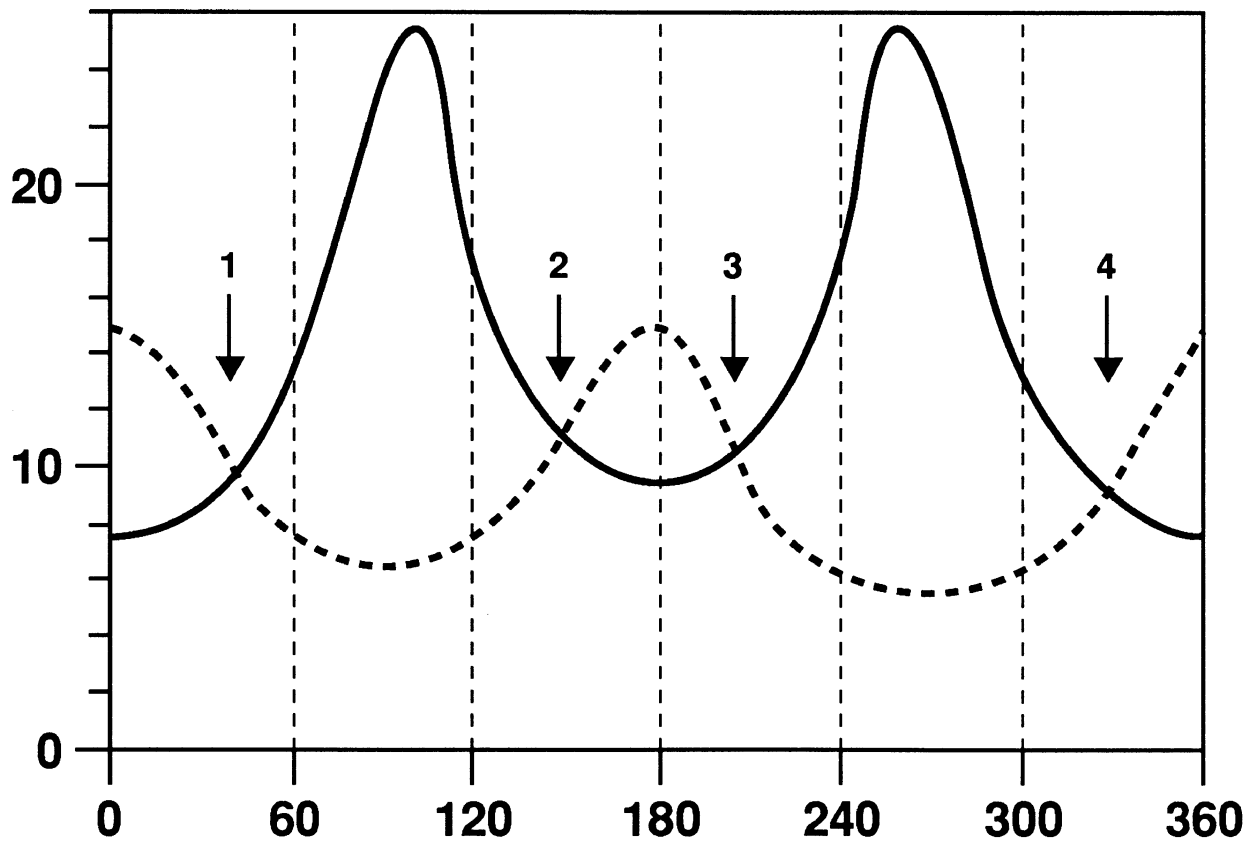


**Figure 8.** Wind speed as a function of wind direction for a fore and aft beam measurement of backscatter from SASS. The arrows indicate the four possible solutions.

needed to obtain an acceptable wind product [*Peteherych et al.*, 1984]. With this product the usefulness for NWP could be shown (see, e.g., *Stoffelen and Cats* [1991]).

In a follow-on design, i.e., NSCAT, a beam was added in between the fore and aft beams to both sides of the swath, as shown in Figure 7. The polarization of the microwave radiation emitted and received by the mid beam was both vertical, called VV, and horizontal, called HH. For the other antennae and instruments only VV polarization is used. For HH polarization, the relationship between backscatter and wind differs from VV, and as such the HH polarization provides useful complementary information, in particular on wind direction. The addition of an antenna with two polarizations makes that at each location in the swath four independent measurements are available. The two additional measurements help resolve a unique wind vector solution. However, an azimuth direction of the mid beam precisely in between the azimuths of the fore and aft beams would have better sampled the harmonic wind direction dependency. This was not done for technical reasons.

NSCAT was mounted on the Japanese Advanced Earth Observation Satellite, ADEOS. After nine months with useful NSCAT data, at the end of June 1997, the Japanese space



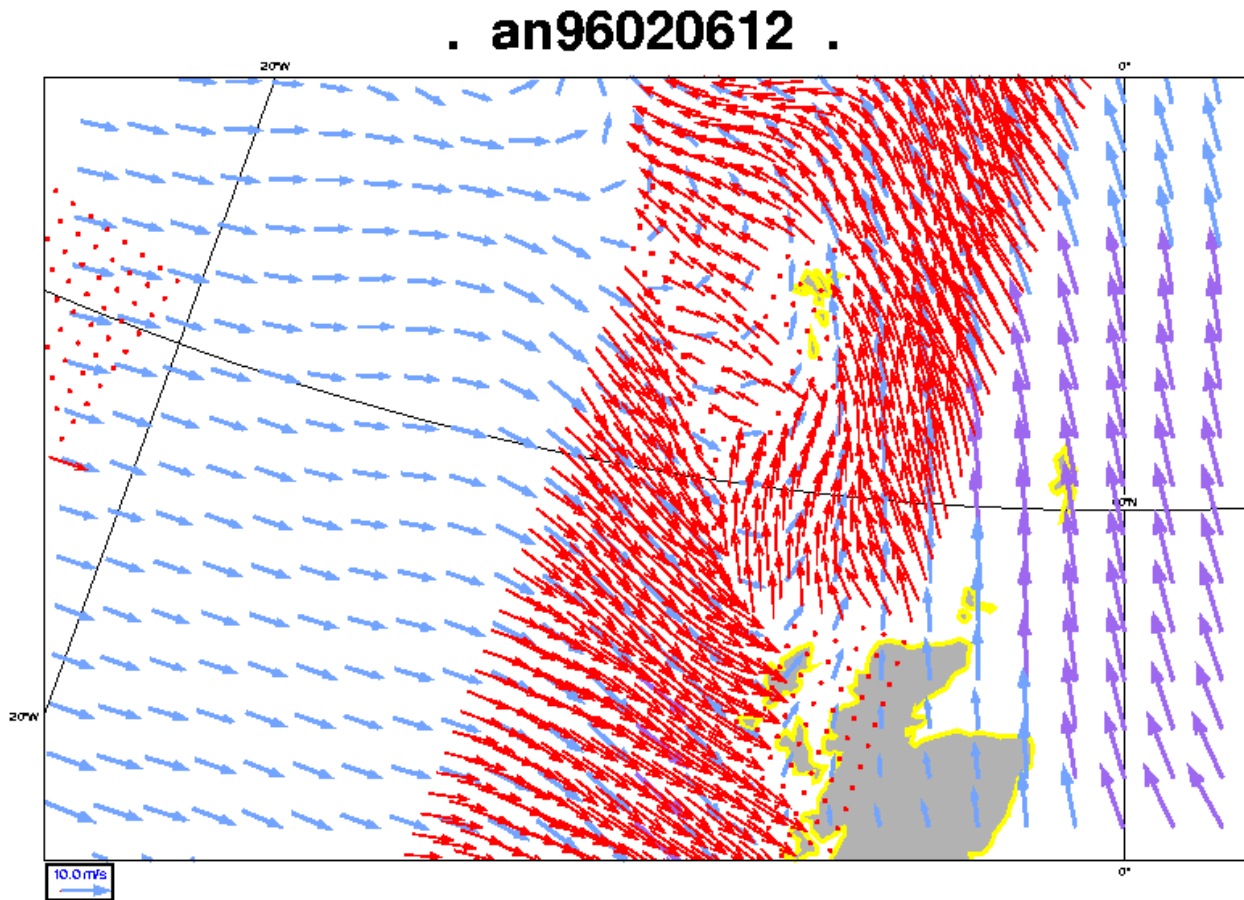


**Figure 9.** An example of a ERS-1 and ERS-2 SCAT retrieved wind field in red obtained with the methodology described in this thesis. Winds from the HIRLAM NWP model are shown as background in blue [Stoffelen and van Beukering, 1997].

agency, NASDA, lost control of the ADEOS after a complete power loss. This dramatic event has been a severe set-back for Earth Observation, and scatterometry in particular.

QuikSCAT, which is the next scatterometer to become operational, is planned on a dedicated polar satellite, projected for launch in November 1998. QuikSCAT is the first scanning scatterometer as depicted in Figure 7. A scanning scatterometer may accommodate a broad swath. However, a disadvantage of such a concept is that at the extreme ends of the swath, the earth surface is only illuminated from a single azimuth direction. Moreover, in the middle of the swath, at the so-called subsatellite track, the ocean is only illuminated from two exactly opposite directions. The limited azimuth sampling means that wind direction can only be poorly resolved at these locations. Fortunately, the total QuikSCAT swath width of 1800 km guarantees that the full wind vector can be determined accurately over a large range across-the swath.

The record-fast QuikSCAT program was planned after the dramatic loss of NSCAT, in order to fill the gap between the ADEOS-I and ADEOS-II missions. ADEOS-II will carry a

scatterometer very similar to QuikSCAT, called SeaWinds, and is planned for launch in early 2000.

SASS, NSCAT, QuikSCAT, and SeaWinds use a microwave wavelength of 2.1 cm (14.6 GHz frequency; denoted Ku-band). This frequency is affected by atmospheric attenuation due to cloud liquid water and rain. Furthermore, rain droplets hitting the ocean surface distort the gravity-capillary waves, and may complicate the backscatter-wind relationship. Latter effects become substantially smaller for a higher wavelength. To avoid such effects and focus on reliable wind data below cloud, the ESA scatterometers on board the ERS-1 and ERS-2 satellites, and the ASCAT scatterometer planned on the European METOP satellite series use a wavelength of 5.7 cm (5.3 GHz frequency, denoted C-band).

### 2.3. ERS Scatterometers and ASCAT

The first ESA remote sensing satellite, ERS-1, was launched on 17 July 1991 into a polar orbit of 800 km height. In 1995 the ERS-1 follow-on, ERS-2, was launched. The ERS-1 and ERS-2 scatterometers, which are identical and denoted SCAT here, each have three antennae, that illuminate the ocean surface from three different azimuth directions, as shown in Figure 7. A point on the ocean surface will first be hit by the fore beam, then by the mid beam and at last by the aft beam. In Chapter II of this thesis it is shown that this measurement geometry generally results in two opposite wind vector solutions. In Chapter V it is discussed how a unique wind vector solution may be selected from the two optional ones. Chapter III describes the estimation of a backscatter-wind relationship for the wavelength used by SCAT. The SCAT wind product has a high quality and shows small scale meteorological structures, as shown in Figure 9.

A limitation of the SCAT is its coverage. In contrast to the NASA Ku-band scatterometers, SCAT only views at one side of the subsatellite track. Moreover, the microwave source is shared with a SAR instrument, so that the operation of SCAT is often not possible in meteorologically interesting regions (e.g., in the Norwegian Sea). Although with ERS-1 and ERS-2 two working SCAT and SAR instruments are in orbit at the moment, for different reasons only the ERS-2 scatterometer is operated, and only part time (shared mode with ERS-2 SAR). Certainly after the decline of NSCAT this is a regretful situation. Tandem ERS-1 and ERS-2 SCAT numerical weather prediction impact experiments by ECMWF [*Le Meur*, 1997] and KNMI [*Stoffelen*, 1997] have shown that two scatterometers have more than twice the value of one.

The ASCAT (advanced) scatterometer due on METOP, which is planned for launch in 2003, will use the same radar wavelength as SCAT, but will be double sided and have a dedicated microwave source. Figure 7 depicts the measurement configuration of ASCAT and Figure 10 shows the coverage that would be obtained by ASCAT over a period of 12

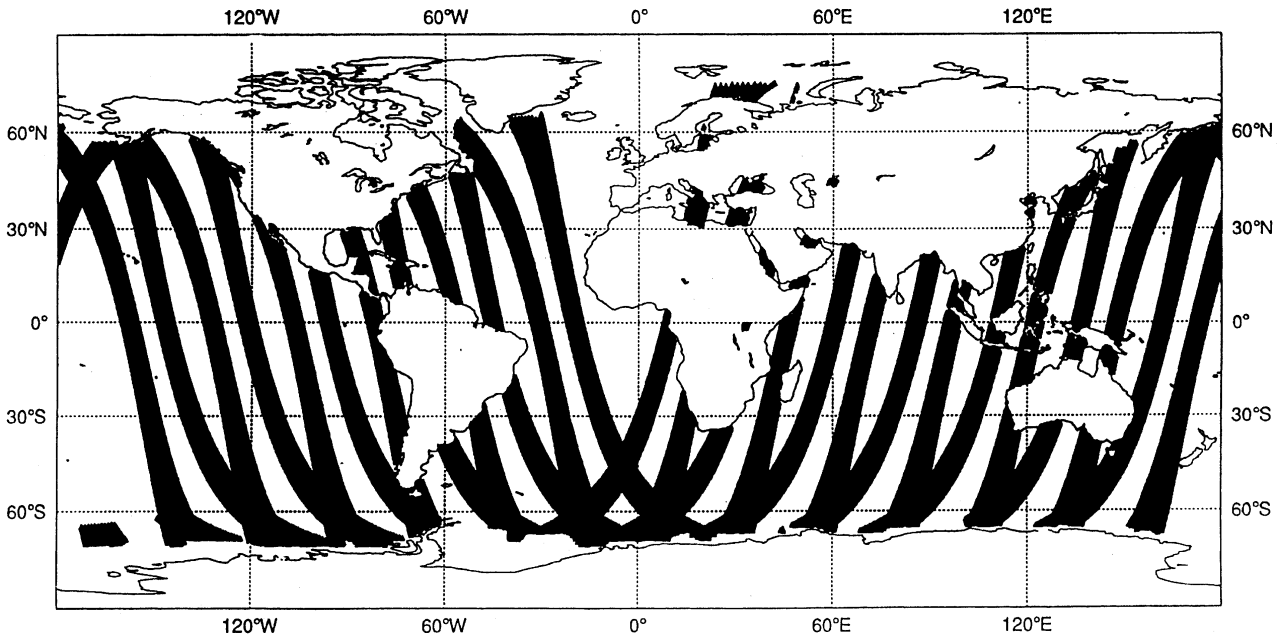


**Figure 10.** The coverage after half a day expected from the ASCAT scatterometer on METOP to be launched in 2002.

hours. The interpretation of ASCAT will benefit much from the knowledge gained during the ERS missions. The extreme outer part of the ASCAT swath, however, corresponds to microwave incidence angles that were not available in the SCAT swath, and may need further investigation.

### 3. The Physics Behind Scatterometry

As already mentioned, scatterometry was developed heuristically. It was found experimentally that the sensitivity to wind speed and direction describes well the changes in backscatter over the ocean. In Chapters II and III of this thesis this is further confirmed and it is found that within the measurement noise of the SCAT, which is as small as 0.2 dB, a dependency on two geophysical parameters generally holds. When, in Chapters III and IV wind speed and direction are taken to be the two geophysical parameters, then a substantially larger uncertainty is introduced that amounts to a wind vector RMS error of approximately  $2.5 \text{ m s}^{-1}$ . However, such an error in a near surface wind observation is quite acceptable.

In this section we will try to relate the empirical methodology followed in this thesis to the current knowledge of the physics involved in scatterometry. It is important to realize that in the approach followed in this thesis  $\mathbf{s}^0$  is related to the wind at 10 meter height above the ocean surface, simply because such measurements are widely available for validation. This means that any effect that relates to the mean wind vector at 10 meter height is incorporated

in the backscatter-to-wind relationship. As such, we will show that air stability, the appearance of surface slicks, and the amplitude of gravity or longer ocean waves, depend to some degree on the strength of the wind and may, to the same degree, be fitted by a backscatter-to-wind transfer function.

Several attempts have been made to provide a theoretical framework in which all aspects of scatterometry are tackled, e.g., *Donelan and Pierson* [1987] or *Snoeij et al.* [1992]. Below we highlight some main aspects.

### 3.1. Electromagnetic Interaction of Microwaves With the Ocean Surface

The relevant physical phenomenon that is important for the working of the scatterometer is the presence of the so-called gravity-capillary waves on the water surface. Gravity-capillary waves have a wavelength of some centimeters and respond almost instantaneously to the strength of the local wind [*Plant*, 1982]. Microwave scattering (see Figure 5) strongly depends on the amplitude of the gravity-capillary waves. Furthermore, the caps of these waves tend to align perpendicular to the local wind direction and thus the ocean radar return is wind direction dependent.

Figure 11 depicts the resonant scattering of microwaves on gravity-capillary waves, called Bragg scattering. The condition for resonance of the incoming microwaves is

$$l_B = \frac{n l}{2 \sin q} \quad (5)$$

where  $l$  and  $q$  are the microwave wavelength and incidence angle respectively,  $l_B$  the gravity-capillary (Bragg) wavelength, and  $n$  a positive whole number. The condition  $n = 1$  contributes predominantly to the microwave return (see, e.g., *Valenzuela* [1978]) and one may approximate  $S^0$  as

$$S^0 = T(q)[E(2k) + E(-2k)] \quad (6)$$

where  $k$  is the vector wave number of the radar beam with amplitude  $k = 2\pi/l$ ,  $E$  is the spectral energy density of the short surface waves, and  $T$  is a transfer function describing the electromagnetic interaction with the ocean surface. It is noted that both approaching and receding waves contribute to the backscattering. This indicates a potential ambiguity in the inversion of this equation. We will come back to this in the next subsection. Bragg scattering is thought to be dominant for an incidence angle range of  $20^\circ > q > 70^\circ$ .

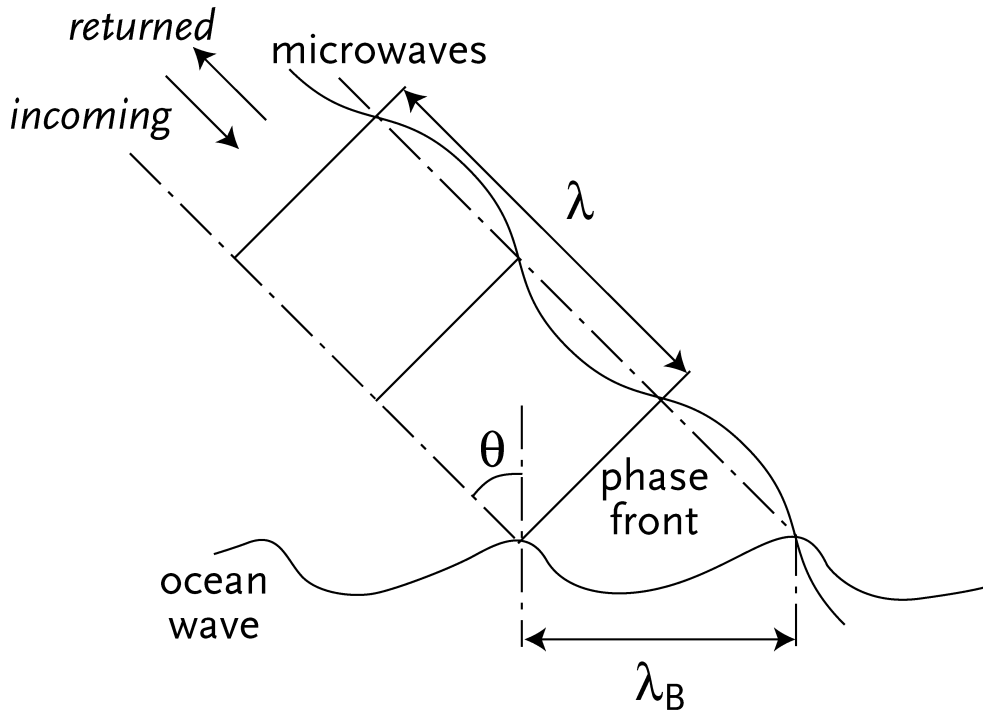


**Figure 11.** Bragg scattering: A plan-parallel radar beam with wavelength  $\lambda$  hits the rough ocean surface at incidence angle  $\theta$ , where capillary gravity waves with Bragg wavelength  $\lambda_B$  will cause microwave resonance.

Specular reflection is another mechanism to get ocean microwave return. Facets of the ocean that are normal to the incident microwaves will reflect the radiation back in the direction of the radar antenna. For increasing incidence angles, the probability that a facet has the appropriate orientation to contribute to specular reflection decreases, since the steepness of ocean waves is limited. As such, this mechanism is thought to provide a non-negligible contribution to  $S^0$  for incidence angles smaller than  $30^\circ$  [Stewart, 1985].

Several approximations exist that theoretically try to describe the interaction of e.m. waves with the ocean surface (see, e.g., *Snoeij et al.*, [1992]). However, for laboratory experiments in a wave tank these different models show a dispersion of several dB, which is large compared to the accuracy of the ERS scatterometer of 0.2 dB.

### 3.2. The Ocean Topography

The topography of a rough ocean surface is much more complicated and dynamic than the relatively simple wave states that are usually generated in laboratory experiments, which is further complicating a useful description of the interaction of a microwave beam with such an ocean surface. Furthermore, the local interaction theories need to be extended in order to provide a useful theory over a scatterometer footprint and take into account the sea state variability.

At low wind speeds the wind direction and speed may vary considerably within the scatterometer footprint. Locally, below a speed of roughly  $2 \text{ m s}^{-1}$ , calm areas are present where little or no backscatter occurs, perhaps further extended in the presence of natural slicks that increase the water surface tension [*Donelan and Pierson, 1987*]. However, given the variability of the wind within a footprint area of  $50 \text{ km}$  it is, even in the case of zero mean vector wind, very unlikely that there are no patches with roughness in the footprint. Likely, for low mean vector wind the patchiness or associated wind variability will determine the amount of backscatter, and not the amplitude of the mean vector wind. However, as the mean vector wind increases, the probability of a calm patch will quickly decrease, and the mean microwave backscatter will increase. Also, natural slicks quickly disappear as the wind speed increases, and as such the occurrence of these is correlated to the amplitude of the mean vector wind over the footprint.

As the mean wind speed increases, gravity waves (decimetric) and longer waves (metric or larger) will be formed. The gravity-capillary waves have a phase speed which is different from that of the gravity and longer waves and all have a complicated dynamic interaction as sketched in Figure 12 (from *Mastenbroek, [1996]*). The wind has maximum impact close to the crest of the long wave, due to the presence here of gravity waves with maximum amplitude. Since the gravity-capillary waves are in quasi-equilibrium with the wind stress, they have also maximum amplitude at the long wave crest. Mastenbroek argues that in turn the growth of the long waves is enhanced by these modulation mechanisms.

For moderate wind speed, waves will start to break and so-called white-caps will occur. The breaking will generate gravity-capillary waves in addition to the wind generated ones (see, e.g., *Phillips [1977]*). This hydrodynamic modulation will cause the energy density of these waves to be different on the lee- and luffward side of the long waves. The two terms on the right-hand side of equation (6) will then be different which may help resolve approaching and receding waves. In fact, there is generally a distinguishable difference in the backscatter level between upwind (approaching) and downwind (receding). However, as shown in Chapter II, it turns out that with the three-antenna geometry of SCAT or ASCAT, this difference does not lead to a possibility to discriminate between the upwind and downwind solutions.

It is also shown in Chapter II that the upwind-downwind backscatter ratio shows a strong dependence on incidence angle at around  $35^\circ$ . This may indicate the transition of a regime where specular reflection plays a role, i.e., the lower incidence angles, to a regime where it is negligible and Bragg scattering is fully dominating (see section 3.1).

At higher wind speeds wave breaking will further intensify, causing air bubbles, foam and spray at the ocean surface, and a more and more complicated ocean topography. Although theoretically not obvious, it is empirically found that  $\sigma^0$  keeps increasing for

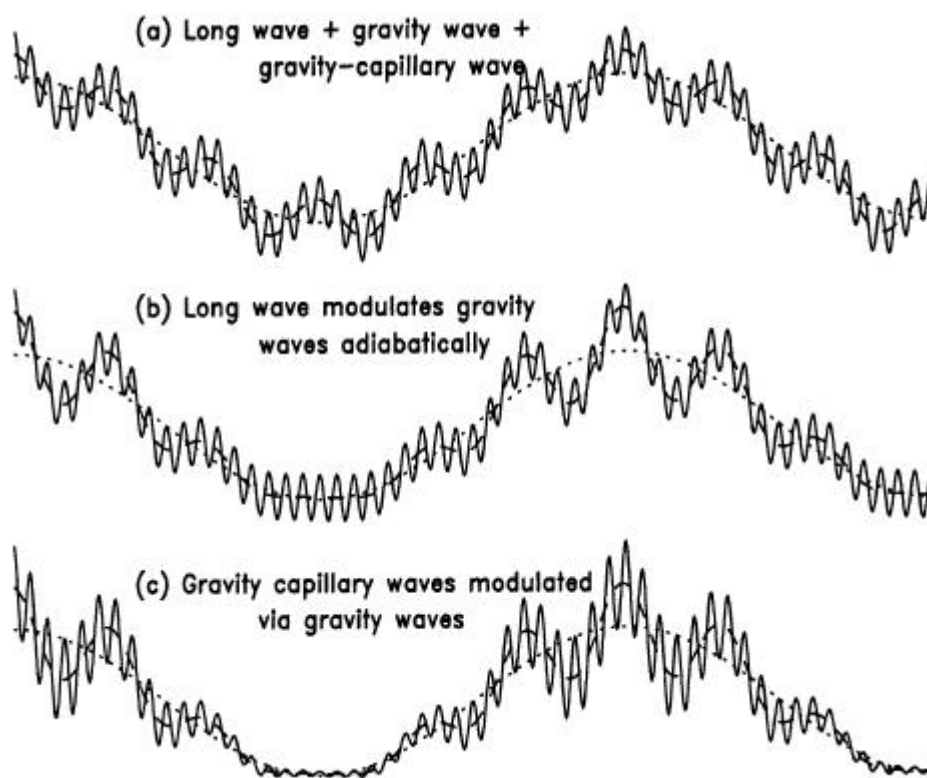


**Figure 12.** Schematic representation of the indirect modulation of short gravity-capillary waves by a long wave. (a) A simplified system consisting of a long wave (dotted), a gravity wave (dashed), and a short gravity-capillary wave (solid line). In (b) the modulation of the gravity wave by the orbital velocity of the long wave is taken into account. The gravity waves have maximum amplitude at the crest of the long wave, and as a result the airflow exhibits maximum shear stress here. In (c) this is taken into account and also the gravity-capillary waves have their maximum amplitude at the crest of the longer wave (Figure 5.1 from *Mastenbroek* [1996]).

increasing wind speed, and that a useful wind direction dependency remains, as discussed in Chapter II.

### 3.3. From Capillary Waves to Winds

Thus, there exists a relationship between the amount of backscattered microwave power and the energy density of the gravity-capillary waves. Also, there is a relationship between the energy density of the gravity-capillary waves and the so-called surface shear stress (momentum flux), denoted  $\mathbf{t}$ , which is a measure of the impact the wind has on the ocean surface. Wind shear stress is not a practical variable to use for calibration or validation, since its observation is complicated and measurements of this quantity are not widely available. On the other hand, wind observations are relatively straightforward and

widely available. The relationship between surface stress and wind at a reference height, let's say 10 m and referred to as  $U_{10}$ , is not without uncertainty, as will be discussed here. Therefore, in order to find an empirical relationship, it appears favorable to correlate  $\mathbf{s}^0$  with  $U_{10}$  rather than with the corresponding  $\mathbf{t}$  computed from  $U_{10}$  with a nonlinear and uncertain equation. Then, the uncertainties in the physics will be mainly in the wind-to- $\mathbf{s}^0$  transfer function, and not in the measurements used for validation or calibration. Obviously, once a wind-to- $\mathbf{s}^0$  relationship is established one can also, with the geophysical uncertainties involved, compute a stress-to- $\mathbf{s}^0$  relationship.

The following definition is widely used to relate  $\mathbf{t}$  and  $U_{10}$  :

$$\mathbf{t} = -\langle \mathbf{u}'\mathbf{w}' \rangle = C_D U_{10} U_{10} \quad (7)$$

where  $\langle \mathbf{u}'\mathbf{w}' \rangle$  is the ensemble average of the product of the horizontal and vertical wind component fluctuations, and  $C_D$  the so-called drag coefficient. In (7) it is assumed that the directions of  $\mathbf{t}$  and  $U_{10}$  are the same. This is a reasonable assumption in the so-called surface layer where  $\mathbf{t}$  is approximately constant with height (see, e.g., *Holton* [1992]). The surface layer extends typically to a height of 30-50 m, but may be more shallow in low wind conditions. The reference height of 10 m for wind observations is thus generally well within the surface layer.

Using (7),  $C_D$  has been investigated in many experimental campaigns over the last 20 years, and shows a large spread, i.e.,  $3 \cdot 10^{-4} > C_D > 5 \cdot 10^{-3}$ . Parameterizations of  $C_D$  may differ by 20 % or more (e.g., compare *Smith et al.* [1992], and *Donelan et al.* [1993]), but commonly show an increase with increasing  $U_{10}$ . This increase will implicitly be incorporated into an empirical wind-to- $\mathbf{s}^0$  transfer function.

Furthermore, atmospheric density effects, through temperature or humidity fluctuations, may affect the drag. Therefore, it has been suggested to correct measured winds to “equivalent neutral” winds [*Liu and Tang*, 1996] in the process of estimating a transfer function or validating scatterometer winds. In this case, one assumes that the scatterometer essentially measures  $\mathbf{t}$ , and by using neutral stability drag, denoted  $C_{DN}$ , one can relate this to a unique “equivalent neutral” wind,  $U_{10N}$ , by using equation (7). This scatterometer wind may then be compared to an independently obtained  $U_{10}$ , e.g. from an anemometer, after multiplication of it by  $(C_D/C_{DN})^{1/2}$  in order to obtain an “equivalent neutral” wind. An example of such correction in the tropics is shown in Figure 13. It is clear that stability is expected to be a function of wind speed.



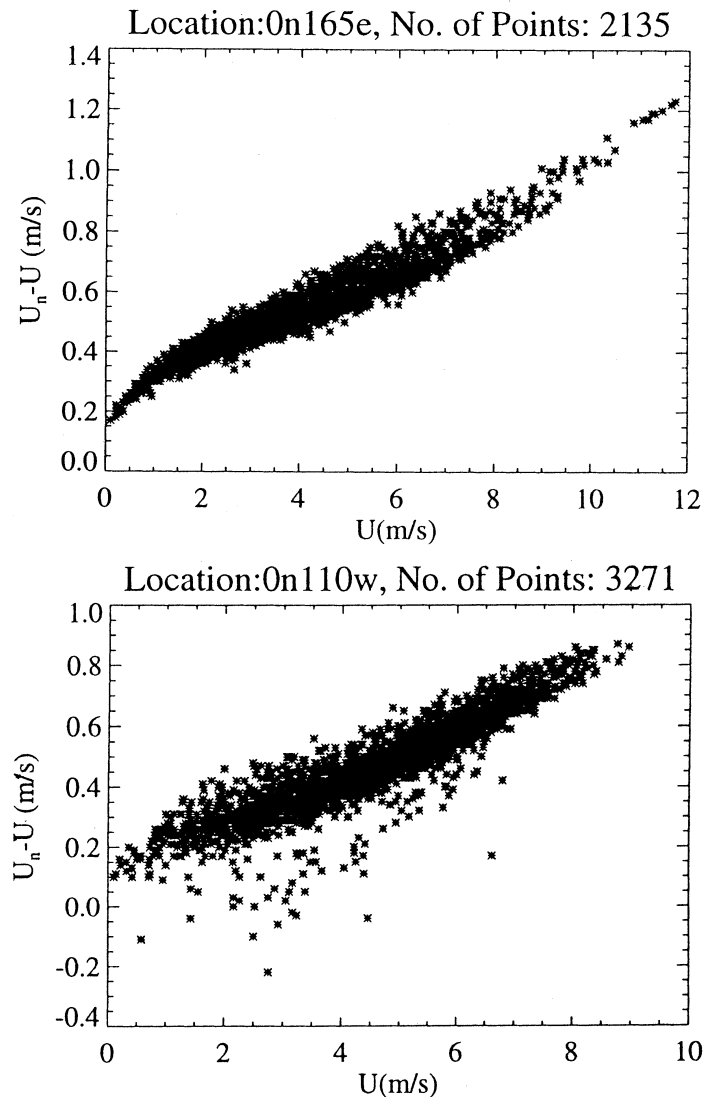


**Figure 13.** The difference of equivalent neutral wind,  $U_N$ , and actual wind,  $U$ , measured at a reference anemometer height, versus  $U$  at two TAO buoys in the western and eastern equatorial Pacific [Liu and Tang, 1996].

When estimating a transfer function by using weather model winds, as described in Chapter III, it is difficult to obtain accurate knowledge on the atmospheric stability. In the absence of such information, a correction as suggested by Liu and Tang [1996] is merely a source of wind error, the more so as the correction depends in a critical way on stability information. Since stability is a function of wind speed, using  $U_{10}$ , rather than  $U_{10N}$  in an estimation will implicitly incorporate some stability correction. Even if we had used anemometer winds to estimate and validate the transfer function, it is doubtful whether a correction based on the local stability, as inferred from e.g. buoy measurements of temperature and humidity, would have been representative of the stability averaged over the 50 km scatterometer footprint. In fact, this could be investigated by comparing scatterometer

and buoy wind speed differences to the anticipated residual stability correction computed from the buoy temperature and humidity information. Since this is not done yet, we did not attempt stability correction of the validation wind data sets in this thesis.

When the wind picks up suddenly, the gravity-capillary waves at the ocean surface start to grow immediately and gradually propagate their energy onto the longer waves. As the longer waves grow and move in the direction of the wind, the surface stress will gradually decrease. For a given wind speed, one could thus distinguish “young” and “rough”, and, “developed” and “smooth” sea states, corresponding to relatively large and small drag respectively. At  $10 \text{ m s}^{-1}$  *Smith et al.* [1992] and *Donelan et al.* [1993] parameterizations show a large effect due to sea state, but which is different by a factor of two. In contrast, *Mastenbroek* [1996] estimates the effect of a varying amplitude of the longer waves on the mean surface roughness to be generally small, which suggests that the sea state is generally not very important for the interpretation of scatterometer data. The generally high accuracy of scatterometer winds, as described in Chapters III and IV, indeed suggests that an additional parameter such as sea state is of secondary importance. Nonetheless, we found that in 1-2% of cases, often very close to intense fronts or lows our empirical two-parameter wind-to-backscatter transfer function provided a less good description. A probable cause is that longer waves exist that are not in equilibrium (yet) with the wind, i.e., what is called a confused sea state in Chapter IV. It is noted however, that rain, air stability, or spatial processing effects may also be the cause.

#### **4. Aim and Overview of the Thesis**

The aim of this thesis is to provide an accurate interpretation of ERS scatterometer winds for use in meteorological applications. It has become clear that a dependency of the microwave backscatter on the near surface wind vector explains much of its variability. Secondary geophysical effects may be investigated by correlating the residual errors to other quantities, such as sub-footprint wind variability, sea state or air stability, as mentioned earlier in this chapter. In line with the discussion in the previous paragraph on the prime wind dependency, these secondary geophysical dependencies may be mixed with effects of a statistical nature, and a careful analysis will be necessary to separate physics from statistics.

Thus, it may not be a surprise that for the interpretation of scatterometer observations statistical methods have been used to complement the physical knowledge. This thesis is concerned with these, and gives, with the aid of scientific publications, a reasonably complete overview of the state-of-the-art as achieved with the ERS scatterometer processing (ERS-1 from 17 July 1991 and later ERS-2 from 22 November 1995).

A careful analysis of the accuracy of the data is often shown to be essential in order to

demonstrably improve the interpretation. What appears as residual error may be associated to effects resulting from nonlinear transformation of random error, or a nonuniform sampling of harmonic dependencies (e.g., in Chapters II, III, and IV, and the appendix). In literature, such residuals of statistical origin are often erroneously assigned to physical processes. Obviously, this leads to a wrong geophysical and statistical interpretation and examples of this will be given, in particular in Chapter IV.

The triplet of SCAT measurements (see section 2.3) can be put in a 3D axes system, where the measurement of each beam is represented along one of the three axes. By making clever cross-sections through the 3D distribution of the triplets, the coherence in the measurements may be investigated qualitatively. By doing so, the coherence of the measurements is shown to be very strong and may be explained by two geophysical parameters. The triplets are namely generally located near a conical (2D) surface (see Figure 1, Chapter II). It turns out that along the major axis of this cone mainly the wind speed (sea surface roughness) varies, and the length of the minor axis is related to the wind direction sensitivity (anisotropy of backscattering due to the orientation of the gravity-capillary waves). The characterization and modeling of this surface gave rise to a considerable improvement in the interpretation of the scatterometer, as is described in this thesis. The visualization of the measured triplets in 3D measurement space, the scatter of triplets around the cone, and the determination of the most likely “true” triplet on the cone, given the measurements and their accuracy (inversion), will be addressed in Chapter II. The notion that the triplets are with great probability close to a conical surface, is essential prior information for the inversion. An inversion procedure based on probability theory is derived. Given the position of a triplet with respect to the cone, indicators can be derived that may be used for quality control, instrument monitoring, and the further processing.

In the appendix a method will be discussed that describes how, with the aid of collocated and edited ocean wind data and an accurate microwave-wind transfer function (CMOD4), the scatterometer may be calibrated. The calibration, performed for each antenna separately, turns out to be very accurate and, when applied, gives a better match between the measured triplets and the cone surface from CMOD4. This leads to a small improvement of the scatterometer wind product.

From a collocation data set of weather model winds, backscatter measurements and their estimated accuracies, a wind-to- $\sigma^0$  transfer function, called CMOD4, is derived with Maximum Likelihood Estimation (MLE) as described in Chapter III. The nonlinearity and inaccurate formulation of the transfer function, the nonuniformity of the distribution of data, and the inaccurate formulation of the estimated data accuracies are shown to potentially lead to substantial errors.

For the validation of the transfer function, the fit of the transfer function cone to the

distribution of measured backscatter triplets in the 3D measurement space is investigated first. In case of an optimal fit, the combined effect of the measurement and inversion error should correspond to less than  $0.5 \text{ m s}^{-1}$  in wind vector RMS. CMOD4 fits the data within this amount of error, and as such the fit in measurement space contributes little to the uncertainty of the inverted winds. The second validation concerns statistics of differences between inverted scatterometer winds and collocated weather model or *in situ* winds. In practice it turns out that a transfer function that provides a better fit in the 3D measurement space, also shows (slightly) smaller RMS wind difference statistics. The accuracy of scatterometer winds is mainly determined by the interpretation error, i.e., the assigning of a unique wind speed and direction to a certain position on the cone surface. The uncertainty in a scatterometer wind is thus best described in the wind domain.

Chapter IV further explores latter issue, and a detailed wind calibration is sought using *in situ*, scatterometer and weather model winds. Wind observations are relatively noisy. It will be illustrated that calibration or regression of such data is not possible when comparing just two observation systems, unless the accuracy of one of the two systems is known. In practice this is usually not the case. A method is proposed for the simultaneous calibration and error modeling of three observation systems. By using triple collocation data, sufficient statistical moments may be computed to perform this task. Application of the method shows that scatterometer winds obtained with CMOD4 are roughly 5% low, whereas the surface wind of the NCEP weather model appears roughly 5% high, with respect to ocean buoy winds.

The cone surface consists of two closely overlapping sheaths. One sheath represents conditions where the wind has a component in the direction of the pointing of the mid beam (downwind), whereas the other sheath corresponds to winds with an opposite component (upwind). From a (noisy) triplet, it will generally not be possible to determine a unique wind vector, but two roughly opposite solutions are present (see also Eq. 6), one from the upwind sheath and one from the downwind sheath. This ambiguity in wind direction can in practice be solved by selecting the solution closest to a short range weather forecast. Furthermore, constraints can be applied to increase the continuity of the resulting scatterometer wind vector field. Such a method can provide the best wind solution in more than 99 % of the cases, as described in Chapter V. As such, a scatterometer wind product with high quality can be obtained from ERS.

Chapter V also deals with the assimilation of scatterometer winds in Numerical Weather Prediction (NWP) models. The direct use of backscatter measurements in a variational data assimilation system is shown to be cumbersome, whereas the assimilation of ambiguous winds is effective. The reason is that the scatterometer observation error can be easily expressed and dealt with in the wind components, but due to the nonlinearity of the

transfer function, is quite complex to account for in the backscatter domain.

## References

- Daley, R., Atmospheric data analysis, Cambridge atmosph. and space science series, Cambridge University Press, 1991.
- Donelan, M. A., and W. J. Pierson, Radar scattering and equilibrium ranges in wind-generated waves with application to scatterometry, *J. Geophys. Res.*, 92, 4971-5029. , 1987
- Donelan, M.A., F. W. Dobson, S. D. Smith, and R. J. Anderson, On the dependence of sea surface roughness on wave development, *J. Physical Oceanography*, 23, 2143-2149, 1993.
- ESA, The Nine Candidate Earth Explorer Missions - Atmospheric Dynamics Mission, *Special report published by the Eur. Space Agency, ESA SP-1196(4)*, ESTEC, Noordwijk, the Netherlands, 1996.
- Gill, A., Atmosphere-ocean dynamics, Academic Press, New York, 1982.
- Holton, J. E., An introduction to dynamic meteorology, 3rd ed., Academic Press, New York, 511p., 1992.
- Kelly, Graeme, Observation System Experiments at ECMWF, *ECMWF Newsletter Summer 1997*, ECMWF, Reading, England, 1997.
- Mastenbroek, Kees, "Wind-Wave Interaction", *thesis at the Delft University of Technology*, Delft, the Netherlands, 12 December 1996.
- Moore R.J. and W.J. Pierson, "Microwave determination of winds at sea", *Proc. IEEE*, 67, 1504-1521, 1967.
- Le Meur, Didier, Impact of ERS-1/ERS-2 scatterometer tandem on the ECMWF 3D Var assimilation system, *Proc. of the 3<sup>rd</sup> ERS Symposium - Space at the Service of our Environment, Florence, 17-21 March 1997, Eur. Space Agency Special Publication*, ESA, Noordwijk, the Netherlands, 1997.
- Lorenc, A., Analysis methods for numerical weather prediction, *Quart. J. R. Meteor. Soc.*, 112, 1177-1194, 1986.
- Okland, H., On the adjustment toward balance in primitive equation weather prediction models, *Mon. Wea. Rev.*, 98, 271-279, 1970.
- Peteherych, S., M. G. Wurtele, P. M. Woiceshyn, D. H. Boggs, and R. Atlas, First global analysis of SEASAT scatterometer winds and potential for meteorological research, *NASA Conf. Publ. CP2303*, 575-585 , 1984.
- Phillips, N. A., Dispersion processes in large-scale weather prediction, *Sixth IMO lecture, WMO-No.700*, 126 pp., 1990.
- Phillips, O. M., The dynamics of the upper ocean, 2nd ed., Cambridge Un. Press, New

York, 366 pp., 1977.

- Plant, W. J., A relation between wind stress and wave slope, *J. Geophys. Res.*, 87(C), 1961-1967, 1982
- Rabier, F., J.-F. Mahfouf, M. Fisher, H. Järvinen, A. Simmons, E. Andersson, F. Bouttier, P. Courtier, M. Hamrud, J. Haseler, A. Hollingsworth, L. Isaksen, E. Klinker, S. Saarinen, C. Temperton, J.-N. Thépaut, P. Undén and D. Vasiljevic, The ECMWF operational implementation of four-dimensional variational assimilation, *ECMWF Research Dept. Technical Memorandum No. 240*, ECMWF, 1997.
- Smith, S. D., R. J. Anderson, W. A. Oost, C. Kraan, N. Maat, J. DeCosmo, K. B. Katsaros, K. L. Davidson, K. Bumke, L. Hasse, and H.M. Chadwick, Sea surface wind stress and drag coefficients: the HEXOS results, *Boundary Layer Meteor.*, 60, 109-142, 1992.
- Snoeij, P., E. van Halsema, J. Vogelzang, S. Waas, S. Zechetto, H. Janssen, W. Oost, B. Jähne, Ch. Calkoen, VIERS-1 Final Report Phase 3", *Project reports No. 92-24 for the Dutch National Remote Sensing Board BCRS*, BCRS Program Bureau, Delft, the Netherlands, 1992.
- Stewart, R. H., *Methods of Satellite Oceanography*, University of California Press, 1984.
- Stoffelen, Ad, and Gerard Cats, The impact of SeaSat-A scatterometer data on high-resolution analyses and forecasts: The development of the QEII storm, *Mon. Wea. Rev.*, 119, 2794-2802, 1991.
- Stoffelen, Ad, Doppler wind lidar observations: NWP requirements, *Proc. of 7th conference on coherent laser microwave technology and applications, topical meeting held from 19-23 July 1993 in Paris, France*, 1993.
- Stoffelen, Ad, and Paul van Beukering, Improved backscatter processing and impact of tandem ERS winds on HIRLAM, *HIRLAM project report nr 31*, IMET, Dublin, Ireland, 1997.
- Valenzuela, G. R., Theories for the interaction of electromagnetic and ocean waves - a review, *Bound. Layer Meteor.*, 13, 612-685, 1978.
- Wentz, F. J., S. Peteherych and L. A. Thomas, A model function for ocean radar cross sections at 14.6 GHz, *J. Geophys. Res.*, 89, 3689-3704, 1984.

## CHAPTER II

Scatterometer Data-Interpretation:  
Measurement Space and Inversion\*

**Abstract.** The geophysical interpretation of the radar measurements from the ERS-1 scatterometer, called  $\sigma^0$ , is considered. An important tool in the interpretation of the data is the visualization of the triplets of radar backscatter in measurement space. For a given position (or node) across the swath it is shown that the measured triplets of  $\sigma^0$  are distributed around a well-defined “conical” surface and hence that the signal largely depends on just two geophysical parameters, which can be taken to be wind speed and direction. In general, the scatter of triplets is comparable to the instrumental measurement noise of 0.2 dB, which corresponds to an uncertainty in wind speed of only  $0.5 \text{ m s}^{-1}$ . In extreme meteorological conditions, a small number of anomalous triplets is found, but these can be identified by their distance from the conical surface and flagged or rejected by our quality control procedure.

The prelaunch transfer function developed by the European Space Agency (ESA), denoted CMOD2, is shown to give a poor representation of the conical surface, with typical errors an order of magnitude larger than instrumental noise. Its sensitivity to both wind speed and direction needs revision in order to fit the backscatter characteristics, as quantified in this paper. A fourth-order harmonic appeared essential to provide the particular shape of the conical surface. The full specification of a new transfer function, known as CMOD4, adopted by ESA since March 1993 has been derived by Stoffelen and Anderson (Chapter III).

An inversion algorithm, based on Bayes' probability theorem, is developed that takes account of the a priori known distribution of measured backscatter triplets in measurement space, in contrast to previous inversion algorithms that have implicitly assumed a uniform distribution. To keep the transfer function as simple as possible and to optimize the inversion procedure, it is shown to be advantageous to operate in a transformed space:  $z = (\mathbf{s}^0)^{0.625}$ . The conical surface on which the data lie consists of two closely overlapping sheaths, which results, after the inversion, in two wind vector solutions of roughly opposite

---

\* Based on:

Stoffelen, Ad and David Anderson, Scatterometer Data Interpretation: Measurement Space and inversion, *J. Atm. and Ocean Techn.*, 14(6), 1298-1313, 1997, © American Meteorological Society.

direction and almost equal probability. Visualization of this data surface shows clearly that there is little possibility of removing the above directional ambiguity from backscatter data alone: external information, for example, from a numerical weather forecast model is needed to resolve the ambiguity. A wind direction skill parameter, useful in the ambiguity removal, is introduced, based on the position of a measured triplet relative to the cone.

## 1. Introduction

The ERS-1 satellite was launched on 17 July 1991, into a polar orbit at about 800-km height, carrying a C-band scatterometer with three independent antennas pointing in directions of  $45^\circ$ ,  $90^\circ$ , and  $135^\circ$  to the right of the satellite track. A site in the scatterometer swath is illuminated three times, by the fore, mid and aft beams, respectively. The incidence angle of the radar beam varies from  $18^\circ$  to  $47^\circ$  for the mid beam, and from  $24^\circ$  to  $57^\circ$  for the fore and aft beams. The swath, approximately 500 km wide, is sampled every 25 km in both the along-track and cross-track directions although the effective spatial resolution of the instrument on the earth's surface, called the footprint, is approximately 50 km. Nineteen across-track nodes exist, numbered from 1 at the inner swath to 19 at the outer swath. In the first few months of the mission, the normalized radar backscatter cross section, denoted  $\mathbf{s}^0$ , was calibrated by the European Space Agency (ESA) using transponders and radar returns over the Amazon rain forest, while the European Centre for Medium-range Weather Forecasts (ECMWF) provided real-time validation [Stoffelen and Anderson, 1995; Appendix]. On February 24, 1992, the last engineering calibration on  $\mathbf{s}^0$  was carried out. The  $\mathbf{s}^0$  measurement error  $K_P$ , as computed by ESA, is generally around 0.2 dB or 5%. The results in this paper mostly use collocated ERS-1 and ECMWF numerical weather prediction (NWP) model data from after this date.

The prelaunch transfer function defined by ESA, denoted CMOD2 and given in Appendix A, was derived from aircraft-mounted instrument data [Long, 1985]. In section 2, CMOD2 is used to define cross sections through the three-dimensional (3D) measurement space in which the backscatter values of the fore, mid, and aft beam are plotted along separate axes. The distribution of measured triplets in these cross sections highlighted several deficiencies of CMOD2. The full determination of the transfer function used by ESA since March 1993, denoted CMOD4, is described in Stoffelen and Anderson [1997a; Chapter III] although the need for a revised formulation is shown in this manuscript. For comparison, the definition of CMOD4 is also given in Appendix B of Chapter III.



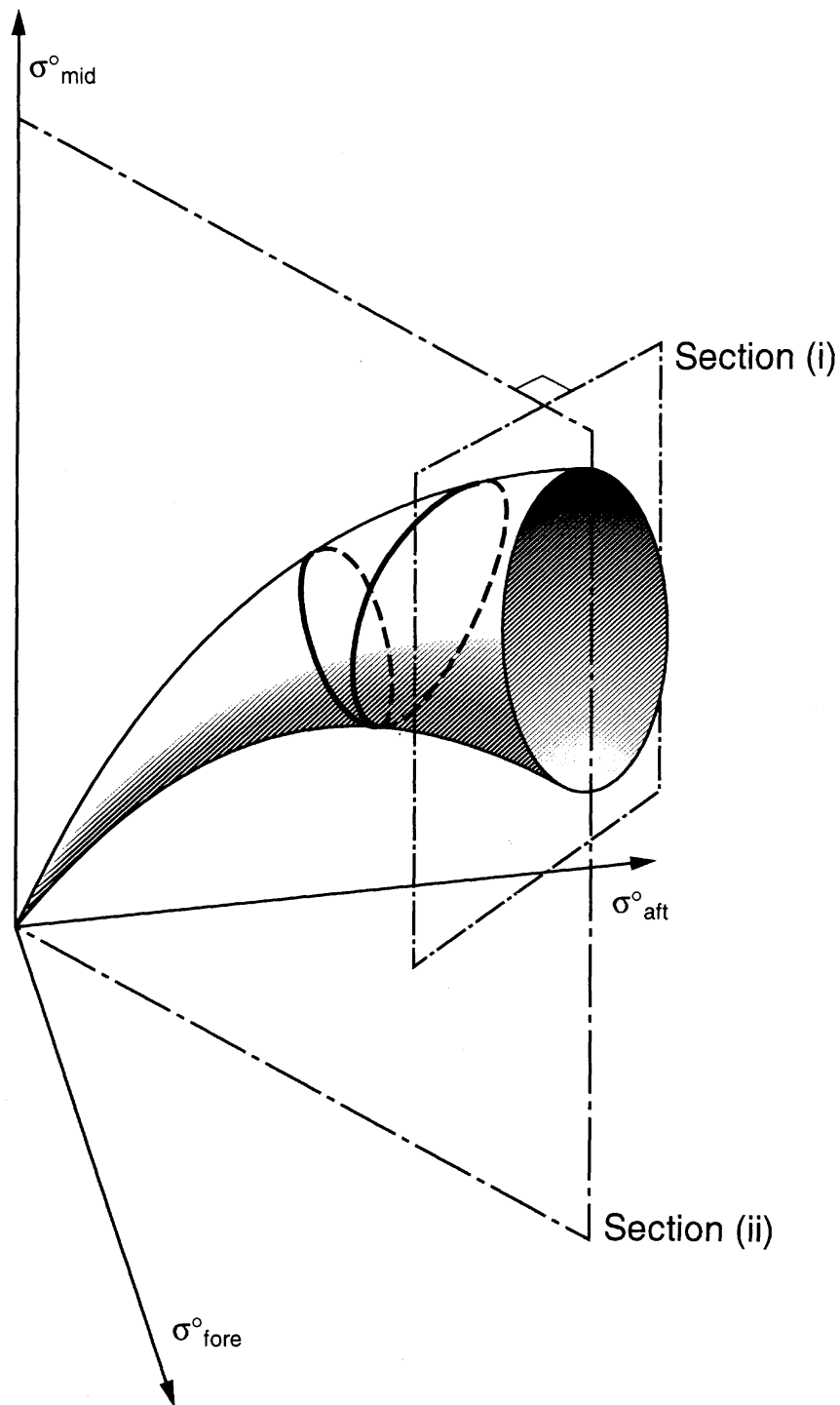


**Figure 1.** Schematic representation of the surface on which  $s^0$  triplets should lie for a given node. The surface actually consists of two sheaths that can intersect, but this is not shown in the schematic. The shape and proximity to each other of the two sheaths is a function of the node number across the swath. The line on the surface is a schematic of a line of constant wind speed, shown solid on the front surface and dashed on the rear surface of the cone. Intersections of the planes defined as section types (i) and (ii), are shown (based on *Cavanié and Lecomte* [1987]).

As for the first spaceborne scatterometer on board SEASAT-A, CMOD2 relates  $\mathbf{s}^0$  to wind speed and wind direction only, implying that a triplet of backscatter from the ERS-1 scatterometer is largely determined by two geophysical parameters and that the distribution of triplets is scattered around a surface in the 3D measurement space. As the backscatter could be a function of other parameters, such as wave age, temperature, surfactants etc. (e.g., *Donelan and Pierson* [1987]), it is important to assess the magnitude of the departures from a two-parameter function. The first task we address is to verify that the scatterometer data can indeed be represented by a two-parameter transfer function. By determining the scatter of triplets around the surface we show that the scatter is small and that, in general, the data do indeed closely lie on such a surface. In section 3 an inversion procedure is developed to find the most probable triplet on the two-dimensional (2D) surface from a measured triplet that is located close to this surface. The prior knowledge of the distribution of backscatter triplets in the 3D measurement space proves essential to reach a satisfactory inversion. Previous methods did not take into account this prior information. From the location of a measured triplet with respect to the surface, parameters identifying quality and skill of the wind retrieval are derived. Results are summarized in section 4.

## 2. Visualization in Measurement Space

In this section we display data in measurement space to assess the degree to which they lie on a surface. In principle it is not necessary to define the two parameters needed to define a surface, but both theoretical and empirical transfer functions, such as CMOD2, use speed and direction, and we show a posteriori that these are indeed suitable parameters. Although CMOD2 is shown to need modification, its main characteristics can still be used to define cross sections in measurement space. Two cross sections in particular are shown to be useful.

CMOD2 has the form

$$\mathbf{s}^0 = B_0[1 + B_1 \cos(\mathbf{f}) + B_2 \cos(2\mathbf{f})] \quad (1)$$

where

$$B_0 = 10^a V^g \quad (2)$$

and  $B_1$  and  $B_2$  are parabolic functions of the incidence angle  $\mathbf{q}$  and linear functions of wind speed  $V$ , the exact specifications of which are given in Appendix A. The  $B_2$  term represents the large difference in backscatter between a wind blowing up or down the beam compared to a wind blowing across the beam, while the  $B_1$  term represents the smaller difference between a wind blowing up versus one blowing down the beam.

Wind direction  $\mathbf{f}$  is measured relative to the pointing direction of a beam (projected

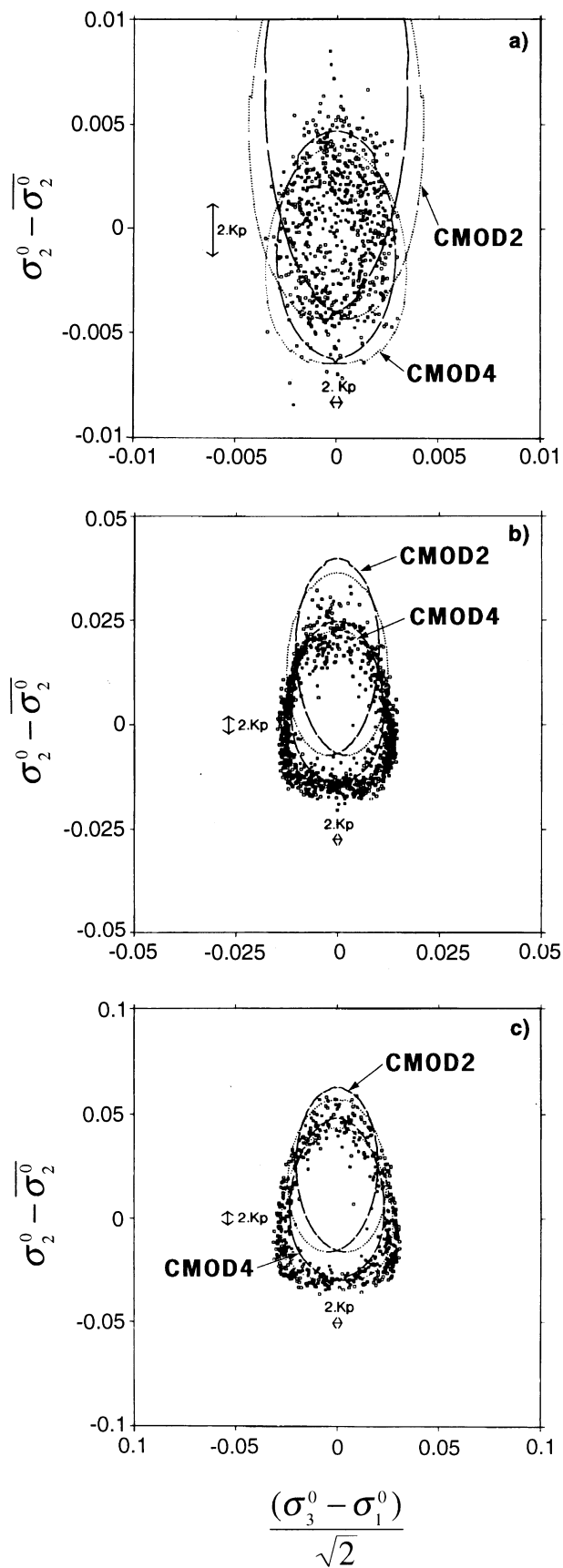


**Figure 2.** Intersection of the cone with the plane  $\mathbf{s}_1^0 + \mathbf{s}_3^0 = 2 \mathbf{s}_{\text{ref}}^0$ , with a thickness of  $0.05 \mathbf{s}_{\text{ref}}^0$  for node 11, for values of  $\mathbf{s}_{\text{ref}}^0$  corresponding approximately to a speed of (a)  $4 \text{ m s}^{-1}$ , (b)  $8 \text{ m s}^{-1}$ , and (c)  $12 \text{ m s}^{-1}$ . Note that the scaling of the axes changes from top to bottom, but the ratio of ordinate to abscissa remains constant. A measure of instrumental noise in the plane of section is shown, indicated as  $2K_P$ . The uppermost triplets correspond to winds blowing exactly along the mid beam, whereas at the lowest points the wind blows roughly across the mid beam. The curves for both CMOD2 and CMOD4 are plotted with the solid curve marking upwind and the dotted curve downwind flow. The curves are broken at every  $10^\circ$  in wind direction to show the wind direction dependency. The data do not fit the CMOD2 curve at all well, but do fit the CMOD4 curve. In fact, in panels (b) and (c) the CMOD4 curve is largely obscured by the data points. The data define a triangular type section rather than elliptic as for CMOD2. The data have been offset by  $\overline{\mathbf{s}}_2^0$  before plotting.

onto the horizontal plane), with  $f = 0$  corresponding to a wind blowing directly towards the beam. Wind direction can also be defined with respect to the subsatellite track. To distinguish which frame is being used we will use  $\mathbf{j}$  to indicate directions measured relative to the satellite pointing direction and  $\mathbf{f}$  for directions relative to a beam.

According to the transfer function (1), a  $\mathbf{s}^0$  triplet ( $\mathbf{s}^0_1, \mathbf{s}^0_2, \mathbf{s}^0_3$ ) can be written as

$$\begin{aligned} \mathbf{s}^0_1 &= B_0[1 + B_1(\sin \mathbf{j} + \cos \mathbf{j}) / \sqrt{2} + B_2 \sin 2\mathbf{j}] \\ \mathbf{s}^0_2 &= B_0^*[1 + B_1^* \sin \mathbf{j} - B_2^* \cos 2\mathbf{j}] \\ \mathbf{s}^0_3 &= B_0[1 + B_1(\sin \mathbf{j} - \cos \mathbf{j}) / \sqrt{2} - B_2 \sin 2\mathbf{j}] \end{aligned} \quad (3)$$

where  $\mathbf{s}^0_1$ ,  $\mathbf{s}^0_2$ , and  $\mathbf{s}^0_3$  refer to the fore, mid, and aft beams, respectively. We have assumed that the fore and aft beam incidence angles, and therefore their respective  $B_1$  and  $B_2$  are identical. The values for the mid beam incidence angle are denoted  $B^*_1$  and  $B^*_2$ . For a given node number, the parameters  $B_1$ ,  $B_2$ ,  $B^*_1$ , and  $B^*_2$  depend only on wind speed  $V$ . Thus, at a given node (with known incidence angles for the three beams), the location of a backscatter triplet in the 3D measurement space depends on only two free parameters, that is,  $(V, \mathbf{j})$ . Consequently, (3) defines a surface in 3D  $\mathbf{s}^0$  space for varying  $(V, \mathbf{j})$  as shown symbolically in Figure 1.

## 2.1. Visualization of Anisotropy

Sections through the cone were used to obtain quantitative information on the geometry of the expected conical surface, in particular cross sections roughly normal to the cone and cross sections along the main axis of the cone. From (2) and (3), it can be shown that the vector length of the 3D backscatter vector  $\mathbf{s}^0 = (\mathbf{s}^0_1, \mathbf{s}^0_2, \mathbf{s}^0_3)$  depends mainly on wind speed, whereas changes in wind direction mainly result in a different pointing direction of the vector (which we denote anisotropy). Cross sections normal to the cone can provide information on the dependence of the backscattering on wind direction, and those along the cone axis can provide information on wind speed. CMOD2 will be used as a guide to select appropriate cross sections. Although we show that CMOD2 needs to be revised, the assumption that  $B_1$  is small relative to  $B_2$  still holds. We will later show that  $B_1$  cannot be ignored, but to aid the reader in the interpretation it is convenient, for now, to neglect  $B_1$  and  $B^*_1$  in (3) when

$$\mathbf{s}^0_1 + \mathbf{s}^0_3 \approx 2B_0 = 2 \times 10^a V^g \quad (4)$$

showing that a cross section where  $\mathbf{s}^0_1 + \mathbf{s}^0_3 = \text{constant} = 2\mathbf{s}^0_{\text{ref}}$  corresponds to a section of constant speed  $V$ . In such a cross section, denoted as type  $(i)$ , we may write

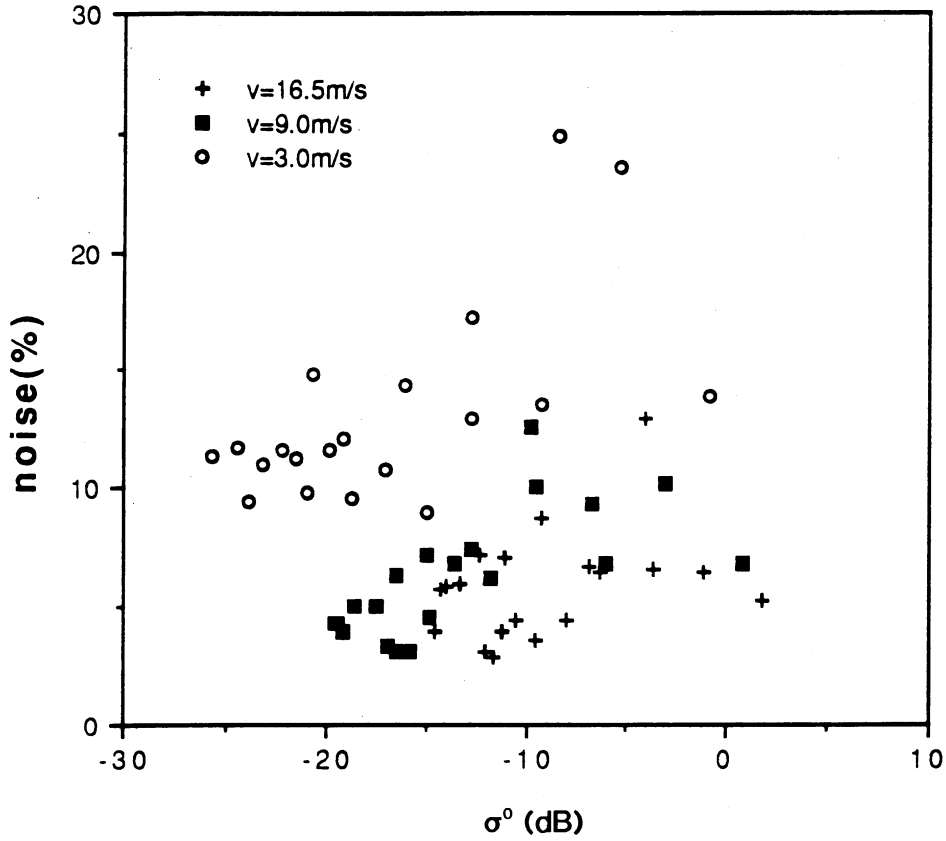


**Figure 3.** Estimated scatter against  $\sigma^0$  for speeds of 3, 9 and 16.5  $\text{m s}^{-1}$ . The scatter is approximately the same size as the instrumental noise (5%), except at low speed when it is considerably higher (10%-15%).

$$\left( \frac{\mathbf{s}_3^0 - \mathbf{s}_1^0}{2B_0B_2} \right)^2 + \left( \frac{\mathbf{s}_2^0 - B_0^*}{B_0^*B_2^*} \right)^2 = \cos^2 2\mathbf{j} + \sin^2 2\mathbf{j} = 1 \quad (5)$$

i.e., for varying  $\varphi$  and a scaled axis system ( $[\mathbf{s}_3^0 - \mathbf{s}_1^0]/[2B_0B_2]$ ,  $\mathbf{s}_2^0/[B_0^*B_2^*]$ ) an upwind circle can be plotted for  $0 < \mathbf{j} < \pi$  and a downwind circle for  $\pi < \mathbf{j} < 2\pi$ . Thus, the main anisotropy of the backscattering can be visualized in such a section. If the parameters  $B_0$ ,  $B_0^*$ ,  $B_2$ , and  $B_2^*$  were known correctly, and CMOD2 was an accurate transfer function, then it would be desirable to plot the quantities of (5), when a circle should result. However, for transfer function validation purposes it makes sense to plot the data in as parameter-free a way as possible. This can be achieved by using axes  $(x, y) = ([\mathbf{s}_3^0 - \mathbf{s}_1^0]/\sqrt{2}, \mathbf{s}_2^0 - \overline{\mathbf{s}_2^0})$  where  $\overline{\mathbf{s}_2^0}$  is the average value of  $\mathbf{s}_2^0$  for the data plotted. Examples of section (i) are shown in Figure 2 for node 11 at speeds of approximately (a) 4  $\text{m s}^{-1}$ , (b) 8  $\text{m s}^{-1}$ , and (c) 12  $\text{m s}^{-1}$ . The speed was obtained by evaluating the maximum of the distribution of ECMWF analyzed wind speeds collocated with the triplets in the cross section. Typically, one

month's worth of data is used to plot a particular section. Triplets within a distance of  $0.035\mathbf{s}_{\text{ref}}^0$  normal to and on either side of the plane of section were plotted, such that the total thickness of the cross section is approximately equal to the expected instrumental noise. We plotted thinner cross sections using data distributed over longer time periods (up to 6 months), but did not detect much difference in the standard plots such as in Figure 2 (and Figure 5 later). According to (5)  $\overline{\mathbf{s}}_2^0$ , should correspond to  $B_{0}^*$ , and will be a function of wind speed.

Clearly the data in Figure 2 do not lie exactly on a curve (a Lissajous-type figure in this section), nor should they because of instrumental noise. The width of  $2K_p\mathbf{s}^0$ , which varies as one goes round the curve, is indicated in Figure 2 at some locations, to show the extent to which data do in fact lie within this distance of the surface. For panels b and c, the bulk of the data lie within  $K_p\mathbf{s}^0$  of some mean curve. For panel a, corresponding to a low wind speed of approximately  $4 \text{ m s}^{-1}$ , this is less clear, but we will return to this point later. The appropriate curves for CMOD2 are plotted on Figure 2. It is clear that the data are poorly represented by CMOD2, showing that CMOD2 had to be modified. Figure 2 also shows that the upwind and downwind triplet distributions overlap to a high degree indicating that upwind cases can not be separated from downwind cases on the basis of the triplet measurement alone. External information is necessary to solve this ambiguity. We return to this point later in section 3.

### 2.1.1. Validation of the Existence of a Solution Surface

In this section we will quantify the scatter as observed in type (i) cross sections (see at equation (5) for definition), and estimate its geophysical effect in terms of wind error. This was done for each odd node 1, 3, ...19 and for different values of  $\mathbf{s}_{\text{ref}}^0$ , corresponding to different wind speeds. The vertical distribution of measurement points near the bottom of the curve was used to subjectively estimate the scatter for the mid beam and the horizontal distributions at the left and right extremities were used to give estimates of the scatter for the fore and aft beams. A normalized measure of the scatter, similar to  $K_p$ , was calculated. For the mid beam, the normalization was the local value of  $\mathbf{s}_2^0$ , and for the fore and aft beams  $\mathbf{s}_{\text{ref}}^0$ . To refer the value of  $\mathbf{s}_{\text{ref}}^0$  to a specific wind speed, the maximum of the ECMWF wind speed probability density function (PDF) was used.

Figure 3 shows that for medium and high wind speeds, the variance of the scatter present in  $\mathbf{s}^0$  is generally of the order of instrumental noise (approximately 5%), which implies that instrumental noise is the main contribution to the scatter of Figure 2 (and also Figure 5 discussed later). On the other hand, some wind speed dependency is evident: for low wind speeds of order  $3 \text{ m s}^{-1}$  the scatter was more than 10%. We did not further

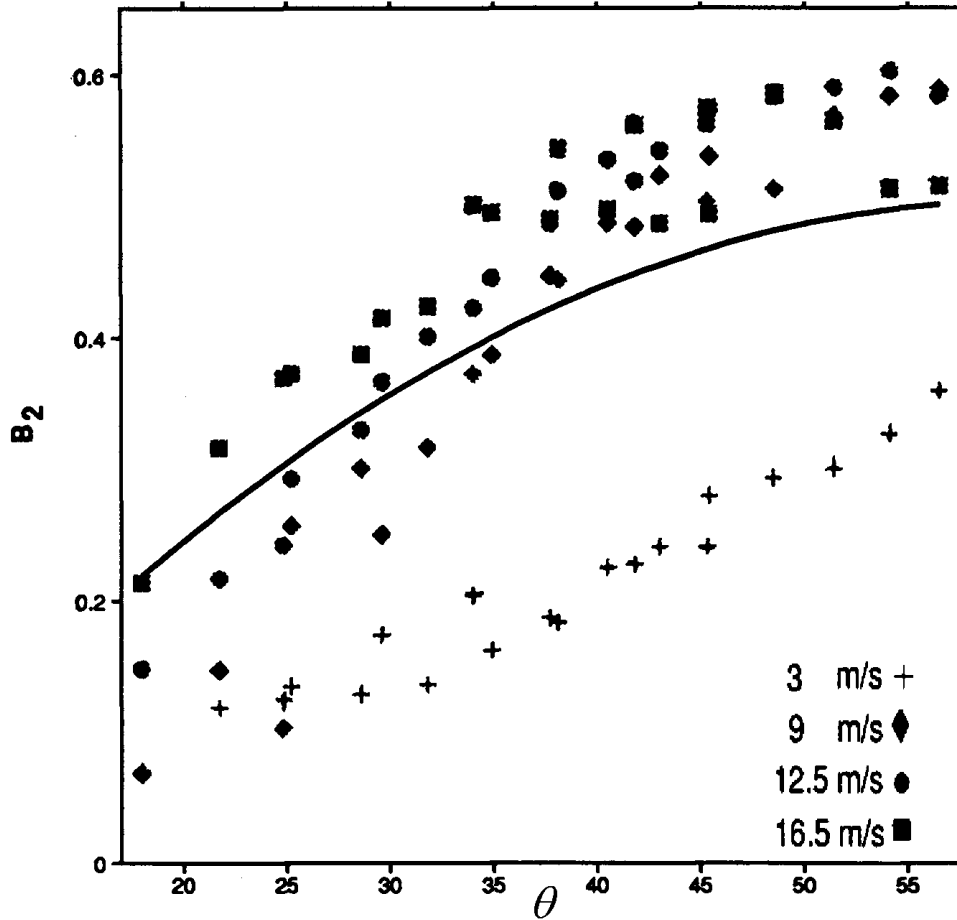


**Figure 4.** Estimated value of upwind-crosswind amplitude  $B_2$  against incidence angle  $\theta$  for speeds of 3, 9, 12.5 and  $16.5 \text{ m s}^{-1}$ . At higher speeds and incidence angles,  $B_2$  saturates, but at lower speeds and incidence angles it is speed dependent. The solid curve shows the CMOD2 relationship in which  $B_2$  is independent of speed and does not fit the data well.

investigate whether or not this could be accounted for from known geophysical effects, since 10% at  $3 \text{ m s}^{-1}$  results only in a small wind error (approximately  $0.3 \text{ m s}^{-1}$ ).

To put the scatter into perspective, we simulated the average wind vector RMS error, due to scatter in  $\mathbf{s}^0$ , to be approximately  $0.5 \text{ m s}^{-1}$  using CMOD4 as the transfer function. As shown in *Stoffelen and Anderson [1997a; Chapters III and IV]*, typical wind errors for other observational systems are  $3 \text{ m s}^{-1}$  vector RMS. Therefore we may conclude that *the ERS-1 scatterometer is providing accurate  $\mathbf{s}^0$  measurements, and that we may in general regard the triplets as being scattered around a well-defined and relatively simple surface.*

### 2.1.2. Estimation of $B_2$

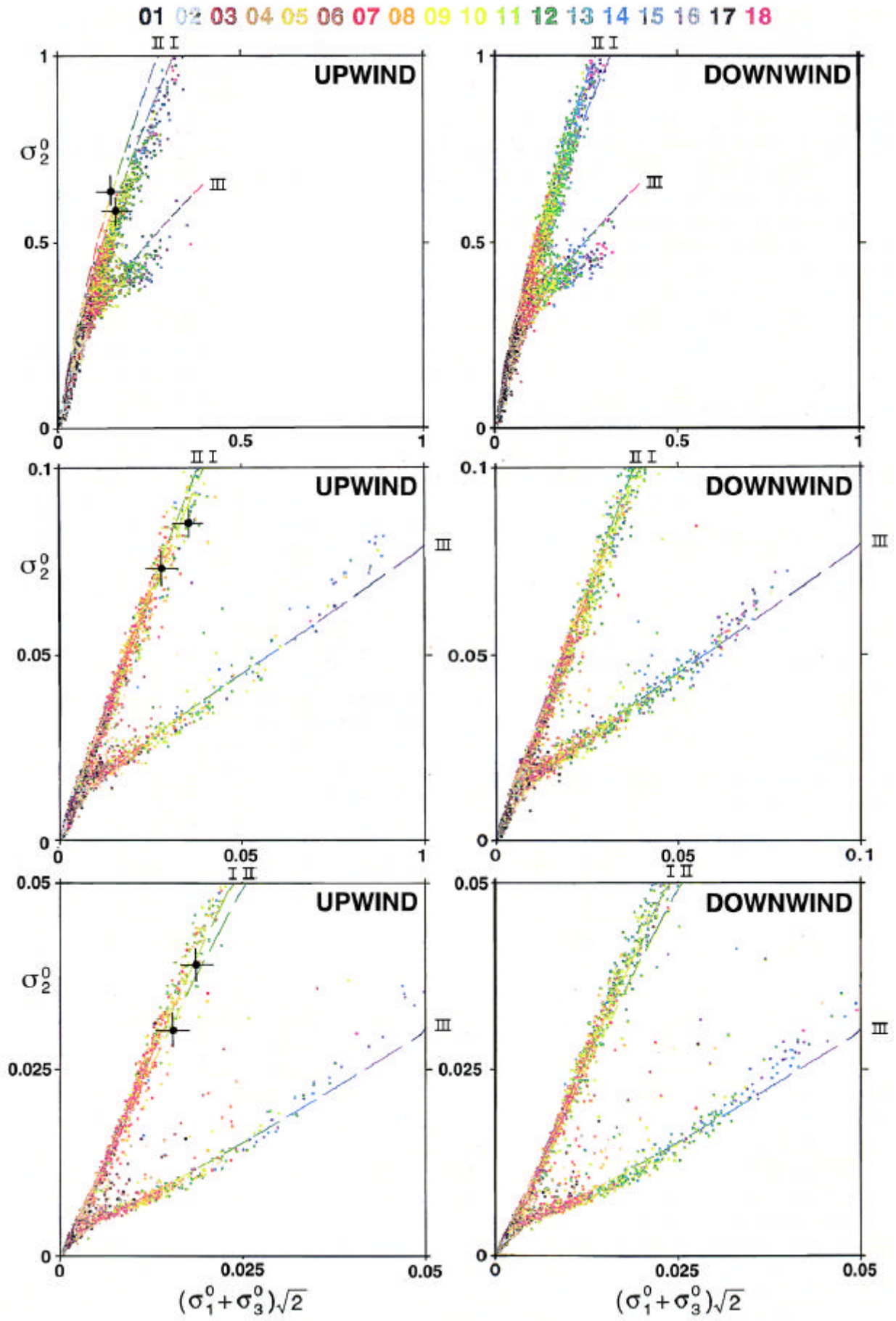
The provision of the cone surface to within 0.2 dB allows the unique possibility to study characteristics of the transfer function in great detail. In aircraft and wave tank experiments agreement to within 1 dB is considered satisfactory (see, e.g., *Keller et al.*

**Figure 5.** On the right, a vertical slice through the cone for node 3 along the line  $\mathbf{s}^0_1 = \mathbf{s}^0_3$ , with triplets on either side of this plain plotted, provided that  $|\mathbf{s}^0_1 - \mathbf{s}^0_3| < 0.018 (\mathbf{s}^0_1 + \mathbf{s}^0_3)$ . The horizontal axis is  $(\mathbf{s}^0_1 + \mathbf{s}^0_3) / \sqrt{2}$  and the vertical  $\mathbf{s}^0_2$ . Note that the scaling of the axes changes from top to bottom, but the ratio of ordinate to abscissa does not. The  $\mathbf{s}^0$  triplets are colored by wind speed and classified as “upwind” (left) and “downwind” (right). Speed coloring is in  $1 \text{ m s}^{-1}$  intervals starting at  $0 \text{ m s}^{-1}$ , where the respective colors for increasing wind speed can be read in the legend at the top of the plot. The upwind classification holds when the wind component upwind to the mid beam is positive, and downwind classification is used otherwise. Wind classification was done using the collocated ECMWF model winds. For reference, the three curves show CMOD4 at upwind (I), downwind (II), and crosswind (III) to the mid beam in all panels and colored by speed in the same fashion as the triplets: (a) upwind triplets for node 3, (b) downwind triplets for node 3, (c) upwind triplets for node 11, (d) downwind triplets for node 11, (e) upwind triplets for node 19, and (f) downwind triplets for node 19. The triplets clearly line up with the curves, confirming the strong coherence of the triplets (see text). Note that the “slope” of the cone changes with node number. The lines along which the triplets are densest are not very different for the left and right panels indicating that (autonomous) upwind-downwind separation in the interpretation will be difficult. Crosses corresponding to  $10.5 \text{ m s}^{-1}$  have been marked for both upwind and downwind to illustrate the displacement along the cone. For medium and high speeds at the middle and outer swath, the upwind-downwind term manifests itself along the cone and not perpendicular to it (see text for further explanation).

[1992]). So, by subjectively estimating the diameter of the cone in the horizontal and vertical directions, the upwind-crosswind amplitude for the fore-aft and mid beam (i.e.,  $B_2$  and  $B^*_2$ ) were calculated according to (5). The bias terms were  $B^*_0$  and  $B_0$  were obtained from  $\overline{\mathbf{s}^0_2}$  and  $\mathbf{s}^0_{\text{ref}}$ , respectively. By plotting many triplets,  $B_2$  and  $B^*_2$  may be approximated very accurately. Given the fact that the scatter generally amounts to 5 % of  $\mathbf{s}^0$ , sufficient data allow uncertainties in the  $B_2$  terms to be refined to less than 0.01 which corresponds to an error in  $\mathbf{s}^0$  of 1%. For low incidence angles and speeds, the scatter in  $\mathbf{s}^0$  is larger and the accuracy of  $B_2$  is consequently lower. In fact, the scatter in such cases is so large as to be comparable to the difference in  $\mathbf{s}^0$  between upwind and crosswind directions (see, e.g., Figure 2a). One can anticipate that the skill in wind direction retrieval will be low in the case of low speed, especially so near the inside edge of the swath, as will be confirmed in section 3.

Using the above speed assignment procedure, the resulting dependence of  $B_2$  on incidence angle was calculated and shown in Figure 4 for four different speeds. For higher wind speeds and higher incidence angles, the upwind-crosswind amplitude saturates at a value of 0.6, peaking at around  $12 \text{ m s}^{-1}$  and dropping a little for the highest wind speeds and incidence angles. The corresponding curve of  $B_2$  for CMOD2 is shown by the solid line. It does not fit the data and in fact is, for the coefficients of Appendix A, independent of speed. Further, the behavior shown in Figure 4 cannot be described with a parabolic





dependence on incidence angle as assumed in CMOD2, an indication that CMOD2 needs to be *reformulated*, not just recalibrated.

### 2.1.3. The Need for Higher Harmonics

Figure 2 shows that the distribution of triplets appears to be scattered around a *triangular* surface, rather than the elliptic surface of CMOD2 shown. By making plots like Figure 2 for various nodes and a range of wind speeds we found that the triangular shape is universal for all nodes and wind speeds. One possible way of representing this shape is to add higher harmonics to Equation (1), but the universal shape suggests a universal relationship between these higher harmonics and the lower harmonics present in CMOD2. A transformation of variable from  $\mathbf{s}^0$  to  $z$  where  $z = (\mathbf{s}^0)^{0.625}$ , provides such a universal relationship. For completeness we plot on Figure 2 the transfer function CMOD4, defined in Appendix B of Chapter III, which illustrates how well the triangularity can be represented by a new transfer function specified in  $z$ -space without explicitly adding higher order harmonics.

The higher harmonic terms in  $\mathbf{s}^0$  space can be computed from the harmonic part of the

transfer function in  $z$  space. For  $H = B_1^z \cos(\mathbf{f}) + B_2^z \cos(2\mathbf{f})$  we have

$$\mathbf{s}^0 = (B_0^z)^{1.6} [1 + 1.6H + 0.48H^2 + O(H^3)] \quad (6)$$

after third-order Taylor expansion. Ignoring  $O(H^3)$  and reducing the terms to single harmonics we find

$$\begin{aligned} \mathbf{s}^0 &= (B_0^z)^{1.6} [1 + 0.24(B_1^z)^2 + 0.24(B_2^z)^2 \\ &+ (1.6B_1^z + 0.48B_1^z B_2^z) \cos(\mathbf{f}) \\ &+ (1.6B_2^z + 0.24(B_1^z)^2) \cos(2\mathbf{f}) \\ &+ 0.48B_1^z B_2^z \cos(3\mathbf{f}) \\ &+ 0.24(B_2^z)^2 \cos(4\mathbf{f}) ] \end{aligned} \quad (7)$$

In this analysis, terms  $A$ ,  $B$ , and  $C$ , where

$$\begin{aligned} A &= 1 + 0.24(B_1^z)^2 + 0.24(B_2^z)^2 \\ B &= 1.6B_1^z + 0.48B_1^z B_2^z \\ C &= 1.6B_2^z + 0.24(B_1^z)^2 \end{aligned}$$

can be approximated as  $A = 1$ ,  $B = B_1 = 1.6B_1^z$ ,  $C = B_2 = 1.6B_2^z$ , since  $B_1$  is less than 0.15 (from Figure 6) and, from Figure 4 we know  $B_2 < 0.6$ . Thus, the transformation to  $z$ -space results in a reduction of the first and second harmonic terms by 1.6. The third

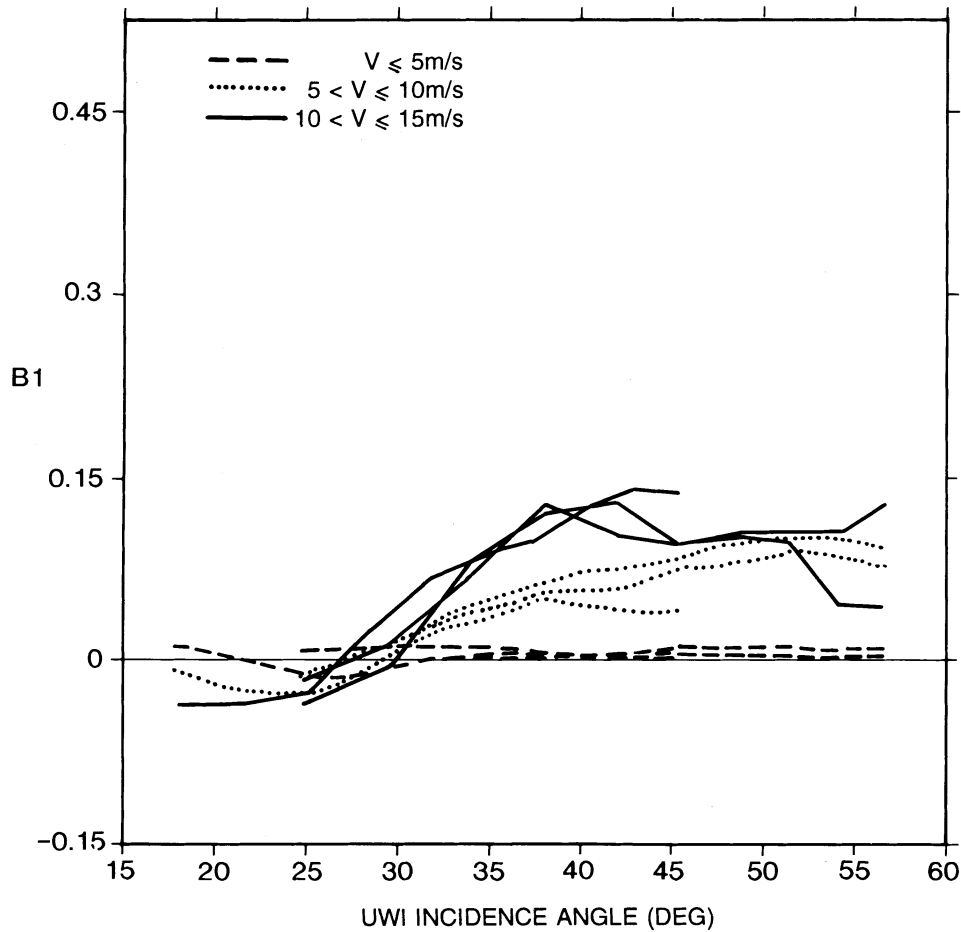


**Figure 6.** The value of  $B_1$ , the upwind-downwind amplitude, versus incidence angle for different wind speed intervals, based on the average of the scatterometer and ECMWF wind speed. The three beams are shown separately for each speed. At low incidence angles  $B_1$  is small and negative, but has a marked speed dependence at higher incidence angles.

harmonic is very small, that is,  $0.48 B_1^Z B_2^Z \leq 0.02$ . The fourth harmonic is the main cause for the triangular cone shape. Although it is not large—that is  $0.24 (B_2^Z)^2 \leq 0.04$ —it is needed for an accurate representation of the shape of the conical surface.

## 2.2. Visualization of the Triplet Distribution Along the Cone

A second and independent cross section, denoted as type (ii), can be made for  $\mathbf{s}_1^0 = \mathbf{s}_3^0$ . This equation is satisfied for:

- I:  $\varphi = \pi/2$ , which is upwind to the mid beam pointing direction,
- II:  $\varphi = 3\pi/2$ , which is downwind to the mid beam and
- III:  $\varphi = -\arcsin[ B_1 / (\sqrt{8} B_2 ) ]$ , which is approximately at  $\varphi = 0$  and  $\varphi = \pi$ , i.e., crosswind to the mid beam.

So, cross section (ii) should have data clustered along three lines corresponding to the wind directions I, II, III above. If we plot  $y = \sigma_{02}$  versus  $x = (\mathbf{s}_1^0 + \mathbf{s}_3^0) / \sqrt{2}$  then for CMOD2

$$\begin{aligned} \begin{pmatrix} x \\ y \end{pmatrix}_I &= \begin{pmatrix} B_0(\sqrt{2} + B_1) \\ B_0^*(1 + B_1^* + B_2^*) \end{pmatrix} \\ \begin{pmatrix} x \\ y \end{pmatrix}_{II} &= \begin{pmatrix} B_0(\sqrt{2} - B_1) \\ B_0^*(1 - B_1^* + B_2^*) \end{pmatrix} \\ \begin{pmatrix} x \\ y \end{pmatrix}_{III} &= \begin{pmatrix} \sqrt{2}B_0 \\ B_0^*(1 - B_2^*) \end{pmatrix} \end{aligned} \quad (8)$$

The  $x$  value for III (crosswind) is the average of I and II, while the value for III is smaller than the  $y$  value for I and II by approximately  $dy = 2 B_0^* B_2^*$ . The average of I, II and two times III contains only the bias terms  $B_0$ , and  $B_0^*$  and defines for varying wind speed the main axis of the cone. When  $B_1$  is ignored,  $x$  depends only on  $B_0$ , which in turn depends on wind speed (Equation (2)). However,  $B_1$  cannot be completely ignored as illustrated in Figure 6. In I,  $y$  represents the upwind, in II the downwind, and in III the crosswind backscatter of the mid beam.

In Figures 5a-f cross sections of type (ii) are shown for nodes 3, 11 and 19. The diameter of the cone relative to the scatter normal to its surface is large for medium and high speeds and for most node numbers, except for the first few at the inner swath. This ratio is a good measure of the quality of the wind direction information in a triplet as will be discussed further in section 3.

### 2.2.1. Upwind-Downwind Effect

In Figure 1 the upwind and downwind cones are sketched to overlap for illustration purposes, while, in reality, for  $B_1 \neq 0$  they will be slightly separated. Figures 5a, 5c, and 5e show triplets where the collocated ECMWF wind has a component toward the mid beam (“upwind”), while Figures 5b, 5d, and 5f show triplets where the collocated ECMWF wind has a component away from the mid beam (“downwind”). For reference, the full section (showing I, II, and III) through the CMOD4 transfer function is also shown in each plot. The location of “upwind” and “downwind” triplets is similar, confirming the inherent dual ambiguity noted earlier. However, the collocated wind speeds are different for upwind and downwind, that is, the “average” color at a certain location on the plot can be different for upwind and downwind by up to  $1.5 \text{ m s}^{-1}$  at some nodes. This can be explained by (8). For a fixed wind speed we note that the difference between I (upwind) and II (downwind) is  $(\Delta x, \Delta y) = (2 B_0 B_1, 2 B_0^* B_1^*)$ , that is, a shift in both  $x$  and  $y$  directions. A small change in wind speed will also change both  $x$  and  $y$ , that is,  $(\mathcal{J}_x / \mathcal{J}_V, \mathcal{J}_y / \mathcal{J}_V) = V^{-1}$

$(\sqrt{2} \mathbf{g} B_0, \mathbf{g}^* B_0^*)$ , and so it is difficult in general to separate upwind-downwind effects from speed effects. This is particularly acute if  $\sqrt{2} \mathbf{g} / \mathbf{g}^* = B_1 / B_1^*$  as the upwind-downwind triplet difference is then directed exactly along the cone. For medium and high node numbers  $B_1$  is positive for outer nodes and so the upwind distribution extends further along the cone than the downwind distribution. Indeed, the effect on a backscatter triplet of the upwind-downwind amplitudes  $B_1$  and  $B_1^*$  is partly directed along the cone surface, and more specifically in the direction of  $\mathbf{s}^0 / \mathbf{V}$ . So, the upwind-downwind amplitude is manifest along the cone surface, but much less so normal to it.

In Figure 5, triplets are color-coded based on ECMWF collocated wind speeds. A close inspection of curves such as those in Figure 5, made over many different periods of data, shows that the center of the distribution of a particular color for upwind is displaced relative to that for downwind in a direction mainly along the cone. For example in Figures 5c and 5e, the dominating color of the triplets close to the top is yellow, while in Figures 5d and 5f it is green. Quantitative estimation from Figure 5 of this effect is difficult, but it is represented in the transfer function. To guide the reader, crosses corresponding to  $10.5 \text{ m s}^{-1}$  have been marked for both upwind and downwind. For the inner swath, by comparing the upper parts of panels a and b, we detect a small difference in the upwind and downwind distributions normal to the cone as well. Here, downwind triplets have a clearly higher  $\mathbf{s}_2^0$  than upwind triplets, indicating a negative but small upwind-downwind amplitude as found earlier in experimental campaigns [Unal *et al.*, 1991], and as independently confirmed below (Figure 6).

While all properties of the transfer function can in principle be illustrated by the visualization of the distribution of backscatter triplets, quantification of the transfer function properties is much more difficult and requires alternative, but complementary tools. Thus, to objectively estimate the upwind-downwind amplitude, we used the following approach. First, we filtered a  $\mathbf{s}^0$  and ECMWF analysis wind collocation data set to a constant wind direction PDF over the 3 wind speed ranges  $0 < V < 5$ ,  $5 < V < 10$ , and  $10 < V < 15$ , and tagged the  $\mathbf{s}^0$  measurements for each beam either upwind  $-\pi/2 < \mathbf{f} < \pi/2$  or downwind  $\pi/2 < \mathbf{f} < 3\pi/2$ . Then we computed the average upwind value,  $\langle \mathbf{s}^0 \rangle_U$ , the average downwind value,  $\langle \mathbf{s}^0 \rangle_D$ , and  $(\langle \mathbf{s}^0 \rangle_U - \langle \mathbf{s}^0 \rangle_D) / (\langle \mathbf{s}^0 \rangle_U + \langle \mathbf{s}^0 \rangle_D)$ , which is equal to  $2B_1/\pi$  according to Equation (1), provided several assumptions, explained in appendix B, hold. Had we used  $z$  space for the analysis of  $B_1$ , (7) shows that to first order the first harmonic term would be changed by a factor of 1.6.

Figure 6 shows  $B_1$  estimated by the above method. As indicated previously, it is small and negative for low incidence angles, but shows a large wind speed dependence for mid range incidence angles. As for  $B_2$ , a saturation level (0.12) can be observed for high wind

speeds and incidence angles, a behavior that cannot be described by the linear speed and parabolic incidence angle dependency of CMOD2. In this section we have shown why the form of CMOD2 had to be modified. Retuning parameters, but retaining the basic structure of CMOD2 would not have been sufficient.

### 2.3. Wind Speed Dependence

In (1) the major speed dependence is in the  $B_0$  term. From (4) one can estimate this speed dependence by averaging  $\mathbf{s}^0_1$  and  $\mathbf{s}^0_3$  and comparing with the collocated ECMWF wind speed. In Figure 7 we plot the joint distribution of  $\log(V)$  estimated from the scatterometer by this method and  $\log(V)$  from ECMWF. We used  $\log(V)$  in order to be able to compute the optimal values of  $\mathbf{a}$  and  $\mathbf{g}$  of (4) by linear regression. If we assume that both estimates of the true wind contain the same amount of random error, then this joint distribution should be symmetric around the  $45^\circ$  line. The distributions calculated for all nodes using the  $\log(V)$  dependence are in general not symmetric as illustrated in Figure 7 for node 17. When the  $\log(V)$  dependence was modified to a  $\log(V + \mathbf{b}(\mathbf{q}))$  dependence, the distributions became more symmetric, with the absolute value of  $\mathbf{b}$  generally below  $1 \text{ m s}^{-1}$ . A stronger modification of functionality, such as a  $\sqrt{V}$  dependence gave unrealistic distributions for the lower wind speeds, but a more symmetric distribution for high wind speeds. This high wind speed asymmetry is not noticeable in Figure 7, but it was more evident for nodes at the inner half of the swath. The transfer function dependency is therefore best described by including the parameter  $\mathbf{b}$  and a log-dependency for low wind speeds and a  $\sqrt{V}$  dependency for average and high speeds.

### 2.4. Other Geophysical Dependencies

By collocation of the  $\mathbf{s}^0$  triplets to a geophysical parameter, sensitivity to it can be studied. For example, for low wind speeds of order  $3 \text{ m s}^{-1}$  the  $\mathbf{s}^0$  scatter increases to approximately 15%, which is considerably larger than for the value for higher wind speeds. It is possible that this increase is a result of geophysical effects, such as variations in sea surface temperature, wind variability, or surface slick variations at a given wind speed (wind speed dependent effects do not increase the scatter). The first dependency we tested used cross section (ii) to investigate the sensitivity of the distribution of  $\mathbf{s}^0$  triplets to sea surface temperature (SST), in bins from  $0^\circ\text{C}$  to  $10^\circ\text{C}$ ,  $10^\circ\text{C}$  to  $20^\circ\text{C}$ ,  $20^\circ\text{C}$  to  $30^\circ\text{C}$ , and above  $30^\circ\text{C}$ , for low wind speeds (less than  $2 \text{ m s}^{-1}$ ). If SST systematically influenced the backscatter, then one would expect either that the distribution of triplets would shift in the 3D space, dependent on SST, or that the density of the distribution would change. Neither of these effects could be identified.

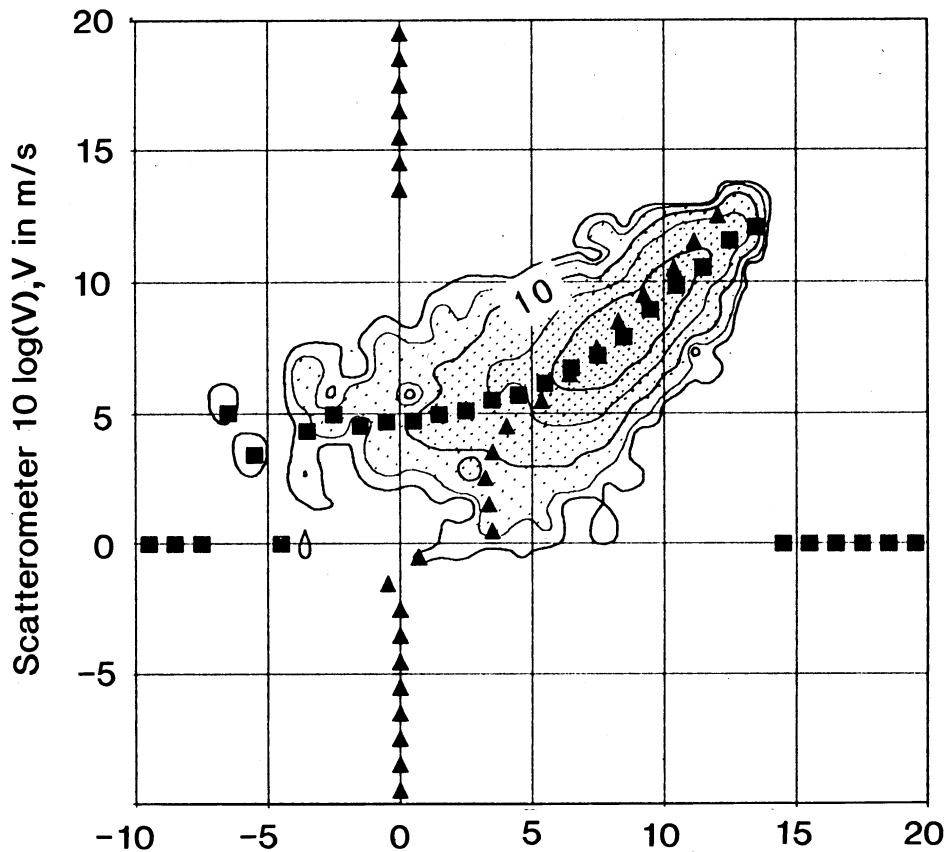


**Figure 7.** Two-dimensional distribution in  $10 \log V$ , with  $V$  measured in meters per second. The vertical axis is  $V$ , estimated from the fore and aft beam measurements using Eq. (4), while the horizontal axis is the collocated ECMWF speed. Solid squares represent vertical averages over the distribution and solid triangles, horizontal averages. Even though a regression on  $\mathbf{a}$  and  $\mathbf{g}$  has been performed to optimize the distribution (see text), the distribution is not symmetric around the  $45^\circ$  line. Data are for node 17 from 30 September 1991 to 1 October 1991.

On the other hand, there has been some evidence that SST gradients may have an effect [Boehnke and Wismann, 1994] but we were unable to detect such a dependency. It is likely that geophysical effects at low wind speeds will vary substantially on scales smaller than the footprint size (50 km) but, by averaging the backscatter over an area the size of the footprint, these effects are smoothed. However, it is difficult to find verification data of wind, SST gradient and radar backscatter at one location with sufficient accuracy to investigate this hypothesis rigorously.

Another relevant geophysical parameter is the sea ice extent. This is a dynamic quantity, and it is therefore worthwhile to investigate whether measurement space can be used to distinguish ocean scattering from ice scattering. It was found that the distribution of

$\mathbf{s}^0$  triplets from ice is largely distinct from the open ocean distribution of triplets at the inner and outer swath, and so ice and open ocean could be distinguished. At mid swath, however, there is a considerable overlap in both distributions of  $\mathbf{s}^0$  triplets and, for this case, time or space continuity would have to be used to distinguish open sea from ice (e.g., *Lecomte* [1993]).

### 3. Inversion

The 2D surface sketched in Figure 1, and shown more fully in Figures 2 and 5 describes the wind speed and direction dependence of the  $\mathbf{s}^0$  triplet measurements. We will formulate in this section an inversion procedure that seeks to find the most probable triplet on the cone surface from a measured triplet that is located close to it. In earlier work the inversion was generally based on minimization of the following maximum likelihood estimator (MLE) for varying wind speed and direction (e.g., *Graham et al* [1989])

$$\text{MLE} = \sum_{i=1}^3 \left[ \frac{\mathbf{s}_{O_i}^0 - \mathbf{s}_{S_i}^0}{\text{SD}(\mathbf{s}_{N_i}^0)} \right]^2 \quad (9)$$

where  $\mathbf{s}_{O_i}^0$  is the measured (observed) value,  $\mathbf{s}_{S_i}^0$  is the simulated value obtained from the  $\mathbf{s}^0$ -to-wind transfer function for a trial value of the wind vector, and  $\mathbf{s}_{N_i}^0$  is usually taken to be either  $\mathbf{s}_{O_i}^0$  or  $\mathbf{s}_{S_i}^0$ . The index  $i$  indicates beam position: 1 = fore, 2 = mid, 3 = aft. Here,  $\text{SD}(\mathbf{s}_{N_i}^0)$  is a measure of the noise in  $\mathbf{s}^0$  and has the form  $K_{P_i} \times \mathbf{s}_{N_i}^0$ , where  $K_{P_i}$  is a dimensionless constant (typically 0.05) whose value is determined by instrument noise. (Strictly speaking, when assuming Gaussian errors, a term  $2 \ln [\text{SD}(\mathbf{s}_{N_i}^0)]$  should be added to the right-hand side of (9) but this term is not significant and is not used in this paper.) The minimization is done for each triplet of measured  $\mathbf{s}^0$  values at each node.

The MLE minimization generally results in two local wind minima when the normalization factor SD is equal to a constant, and generally four, but sometimes up to six, when normalization is by the solution or the measurement [*Graham et al.*, 1989]. The two primary minima, corresponding to the two most likely solutions differ by approximately 180° in direction. The occurrence and location of the other minima frequently depend strongly on the normalization, making one doubt their validity. We will show that the two solutions describe the main ambiguity.

Normalization can be loosely thought of as a scaling of the axes of the 3D  $\mathbf{s}^0$  space, and provides a means of optimizing the way distances from the cone are penalized in this space. We will show that the cost function of (9) is not optimal and suggest an improvement, based on Bayes' probability theorem and visualization in measurement space.



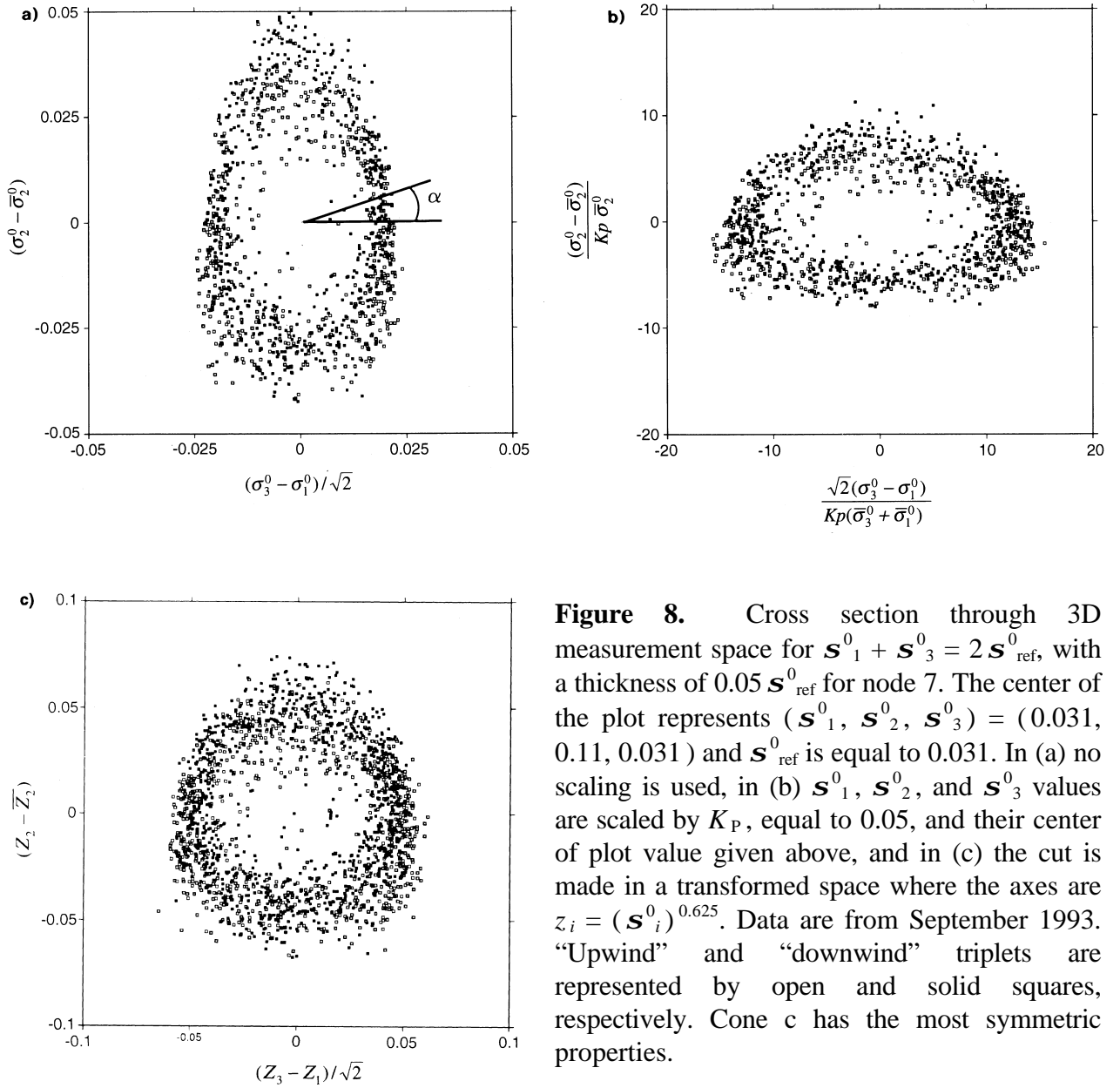


**Figure 8.** Cross section through 3D measurement space for  $\mathbf{s}_1^0 + \mathbf{s}_3^0 = 2\mathbf{s}_{\text{ref}}^0$ , with a thickness of  $0.05\mathbf{s}_{\text{ref}}^0$  for node 7. The center of the plot represents  $(\mathbf{s}_1^0, \mathbf{s}_2^0, \mathbf{s}_3^0) = (0.031, 0.11, 0.031)$  and  $\mathbf{s}_{\text{ref}}^0$  is equal to 0.031. In (a) no scaling is used, in (b)  $\mathbf{s}_1^0$ ,  $\mathbf{s}_2^0$ , and  $\mathbf{s}_3^0$  values are scaled by  $K_P$ , equal to 0.05, and their center of plot value given above, and in (c) the cut is made in a transformed space where the axes are  $z_i = (\mathbf{s}_i^0)^{0.625}$ . Data are from September 1993. “Upwind” and “downwind” triplets are represented by open and solid squares, respectively. Cone c has the most symmetric properties.

### 3.1. Measurement Space Transformation

We investigated the effect of normalization in (9) through visualization of differently scaled 3D measurement spaces. Figure 8 shows cross sections of type (i). Panel (a) shows normalization by a constant and panel (b) shows a scaling of  $\mathbf{s}^0$  by the  $\mathbf{s}^0$  value at the origin (0,0) of the plot, given in the caption of Figure 8. The latter scaling visualizes approximately the space used to compute a distance, for a normalization of (9) by either  $SD(\mathbf{s}_{oi}^0)$  or  $SD(\mathbf{s}_{si}^0)$ . To be able to obtain both accurate wind directions and a realistic wind direction PDF after inversion, it is desirable that equal portions of the  $\mathbf{s}^0$  triplets are thrown onto equal wind direction intervals. This is the case if the solution surface has no

**Figure 9.** On the right, comparison of scatterometer direction distribution (a) when using inversion with normalization by solution and (b) when using Eq. (10) for the inversion. Wind direction is with respect to the subsatellite track. The solid line in (b) represents the ECMWF direction distribution and the dotted line the scatterometer distribution. The dash-dotted curve describes the mean distance to the cone in arbitrary units (the square root of the MLE). Data are for node 3 for average wind speeds above  $4 \text{ m s}^{-1}$  and from 13 February 1994 2100 UTC to 16 February 1994 0900 UTC. In (a) the scatterometer direction distribution shows marked peaks and troughs approximately  $90^\circ$  apart, as does the mean distance to the cone. In (b) in contrast the scatterometer distribution is more physically plausible and indeed resembles the ECMWF angular distribution rather well, while the mean distance to the cone is more uniform.

sharp curvature and is circular rather than elliptic. Furthermore, if the cone surface, as defined by the transfer function, does not properly represent the measured  $\mathbf{s}^0$  triplet distribution, then more serious wind direction errors will result in the case of a sharply curved solution surface. With this in mind, normalization by solution or measured  $\mathbf{s}^0$  looks unfavorable, whilst normalization by a constant appears favorable. Figure 8c shows that the transformation to  $z$  space where  $z = (\mathbf{s}^0)^{0.625}$  results in a circular distribution that is ideal for inversion. In Appendix C a mathematical derivation based on probability theory is given to support the above argument that no normalization in  $z$  space is the preferred approach, in which case we can reformulate the MLE as

$$\text{MLE} = \frac{1}{\text{SD}^2} \sum_{i=1}^3 (z_{0i} - z_{s_i})^2 \quad (10)$$

where SD contains the estimated scatter normal to the true cone surface. This is, of course, not perfectly known but it can be shown that the uncertainty in the location of the true cone surface can be accounted for in SD. The form of SD is discussed in appendix D, but for the present it is sufficient to note that Eq. (10) represents normalization by a constant in  $z$ -space.

It is shown by *Stoffelen and Anderson* [1997a; Chapter III] that CMOD4 provides a satisfactory relationship between  $\mathbf{s}^0$  and wind speed and direction, and this is used here to examine normalization issues. ECMWF forecast model velocities were compared with those retrieved with the different normalization functions. The solid line in Figure 9b shows the distribution of ECMWF wind directions relative to the direction of the subsatellite track over a large sample of cases. The distribution varies substantially with wind direction, which is related to the sampling of the trades and the westerlies at higher latitudes. When using solution normalization in Eq. (9) the distribution of retrieved winds shows minima roughly every  $90^\circ$  (Figure 9a, dotted curve), which indicates that there is a problem with the retrieved directions. The MLE for Eq. (9) averaged over speed for a given wind direction is

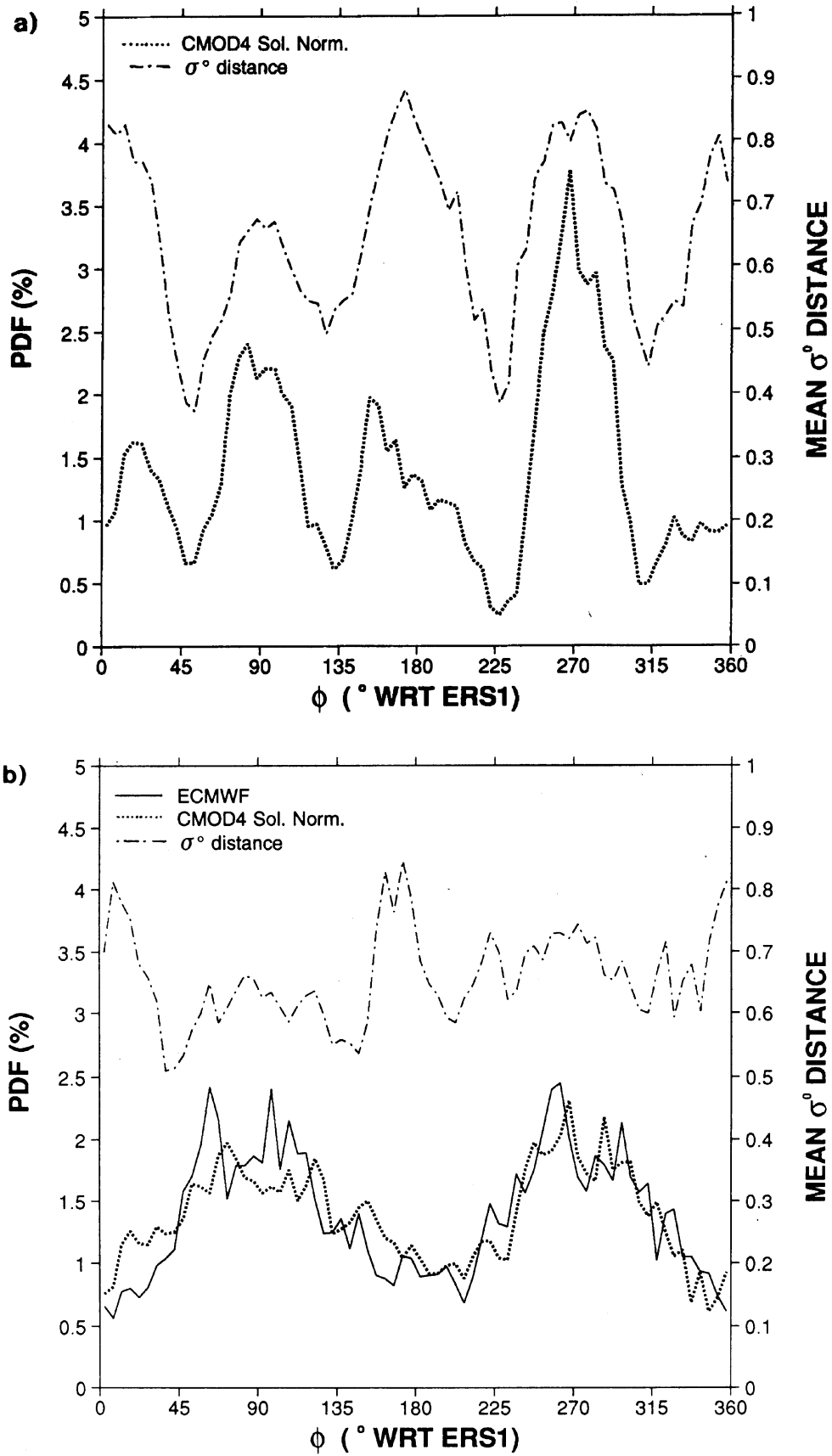


Figure 9. Continued.

also shown in Figure 9a by the dot-dash curve. This shows that at the direction “gaps”, the average MLE (dash-dotted) is relatively small; only points close to the cone surface can be projected onto these directions, while points further from the surface are always projected onto other directions. The distribution of retrieved directions (dotted) in Figure 9a, based on solution normalization, and in Figure 9b, based on Eq. (10), are very different, but the latter distribution is very similar to the independent reference distribution from ECMWF. Moreover, in Figure 9b the average MLE (dash-dotted) is reasonably constant for all wind directions, indicative of a constant probability. The improvement in direction accuracy when using Eq. (10), rather than the other forms of MLE discussed, is most significant at the inside swath, but present over the whole swath.

A synoptic consequence of the normalization by measurement or solution is a granularity in the resulting wind field. Instead of winds turning smoothly with position, they would all point in one direction and then jump abruptly to a new direction. (An example of this is shown in *Stoffelen and Anderson* [1993]). With the constant normalization of Eq. (10) this problem has been removed and the winds show no abrupt unmeteorological jumps in direction.

Generally if points lie outside the cone then there will be two minima approximately  $180^\circ$  apart. The fact that two solutions exist emerges directly from the fact that the cone has an upwind and a downwind sheath, as shown in Figures 2 and 5. There may be other minima, but they are not likely to be meaningful and will correspond to large distances from the cone—that is, large values of the MLE. On the other hand, points near the central axis of the cone may have several solutions, all about the same distance from the surface and therefore all equally probable, but not representative of the real wind direction.

As seen in Figures 2 and 5, the separation of the distribution of upwind and downwind triplets is comparable to the  $\mathbf{s}^0$  triplet scatter. If upwind and downwind were well separated then one would have a good chance of distinguishing between the two possible wind directions, on the basis of the  $\mathbf{s}^0$  measurements alone, a procedure often called “autonomous” ambiguity removal. However, Figures 2 and 5 show that in general the sheaths are rather close, a consequence of which is that the two wind directions are almost equally probable, so autonomous ambiguity removal is not very likely to succeed.

### 3.2. Quality Tests in the Transformed Space

Measurement space reveals a clear signature of a cone surface, and in the inversion procedure we compute the distance of a measured triplet to this surface, which is a measure of the quality (interpretability) of the measurement. On this basis we developed quality control tests that just depend on the measured triplet values and not on external information as is usually done. For quantitative use, we normalize the distance from the measurement

point to the solution cone by an estimate of the triplet scatter to produce the normalized distance  $d$ . (The exact definition and derivation of  $d$  are given in Appendix C.)

The minimum normalized distance (corresponding to the first solution) is denoted  $d_1$ . The normalization is such that the expectation value of  $d_1^2$  should be 1. A test has been implemented to reject points for which  $d_1$  is greater than 3, that is, to reject points lying more than three standard deviations away from the cone (called the “3SD” test). The 3SD distance typically amounts to a wind vector RMS error contribution of only  $1.5 \text{ m s}^{-1}$  and represents a sensitive quality control test. Between 1% and 2% of triplets fail the 3SD test, as one may expect. Generally they lie in areas of extreme meteorological conditions—that is, within a distance of approximately 100 km of intense fronts or low pressure systems, or close to tropical storms. We assume a confused sea state is present in these cases due to the temporal variability of wind direction, fetch effects, or rain, but other effects like stability are also possible candidates.

The probability information in  $d$  is used further to assign a quantitative skill index for wind direction retrieval. For a given triplet we calculate a mean squared normalized distance to the surface, averaged over all wind directions, denoted  $\overline{d^2}$ , that increases going from the cone center outwards. Each point is given a skill rating based on the minimum distance  $d_1$  and the mean distance  $\overline{d^2}$ . Specifically, the skill index is calculated from

$$I = \frac{(\overline{d^2} - d_1^2)^{1/2}}{\max(d_1, 1)} \quad (11)$$

According to this formula, directional skill will increase monotonically from the center of the cone outward, reaching a maximum just outside the cone, and will then decrease for points far outside the cone. This reflects the fact that for triplets near the center of the cone, wind direction discrimination will be poor, whereas points at a similar distance outside the cone may still provide valuable directional information. The test works well in that points at the center of the cone have low skill ratings, while those near the cone have high skill values. The directional skill increases as the cone opens up at increasing wind speeds.

#### 4. Summary and Conclusions

The 3D  $\mathbf{s}^0$  space visualization introduced in this paper is extremely useful in considering the quality of the measured triplets, in designing the form of a suitable transfer function, and in developing a wind inversion procedure. We verified the existence of a cone-shaped surface in 3D  $\mathbf{s}^0$  space and found the  $\mathbf{s}^0$  scatter perpendicular to the cone to be close to measurement noise specification (approximately 5% or 0.2 dB), except at low wind speeds and at the inside edge of the swath, implying that in general a two parameter transfer

function is sufficient to describe the  $\mathbf{s}^0$  triplet distribution. Such a transfer function would be able to describe the backscatter measurement coherence to within 0.2 dB, which is exceptional. Usually a validation of backscatter data to within 1 dB is considered appropriate ( See, e.g., *Keller et al.* [1992]). Therefore, we consider the ability of the transfer function to fit the distribution of measured  $\mathbf{s}^0$  triplets in the 3D  $\mathbf{s}^0$  space as the most important validation test. This is used extensively in *Stoffelen and Anderson* [1997a; Chapter III].

In the cases where the scatter exceeds measurement noise, the deviation from the cone surface may be related to geophysical parameters other than wind speed and direction. Such a relation would not have a substantial effect on the global quality of the scatterometer wind product, however, since the  $\mathbf{s}^0$  scatter normal to the cone is small in terms of the error in the derived wind. It might lead to a local improvement in cases where the quality control procedure of section 3 rejects anomalous  $\mathbf{s}^0$  triplets lying too far away from the cone (less than 2% of cases). This occurs in cases associated with extreme weather conditions, such as within approximately 100 km of intense fronts, lows and tropical cyclones. Further research is needed to investigate whether these anomalous triplets are caused by, for example, wave effects, rapid changes in wind direction, or rain and whether they could be usefully included in the transfer function.

Each point on the cone surface has a geophysical interpretation. Physically, the extension of the cone in the 3D  $\sigma^0$  space is related to the amplitude of capillary ocean waves, whereas the diameter of the cone is related to the anisotropy of backscattering of radar waves from these centimeter-wavelength ocean waves. In the empirically derived transfer functions these two parameters are assumed to be explicitly related to wind speed and direction, an assumption justified by *Stoffelen and Anderson* [1997a; Chapters III and IV]. The behavior of the bias term, the upwind-crosswind term, and the upwind-downwind term of the empirical transfer function show important features that were not anticipated before launch and so were not taken into account in the ESA prelaunch transfer function CMOD2—for example, a nonlogarithmic wind speed dependency, saturation of the harmonic terms for increasing wind speeds and incidence angles, and the necessity for higher harmonic terms. The nonlogarithmic speed dependence as found by us for the ERS-1 scatterometer is confirmed by *Keller et al.* [1992], although their experiments were for a much smaller footprint than for the ERS-1 scatterometer. The higher harmonic terms are, however, not necessary in a slightly transformed space  $z = (\mathbf{s}^0)^{0.625}$ , which has the further advantage that the inversion procedure is done better. The transformation results in a fourth-order harmonic of roughly 4% at maximum which agrees well with earlier aircraft campaigns where 96% of the power was in the first two harmonics [*Unal et al.*, 1991] at C band and VV polarization. Although not yet theoretically supported, we would recommend

using  $z$  space in the interpretation of ERS scatterometer measurements.

When we assume that a  $z$  triplet measurement originates from a “true”  $z$  triplet on the cone surface, then the inversion problem is reduced to finding the most likely location of this triplet on the cone surface. The curvature of the cone and the general distribution of measured  $z$  triplets around the cone determines the optimal projection of a measured  $z$  triplet onto the cone surface. We found an optimal and practical solution for the inversion problem by making use of the symmetric geometry of the ERS-1 scatterometer. A less symmetric geometry (such as the NSCAT or SeaWinds design developed by the National Aeronautical and Space Administration (NASA)) would complicate the inversion problem. In earlier inversion algorithms (see, e.g., *Graham et al.* [1989]), no account was taken of the prior knowledge of the shape of the cone surface and the distribution of measured  $\mathbf{s}^0$  triplets around it.

The inversion process delivers two significant solutions in roughly opposite directions, which is directly related to the fact that the “upwind” and “downwind” leaves of the cone in 3D  $\mathbf{s}^0$  space are closely overlapping. The upwind-downwind amplitude  $B_1$  is not zero, but it results in a triplet distribution for upwind and downwind that mainly differs in a direction along the cone. Ambiguity removal filters are needed to select a unique solution from the two ambiguous wind vectors of similar strength and approximately opposite direction. Directional accuracy, as measured by the position of a triplet relative to the cone surface, can be quantified in a skill index that in turn can be used in ambiguity removal filters [*Stoffelen and Anderson, 1997b; Chapter V*].

## Appendix A: The Prelaunch Transfer Function CMOD2

The Prelaunch transfer function CMOD2 has the form

$$\mathbf{s}^0 = B_0[1 + B_1 \cos(\mathbf{f}) + B_2 \cos(2\mathbf{f})] \quad (\text{A1})$$

where

$$B_0 = 10^a V^g \quad (\text{A2})$$

and  $B_1$  and  $B_2$  are parabolic functions of the incidence angle  $\mathbf{q}$  in degrees and linear functions of wind speed  $V$  in meters per second. The form of the coefficients is as follows.

$$\mathbf{a} = C(1) + C(2)P_1 + C(3)P_2$$

$$\mathbf{g} = C(4) + C(5)P_1 + C(6)P_2$$

$$B_1 = [C(7) + C(8)P_1 + C(9)P_2] + [C(10) + C(11)P_1 + C(12)P_2]V$$

$$B_2 = [C(13) + C(14)P_1 + C(15)P_2] + [C(16) + C(17)P_1 + C(18)P_2]V$$

where  $P_1$  and  $P_2$  are the first and second Legendre functions, given by

**Table A1.** CMOD2 Coefficients

Parameter	Coefficient	Value	Parameter	Coefficient	Value
$\alpha$	$C(1)$	-2.217986	$B_2$	$C(10)$	-0.000709
	$C(2)$	-1.769950		$C(11)$	0.0
	$C(3)$	0.296464		$C(12)$	0.0
$\gamma$	$C(4)$	1.068610		$C(13)$	0.404800
	$C(5)$	0.652920		$C(14)$	0.161600
	$C(6)$	0.044130		$C(15)$	-0.065200
$B_1$	$C(7)$	0.137300		$C(16)$	0.0
	$C(8)$	0.162000		$C(17)$	0.0
	$C(9)$	0.0		$C(18)$	0.0

$$P_1 = x \quad P_2 = (3x^2 - 1) / 2$$

where  $x = (\mathbf{q} - 40) / 25$ , and the coefficients are given in Table A1.

### Appendix B: Assumptions for $B_1$ Estimation

The first assumption is that the ECMWF analysis wind direction error can be ignored. The standard deviation of error in the ECMWF analysis wind direction as a function of wind speed was estimated by comparison to ship winds, and a correction was made for the effect of this wind direction error on the calculated amplitudes. The correction was not very significant because the upwind-downwind amplitude is small for low wind speeds, and it is only for low wind speeds that the standard deviation of wind direction error is large (i.e., a substantial fraction of  $90^\circ$ ).

The second assumption is that  $B_1$  and  $B_0$  are statistically independent. However, both terms vary roughly linearly in  $V$  (i.e., exactly for  $\mathbf{g} = 1$ , which occurs in the middle of the swath), and the error we will make will roughly be a factor  $1 + (\Delta V / V)^2$ . This amounts to 16% for a wind speed of  $5 \text{ m s}^{-1}$  with an error  $\Delta V = 2 \text{ m s}^{-1}$ , but for this speed  $B_1$  is small. For higher speeds the ratio  $(\Delta V / V)^2$  becomes very small, implying that this error is unlikely to be significant for any speed.

The third assumption is of symmetry around  $\mathbf{f} = \pi$  for the harmonic terms of period 2 and higher, which is valid if Eq. (1) is used. However, Eq. (1) does not include the term  $B_3 = 0.48 B_1^Z B_2^Z$  (see Eq. (7)), which contributes by an amount of  $0.21 B_0 B_3$  in the upwind bin and by an amount of  $-0.21 B_0 B_3$  in the downwind bin, and thus contributes at maximum 2.5% to  $B_1$ . The term associated with  $B_4$  has the required symmetric property.



### Appendix C: Theoretical Derivation of the Inversion Procedure

From a theoretical point of view, the maximum likelihood estimator (MLE) is not optimal for this estimation problem involving a nonlinear surface. A nonquadratic formulation of the MLE may be useful, but because of the complexity of the cone surface, the derivation of this MLE is not easy. So, we sought an optimal practical solution by transformation of  $\mathbf{s}^0$  space on probabilistic grounds. Provided we have an accurate mathematical description of the cone surface indicated by  $S$ , then given a measured vector  $\mathbf{s}^0_o$ , we may be able to analyze the most probable value of the “true” vector  $\mathbf{s}^0_T$  lying on the cone surface. According to Bayes’ probability theorem we may write

$$p(\mathbf{s}^0_s / \mathbf{s}^0_o) = p(\mathbf{s}^0_o / \mathbf{s}^0_s) p(\mathbf{s}^0_s) / p(\mathbf{s}^0_o)$$

where  $p(\mathbf{s}^0_s | \mathbf{s}^0_o)$  is the conditional probability density for  $\mathbf{s}^0_s$  given a fixed  $\mathbf{s}^0_o$ . This equation can be maximized for varying  $\mathbf{s}^0_s$ . The a priori probability density  $p(\mathbf{s}^0_o)$  is a constant in this process, since  $\mathbf{s}^0_o$  is given. The analysis equation requires a description of  $p(\mathbf{s}^0_s)$ , the a priori probability density of having a “true” triplet somewhere in the 3D  $\mathbf{s}^0$  space. Since we have assumed a perfect description of the cone surface, we have  $p(\mathbf{s}^0_s) = 0$  for  $\mathbf{s}^0_s \notin S$ . Therefore, we only need to search trial values  $\mathbf{s}^0_s \in S$ . For convenience we may assume

$$p(\mathbf{s}^0_s) = \begin{cases} p(\mathbf{a} | \mathbf{s}^0_{s1} + \mathbf{s}^0_{s3}) p(\mathbf{s}^0_{s1} + \mathbf{s}^0_{s3}), & \mathbf{s}^0_s \in S \\ 0 & , \mathbf{s}^0_s \notin S \end{cases}$$

Here,  $\mathbf{a}$  is a cylindrical angular variable in the range  $0 \leq \mathbf{a} < 2\pi$  as depicted in Figure 8a (the exact choice of the two parameters describing the surface is not significant at the moment, but later we will use wind speed and direction), and  $\int p(\mathbf{a} | \mathbf{s}^0_{s1} + \mathbf{s}^0_{s3}) d\mathbf{a} = 1$ . Given the low scatter normal to the cone we can make the assumption that  $p(\mathbf{s}^0_{s1} + \mathbf{s}^0_{s3})$  is constant, for  $\mathbf{s}^0_s - \mathbf{s}^0_o$  close to or smaller than the scatter of triplets normal to the cone, without any significant impact on the retrieved  $\mathbf{s}^0_T$ . Figure 8a shows a cross section through 3D measurement space, in the plane of the angular variable  $\mathbf{a}$ . Given the distinct triangular shape of the surface, the probability of finding a certain number of  $\mathbf{s}^0$  triplets in an angular sector  $\Delta\mathbf{a}$  depends on  $\mathbf{a}$ , and therefore  $p(\mathbf{a} | \mathbf{s}^0_{s1} + \mathbf{s}^0_{s3})$  is not constant.

Figure 8c shows the same cross section in  $z$ -space after the transformation. The data now lie on a conical surface  $\Sigma = f(S)$ , with an approximately uniform distribution in  $\mathbf{a}$ . Therefore, the assumption that  $p(\mathbf{a})$  is constant is appropriate in this space. We may assume that the conditional probability density  $p(\mathbf{z}_o | \mathbf{z})$  is normal—that is,  $p(\mathbf{z}_o | \mathbf{z}) = N(\mathbf{z}, \mathbf{e})$ —where  $N$  is a 3D normal distribution with mean  $\mathbf{z}$  and standard deviation  $\mathbf{e}$ . The

assumption of normal error distribution was verified a posteriori by considering the distribution of triplets over the different cross sections introduced in section 2 , but in  $z$  space.

### Appendix D: Estimation of the Triplet Scatter

In section 2.1.1, the scatter of  $\mathbf{s}^0$  values around the cone surface was computed for the three beams individually. In the inversion as of Eq. (10) not scatter values per beam are needed but scatter of the vector  $\mathbf{z}_O$  around the cone. We derived the triplet scatter SD from the results presented in section 2.1.1 for  $\mathbf{s}^0$ , assuming isotropic scatter, and represent it analytically as

$$SD = 0.625 \left( \sum_{i=1}^3 (\mathbf{s}^0_{oi})^{1.25} \right)^{1/2} g \quad (D1)$$

Figure D1 shows the estimated isotropic scatter normal to the cone,  $\Delta \mathbf{s}^0 / |\mathbf{s}^0|$ , and the functional form  $g$ , subjectively chosen to represent it, given by

$$g = 0.02 \left( 1 + \frac{45 - \theta_2}{27} \right) \left( 1 + \frac{5}{V} + \frac{1}{2V^2} + \frac{5}{2V^3} \right) h(V) \quad (D2)$$

where  $\theta_2$  is the incidence angle of the mid beam measured in degrees,  $V$  is in meters per second and  $h(V)$  represents an additional  $\mathbf{s}^0$  scatter contribution for winds above  $15 \text{ m s}^{-1}$  with the form

$$h = \begin{cases} 1 & , V \leq 15 \\ 1 + (V - 15)^2 / 100 & , V > 15 \end{cases}$$

For winds above  $15 \text{ m s}^{-1}$  it is unclear whether the  $\mathbf{s}^0$  scatter increases by the amount specified in  $h$ . The factor  $h$  is introduced to account for the fact that the collocation data base used for the derivation of the transfer function was rather sparse above speeds of  $15 \text{ m s}^{-1}$  and has been determined empirically to obtain a threshold below which the wind retrieval quality is not affected by the distance of the measured triplet to the cone.

**Acknowledgments.** It is a pleasure to acknowledge the constructive discussions we have had with members of the ESA analysis team and with ECMWF staff and visitors, in particular Evert Attema, Alf Long, Alain Cavanié, John Eyre, Peter Woiceshyn and Ross Hofmann. Tony Hollingsworth and the anonymous reviewers provided useful comments on the draft manuscript. The work was carried out at ECMWF under ESA contract 9097/90/NL/BI.

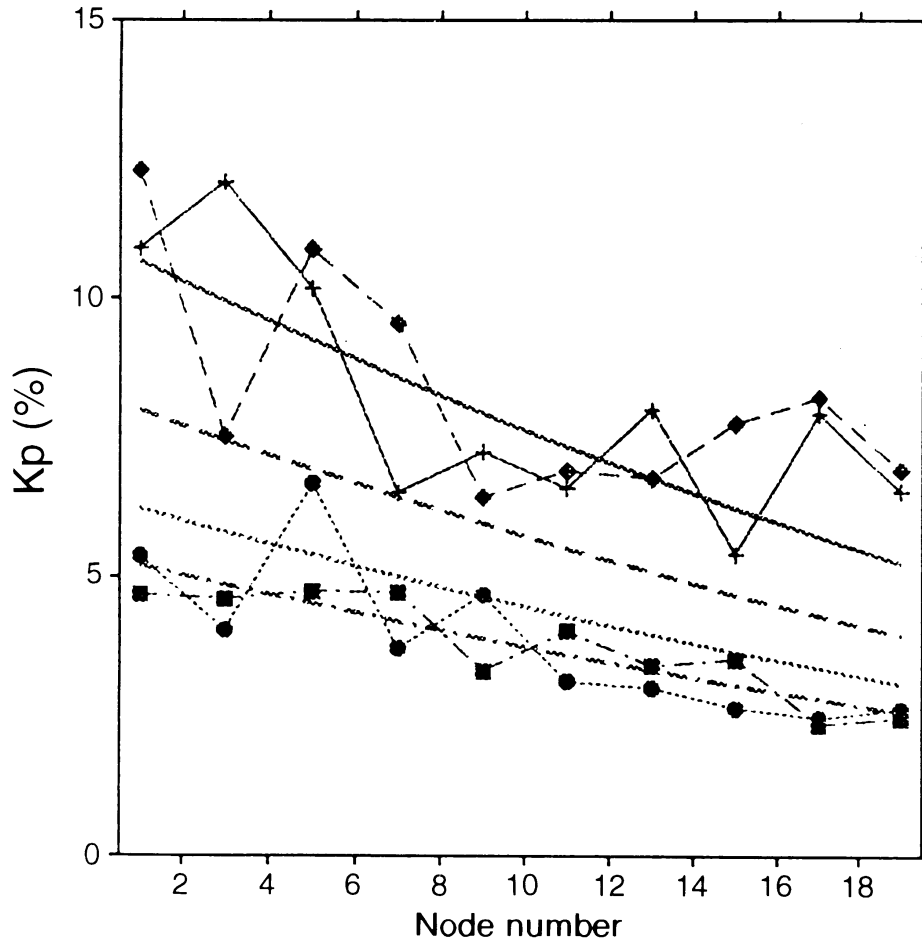


**Figure D1.** Plot of the estimated scatter in  $\sigma^0$  triplets normal to the cone surface (as a percentage of  $\|\sigma^0\|$ ) as a function of node number (see text). Speeds of 3, 9, 12.5, and 16.5  $\text{m s}^{-1}$  are denoted by crosses, diamonds, circles, and squares, respectively. The function  $g$  used to represent noise is also shown for the above speeds by the smooth lines.

## References

- Anderson, D. L. T., A. Hollingsworth, S. Uppala and P. M. Woiceshyn, A study of the use of scatterometer data in the ECMWF operational analysis-forecast model Part I. Quality assurance and validation. *J. Geophys. Res.*, 96, 2619-2634, 1991.
- Boehnke, K. and V. Wismann, Radar signatures of equatorial upwelling regions measured by the ERS-1 scatterometer, *Proc. Second ERS-1 Symp.—Space at the Service of Our Environment, Hamburg, Germany, Eur. Space Agency Special Publ., ESA SP-361(I)*, 507-512, 1994.
- Cavanié, A. and P. Lecomte, Vol 1 - Study of a method to dealias winds from ERS-1 data. Vol 2 - Wind retrieval and dealiasing subroutines, *ESA contract 6874/87/CP-I(sc)*

- report*, ESA publications division, Noordwijk, the Netherlands, 1987.
- Donelan, M. A. and W. J. Pierson Jr., Radar scattering and equilibrium ranges in wind-generated waves with application to scatterometry, *J. Geophys. Res.*, 92(C5), 4971-5029, 1987.
- Graham, R., D. Anderson, A. Hollingsworth and H. Böttger, Evaluation of ERS-1 wind extraction and ambiguity removal algorithms: meteorological and statistical evaluation, *ECMWF report*, ECMWF, Reading, England, 1989.
- Keller, M. R., W. C. Keller and W. J. Plant, A wave tank study of the dependence of X-band cross sections on wind speed and water temperature, *J. Geophys. Res.*, 97(C4), 5771-5792, 1992.
- Lecomte, P., Wind scatterometer processing requirements for ice detection, *Document ER-SA-ESA-SY-1122, Issue 2.1* (Available from ESRIN DPE/OM, Via Galileo Galilei 5, I-00044, Frascati, Italy), 1993.
- Long, A. E., Towards a C-Band radar sea echo model for the ERS-1 scatterometer, *Proceedings Conference on Spectral Signatures, Les Arcs, France, December 1984, Eur. Space Agency Special Publ., ESA SP-247*, 29-34, 1985.
- Stoffelen, A. C. M. and D. L. T. Anderson, ERS-1 scatterometer data characteristics and wind retrieval skill, *Proceedings of the First ERS-1 Symposium, Cannes, France, November 1992, Eur. Space Agency Special Publ., ESA SP-359*, 41-47, 1993.
- Stoffelen, A. C. M. and D. L. T. Anderson, The ECMWF contribution to the characterisation, interpretation, calibration and validation of ERS-1 scatterometer backscatter measurements and winds, and their use in numerical weather prediction models, *ESA contract 9097/90/NL/BI report*, Eur. Centre for Medium-range Weather Forecasts, Reading, England, 1995.
- Stoffelen, A. C. M. and D. L. T. Anderson, Scatterometer data interpretation: Estimation and validation of the transfer function CMOD4, *J. Geophys. Res.*, 102(C3), 5767-5780, 1997a.
- Stoffelen, A. C. M. and D. L. T. Anderson, Ambiguity removal and assimilation of scatterometer data, *Q. J. Roy. Meteorol. Soc.*, 123, 491-518, 1997b.
- Unal, C. M. H. P., P. Snoeij and P. J. F. Swart, The polarization-dependent relation between radar backscatter from the ocean surface and surface wind vector at frequencies between 1 and 18 GHz, *IEEE Trans. Geosci. Remote Sens.*, 29(4), 621, 1991.

## CHAPTER III

## Scatterometer Data Interpretation: Estimation and Validation of the Transfer Function CMOD4\*

**Abstract.** In this paper we estimate the 18 coefficients of the CMOD4  $\mathbf{s}^0$ -to-wind transfer function using a Maximum Likelihood Estimation (MLE) method in order to improve the prelaunch function. We show that a MLE method has to be used with caution when dealing with a nonlinear relationship, or with measurement errors that depend on the measured values. In the transfer function estimation it is crucial to use the components of the wind, rather than wind speed and direction, to use  $\mathbf{s}^0$  in logarithmic units rather than physical ones, and to use well-sampled input data. In *Stoffelen and Anderson* [1997a; Chapter II], we showed that the triplets of measured backscatter are very coherent, and, when plotted in a three-dimensional measurement space, they lie on a well-defined conical surface. Here we propose a strategy for validation of a transfer function, the first step of which is to test the ability of a transfer function to fit this conical surface. We derive an objective measure to compute the average fit of the transfer function surface to the distribution of measured  $\mathbf{s}^0$  triplets. The transfer function CMOD4, derived in the first part of this paper, is shown to fit the cone surface to within the observed scatter normal to the cone, i.e., within roughly 0.2 dB, equivalent to a root-mean-square wind vector error of  $\sim 0.5 \text{ m s}^{-1}$ . The second step in the validation strategy is the verification of retrieved scatterometer winds at each position on the cone surface. Scatterometer winds computed from CMOD4 compare better to the European Centre for Medium-range Weather Forecasts model winds than real-time conventional surface wind data (ship, buoy or island reports) with the root-mean-squared wind vector difference typically  $3.0 \text{ m s}^{-1}$ . This surprising result can be explained by the so-called representativeness error. We further show that no significant spatial wind error correlation is present in scatterometer data and therefore conclude that the ERS-1 scatterometer provides winds useful for weather forecasting and climate studies.

## 1. Introduction

The ERS-1 satellite was launched on July 17, 1991, carrying a C-band scatterometer

---

\*Based on:

Stoffelen, Ad , and David Anderson, Scatterometer Data Interpretation: Derivation of the Transfer Function CMOD4, *J. Geophys. Res.*, 102(C3) , 5767-5780, 1997, © American Geophysical Union.

providing at each node within the swath three radar backscatter measurements, called  $\mathbf{s}^0$ . In *Stoffelen and Anderson* [1997a; Chapter II] the visualization of these radar backscatter triplets in the three-dimensional (3D) measurement space was discussed. At each node across the swath the distribution of measured backscatter triplets was shown to lie close to a cone-shaped surface. The scatter of triplets normal to the surface is typically 0.2 dB, which is comparable to the instrument noise. Furthermore, given the sensitivity of backscatter to wind, this scatter is equivalent to an uncertainty in the wind domain of  $0.5 \text{ m s}^{-1}$  vector root-mean-square (RMS). A backscatter-to-wind transfer function, as will be derived in this paper, should be able to reproduce the conical surface and fit the distribution of backscatter triplets to within 0.2 dB. It may be clear that this is a very stringent test for validation, since an agreement of 1.0 dB between laboratory experiments and aircraft campaigns is considered close [e.g., *Keller et al*, 1992]. In section 5 we will show that CMOD4 does generally fit the distribution of measured backscatter triplets to within the required limit of 0.2 dB.

In *Stoffelen and Anderson* [1997a; Chapter II] described an accurate method to map a measured triplet onto the cone surface, thereby providing the two coordinates of the surface. CMOD4 uses the surface wind, i.e., wind speed and direction  $(V, \mathbf{f})$ , or alternatively the wind components  $(u, v)$ , to describe the geometry of the cone surface. A second validation step, as discussed in section 5, is therefore to validate how well the two parameters are related to the 10-m wind. Prior to the transfer function validation we discuss transfer function estimation using a Maximum Likelihood Estimator (MLE) method.

The pre-launch transfer function CMOD2 relating  $\mathbf{s}^0$  to wind speed  $V_N$  and direction  $\mathbf{f}_N$  for neutral stability at 10-m height was discussed in *Stoffelen and Anderson* [1997a; Chapter II], but for convenience we repeat it here.

$$\mathbf{s}^0 = B_0[1 + B_1 \cos(\mathbf{f}_N) + B_2 \cos(2\mathbf{f}_N)] \quad (1)$$

where  $B_0 = 10^a V_N^g$  and  $B_1$  and  $B_2$  are linear functions of wind speed  $V_N$  and parabolic functions of the incidence angle  $\mathbf{q}$  and thus each contain six tunable coefficients. With  $\mathbf{a}$  and  $\mathbf{g}$  also parabolic functions of  $\mathbf{q}$ , containing three coefficients each, the total number of tunable coefficients is 18. The parabolic incidence angle dependency is established by using Legendre polynomials of order 0, 1, and 2 in  $x = (\mathbf{q} - 40)/25$  with  $\mathbf{q}$  the radar beam incidence angle measured in degrees, e.g.,  $\mathbf{a} = C_1 + C_2 x + C_3 (3x^2 - 1)/2$ . Stability effects will be further ignored in this paper and in the above equations  $(V_N, \mathbf{f}_N)$  will be replaced by  $(V, \mathbf{f})$ . This is equivalent to assuming that stability is only wind speed dependent.

*Stoffelen and Anderson* [1997a; Chapter II] showed that the behavior of the bias term  $B_0$ , the upwind-crosswind term  $B_2$ , and the upwind-downwind term  $B_1$  of the empirical

transfer function shows important features that are not represented in CMOD2. A nonlogarithmic wind speed dependency, saturation of the harmonic terms for increasing wind speeds and incidence angles, and the presence of higher harmonic terms in  $\mathbf{f}$  are the most relevant. It was shown, however, that the higher harmonic terms, i.e.,  $\cos(3\mathbf{f})$  and  $\cos(4\mathbf{f})$ , were unnecessary in a transformed space:  $z = (\mathbf{s}^0)^{0.625}$ .

To accommodate these shortcomings of CMOD2, we propose a transfer function of the form

$$z = B_0^z [1 + B_1^z \cos(\mathbf{f}) + B_2^z \cos(2\mathbf{f})] \quad (2)$$

with

$$B_0^z = 10^{a + LUT(\mathbf{q}) + g f_1(V+b)} \quad (3)$$

where  $\mathbf{a}$  and  $\gamma$  are formulated as in CMOD2, but whose values will be re-estimated in this paper.  $LUT(\mathbf{q})$  is computed from a comparison between the ERS-1 scatterometer  $\mathbf{s}^0$  and  $\mathbf{s}^0$  simulated from European Centre for Medium-range Weather Forecasts (ECMWF) analysis winds [Stoffelen and Anderson, 1995] and is fixed. The parameter  $\mathbf{b}$  has a parabolic dependency on  $\mathbf{q}$  and is used to allow some flexibility in fitting  $\mathbf{s}^0$  at low wind speeds, while  $f_1(s)$  has the form recommended in Stoffelen and Anderson [1997a; Chapter II]

$$f_1(s) = \begin{cases} -10 & , \quad s \leq 10^{-10} \\ \log s & , \quad 10^{-10} < s \leq 5 \\ \sqrt{s} / 3.2 & , \quad s > 5 \end{cases} \quad (4)$$

The form of  $B_1^z$  is

$$B_1^z = a_1 + a_2 V + (a_3 + a_4 V) [ \tanh(2.5y) - 0.61y ] \quad (5)$$

where  $a_1$ - $a_4$  are tunable coefficients and  $y = (\mathbf{q} - 31.25)/25$ . The tanh term describes the saturation behaviour for increasing  $\mathbf{q}$  and  $V$  and the large sensitivity to  $\mathbf{q}$  around  $\mathbf{q} = 31.25^\circ$ , as discussed by Stoffelen and Anderson [1997a; Chapter II]. For the upwind-crosswind amplitude we also tried to describe the saturation behaviour for increasing incidence angles and wind speeds, using the following form for  $B_2^z$

$$B_2^z = [ 0.42 + a_5(a_6 + x)(a_7 + V) ] \tanh[ a_8 + a_9(1 + x)V ] \quad (6)$$

where  $x$  is as defined before,  $x = (\mathbf{q} - 40)/25$ . In this formulation, called CMOD4, there are 18 tunable coefficients. An MLE method will be used to determine these coefficients, as was done for CMOD2 [Long, 1985].

The nonlinear nature of the  $\mathbf{s}^0$ -to-wind relationship and the fact that the error of the radar measurements depends on the measured value complicate the estimation problem. In section 2 we give examples using simulated data to provide guidance on how to modify the

MLE process to cope with these complications. In particular, we used the wind components, rather than wind speed and direction, and  $\mathbf{s}^0$  in logarithmic units, rather than physical ones, in order to represent accurately the error characteristics of the measurements and minimize the nonlinearities in the transfer function. We also consider how best to represent the error in the wind data. In section 3 estimation with real data is discussed using well-sampled collocated sets of ERS-1 scatterometer  $\mathbf{s}^0$  and ECMWF numerical weather prediction (NWP) model analysis winds. In section 4 it is shown that two apparently “obvious” a posteriori checks on the quality of the transfer function are in fact not reliable indicators of the quality at all. Specifically, in section 4.1 it is shown that simple direct comparisons of measured  $\mathbf{s}^0$  with  $\mathbf{s}^0$  simulated from wind data are not a reliable indicator of a good transfer function, while in section 4.2 it is shown that biases in retrieved wind speed are not necessarily caused by an offset in the level of measurement of one system with respect to the other but can result from different levels of noise in the two systems. In section 5, it is shown preferable to adopt a two-step validation procedure, where verification of the coherence of the  $\mathbf{s}^0$  triplets in 3D measurement space and the validation of the wind vector interpretation are done separately. Results are summarized in section 6.

## 2. Estimation of the Transfer Function: Simulation Studies

The problem is to find the best estimate of the coefficients relating a set of  $\mathbf{s}^0$  measurements with collocated “ground truth” wind data, given estimates of both the ground truth and  $\mathbf{s}^0$  measurement errors. (The ground truth data should not be considered to be error-free, although this is frequently done). The MLE procedure of *Britt and Luecke* [1973] allows errors to be assigned to both  $\mathbf{s}^0$  and the 'ground truth' wind, when seeking the best fit. *Long* [1985] employed this procedure when determining the prelaunch transfer function CMOD2. He used wind speed and direction measurements from research ships and buoys participating in calibration and validation campaigns as the ground truth, while the  $\mathbf{s}^0$  were from airborne radars. Our data differ from Long's in that we used satellite  $\mathbf{s}^0$  and 10-m winds from the ECMWF analysis. It is important to use accurate estimates of the error characteristics of both sets of information. The prelaunch specification for the  $\mathbf{s}^0$  error was 10% and was therefore a proportional error. We used this as a starting point for our simulations.

By verification of the ECMWF 6-hour wind forecast with conventional ship observations, it was found that the standard deviation (SD) of the difference between the observed and forecast wind components is rather independent of the magnitude of the wind. In contrast, although the SD of the speed difference depends only weakly on wind speed, the SD of the wind direction difference shows a strong variation with wind speed. So error



estimates are more easily quoted in terms of wind components than in terms of speed and direction. Assuming that the observed and forecast wind errors are equal we used  $\Delta u = \Delta v = 2.25 \text{ m s}^{-1}$ . Since  $V = (u^2 + v^2)^{1/2}$  and  $f = \arctan(u/v)$ , the wind speed and direction error distributions will then become quite complicated. It implies that for low speeds around  $2 \text{ m s}^{-1}$  the speed error distributions will be very asymmetric and therefore not Gaussian since no negative speeds occur in the distribution. The SD of the direction error distribution is strongly dependent on wind speed as was the case for real data.

Before discussing results on real data, we present two examples using simulated data to illustrate problems we found when tuning. The first example considers the effect of assigning error characteristics to the ground truth information in terms of speed and direction rather than in terms of wind components. The second addresses the use of a quadratic MLE to estimate parameters of a nonlinear function. If a linear relationship exists between  $\mathbf{s}^0$  and wind, then a quadratic MLE is appropriate, but nonlinearity poses limits on the usefulness of a quadratic formulation in a MLE problem. However, given the nonlinearity and complexity of the transfer function (equations (2)-(6)), a mathematically optimal solution would be difficult to find (see Appendix A), and so we retain a quadratic formulation but try to pose the problem in a more linear and symmetric space. The second example shows that fitting in  $\ln(z)$  space is preferable to fitting in physical space.

In appendix A we give two analytic examples to illustrate the following points: (1) using a quadratic MLE to estimate a nonlinear relationship may lead to substantial second order errors, (2) proportional measurement error will generally lead to first-order errors if not taken into account properly, (3) errors in the estimation procedure can be further inflated by an unbalanced data selection, and (4) in the fitting process, errors can be reduced by incorporating prior knowledge on the relationship to be fitted.

A further point of concern is that an error in the estimation of one coefficient will be correlated with the errors in the other coefficients. In our experiments we found, for instance, very often that errors in the speed dependence were associated with errors in the estimated wind direction dependence, such that on average the curve still remains as close as possible to the data distribution.

To take account of these points in the estimation, we simulated data for which the true solution was known. Analysis winds were chosen to be “true” winds, and true  $\mathbf{s}^0$ s were simulated from them using CMOD2. Noise with a normal distribution was then added both to the true winds with a standard deviation of  $2.25 \text{ m s}^{-1}$  in the wind components and to the  $\mathbf{s}^0$ s with a standard deviation of 10%, i.e., proportional to the signal. In the examples below we use the same wind distributions that are used for tuning with real data in section 3. The filtering procedures used to obtain the collocated dataset are described later in section 3. The number of collocated points is typically 20,000.

## 2.1. Example 1: Tuning Simulations using Wind Components rather than Speed and Direction

The simulation will be most meaningful when the noise characteristics resemble the noise that will be experienced in the real problem. For example, specification of the noise in the wind as Gaussian and 20% in wind speed and 20° in direction for all wind velocities (as was used by *Long* [1985] in deriving the CMOD2 model function, for example) will give misleading simulations, since in reality such a noise specification is not a good approximation. Since the statistical properties of errors in the components of the wind are much simpler than the statistical properties of errors in wind speed and direction, it is more advantageous to derive a transfer function using wind components rather than speed and direction. To illustrate this, we compare the upwind-crosswind amplitude for two simulations, differing only in that in one case we used wind speed and direction in the objective function, and wind components in the other. The MLE software used is similar to that used by *Long* [1985].

In case of using wind speed and direction we used

$$J_3 = \frac{1}{N} \sum_{i=1}^N \left( \frac{\mathbf{s}_i^0 - \mathbf{s}_{Si}^0}{K \mathbf{s}_i^0} \right)^2 + \left( \frac{V_i - V_{Si}}{\Delta V} \right)^2 + \left( \frac{\mathbf{f}_i - \mathbf{f}_{Si}}{\Delta \mathbf{f}} \right)^2 \quad (7)$$

where  $\mathbf{s}_i^0$  is the (simulated) measured value,  $\mathbf{s}_{Si}^0 = f(V_{Si}, \mathbf{f}_{Si})$ .  $V_i$  and  $\mathbf{f}_i$  are ECMWF analysis wind speed and direction respectively, and  $V_{Si}$  and  $\mathbf{f}_{Si}$  are the estimated true wind speed and direction respectively. The transfer function,  $f$ , has 18 coefficients and is defined in (1). We used noise estimates of  $K = 0.1$  for  $\mathbf{s}^0$ ,  $\Delta V = 2.6 \text{ m s}^{-1}$  for wind speed, and  $\Delta \mathbf{f} = 20^\circ$  for wind direction. The number of measurements  $\mathbf{s}_i^0$  collocated with  $(V_i, \mathbf{f}_i)$  is denoted  $N$ .

When using the wind components for the estimation, we used

$$J_4 = \frac{1}{N} \sum_{i=1}^N \left( \frac{\mathbf{s}_i^0 - \mathbf{s}_{Si}^0}{K \mathbf{s}_i^0} \right)^2 + \frac{(u_i - u_{Si})^2 + (v_i - v_{Si})^2}{(\Delta u)^2} \quad (8)$$

where  $u$  and  $v$  denote the components of the wind, and  $\Delta u = 2.25 \text{ m s}^{-1}$ . In Figure 1 the upwind-crosswind amplitude for CMOD2 is plotted for reference together with the tuned values derived using speed and direction ( $J_3$ , dotted curve) and components ( $J_4$ , solid curve). It is evident that neither gives the correct specification but estimation using wind components gives a much closer fit to the “true” solution than using speed and direction.

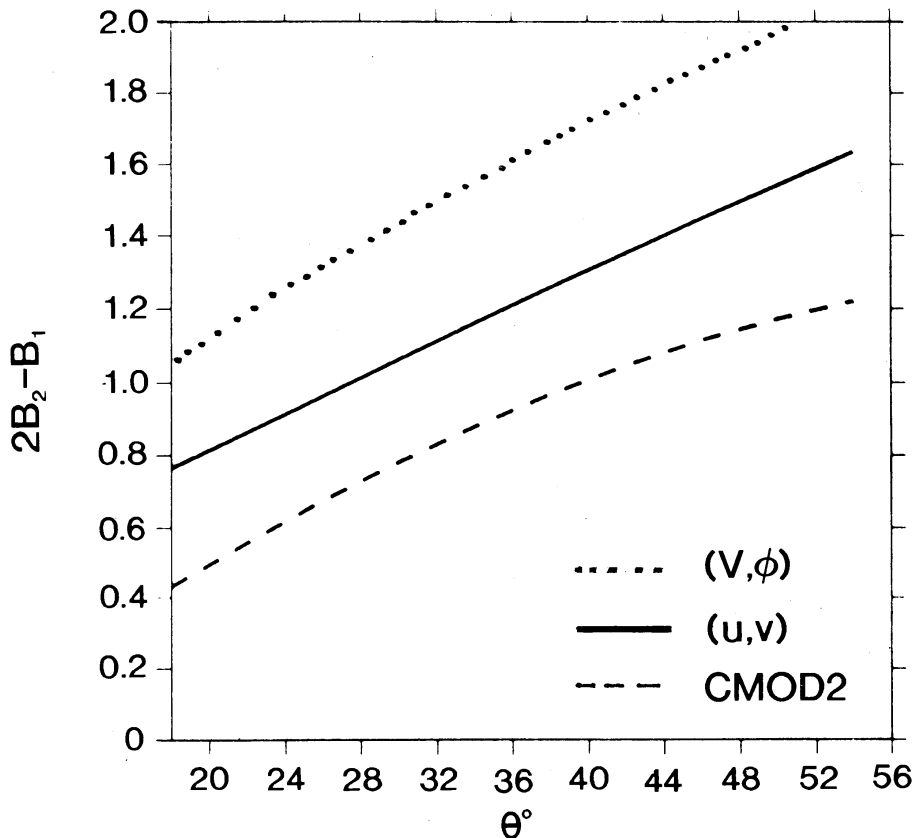


**Figure 1.** Upwind-crosswind amplitude as a function of incidence angle derived using as input to the Britt-Luecke tuning algorithm speed and direction (dotted curve) and wind components (solid curve). The “correct” solution is shown by the dashed curve. The wind speed is  $10 \text{ m s}^{-1}$ . This shows that a more accurate form of the transfer function is obtained using wind components than speed and direction, because the error can be more accurately specified in the former case. Neither using components nor speed and direction returns the correct answer however.

## 2.2. Example 2 :Tuning Simulations in Logarithmic Space

A further consideration is the consequence of proportional errors for MLE. The expected value of the standard deviation of error in  $\mathbf{s}^0$  is proportional to the true value of  $\mathbf{s}^0$ . One way to accommodate this proportional error is to perform the estimation using  $\mathbf{s}^0$  measured in dBs, rather than as a physical quantity. This has the obvious advantage that the instrument error ( $K_p$ ) is approximately constant at 10%, or 0.4 dB, but a further advantage is that some of the nonlinear aspects of the transfer function are eliminated by posing it in  $\ln(z)$  rather than  $\mathbf{s}^0$ . A possible disadvantage is that the error distribution, which is by approximation Gaussian in physical space [Stoffelen and Anderson, 1997a; Chapter II], will

not be strictly so in logarithmic space.

Figure 2 shows the upwind-crosswind amplitude for two simulation cases differing only in that the upper curve is obtained by MLE in physical space, whereas the lower curve is obtained by MLE in logarithmic space for  $z$  where

$$J_5 = \frac{1}{N} \sum_{i=1}^N \left( \frac{10 \log(z_i / z_{Si})}{\Delta z} \right)^2 + \frac{(u_i - u_{Si})^2 + (v_i - v_{Si})^2}{\Delta u^2} \quad (9)$$

The perceived back-scatter noise is  $\Delta z = 0.25$  dB and corresponds to  $K = 0.1$ . Not only is the upwind-crosswind amplitude in error, but the bias term and upwind-downwind amplitude are also significantly worse when estimation is made in physical space. Only the case using wind components is tested as this was shown to be desirable in the previous example. Experiments where we changed the backscatter error standard deviation to be Gaussian in logarithmic space did not show any significant difference in the results (not shown), indicating that the transformation of the error distribution from physical to logarithmic space is not our first concern here.

In most experiments the upwind-crosswind amplitude was found to be very sensitive to slight changes in the bias term, however, indicating that in reality we need a formulation for the bias term which fits the data accurately as in CMOD4. Different, but reasonably uniform wind distributions containing up to 20,000 points, gave slightly different answers after convergence of the MLE procedure, but, in general, there was no dependence of the result on initial conditions, and in most cases, 25 iterations were sufficient to converge to the solution. At the time we made the simulations we were not yet able to accurately estimate the noise level in either the wind components or in  $\mathbf{s}^0$ . In retrospect, both were a little too high, the error in the wind components will later be shown to be  $\sim 1.5 \text{ m s}^{-1}$  and the error in  $\mathbf{s}^0$  is close to 5% as shown in *Stoffelen and Anderson* [1997a; Chapter II]. These more accurate estimates are used in the estimation with real data in next section, and as such results better than those presented here in the simulations may be feasible.

### 3. Estimation of the Transfer Function: Real Data

#### 3.1. Data Selection

Since the quality of the transfer function will be a function of the quality and distribution of the data used to derive it, it is important to select a high-quality and statistically well-conditioned input data set. As spatial correlation in the data introduces local minima in solution space, input winds and  $\mathbf{s}^0$  should be spatially decorrelated. So we created data sets where the spatial separation was at least 300 km between one selected data point and the next. Returns over ice and fractional ice were excluded by a sea surface

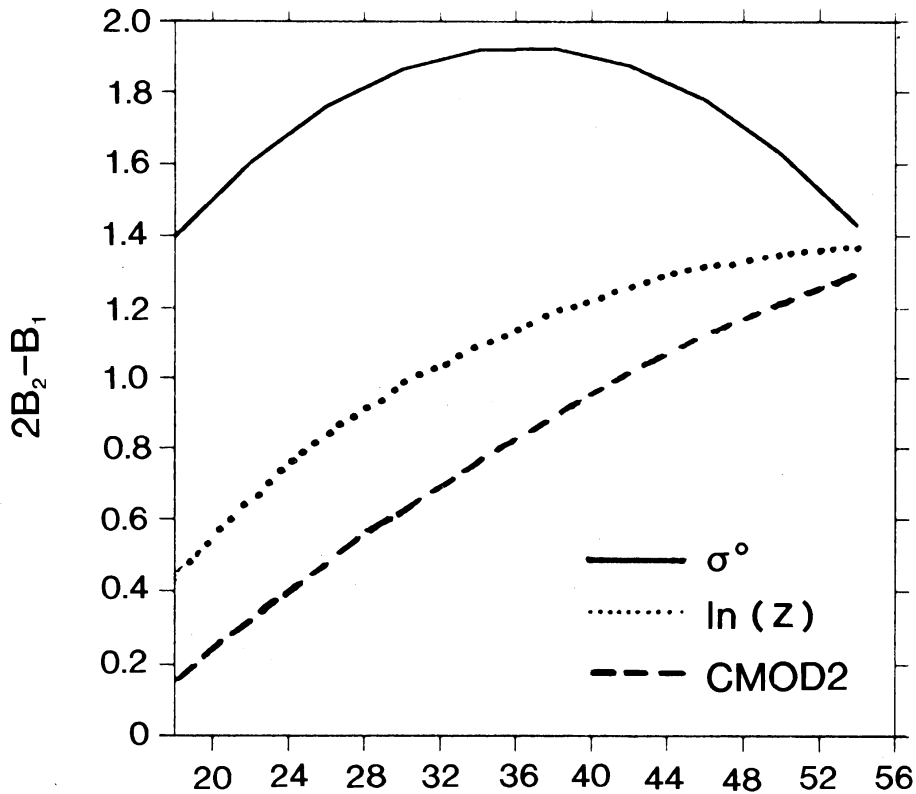


**Figure 2.** Upwind-crosswind amplitude as a function of incidence angle derived using  $\sigma^0$  (solid curve) and  $\ln(z)$  (dotted curve). The wind speed is  $5 \text{ m s}^{-1}$ . Wind input is supplied in component form. The correct solution is given by the dashed curve. This Figure shows that a more accurate representation of the transfer function is obtained using log sigma space rather than sigma space.

temperature (SST) filter such that if the SST was below  $6^\circ\text{C}$  no data were extracted. The distribution of incidence angles covered is irregular because the fore and aft beams have a range of incidence angles only partly overlapping that of the mid beam. We used a filter to achieve a smooth distribution of incidence angles over the full range. We also made a filter selecting beams in such a way as to achieve equal coverage for all three antennae. (If there were no relative biases between the three antennae this filter would be redundant.) We selected only those winds which were sufficiently steady over a certain time period. For each selected ERS-1 scatterometer node we compared the ECMWF forecast wind vector difference between the 3- and 6-hour, and the 6- and 9-hour forecasts. The average of both vector differences was normalized by  $5 \text{ m s}^{-1}$  plus the average of wind speed over the three times considered. The normalization is such that this steadiness filter excludes both high and low winds, if unsteady. The selection threshold was set to 0.2.

In addition, we tested the importance of time and space filtering. Normally, ERS-1 data with observation times differing by up to three hours from the analysis time were selected. Bringing the time window down to two hours did not show any impact in our initial experiments using CMOD2. With hindsight we would recommend using a short-range forecast valid at observation time, called first guess at appropriate time (FGAT), rather than the analysis winds, in which case time filtering becomes redundant [Stoffelen and Anderson, 1995]. The ECMWF analyses are believed to be more accurate in the Atlantic than, for instance, in the southern hemisphere. However, we did not see any statistical difference in surface wind speed verifications between those areas so we did not filter the data regionally in deriving CMOD4.

If a reasonable transfer model already existed, then one could reject  $\mathbf{s}^0$  data if the triplet of measurements had too large a distance to the transfer function solution surface in measurement space [Stoffelen and Anderson, 1997a; Chapter II]. This filter has to be used carefully since it could bias the MLE result towards the transfer function used for selection. The filter was not used in deriving CMOD4.

### 3.2. Estimation

Our first attempts of tuning the transfer function parameters using (7) and the structure of CMOD2 did not lead to an improved transfer function, but, as expected, the use of (9) and the formulation of CMOD4 resulted in substantial progress. Further, in our revised formulation (equations (2)-(6)) there are 18 coefficients to be determined. Our experience with MLE for this problem is that, in general, more degrees of freedom lead to instability, although this depends on how well the transfer function formulation can potentially fit the data. Because of the nonlinearities in the transfer function relationship, our feeling is that even a perfectly formulated function with too many degrees of freedom would show aberrations after estimation. Therefore the diagnostics of the transfer function terms described in *Stoffelen and Anderson* [1997a; Chapter II] were used here to select the transfer function formulation.

Equation (9) was used in the estimations with real data, but with  $\Delta z = 0.125$  dB reflecting a 5% error in  $\mathbf{s}^0$ . Several tests with transfer function formulations slightly different from (2)-(6) were carried out, resulting in different values for  $J_5$  (equation (9)). The lowest value found was 1.4, corresponding to CMOD4. *Stoffelen and Anderson* [1997a; Chapter II] showed that noise in  $\mathbf{s}^0$  increases at low wind speeds, but a noise formulation taking this into account failed to give better results, probably as a result of the strong nonlinearity in the transfer function for low wind speed.

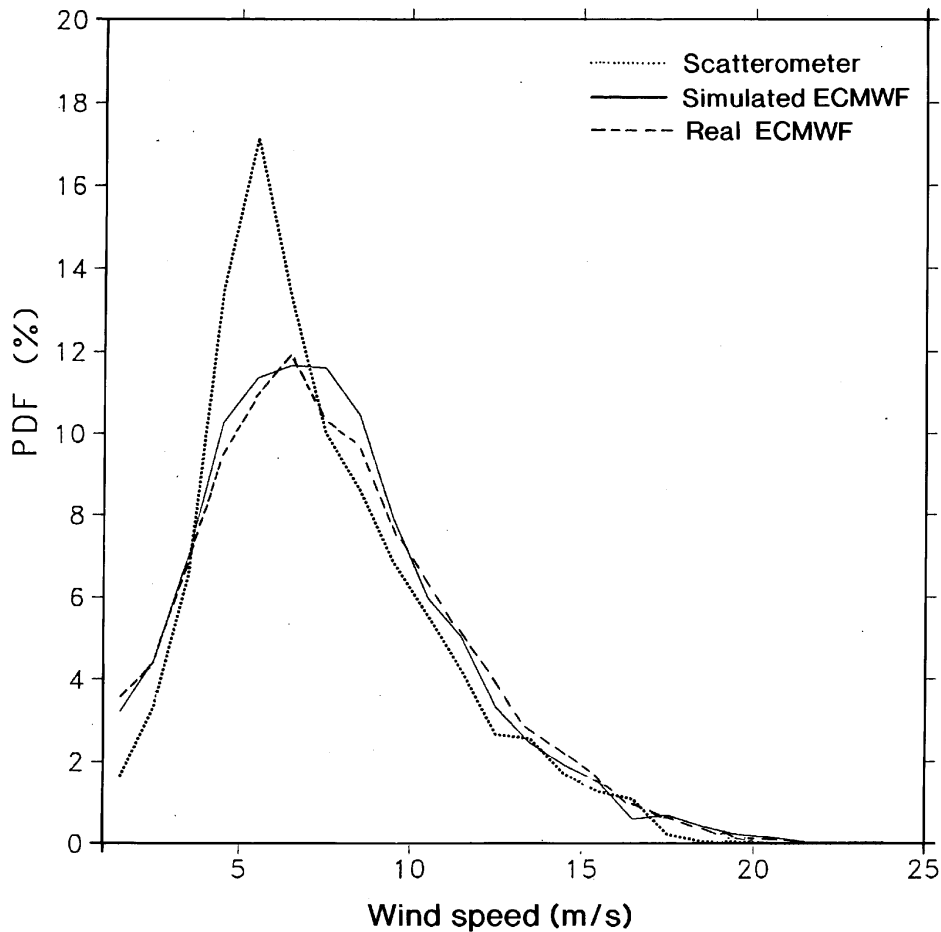


**Figure 3.** Probability density function (pdf) of scatterometer winds (dotted curve) and simulated ECMWF model winds (solid curve). The latter was obtained by adding a Gaussian wind component error of  $2.25 \text{ m s}^{-1}$  to the former. The dashed curve corresponds to the real ECMWF pdf.

The  $B_2$  coefficient as found by *Stoffelen and Anderson* [1997a; Chapter II] is used in CMOD4 and replaces the tuned  $B_2$  coefficient. The revision does not result in a different performance of CMOD4. A revision of the  $B_1$  coefficient has not been tested, although the tuned values and those derived statistically by *Stoffelen and Anderson* [1997a; Chapter II] are close. The details of CMOD4 are given in Appendix B, but before showing verification results for CMOD4 we will discuss two statistical problems which affect the validation procedure.

## 4. Validation Procedure

### 4.1. Interpretation of $\sigma^0$ Differences

Differences between measured and simulated backscatter are caused by (1) noise or scatter in  $\mathbf{s}^0$ , (2) errors in the ECMWF winds, and (3) errors in the transfer function. The actual scatter of triplets around the cone surface corresponds to errors of only a few tenths of a dB in  $\mathbf{s}^0$ , which roughly corresponds to a wind error variance of  $0.5 \text{ m s}^{-1}$  [Stoffelen and Anderson, 1997a; Chapter II]. For comparison, the errors in the ECMWF analysis are estimated to have a standard deviation of  $\sim 2.0 \text{ m s}^{-1}$  in the components of the wind or  $\sim 3.0 \text{ m s}^{-1}$  in vector RMS. The statistics of wind errors are best defined in terms of the components of the wind as discussed in section 2. However, a symmetric error distribution in the components (e.g. a normal distribution with a width of  $2 \text{ m s}^{-1}$ ) around a hypothetical true state corresponds to “biased” and skew error distributions in  $\mathbf{s}^0$  because of the nonlinearity in the transfer function. Since this nonlinearity is wind speed and direction dependent, the interpretation of the  $\mathbf{s}^0$  differences and its average bias and variance is rather complicated. For example, with an upwind-crosswind amplitude ( $B_2$ ) that may be as large as 0.6, we find that a large wind direction departure of, say,  $90^\circ$  may amount to a factor of 4 (6 dB) difference, while a smaller  $20^\circ$  departure may amount to around 2 dB. On the other hand, because of the harmonic dependency of  $\mathbf{s}^0$  on wind direction, a wind direction departure of  $90^\circ$  can also result in a zero difference in  $\mathbf{s}^0$ . Equally, the nonlinear mappings of wind component errors into speed errors and subsequently into  $\mathbf{s}^0$  errors cause asymmetric and wind dependent  $\mathbf{s}^0$  error distributions. Thus in these  $\mathbf{s}^0$  error distributions it is difficult to separate the effect of the known errors in the ECMWF analysis winds from the unknown errors of the transfer function.

### 4.2. Simulation of the Effect of Noise on the Validation

We simulated the effect of the noise of a wind-observing system on the wind speed bias, computed when comparing against a reference observing system. The dotted line in Figure 3 shows a scatterometer wind speed probability density function (PDF) which was taken as a reference (“truth”). The scatterometer winds constituting the PDF were distorted by a random Gaussian noise with zero mean and a standard deviation of  $2.25 \text{ m s}^{-1}$  in the components of the wind. As a result the peak in the distorted PDF, represented by the solid line, is shifted, and a wind speed bias of  $0.5 \text{ m s}^{-1}$  is created in the noisy system with respect to the reference system. Further, the noisy winds are biased high at low speeds and biased low at high speeds with respect to the true winds, due to the broadening of the PDF. The



dashed line in Figure 3 shows the real ECMWF PDF. The resemblance of the dashed and solid lines is remarkable. This shows that studies of bias, especially at high and low speeds, can only be done after an analysis of the random wind error of both comparison systems. Wind validation and error analysis are further discussed in section 5.2.

## 5. A Posteriori Verification

### 5.1. Validation in $\sigma^0$ Space

A fundamental test of a transfer function is its ability to describe the cone surface to within the measurement scatter. We therefore made several cross sections through 3D  $\mathbf{s}^0$  space as defined by *Stoffelen and Anderson* [1997a; Chapter II] for the transfer functions we computed. Measured  $\mathbf{s}^0$  triplets and the transfer function CMOD4 were plotted for various cross sections [*Stoffelen and Anderson*, 1995]. In general, CMOD4 fits the distribution of  $\mathbf{s}^0$  triplets very well. To have an objective score for the fit in  $\mathbf{s}^0$  space, we compute for each measured triplet the distance to the cone surface in  $z$  space as  $\left[ \sum_{i=1}^3 (z_i - z_{Si})^2 \right]^{1/2}$ , where  $z_i$  and  $z_{Si}$ , ( $i=1, 2, 3$ ) are the transformed fore, mid and aft beam measurements and cone values, respectively. This distance is normalized by the standard deviation of the scatter we estimate for this triplet [*Stoffelen and Anderson*, 1997a; Chapter II] and given by

$$SD = 1.25 \left( \sum_{i=1}^3 z_i \right)^{1/2} \left( 1 + \frac{45 - \mathbf{q}_2}{27} \right) \left( 1 + \frac{5}{V} + \frac{1}{2V^2} + \frac{5}{2V^3} \right) \quad (10)$$

where  $\mathbf{q}_i$  is the mid beam incidence angle in degrees and  $V$  the retrieved wind speed. For speeds above  $15 \text{ m s}^{-1}$  a correction  $\sqrt{1 + (V - 15)^2 / 100}$  is applied to  $SD$ . For CMOD4 the average of this squared normalized distance versus node number, wind speed, and wind direction is fairly constant. The square of the normalized distance to the cone is on average 1.7. For comparison, the corresponding value for CMOD2 is 4.0. A perfect transfer function would ideally score roughly 1.0 considering the scatter of measured triplets normal to the cone. The error variance of CMOD4 is therefore roughly 0.7, and smaller than the scatter, so verifying the good fit of CMOD4 to the cone surface. Without exception we found a positive correlation between the fits in  $\mathbf{s}^0$  space and the minimum value of the objective function  $J_5$ , as defined in equation 9.

Spatial correlation of the normalized distance from the cone is evident on geographical plots [*Stoffelen and Anderson*, 1995]. This may translate into spatially correlated errors in the retrieved winds. However, *Stoffelen and Anderson* [1997a; Chapter II] showed that measurement noise should result in a wind vector error of only  $\sim 0.5 \text{ m s}^{-1}$ , which is small

compared to errors in the ECMWF analysis or other observational systems which are typically  $3 \text{ m s}^{-1}$ . Therefore we do not expect the spatial correlation in normalized distance to lead to a substantial correlation of wind errors. The latter is discussed further in section 5.4.

## 5.2. Validation against Winds

In the above section we characterized the fit of CMOD4 to the distribution of  $\mathbf{s}^0$  triplets in  $\mathbf{s}^0$  space, which may be defined as the transfer function  $\mathbf{s}^0$  error. For CMOD4 this error is smaller than the instrument error and should lead to only a small wind error. CMOD4 assigns a geophysical interpretation to each location on the cone surface, i.e., a wind speed and a wind direction. The error in this interpretation is best described as the transfer function wind error and will be further discussed here. However, it will also be shown that the use of CMOD2, which does not fit the cone surface very well, leads to large systematic wind errors.

A statistical comparison between the ERS-1 wind speed retrieved using CMOD4 and the ECMWF first guess is shown in Figure 4a for node 11 for a 3-day period. Similar comparisons for the wind component along the mid beam and wind direction are given in Figures 4b and c, respectively. These figures illustrate the good fit between ECMWF model and scatterometer retrieved winds. For comparison, the corresponding plots for CMOD2 are shown in Figure 5. An erroneous transfer function not only distorts the speed distribution (Figure 5a), but also the angular distribution (Figure 5c), giving rise to the S-shaped distribution for the wind component along the mid beam seen in Figure 5b. (The retrieval procedure discussed in *Stoffelen and Anderson* [1997a; Chapter II] was used to derive the winds in both Figures 4 and 5.) The ECMWF and CMOD4 direction distributions are not uniform due to the nonuniform sampling of the trades and the westerlies in the extratropics. Differences between the two PDFs arise because of errors in both ECMWF and CMOD4 inverted wind directions. The statistical problems, evident for CMOD2, occur in areas where the transfer function cone is displaced with respect to the distribution of measured  $\mathbf{s}^0$  triplets [see *Stoffelen and Anderson*, 1995]. At the locations where the CMOD2 cone intersects with the distribution of  $\mathbf{s}^0$  triplets, the probability that the corresponding wind directions will be retrieved is increased, while in other directions that are more distant from the measured  $\mathbf{s}^0$  triplet distribution, there is much less probability. This effect is clearly seen in Figure 5 and illustrates the importance of transfer function  $\mathbf{s}^0$  error validation.

To put the comparisons with scatterometer data into perspective, histograms of collocations of FGAT winds and automatic or non-automatic wind reports (SHIP) were also made. The results are summarized in table 1. To have a favorable comparison for the

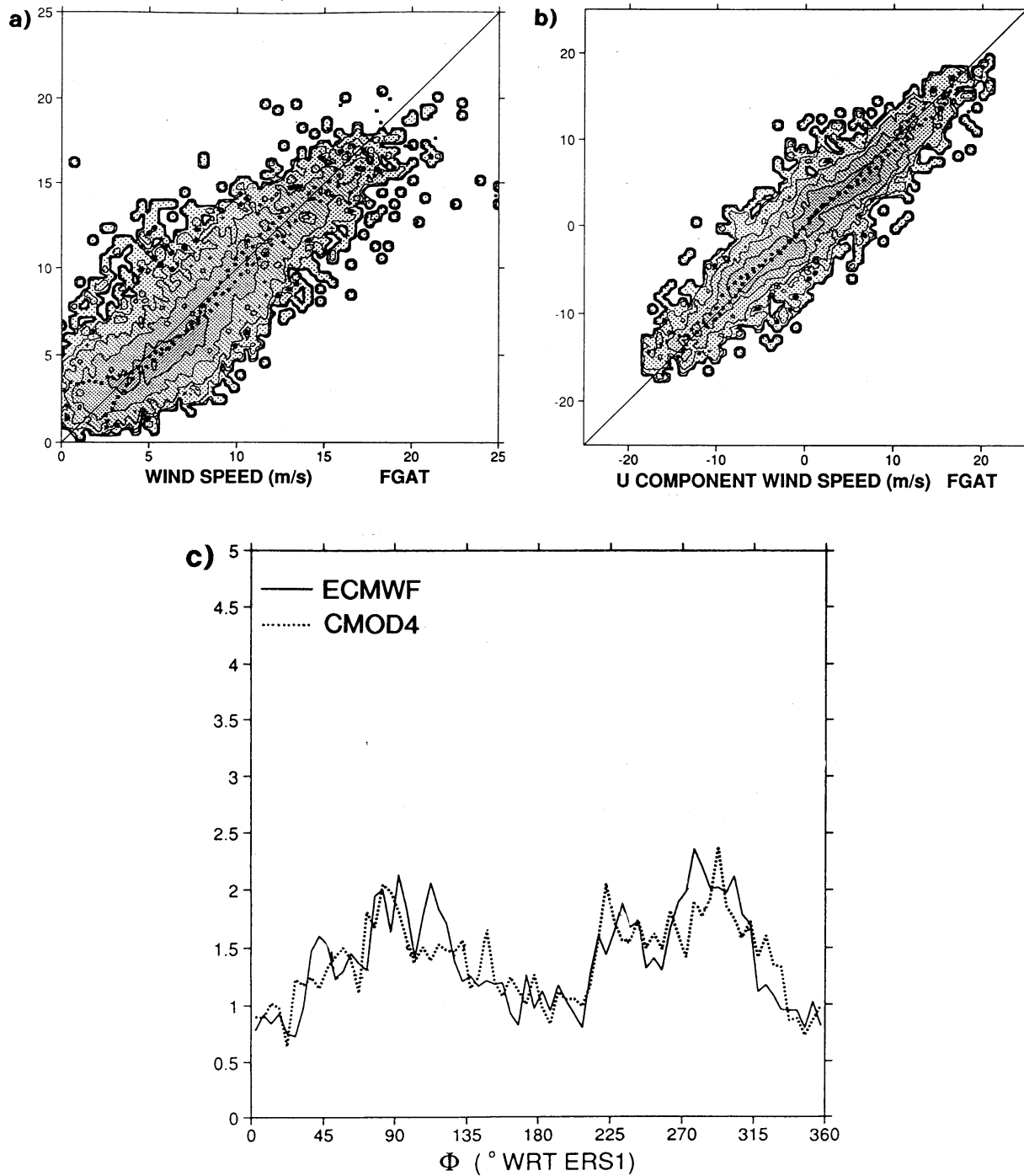


**Figure 4.** Typical examples of (a) the ERS retrieved wind speed versus FGAT speed, (b) the component along the mid beam of retrieved velocity versus the corresponding FGAT component, and (c) the distribution of wind direction measured relative to the satellite direction for ECMWF (solid curve) and retrieved directions (dotted curve). The transfer function CMOD4 was used, together with the inversion scheme described in *Stoffelen and Anderson [1997a; Chapter II]*. Data are over the 3-day period February, 13-15, 1994 for node 11. Figures 4a and 4b show a good speed relationship from 5 to 15  $\text{m s}^{-1}$ . Above 15  $\text{m s}^{-1}$ , it is difficult to reach a conclusion. Figure 4c shows that the angular distributions are also similar.

conventional observations, we excluded conventional wind data more than  $90^\circ$  different from the ECMWF wind direction. For scatterometer data the  $180^\circ$  wind direction ambiguity is resolved by selecting the direction closest to FGAT. The difference statistics incorporate not only wind error due to the observations but also the ECMWF model error, including an error due to the extrapolation from the lowest model level ( $\sim 30$  m) to 10-m height, the nominal height of ship and buoy wind reports. The representativeness error accounts for the mismatch between the spatial and temporal scales that the observations represent and those that the numerical weather prediction model, i.e. FGAT, represents.

“Automatic” SHIP reports include anemometer measurements from the NOAA buoys, the North Sea buoys and some other fixed or moving platforms. “Nonautomatic” SHIP reports often contain winds subjectively estimated from the local sea state (so-called Beaufort estimates). The Beaufort estimates are of lower quality than the anemometer winds. As illustrated in section 4.2, this may give rise to an artificial bias. In Table 1 we see that this may indeed be the case since a positive correlation exists between bias and departure SD, but other well-known factors may also be relevant for creating biases. For example, surface wind should be reported at 10-m height but, in practice, height corrections are either not made or are insufficient. Also, the ship's movement may be ignored or an anemometer may be shielded from the free wind flow. When verifying the ECMWF first-guess (FGAT) by (shallow-) island reports and buoy reports different, but generally lower, biases were found. For these reports the departure wind component SD and observation first-guess correlations are in most cases close to  $3 \text{ m s}^{-1}$  and 94%, respectively (not shown), and their quality is similar to the automatic SHIP winds.

In table 1, the global statistics for retrieved scatterometer winds compared to the ECMWF first guess for node 11 for the wind component along the mid beam show that the highest correlation with the NWP model is for the scatterometer (0.97). Although the first guess is taken from an experiment where SHIP winds were used, but scatterometer winds were not, Table 1 indicates that the scatterometer winds agree better with the ECMWF FGAT than any other real time available surface wind data set. This surprising result may be explained by the representativeness error which will be close to  $2 \text{ m s}^{-1}$  for the conventional data (see section 5.4). Conventional wind measurements are essentially local, whereas scatterometer and NWP model winds both represent large areas ( $\sim 50$  km and  $\sim 200$  km respectively in diameter). The scatterometer wind speed bias is relatively small. This is not surprising since CMOD4 has been tuned to the ECMWF model. However, in section 4.2 it was shown that random error may result in a wind speed bias. This effect is seemingly small, suggesting that FGAT and CMOD4 have a similar wind error SD of  $\sim 1.6 \text{ m s}^{-1}$ . So by tuning to wind we are able to explain a large part of the backscatter signal in the case of CMOD4. From the FGAT accuracy, we compute the wind component error SDs of the

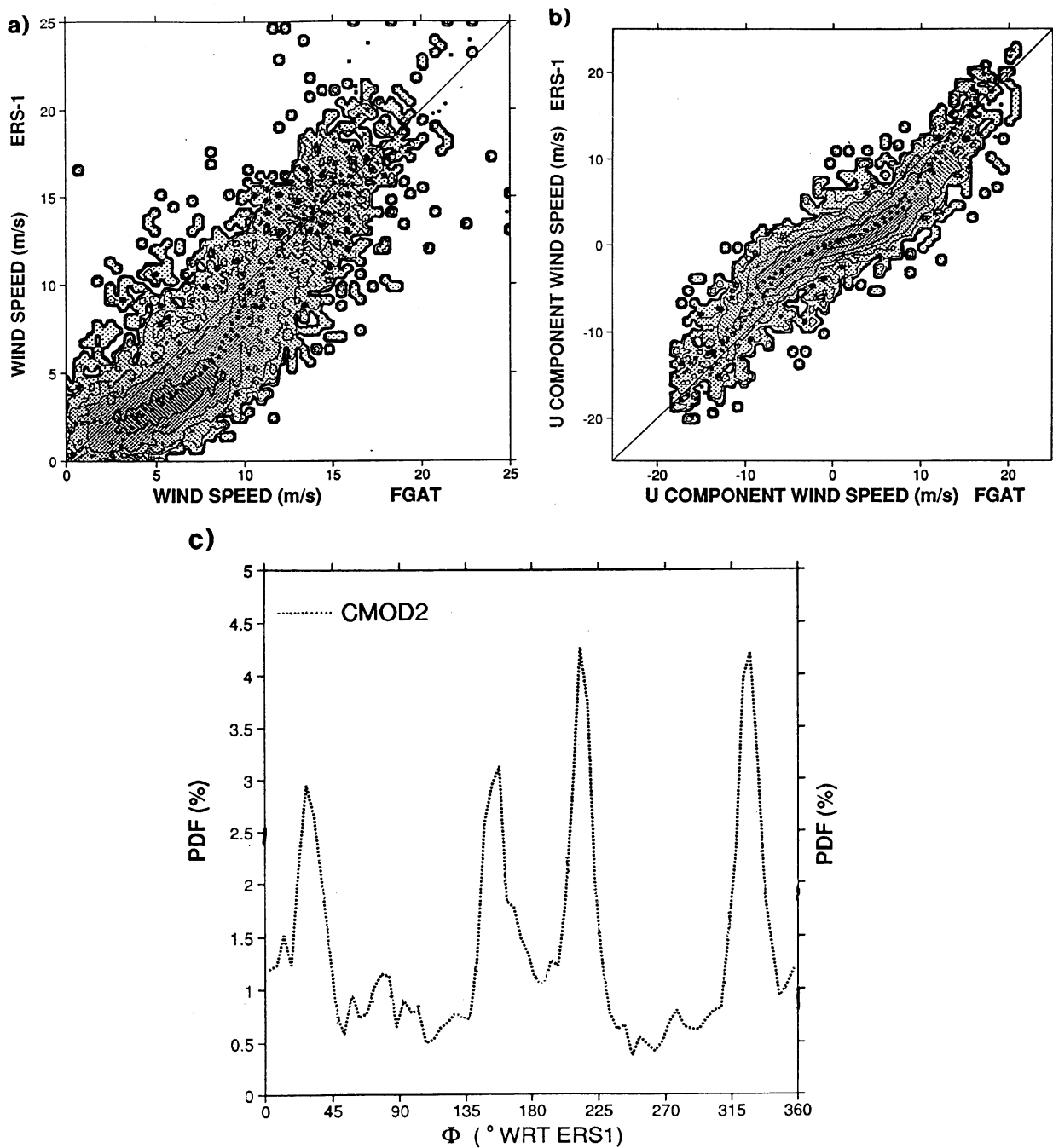


**Figure 5.** As in Figure 4 but for CMOD2. Figure 5a shows that CMOD2 has a speed bias at medium speeds with scatterometer speeds lower than FGAT. For high speeds, the scatterometer is biased high. This speed bias is associated with a peculiar angular distribution (Figure 5c), with certain directions being preferred. Figure 5b shows an S shaped kink in the distribution, consistent with the problems in speed and direction.

**Table 1.** The Standard Deviation (SD) and Correlation of the Wind Component Departures and the Mean Wind Speed Departure for Nonautomatic Ship, Automatic Ship, and Scatterometer Data Compared to the ECMWF First Guess (FGAT).

	SD $u$ ( $\text{m s}^{-1}$ )	Correlation $u$	Bias $V$ ( $\text{m s}^{-1}$ )
Nonautomatic SHIP	3.5	0.93	1.41
Automatic SHIP	2.8	0.95	0.73
Scatterometer	2.2	0.97	-0.2

SHIP data are for March 1993, mainly in the northern hemisphere, and scatterometer data are global for the period March 18, 1993 to March 28, 1993. The scatterometer statistics are for node 11, for the wind component along the beam. Nodes 7 to 19 and the other component have very similar statistics (not shown).

“automatic” and “nonautomatic” ship winds to be  $2.3 \text{ m s}^{-1}$  and  $3.1 \text{ m s}^{-1}$ , respectively.

Table 2 shows more detailed departure statistics of scatterometer minus ECMWF forecast winds, separately for wind speed and direction, for each odd across-swath node. The error, due to the smaller scale of representativeness of scatterometer data in comparison with the NWP model, should not vary with node number. The ECMWF model error contribution should also be the same for all nodes. However, there is a node-to-node variation in the statistics, suggesting that the scatterometer observation error contribution must be nonnegligible for at least some nodes.

We can see that the departure standard deviation (SD) for wind speed increases with increasing node number, whereas for wind direction it decreases. The departure vector RMS (i.e., the square root of the sum of the mean squared wind component differences) decreases with increasing node number, however, indicating that the overall error of the scatterometer system is smallest at far swath. The vector RMS error in the fifth column is slightly higher than the one in the ninth column, because low wind speeds are the most accurate and average speeds below  $4 \text{ m s}^{-1}$  are excluded in the fifth column. Due to differences in the wind distribution, the statistics vary slightly between different seasons and latitudes. However, the errors of both the ECMWF model and the scatterometer wind seem fairly constant across the seasons and the globe. Surprisingly, the error characteristics of the ECMWF model do not result in a substantially larger departure variance in the southern hemisphere as compared to the northern hemisphere (not shown). This suggests that the extrapolation error (projection from  $\sim 30 \text{ m}$  to  $10 \text{ m}$  height), and not the error in the model dynamics, dominates the total ECMWF model error in 10-m wind.

**Table 2.** Departure Statistics of ERS-1 Minus ECMWF Analysis Directions and Wind Speeds for All Odd Nodes

Node	ERS-1 minus ECMWF direction				ERS-1 minus EC wind speed			
	Nbr.	Bias (°)	SD (°)	Vrms (°)	Nbr.	Bias (m s <sup>-1</sup> )	SD (m s <sup>-1</sup> )	Vrms (m s <sup>-1</sup> )
1	9168	0.88	23.81	3.73	10883	-0.48	1.93	3.54
3	9511	0.92	21.13	3.37	11008	-0.41	1.94	3.24
5	9717	1.26	19.89	3.21	11199	-0.30	1.96	3.10
7	9783	1.46	19.17	3.16	11355	-0.28	1.97	3.05
9	9794	1.10	19.07	3.17	11472	-0.26	1.99	3.05
11	9762	1.42	18.86	3.15	11480	-0.24	1.98	3.02
13	9700	1.48	18.69	3.15	11526	-0.25	2.00	3.01
15	9656	1.29	18.71	3.15	11545	-0.25	2.05	3.02
17	9638	1.11	18.31	3.14	11564	-0.24	2.07	3.00
19	9677	0.98	18.36	3.11	11616	-0.24	2.04	2.98

Nodes are numbered from the inside swath. Nbr is the number of collocations. Vrms is the RMS vector wind departure. The values in the fifth column differ from those in the ninth column because direction statistics are only made when the average wind speed exceeds 4 m s<sup>-1</sup>. This restriction does not apply to the ninth column.

CMOD4 was independently tested against Haltenbanken (RENE-91 or ESA's ERS-1 scatterometer calibration and validation campaign) wind data and United Kingdom Meteorological Office analyses and compared with other transfer functions [Offiler, 1994]. A summary of the fit to the Haltenbanken data is given in Table 3, which shows that CMOD4 has the lowest speed bias, the lowest standard deviation on speed and direction, and, most importantly, the lowest vector RMS of all the models tested.

### 5.3. High Speed Comparisons

In deriving the transfer function, a uniform distribution of speed and direction was used as far as possible. Even so, winds above 15 m s<sup>-1</sup> were undersampled for some directions and winds above 18 m s<sup>-1</sup> were hardly present. It is therefore of interest to compare retrieved and FGAT winds in a high wind speed situation. We studied several cases where either scatterometer or FGAT speeds were above 20 m s<sup>-1</sup> but show here only two examples. The first is the "super-storm" which hit the east coast of the United States on March 14, 1993, shown in Figure 6. Figure 6a shows the retrieved winds and Figure 6b the FGAT winds. High wind speeds are more prevalent in the FGAT than in the scatterometer-

**Table 3.** Comparison Between Various Transfer Functions and RENE-91 Campaign Data.

	CMOD2	ESTEC	IFREMER	CMOD4	OREGON
Number of observations	14529	21278	21298	21298	21218
Speed bias ( $\text{m s}^{-1}$ )	0.45	-0.38	0.53	0.06	0.72
Speed SD ( $\text{m s}^{-1}$ )	2.20	1.93	1.71	1.65	2.21
Direction bias ( $^{\circ}$ )	0.94	0.88	-0.15	0.76	0.31
Direction SD ( $^{\circ}$ )	18.96	17.37	17.56	16.69	19.98
Vector RMS ( $\text{m s}^{-1}$ )	4.28	3.25	3.36	3.18	3.60
Figure of merit	0.868	1.081	1.088	1.146	0.949

The transfer function labeled European Space Research and Technology Centre, ESTEC, is tuned on RENE 91 data, the one from Institut Français de Recherche pour l'Exploitation de la Mer, Centre de Brest (IFREMER) is tuned on National Oceanic and Atmospheric Administration (NOAA) buoy data, University of Oregon (OREGON) is based on National Meteorological Center and ECMWF analyses. The figure of merit is an attempt to measure the average performance of a transfer function. Higher values indicate a better performance [Offiler, 1994].

retrieved winds. Nonetheless, the scatterometer records speeds up to  $20 \text{ m s}^{-1}$  indicating that it has apparently not saturated up to this speed. Whether the difference results from a problem with CMOD4 or FGAT is unclear. Figure 7 for May 24, 1993, 00Z shows an example of scatterometer speeds up to  $22 \text{ m s}^{-1}$ . The retrieved speed is, however, an extrapolation from the range of validity ( $4\text{-}18 \text{ m s}^{-1}$ ) of CMOD4. It is therefore not surprising that we find that the average normalized distance [see *Stoffelen and Anderson, 1997a; Chapter II*] is increased to values around 3 for these speeds. It is possible that the sensitivity of the transfer function decreases at higher speeds and therefore the retrieved wind speeds are noisier or it may be that the transfer function fits the cone surface less well at higher speeds. However, these issues have not been fully explored, and are in fact rather difficult to quantify, first, because other observing systems, such as SHIPs are noisy, and the number of collocations few, and second, because the errors in FGAT are unknown at high speed.



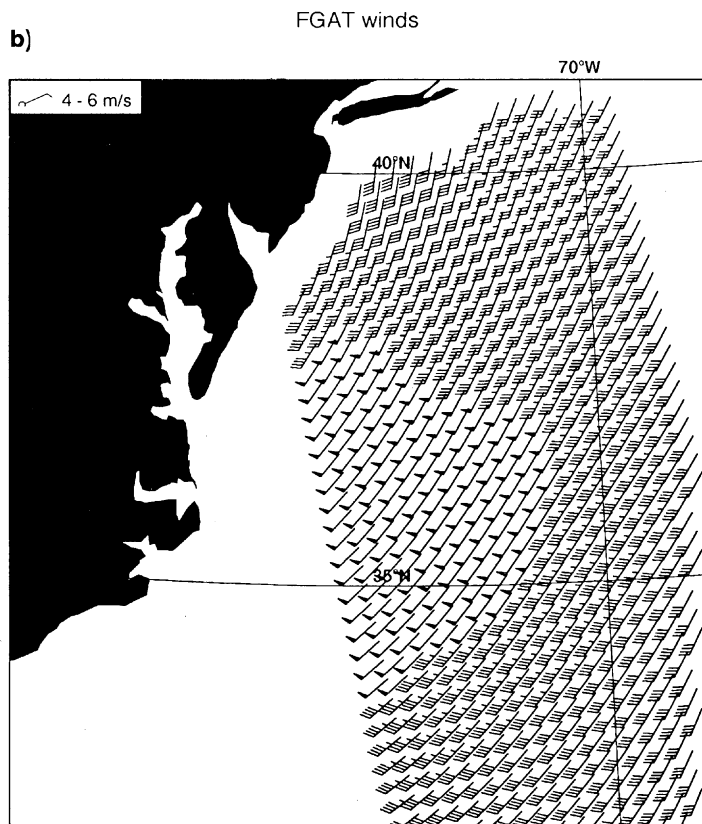
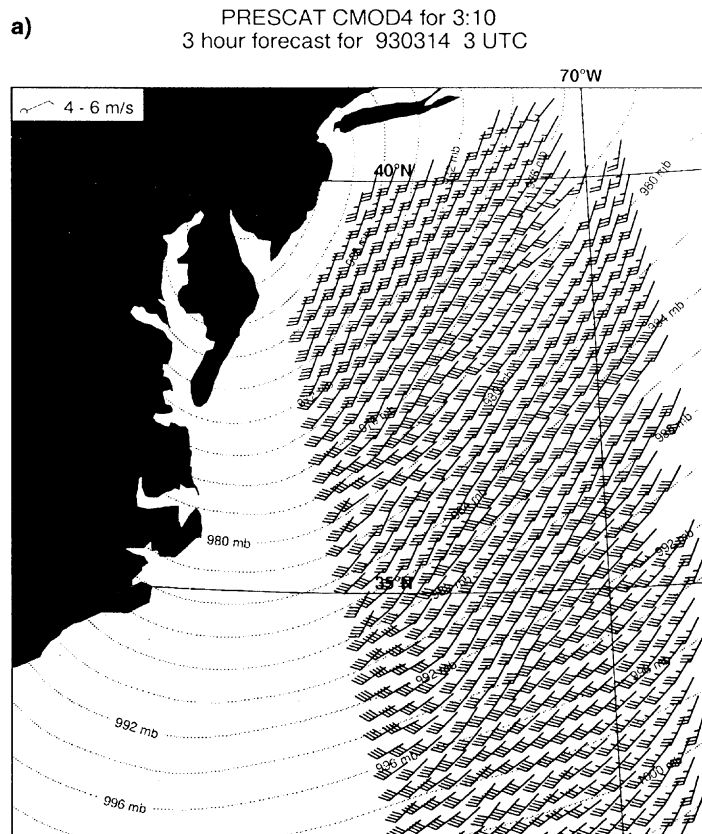


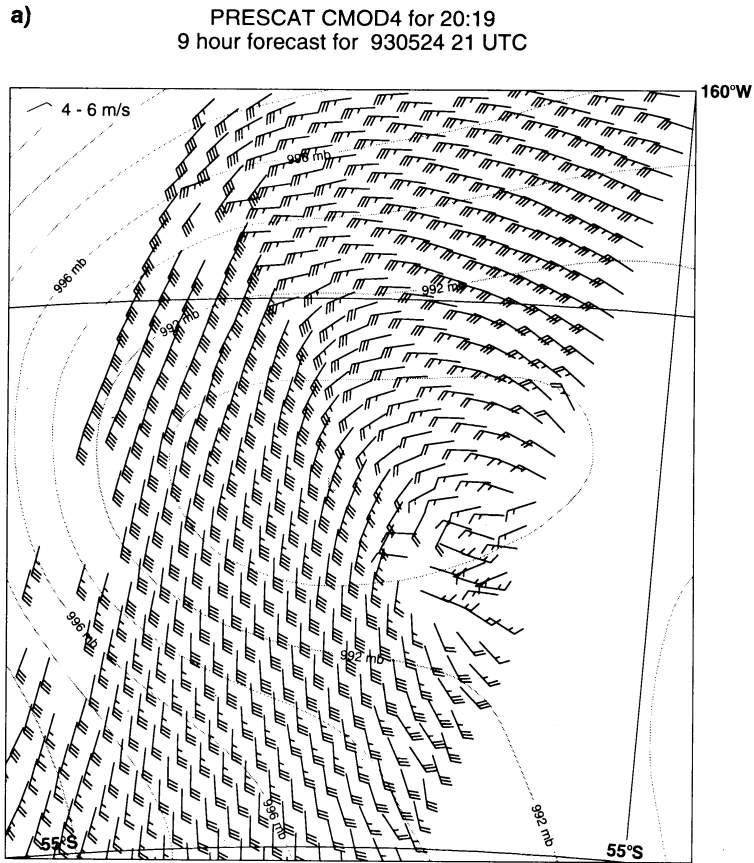
**Figure 6.** Winds for the storm which hit the east coast of the United States on March, 14, 1993: (a) retrieved winds, and (b) FGAT winds.

#### 5.4. Wind Error Correlation

A  $s^0$  measurement is representative of an area with a 50-km diameter, called the footprint, and therefore neighbouring measurements in the swath (at 25 km) are dependent. We examine how the wind vector variance of the departure between scatterometer wind and ECMWF model wind changes with differing degrees of spatial representativeness in the scatterometer data. This can be done by spatially averaging the data, and deducing the scatterometer spatial error characteristics from the different averages. A set of scatterometer data was averaged in square boxes of respectively 1, 3 x 3, 5 x 5, 7 x 7 and 9 x 9 nodes before comparing it to the ECMWF model. The comparisons were done at a fixed set of nodes, all located in the middle of the swath. In the comparisons, the ECMWF winds are kept constant and are assumed to have an error vector variance of  $5 \text{ m}^2 \text{ s}^{-2}$ . The thick line in Figure 8 shows the scatterometer wind vector error variance plotted against the spatial representativeness scale or “resolution”, showing that for increasing horizontal scale the error variance decreases.

Using a wind component energy density spectrum  $E = 0.0012 (2\pi / l)^{-5/3}$ , with  $E$  in  $\text{m}^3 \text{ s}^{-2}$  and  $l$  the wavelength in m, the reduction in wind vector variance for increasing scales was simulated by integration of  $E$  from  $k_B = 2\pi / l_B$  to  $k_B = 2\pi / 50,000$ , with  $k_B$  in  $\text{m}^{-1}$ , and multiplication of the result by 2 (two wind components). The resolution at which the comparison is done is denoted by  $l_B$ . The result plus a fixed offset is given by the thin line in Figure 8. The energy density spectrum was made comparable to the range of tropospheric spectra as found by *Lilley and Petersen* [1983] and the United Kingdom Meteorological Office [*Lorenc et al.*, 1991], but decreased to 75% to account for the smaller variability close to the surface (see Figure 9). The spectra of *Lilley and Petersen* show a variance of 25% around the mean spectrum. The effect of such a spread on the variance reduction is given by the error bar on the right in Figure 8. The computed reduction in variance (thin line) corresponds remarkably well with the observed reduction in vector RMS error after averaging (thick line).

The horizontal diffusion of momentum in the ECMWF model is very effective on scales smaller than  $l = 300 \text{ km}$ , and therefore it is expected that the ECMWF model cannot resolve much of the variability we removed by averaging scatterometer winds. In Figure 8 this is verified by the fact that the thick line has the same slope as the thin line for almost all  $l$ . The scale of representativeness of the model is therefore  $>200 \text{ km}$ , and quite far from the equivalent spatial sampling of  $\sim 60 \text{ km}$  corresponding to a T213 spectral truncation. Thus the model wind field will be relatively smooth, and extreme wind speeds will be underestimated as a consequence. Because the scatterometer was tuned on the ECMWF wind speeds this underestimate may also effect the high wind speed distribution of the scatterometer (see also



b) FGAT winds

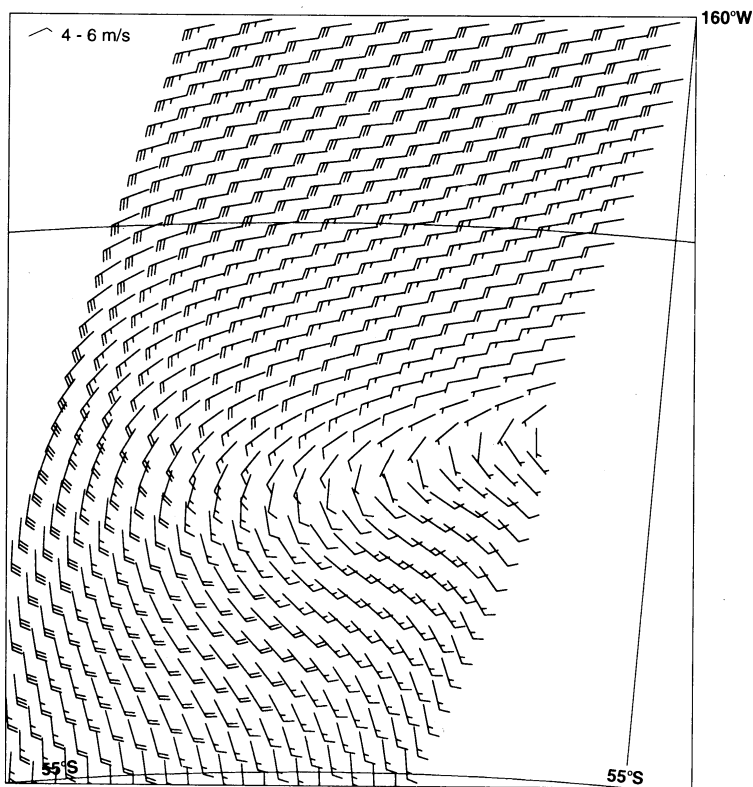


**Figure 7.** (a) Example of PRESCAT winds at 1800 UT on May, 24, 1993, showing speeds up to  $22 \text{ m s}^{-1}$ . (b) FGAT winds, which are much weaker.

previous section).

The 25-km grid sampling and the 50-km footprint cause horizontal error correlation between directly neighbouring scatterometer nodes. If the scatterometer winds had strongly correlated spatial error beyond 50 km, we would expect from Figure 8 that at low  $I$  the reduction in variance would be less than that explained by the  $(2p/I)^{-5/3}$  spectrum (a flat spectral response is expected in this case). We do not see significant signs of this and may conclude that the horizontal error correlation in scatterometer winds is in general not significant, which indicates that a transfer function dependency on spatially smooth geophysical parameters other than wind (e.g. wave effects) is in general not likely to be substantial. The sensitivity of the scatterometer to the wind vector is the main effect. Other geophysical parameters should, however, be investigated for correlation with the remaining departure errors in the more extreme or local conditions.

Global observation-minus-analysis departure statistics provide a good general characterization of observation measurement error but fail to give a complete picture of the usefulness of data. Numerous relevant and complicated synoptic weather patterns were investigated in order to gain experience in dealing with the data. *Stoffelen and Anderson* [1997b; Chapter V] showed and used some examples to illustrate the ambiguity removal problem.

## 6. Summary and Conclusions

A transfer function, CMOD4, was developed which is able to fit the characteristics of the  $\mathbf{s}^0$ -to-wind relationship observed from the ERS-1 scatterometer. The 18 coefficients of the function were estimated with a maximum likelihood estimation (MLE) method. It was necessary to have accurate estimates of the error characteristics of the winds and of the  $\mathbf{s}^0$ s used in the estimation. For this purpose we used the components of the wind, rather than wind speed and direction. Further, the logarithm of the backscatter was used in the estimation, rather than  $\mathbf{s}^0$  to partly take account of the nonlinear  $\mathbf{s}^0$ -to-wind relationship. Before being used in the MLE, the  $\mathbf{s}^0$  and wind data were filtered to obtain smooth distributions and to avoid low-quality or correlated input data.

The validation of a transfer function by the “obvious” method of comparing the simulated  $\mathbf{s}^0$  with the measured value was shown to be rather complicated and more sensitive to the quality of the comparison wind data than to the quality of the transfer function under validation, since the nonlinear mapping of the wind errors in the  $\mathbf{s}^0$  domain dominate the  $\mathbf{s}^0$  departures.

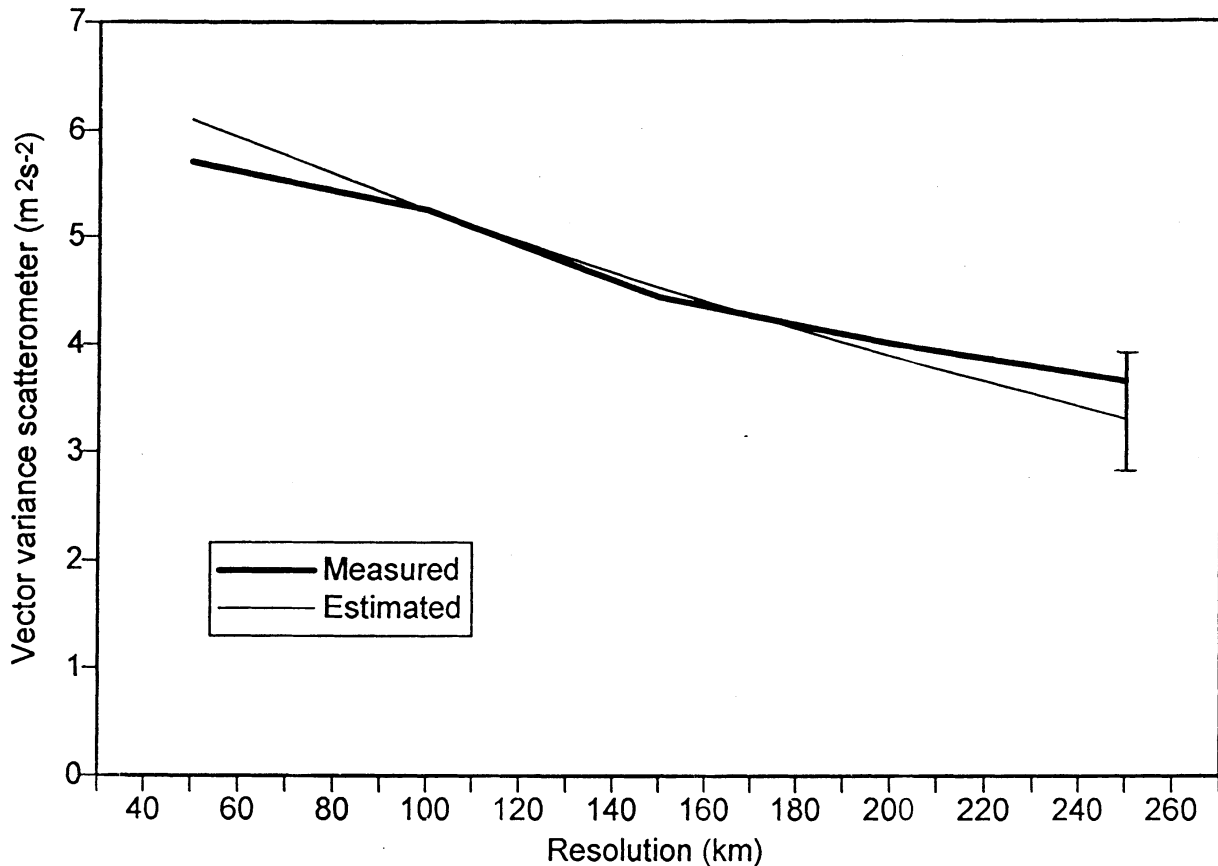


**Figure 8.** Wind vector error variance of processed scatterometer data at a fixed set of scatterometer nodes (thick line). The processing involved averaging over a square box containing 1, 9, 25, 49 or 81 nodes. The spatial scale of representativeness ("resolution") corresponds to respectively 50, 100, 150, 200 and 250 km (horizontal axis). The wind vector error variance of the ECMWF model (FGAT) was estimated to be  $5 \text{ m}^2 \text{ s}^{-2}$ . The thin line indicates the reduction in variance by integration of a climatological wind spectrum (see text). The error bar indicates the spread, due to the natural variability of wind spectra (25%).

An alternative two-step validation strategy was proposed. First, the ability of a transfer function to fit the cone surface was tested. Since the scatter of measured  $\mathbf{s}^0$  triplets normal to the cone surface is small ( $\sim 0.2$  dB corresponding to  $\sim 0.5 \text{ m s}^{-1}$  vector RMS), this test is very sensitive. An objective measure to compute the average fit of the transfer function surface to the distribution of  $\mathbf{s}^0$  triplets was derived in *Stoffelen and Anderson* [1997a; Chapter II]. CMOD4 was shown to fit the cone surface to within the scatter observed normal to the cone. In certain meteorological circumstances, the distance of measured  $\mathbf{s}^0$  triplets to the CMOD4 cone surface may be correlated with other geophysical parameters than wind. This should be investigated in order to obtain further information from the scatterometer, but this was not pursued in this work.

The second step in our strategy concerns the verification of inverted scatterometer

winds. If a transfer function locates the cone surface sufficiently well, this step is essentially independent from the first step, since the effect of the scatter in  $\mathbf{s}^0$  triplets is very small compared to typical wind errors [Stoffelen and Anderson, 1997a; Chapter II]. If, on the other hand, the location of the cone surface is seriously wrong, systematic wind errors will occur. This second step evaluates the wind vector interpretation of each position on the cone surface. Stoffelen and Anderson [1997b; Chapter V] describe a method for resolving the  $\sim 180^\circ$  wind direction ambiguity.

Scatterometer winds computed from CMOD4 compare better to the ECMWF model winds than real-time available conventional surface wind data (ship, buoy, or island reports). This surprising result can be explained by the so-called representativeness error. The ECMWF model represents spatial scales larger than approximately 200 km, which compares better to the equivalent of 50 km for the scatterometer than to conventional wind data which represent all relevant spatial scales as may be estimated from Figure 9. The scatterometer minus ECMWF vector RMS difference is lowest for low wind speeds, and increases slightly with increasing wind speed. CMOD4 was derived from ECMWF winds and may be considered to have a very similar wind speed strength scaling. A further validation of this scaling is planned by taking into account the quality and representativeness of different wind observing systems. Wave models and observations may further help in the assessment, though no such tests have yet been made.

There is no immediate evidence of saturation of the  $\mathbf{s}^0$ s at high wind speeds, as speeds up to  $22 \text{ m s}^{-1}$  are retrieved and seem reasonable, although there is a suggestion that the perceived noise, as measured by distance from the transfer function cone surface is higher at higher speed. This could indicate a general misfit of the transfer function to the true cone surface or a reduced validity of the two-parameter transfer function. Sufficient data have been gathered by now to allow this issue to be further explored.

The spatial structure of the errors in the scatterometer winds was investigated. For scales larger than 50 km no significant spatial error correlation is present. A dependency of the transfer function on spatially smooth geophysical parameters, other than wind, can therefore generally be neglected. In line with this, scatterometer winds were found to contain relevant synoptic detail on scales down to 50 km. Although the general quality of the winds is very good, there may be a correlation of wind departure errors with other geophysical parameters (e.g., stability, waves, rain) in specific cases. The synergy with other satellite data, such as cloud imagery, wave observations, or ocean surface wind speed estimates from passive radar, could be useful in the interpretation of scatterometer data but was not addressed in this work.

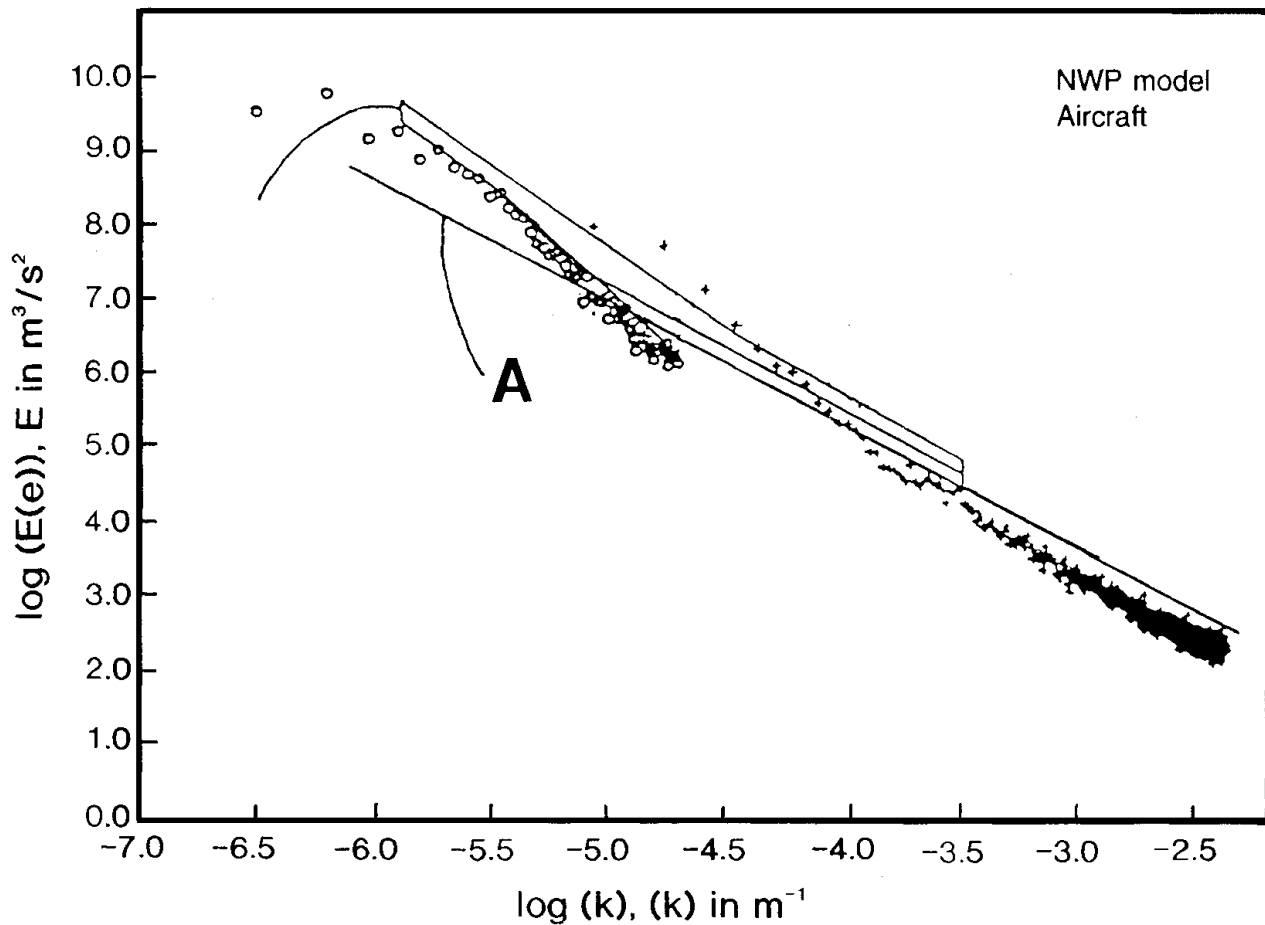


**Figure 9.** Assumed wind spectrum at 10-m height (labelled A) and wind spectra as measured by *Lilley and Petersen* [1983] (solid lines), by United Kingdom aircraft MRF (plusses) and the United Kingdom Meteorol. Office cyber model (circles) for the free troposphere (© British Crown Copyright, *Lorenc et al.* [1991]).

## Appendix A: Analytic Illustration of Curve-Fitting Complications

### A1. Example 1: Nonlinearity in the Transfer Function

In the estimation of a non-linear relationship such as the scatterometer transfer function, the use of a quadratic MLE objective function will lead to errors, even if the measurements are well characterized by Gaussian noise. A simple example illustrates this. Assume we have a two-dimensional (2D) measurement space  $\mathbf{x} = (x, y)$  with axes  $x$  and  $y$ , a true solution  $T: x^2_T + y^2_T = r^2_T$  and an infinite number of measurement pairs  $\mathbf{x}_M = (x_M, y_M)$ , with Gaussian error standard deviations  $\mathbf{s}_X = \mathbf{s}$  and  $\mathbf{s}_Y = \mathbf{s}$  and zero mean error. The convolution of the 2D Gaussian conditional probability density  $p(\mathbf{x}_M | \mathbf{x}) dx_M dy_M$  and the distribution of true points  $p(\mathbf{x}_T) dx_T dy_T$  determines the distribution of measurement points

$$p(\mathbf{x}_M) d\mathbf{x}_M d\mathbf{y}_M = \int \int_x p(\mathbf{x}_M | \mathbf{x}_T) p(\mathbf{x}_T) d\mathbf{x}_T d\mathbf{y}_T d\mathbf{x}_M d\mathbf{y}_M \quad (\text{A1})$$

Since true points  $\mathbf{x}_T$  lie on circle  $T$ ,  $p(\mathbf{x}_T) d\mathbf{x}_T d\mathbf{y}_T$  reduces in polar coordinates  $(r, \mathbf{f})$  to  $p(\mathbf{f}_T) d\mathbf{f}_T = (2p)^{-1} d\mathbf{f}_T$  and in polar coordinates we can write (A1) as:

$$\begin{aligned} p(r_M) dr_M d\mathbf{f}_M &= \\ \int_0^{2p} (2p\mathbf{s}^2)^{-1} \exp[-(2\mathbf{s}^2)^{-1}(r_M^2 + r_T^2 - 2r_M r_T \cos(\mathbf{f}_T - \mathbf{f}_M))] (2p)^{-1} d\mathbf{f}_T dr_M d\mathbf{f}_M \\ p(r_M) dr_M &= \frac{1}{\mathbf{s}^2} I_0\left(\frac{r_M r_T}{\mathbf{s}^2}\right) \exp\left[-\frac{(r_M^2 + r_T^2)}{2\mathbf{s}^2}\right] dr_M \end{aligned} \quad (\text{A2})$$

where we have integrated over  $\mathbf{f}_M$  and  $I_0(r)$  is a modified Bessel function of zeroth order. We note that this distribution does not have its maximum at  $r = r_T$  but at a slightly smaller value, depending on the ratio  $r_T / \mathbf{s}$ . This maximum is therefore in itself not a good estimate of  $r_T$ . We will use MLE to try to estimate a solution lying on a circle with  $r = r_S$ . According to Bayes probability law we write  $p(r_M \cap r_S) = p(r_M | r_S) p(r_S)$ . Note that the direction  $\mathbf{f}_M$  contains no information on  $r_S$ . Assuming that  $p(r_M | r_S)$  is Gaussian and that no further prior knowledge is available, i.e.,  $p(r_S) = \text{constant}$ , we may derive a quadratic log-likelihood objective function

$$J_1 = (r_S - r_M)^2 \quad (\text{A3})$$

However, to approximate  $r_S$ , we minimize (A3) over the measurement distribution  $p(r_M) dr_M$

$$\int \frac{\partial J_1}{\partial r_S} p(r_M) dr_M = 0 \quad (\text{A4})$$

and find

$$\frac{r_S}{r_T} = \frac{\exp[-p_T^2]}{p_T F(p_T)} \quad (\text{A5})$$

with  $p_T = r_T (\sqrt{2} \mathbf{s})^{-1}$  and

$$F(p) = \sqrt{p} \sum_{k=0}^{\infty} \frac{(2k)!}{(k!)^3} (p/2)^{2k} \quad (\text{A6})$$

A Taylor expansion for small  $\mathbf{s} / r_T$  gives

$$\frac{r_S}{r_T} = 1 - \left(\frac{\mathbf{s}}{r_T}\right)^2 \quad (\text{A7})$$



where 3rd order and higher effects have been ignored.

For  $\mathbf{s} = 0.3 r_T$  we have  $r_S / r_T = 1.09$ , i.e., a 9% error in the solution radius. For higher error levels, the result is even more unacceptable, and then the MLE procedure is clearly suitable for solving this nonlinear problem. When the measurement points are not well-sampled, i.e., do not follow the distribution of (A2), then further errors will be introduced, depending on  $\mathbf{s}$ .

## A2. Example 2: Bias Resulting from Proportional Errors

In a second example we consider the case of proportional noise in the above problem; that is, we assume that we know that the noise of the measurement is proportional to the true value, i.e.,  $\mathbf{s} = \varepsilon r_T$ . To allow for this noise, the quadratic objective function (10) is modified to

$$J_2 = \left(1 - \frac{r_M}{r_S}\right)^2 \quad (\text{A8})$$

Minimizing over the measurement distribution, as given in (A1), leads to

$$\frac{r_S}{r_T} = \frac{F'(p_T)}{p_T} \exp[-p_T^2] \quad (\text{A9})$$

where  $F\dot{C}(p) = dF/dp$ . For low values of  $\varepsilon$  and  $r_T = 1$ , the solution can be approximated as

$$\frac{r_S}{r_T} = 1 + 0.10 \frac{\mathbf{s}}{r_T} + 0.51 \left(\frac{\mathbf{s}}{r_T}\right)^2 \quad (\text{A10})$$

$\mathbf{s} / r_T = \varepsilon = 0.3$  will lead to a 8% error on the solution radius  $r_S$ . In this particular example, the errors due to the assumption of proportional error lead to a first-order error and we conclude that fitting a relationship between measurements with a quadratic objective function, where proportional error is present in the measurement system, can lead to substantial errors. The assumption of normal errors in  $r_M$  given  $r_S$  reads  $p(r_M | r_S) = (\sqrt{2\pi} \mathbf{e} r_S)^{-1} \exp[-(r_M - r_S)^2 / (2 \mathbf{e}^2 r_S^2)]$ .

Therefore, in the case of proportional error, a term like  $2 \ln(\mathbf{e} r_S)$  should be added on the right-hand side of (A8). This term results in this particular example in a better solution but still substantial errors in  $\mathbf{s} / r_T$  are introduced. In fact, (A2) indicates that  $p(r_M | r_S)$  is not a normal distribution for this problem. However, the derivation of a more appropriate MLE for this relatively simple solution curve already results in a complex mathematical problem. Most of the problems illustrated above may be reduced by using some prior knowledge on the position of the circle, i.e., constraining the solution into a particular (known) position. This means that any knowledge about the relationship, that can be

obtained before the estimation takes place will improve the solution.

A problem implied in (A6) and (A9) for  $s \approx r_T$  or larger is “aliasing”. In this case, true values for example at  $(x, y) = (0, r_T)$ , i.e., the top of the circle, could be thrown by (Gaussian) noise to the other side of the circle (e.g., around  $(0, -r_T)$ ). The distance of such measurement points to the true point would be large. In MLE, however, the likelihood of such points will be measured by the distance to the closest point on the circle, not the distance to the true point. This effect will give rise to more serious errors in case of a less symmetric solution or in case of a less homogeneous sampling than in the examples above.

## Appendix B: The CMOD4 Model Formulation and Coefficients

The form of the ECMWF CMOD4 model is

$$s_{in}^0 = b_0 \cdot (1 + b_1 \cos f + b_3 \tanh b_2 \cos 2f)^{1.6}$$

where  $b_0 = b_R 10^{a+g \cdot f_1(V+b)}$

and

$$f_1(s) = \begin{cases} -10 & , \quad s \leq 10^{-10} \\ \log s & , \quad 10^{-10} < s \leq 5 \\ \sqrt{s} / 3.2 & , \quad s > 5 \end{cases}$$

and  $\mathbf{a}$ ,  $\mathbf{b}$ ,  $\mathbf{g}$ ,  $b_1$ ,  $b_2$ , and  $b_3$  are expanded as Legendre polynomials to a total of 18 coefficients.  $b_R$  is a residual correction factor to  $b_0$  and is given as a look-up table as a function of incidence angle. CMOD4 coefficients and residual factors for CMOD4 are given in Tables B1 and B2 respectively.

$$\mathbf{a} = c_1 P_0 + c_2 P_1 + c_3 P_2$$

$$\mathbf{g} = c_4 P_0 + c_5 P_1 + c_6 P_2$$

**Table B1.** CMOD4 Coefficients

Parameter	Coefficient	Value	Parameter	Coefficient	Value
$\alpha$	$c_1$	-2.301523	$b_1$	$c_{10}$	0.014430
	$c_2$	-1.632686		$c_{11}$	0.002484
	$c_3$	0.761210		$c_{12}$	0.074450
$\gamma$	$c_4$	1.156619	$b_2$	$c_{13}$	0.004023
	$c_5$	0.595955		$c_{14}$	0.148810
	$c_6$	-0.293819		$c_{15}$	0.089286
$\beta$	$c_7$	-1.015244	$b_3$	$c_{16}$	-0.006667
	$c_8$	0.342175		$c_{17}$	3.000000
	$c_9$	-0.500786		$c_{18}$	-10.00000

**Table B2.** Residual Factors for CMOD4

$q, ^\circ$	$b_R$	$q, ^\circ$	$b_R$	$q, ^\circ$	$b_R$
16	1.075	31	0.927	46	1.054
17	1.075	32	0.923	47	1.053
18	1.075	33	0.930	48	1.052
19	1.072	34	0.937	49	1.047
20	1.069	35	0.944	50	1.038
21	1.066	36	0.955	51	1.028
22	1.056	37	0.967	52	1.016
23	1.030	38	0.978	53	1.002
24	1.004	39	0.988	54	0.989
25	0.979	40	0.998	55	0.965
26	0.967	41	1.009	56	0.941
27	0.958	42	1.021	57	0.929
28	0.949	43	1.033	58	0.929
29	0.941	44	1.042	59	0.929
30	0.934	45	1.050	60	0.929

$$\mathbf{b} = c_7 P_0 + c_8 P_1 + c_9 P_2$$

$$b_1 = c_{10} P_0 + c_{11} V + (c_{12} P_0 + c_{13} V) f_2(x)$$

$$b_2 = c_{14} P_0 + c_{15} (1 + P_1) V$$

$$b_3 = 0.42(1 + c_{16}(c_{17} + x)(c_{18} + V))$$

$$b_R = LUT(\mathbf{q})$$

$$f_2(x) = \tanh\{+2.5(x + 0.35)\} - 0.61(x + 0.35)$$

where the Legendre polynomials are  $P_0 = 1$ ,  $P_1 = x$ , and  $P_2 = (3x^2 - 1) / 2$  with  $x = (q - 40) / 25$ .

Here  $V$  is the wind speed in  $\text{m s}^{-1}$ ,  $f$  the relative wind direction in degrees and  $q$  the incidence angle in degrees.

**Acknowledgements.** It is a pleasure to acknowledge the constructive discussions we have had with members of the ESA analysis team, in particular Alf Long and Evert Attema, and with ECMWF staff and visitors, John Eyre, Peter Woiceshyn and Ross Hoffman. Tony Hollingsworth is appreciated for critically reading the manuscript. The work was carried out at ECMWF under ESA contract 9097/90/NL/BI.

## References

- Britt, H. I. and R. H. Luecke, The estimation of parameters in nonlinear, implicit models, *Technometrics*, 15(2), 233-247, 1973.
- Keller, M. R., W. C. Keller and W. J. Plant, A wave tank study of the dependence of X-band cross sections on wind speed and water temperature. *J. Geophys. Res.*, 97(C4), 5771-5792, 1992.
- Lilley, D. K. and E. L. Petersen, Aircraft measurements of atmospheric kinetic energy spectra, *Tellus*, Ser. A, 35, 379-382, 1983.
- Long, A. E., Towards a C-Band radar sea echo model for the ERS-1 scatterometer, in *Proceedings of a Conference on Spectral Signatures, Les Arcs, France*, Eur. Space Agency Spec. Publ., ESA SP-247, 29-34, 1985.
- Lorenc, A. C., R. J. Graham, I. Dharssi, B. Mcpherson, N. B. Ingleby and R.W. Lannon, Study of preparation for the use of Doppler Wind Lidar information in meteorological assimilation systems, Final report on ESA study contract 9063/90.HGE-I, published by U. K. Meteorol. Office, Bracknell, England, 1991.
- Offiler, D., The calibration of ERS-1 satellite scatterometer winds, *J. Atmos. Oceanic Technol.*, 11, 1002-1017, 1994.
- Stoffelen, A. and D. Anderson, The ECMWF contribution to the characterisation, interpretation, calibration and validation of ERS-1 scatterometer backscatter measurements and winds, and their use in numerical weather prediction models, Final report on ESA study contract 9097/90/NL/BI, published by Eur. Centre for Medium-range Weather Forecasts, Reading, England, 1995.
- Stoffelen, A. C. M. and D. L. T. Anderson, Scatterometer data interpretation: Measurement space and inversion, *J. Atmos. Oceanic Technol.*, 14(6), 1298-1313, 1997a.
- Stoffelen, A. C. M. and D. L. T. Anderson, Ambiguity removal and assimilation of scatterometer data, *Q.J. Roy. Meteorolog. Soc.*, 123, 491-518, 1997b.

**Figure 9.** Assumed wind spectrum at 10-m height (labelled A) and wind spectra as measured by *Lilley and Petersen* [1983] (solid lines), by United Kingdom aircraft MRF(plusses) and the United Kingdom Meteorol. Office cyber model (circles) for the free troposphere (© British Crown Copyright, *Lorenc et al.* [1991]).

## CHAPTER IV

## Toward the True Near-Surface Wind Speed: Error Modeling and Calibration Using Triple Collocation\*

**Abstract.** Wind is a very important geophysical variable to accurately measure. However, a statistical phenomenon important for the validation or calibration of winds is the small dynamic range relative to the typical measurement uncertainty, i.e., the generally small signal-to-noise ratio. In such cases, pseudobiases may occur when standard validation or calibration methods are applied, such as regression or bin-average analyses. Moreover, nonlinear transformation of random error, for instance, between wind components and speed and direction, may give rise to substantial pseudobiases. In fact, validation or calibration can only be done properly when the full error characteristics of the data are known. In practice, the problem is that prior knowledge on the error characteristics is seldom available. In this paper we show that simultaneous error modeling and calibration can be achieved by using triple collocations. This is a fundamental finding that is generally relevant to all geophysical validation. To illustrate the statistical analysis using triple collocations, in situ, ERS scatterometer, and forecast model winds are used. Wind component error analysis is shown to be more convenient than wind speed and direction error analysis. The anemometer winds from the National Oceanic and Atmospheric Administration (NOAA) buoys are shown to have the largest error variance, followed by the scatterometer and the National Centers for Environmental Prediction (NCEP) forecast model winds proved the most accurate. When using the in situ winds as a reference, the scatterometer wind components are biased low by ~4%. The NCEP forecast model winds are found to be biased high by ~6%. After applying a higher-order calibration procedure an improved ERS scatterometer wind retrieval is proposed. The systematic and random error analysis is relevant for the use of near-surface winds to compute fluxes of momentum, humidity, or heat or to drive ocean wave or circulation models.

---

\* Based on:

Stoffelen, Ad, Error modeling and calibration; towards the true surface wind speed , *J. Geophys. Res.*, 103 (C4), 7755-7766, 1998, © American Geophysical Union.

## 1. Introduction

Surface truth is very important for the computation of fluxes of momentum, humidity, or heat, as these are relevant for climate studies on the seasonal scale (El Niño Southern Oscillation) and the interannual scale. Ocean circulation models are driven by the near-surface wind. Surface-based anemometer winds cover the spatial and temporal domains poorly. On the other hand, meteorological analyses and scatterometers provide a wealth of information, but an absolute calibration of these is lacking. In this paper we attempt to solve this problem.

Wind errors are generally large, such that the signal-to-noise ratio (SNR) is not large with respect to 1. In such cases, standard regression or bin-average (BA) analyses could easily lead to pseudobias effects (see also *Tolman* [1998] or *Freilich* [1997]). It is shown in this paper that only by using triple collocations and a profound error analysis such effects may be avoided. We use a 1-month data set of triple collocations of anemometer winds from the National Oceanic Atmospheric Administration (NOAA) buoys, ERS scatterometer winds, and National Centers for Environmental Prediction (NCEP) forecast model winds in a three-way comparison. Thus we readdress the wind calibration of CMOD4.

The current operational ERS scatterometer processing uses the transfer function CMOD4 to derive winds from the backscatter measurements. *Stoffelen* [1998; Appendix] discusses the effect of backscatter calibration on the wind processing. Both backscatter and wind calibration may be performed over the ocean but in an almost independent way [*Stoffelen*, 1998; Appendix]. This is not to say that the backscatter calibration has no effect in the wind domain. For instance, following an onboard hardware problem in mid-1996, the European Space Agency (ESA) switched to a redundant hardware module that slightly affected the radar backscatter calibration. A bias of  $-0.2 \text{ m s}^{-1}$  in the ESA “fast delivery” was the known consequence. In mid-1997 this bias was corrected. The results in this paper apply to ERS scatterometer winds processed from calibrated backscatter measurements using CMOD4 [*Stoffelen and Anderson*, 1997a,b,c; Chapters II, III, and V].

CMOD4 was derived with a maximum likelihood estimation (MLE) procedure using ERS measurements and European Centre for Medium-range Weather Forecasts (ECMWF) analysis winds (operational winds in November 1991) as input [*Stoffelen and Anderson*, 1997 a, b, c; Chapters II, III and V]. Amongst some other proposals this transfer function was verified against winds from the ESA-led Haltenbanken field campaign and winds from the global forecast model of the United Kingdom Meteorological Office (UKMO) [*Offiler*, 1994] and selected as the preferable function. Winds from numerical weather prediction (NWP) models are only a good reference when they in turn are calibrated against in situ winds from conventional platforms. Also, in a calibration exercise it is important that a

representative sample of the day-to-day weather events is present. With hindsight, the Haltenbanken campaign was perhaps too limited in extent to guarantee this.

We study the error characteristics of in situ, scatterometer, and forecast model winds in section 2. We discuss the selection of a measurement domain where the errors can be described simply by a systematic and random part. Pseudobiases after nonlinear transformation of such errors are also discussed. The wind components rather than speed and direction are shown to be the most convenient to provide an accurate description of observation errors. Mean wind components of different measurement systems are generally close to each other. Therefore we first focus on the first-order calibration, which is a multiplication factor or scaling (a linear regression with zero bias term) that would for a particular true value  $t$  provide calibrated measurements  $x$  with expectation value  $\langle x \rangle = t$ . In section 3 it is stated that without prior knowledge it is in the case of intercomparison of two noisy systems not possible to resolve both the observation system error characteristics and the calibration. In section 4 it is shown that with three noisy systems it is possible to calibrate two of the systems with respect to the third and, at the same time, provide an error characterization for all three systems. We have used the in situ winds as a reference and scaled the scatterometer and forecast model winds to have the same average strength. In section 5 a higher-order, or more detailed, calibration is considered. Section 6 provides the error model parameters and calibration factors for the three collocation data sets. Section 7 discusses the implications of this study for scatterometer data processing and wind data interpretation and application.

## 2. Observation Errors and Error Domain

In order to calibrate an observing system we need to have a good notion of what parameter we want to measure, i.e., what variable, but also on what temporal and spatial scales. The variable that we deal with here is the vector wind at a height of 10 m above the ocean surface. We ignore temporal effects and assume that all observing systems involved represent the same temporal scale (10-min averages). We do not consider temporal averaging of the buoy winds, since in our analysis this would not affect the calibrations and would just reduce the random observation error of the buoys. In the spatial domain the in situ data represent a local estimate and therefore include the wind variability on all scales. On the other hand, the scatterometer with a footprint of 50 km does not measure the variability on scales smaller than 50 km. The variability measured by an anemometer and not by the scatterometer is more generally indicated as representativeness error [see, e.g., *Lorenc, 1986*].

For a detailed calibration a good notion of the accuracy of the observation systems is necessary, that is, we need to know what may be called “the cloud of doubt” around the measurement. The nature and amount of system error has to be taken into account. Usually,



errors are classified as systematic (bias) or random (by their standard error (SE)). For most observing systems one could distinguish detection errors and interpretation errors. The detection error includes measurement accuracy and digitizing effects, whereas the interpretation error is made when transforming the measurement(s) to the required variable(s).

For example, for buoys the detection error is determined by anemometer characteristics and buoy motion. The interpretation error for anemometer winds has only to do with the correction of the measurements to a height of 10 m and with the collocation time and space window (see, e.g., *Wilkerson and Earle* [1990] for a more detailed discussion).

For the scatterometer the detection error is fairly small and expressed in vector wind root-mean-square (RMS roughly  $0.5 \text{ m s}^{-1}$  [*Stoffelen and Anderson*, 1997 b, c; Chapters III and V]). On the other hand, the interpretation error is larger and depends mainly on the accuracy of CMOD4 since the inversion error is small. CMOD4 does contain effects for instance of stability, surface slicks, and waves but only as far as they are correlated with the area-averaged 10 m vector wind. However, backscatter effects that are not correlated with the 10 m wind will contribute to the random error of CMOD4.

Although a weather forecast model wind is not a measurement, it may be treated as if it was an observation, since it contains information from all tropospheric observations of mass and wind that were assimilated in the past. Its error will be largely independent from the errors of the current observations. The lowest model level is generally just below the top of the surface layer, which is roughly at 50 m. In a postprocessing step, 10-m winds are derived from model variables. Errors here are caused by errors in the model state (dynamics) and by errors in the extrapolation module for the atmospheric boundary layer.

When trying to characterize measurement errors, it is practical to select a parameter domain where the cloud of doubt is simple to describe. When it is symmetric, then first- and second-order statistical moments may be sufficient to describe the errors. Although we need not limit ourselves to these, for wind the two physical choices are either wind components ( $u, v$ ) or wind speed and direction ( $f, \mathbf{f}$ )<sup>A</sup>. These sets are nonlinearly related, and random errors in the one domain may generate a serious pseudobias in the other domain, as will be shown later.

One way to approach error characterization is to look in detail at the above error sources. The anemometer characteristics for in situ winds will vary but will generally not be the dominant error source. Interpretation errors, including height correction to 10 m and platform motion correction errors, may be more substantial for the conventional winds. Some components of it may be well characterized in the ( $f, \mathbf{f}$ ) domain, while other components are better characterized in the ( $u, v$ ) domain. A major contribution to the observation error for conventional winds when comparing to scatterometer data or forecast model winds will be the spatial representativeness error. This part of the total observation

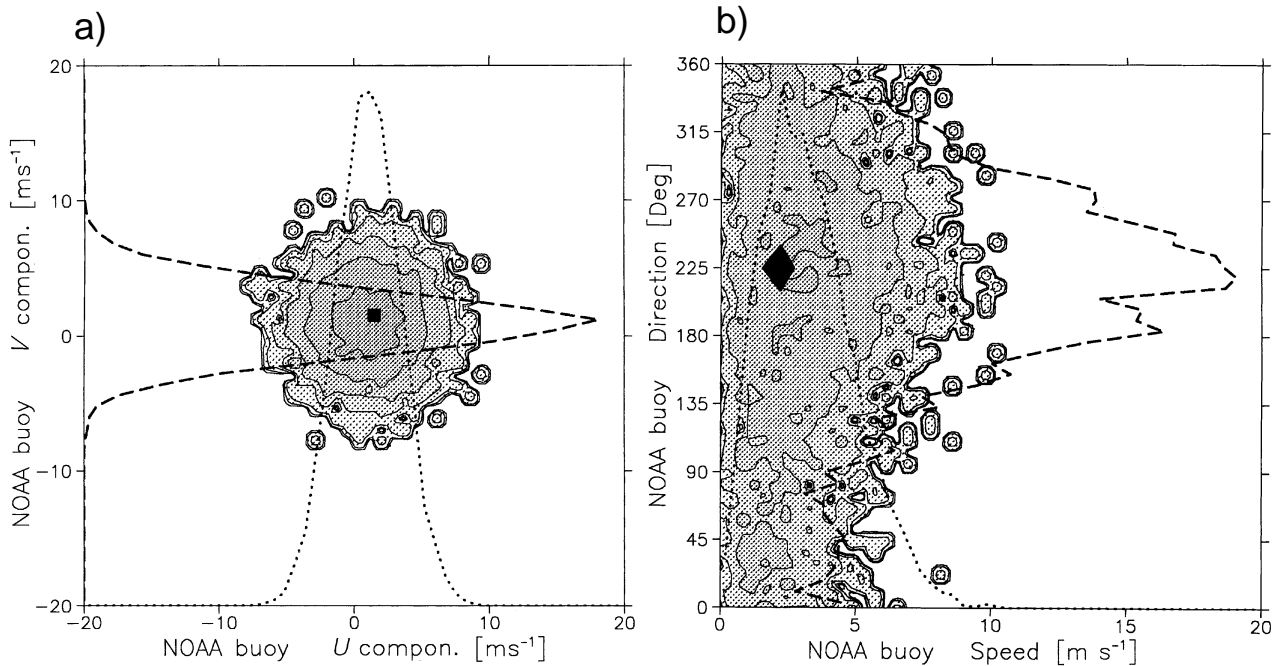


**Figure 1.** The distribution of scatterometer winds for forecast model winds with component values in between  $1.1$  and  $1.9 \text{ m s}^{-1}$  for 6,738 northern hemisphere high-latitude cases in March 1995. The distribution as a function of (a) the components and (b) as a function of speed and direction is shown. The forecast wind subdomain is indicated by a black box. The relative distribution of points (probability density function) along the horizontal and vertical parameter axes are represented by the dotted and dashed lines, respectively. Component errors are simpler to describe than speed and direction errors.

error is well characterized in the wind component domain. Scatterometer winds are empirically derived, and opinions will differ as to which geophysical elements (e.g., waves, stability, rain, or sea surface temperature) determine the interpretation error. The error sources in the forecast model that project onto the surface wind are even more difficult to elaborate on. It may be clear that a characterization of the total observation error from a quantification of all the error sources contributing to it will be undoable. Therefore an empirical approach is needed.

In Figure 1 the distribution of scatterometer winds for a fixed forecast model wind subdomain is shown in both physical spaces. Since the forecast model is not perfect, the subdomain of true winds will be larger than the subdomain of the model winds, and as such, it may be clear that the distribution shown is affected by errors in both the forecast model and the scatterometer. We can see that the combined component errors are well captured by a symmetric distribution, and one may assume that both scatterometer and forecast model error distributions are symmetric (Gaussian) as well. On the other hand, the wind direction random error clearly depends on wind speed, i.e., the lighter the wind the larger the wind

direction error. The wind speed error is not symmetrically distributed for light winds but skew; that is, large positive errors are more likely than large negative errors [Hinton and Wylie, 1985]. This is related to the fact that measured negative wind speeds cannot occur.

Moreover, the cloud of doubt in the  $(f, \mathbf{f})$ B space is quite complicated and cannot be described by second-order statistics, whereas in  $(u, v)$ C space the cloud of doubt seems much simpler to describe. Therefore, as is common practice in meteorological data assimilation, we define an error model in the wind components.

In practice, it is found that the random error on both the  $u$  and  $v$  components is similar, as one may expect (see, e.g., Figure 1a). By verifying the error distributions at higher speeds we found little evidence of a speed dependence of the component errors in the observation systems studied (see, e.g., Figure 2). As such an error model with constant and normal component errors appears appropriate. It implies for speed and direction that the expected RMS wind speed difference  $\langle (f_X - f_Y)^2 \rangle^{1/2}$  of two noisy systems  $X$  and  $Y$  increases monotonically with wind speed, and the wind direction RMS  $\langle (\mathbf{f}_X - \mathbf{f}_Y)^2 \rangle^{1/2}$  increases monotonically to a value of  $104^\circ$  for decreasing wind speed. Hinton and Wylie [1985] used a truncated Gaussian error distribution that did not allow negative speeds, to correct for the low-speed pseudobias. This procedure is rather unsatisfactory since it is not likely that the true error distribution contains discontinuities. By assuming Gaussian error distributions in the wind components the cutoff speed effect is naturally simulated, thereby avoiding an ad hoc correction.

A good way to verify our approach is to simulate the wind speed and direction difference statistics with the error model we have obtained for the wind components. Figure 2 shows such a comparison (compare errors to Table 2). We can see that the average wind speed difference (pseudobias) indeed varies as a function of wind speed and that it can be as large as  $1 \text{ m s}^{-1}$  for realistic errors. The standard deviation of the wind speed difference and the vector RMS difference go to a small value for low wind speed, as is observed for the real data as well. The wind direction standard deviation increases for decreasing wind speed and goes to a value of a hundred odd, as expected (random direction). Thus our error model set up to describe the observed difference statistics in the wind components also qualitatively describes the observed difference statistics in wind speed and direction very well, thereby confirming its adequacy. A quantitative validation of the error model can be made when the wind component errors are known.

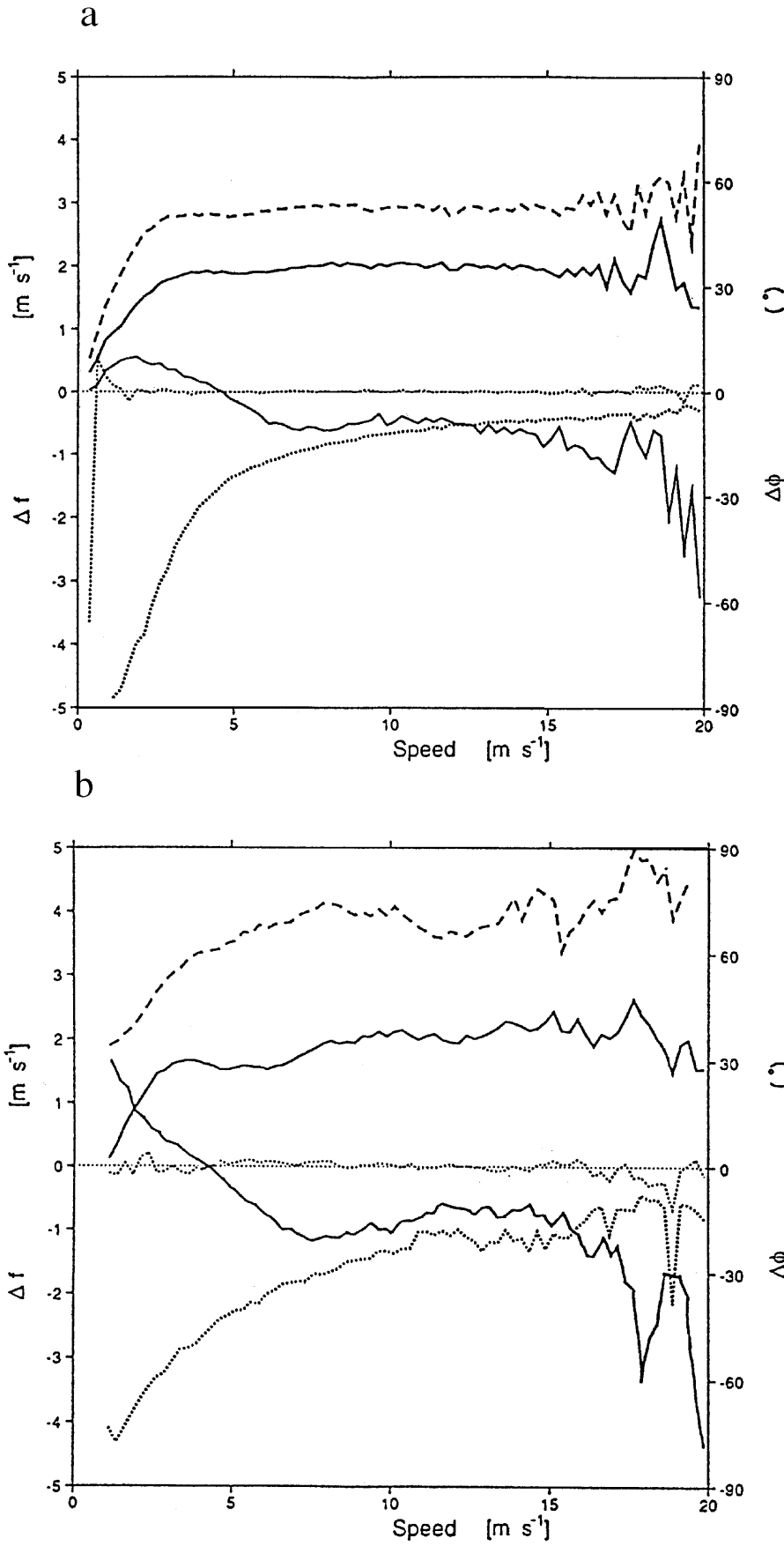


**Figure 2.** (a) Simulated and (b) true wind speed and direction difference statistics of ECMWF forecast model minus scatterometer as a function of average wind speed for all global collocations from February 13-16 1994. Speed bias (thin solid line), standard deviation (thick solid line), direction bias (thin dotted line), standard deviation (thick dotted line), and vector root-mean-square (dashed line) of differences are shown. The simulation (Figure 2a) is done with the scatterometer wind distribution as “truth” and wind component standard errors of 1.0 and 1.8 m s<sup>-1</sup> for the forecast model and scatterometer, respectively (compare Table 2). Figure 2b is for the first node at the inner swath, which is the noisiest of all nodes. Although Figure 2b is noisier, the general speed and direction error characteristics are qualitatively well simulated in Figure 2a by the wind component error model.

### 3. Error Modeling and Calibration With Two Systems

Unfortunately, all observation systems contain error. This means that we cannot assume that one measurement represents the true state and calibrate the other against it, as is illustrated here. Assume we have a distribution of “true” states, indicated by the variable  $t$ , with expected variance  $\langle t^2 \rangle = \mathbf{s}^2$ , and two independent measurement systems  $X$  and  $Y$ , indicated by the variables  $x$  and  $y$  with respective error variances of  $\langle (t - x)^2 \rangle = \mathbf{e}_X^2$  and  $\langle (t - y)^2 \rangle = \mathbf{e}_Y^2$ . If the distribution of true values and the error distributions are normal, one can show that for fixed  $x$  the average of  $y$  does not lie at  $\langle y \rangle = x$  but at  $\langle y \rangle = \mathbf{s}^2 (\mathbf{s}^2 + \mathbf{e}_X^2)^{-1} x$  (see appendix A); that is for  $\mathbf{s} = 5 \text{ m s}^{-1}$  and a typical wind error of  $\mathbf{e}_X = 2 \text{ m s}^{-1}$  we find  $\langle y \rangle = 0.84 x$ , which implies a  $1.6 \text{ m s}^{-1}$  difference at  $10 \text{ m s}^{-1}$ . So, for unbiased Gaussian error distributions, computing the mean of  $y$  for a fixed subrange or bin of  $x$  (bin-average analysis) does, in general, reveal a pseudobias that depends on the error characteristics of system  $X$ .

Scatterometer data are often verified against buoy data, where the buoy data are assumed to be “surface truth” [see, e.g., *Rufenach*, 1995]. However, the representativeness error (see sections 1 and 4) for anemometer winds is substantial, and therefore this assumption does not hold. As such, in this work the observation error of in situ winds will be accounted for in the interpretation in order to be able to draw valid conclusions on the scatterometer and forecast model bias.

A better assumption often used either implicitly (e.g., in “geometric mean” linear regression) or explicitly is  $\mathbf{e}_Y = \mathbf{e}_X = \mathbf{e}$ , leading to the expectation  $\langle x^2 \rangle = \langle y^2 \rangle = \mathbf{s}^2 + \mathbf{e}^2$ . Again, for  $\mathbf{s} = 5 \text{ m s}^{-1}$  but now for the common wind errors of  $\mathbf{e}_X = 3 \text{ m s}^{-1}$  and  $\mathbf{e}_Y = 1 \text{ m s}^{-1}$ , we find a ratio of total variances of  $\langle x^2 \rangle \langle y^2 \rangle^{-1} = 1.32$ , which would lead after linear regression to the conclusion that system  $Y$  is biased low by 16% if system  $X$  is assumed to be bias free. Thus the assumption may imply a  $1.6 \text{ m s}^{-1}$  pseudobias at  $10 \text{ m s}^{-1}$  for, in reality, unbiased Gaussian error distributions. The examples illustrate that when a noisy system is used as a reference for calibration in a dual collocation, we will need to know the error characteristics of that system. Further proof of this is given in Appendix A.

Another possibility of generating pseudobias is by nonlinear transformation. An unbiased symmetric error distribution may then be transformed into a skew and biased error distribution. For example, Gaussian errors on the wind components  $u$  and  $v$  for system  $X$  or  $Y$  will not correspond to Gaussian error distributions on wind speed  $f$  and direction  $\mathbf{f}$ . Using the same notation and assumptions common to the previous two examples, we show in Appendix B that  $\langle f_X \rangle = \sqrt{p/2} \mathbf{s}_X$ , where  $\mathbf{s}_X^2 = \mathbf{s}^2 + \mathbf{e}_X^2$ , with  $\mathbf{s}$  the standard deviation (SD) of the true wind component distributions,  $\mathbf{e}_X$  the SE of system  $X$ , and where the errors are assumed identical for the  $u$  and  $v$  components. A similar expression can be

derived for system YQ. The expected mean wind speed difference is approximated as  $\langle f_X - f_Y \rangle = \sqrt{\pi/2}(\mathbf{s}_X - \mathbf{s}_Y) \approx \sqrt{\pi/2}(\mathbf{e}_X^2 - \mathbf{e}_Y^2) \mathbf{s}^{-1} \mathbf{R}$ . For example, the typical values of  $(\mathbf{s}, \mathbf{e}_X, \mathbf{e}_Y) = (5, 3, 1) \text{ S m s}^{-1}$  will lead to an average wind speed bias of  $0.4 \text{ m s}^{-1}$ . This is a pseudobias since the error in the wind components is unbiased. One can show that the pseudobias generally oscillates from positive to negative as a function of wind speed and is largest in a relative sense for low speeds (as in Figure 2).

It may be clear from the above that it is desirable that the error characteristics of measurement systems are well described, thereby avoiding pseudobias effects only caused by inaccurate assumptions on the errors. Moreover, in order to provide a calibration and error model of observing systems it is desirable that a domain is chosen where the errors are simple to describe, preferably avoiding statistical moments of order higher than 2 (see section 2). Also, in geophysical applications the use of data with complex error characteristics may lead to biased results when the error characteristics are not properly accounted for.

*Freilich* [1997] and *Tolman* [1998] recognize the nonlinear effects described above and the underdetermination of the dual collocation problem, but subsequently use assumptions on the statistical properties of the true or error distributions in order to close the problem. Below it is shown that such assumptions are not needed in a three-way comparison.

#### 4. Error Modeling and Calibration With Three Systems

In the previous section it was indicated that calibration of one noisy system against another is not possible without fundamental assumptions on the noise characteristics of at least one system. It was shown that these assumptions may lead to substantial pseudobias problems. This is further elaborated in appendix A. Here a method is introduced to perform calibration and error modeling using triple collocations. The method is quite general and is introduced as such. Later on, the method is applied on in situ, scatterometer, and forecast model wind components. Now suppose three measurement systems X, Y and Z measuring a true variable  $t$ . Let us define

$$\begin{aligned} x &= t + \mathbf{d}_X, & \mathbf{e}_X^2 &= \langle \mathbf{d}_X^2 \rangle \\ y &= s_Y(t + \mathbf{d}_Y), & \mathbf{e}_Y^2 &= \langle \mathbf{d}_Y^2 \rangle \\ z &= s_Z(t + \mathbf{d}_Z), & \mathbf{e}_Z^2 &= \langle \mathbf{d}_Z^2 \rangle \end{aligned} \tag{1}$$

with as before,  $\mathbf{s}^2 = \langle t^2 \rangle$ , and now  $\mathbf{d}_X, \mathbf{d}_Y, \mathbf{d}_Z$  are the random observation errors in the measurements  $x, y$ , and  $z$  respectively. Here  $s_Y$  and  $s_Z$  are the calibration (scaling) constants. We have assumed no bias such that  $\langle \mathbf{d}_X \rangle = \langle \mathbf{d}_Y \rangle = \langle \mathbf{d}_Z \rangle = 0$ . For marine winds this is valid to good approximation (see section 5), but otherwise, bias

may be easily removed.

It is unlikely that the three systems represent the same spatial scales. Therefore we will arbitrarily assume that observation systems  $XY$  and  $YZ$  can resolve smaller scales than system  $ZAA$  by taking  $\langle \mathbf{d}_X \mathbf{d}_Y \rangle = r^2 \mathbf{B}\mathbf{B}$ . Here  $r^2$  is the variance common to these smaller scales and taken as part of the observation errors  $\mathbf{d}_X$  and  $\mathbf{d}_Y$  and  $t$  only  $CC$  represents the spatial scales resolved by  $zDD$ . By definition  $r^2$  is the correlated part of the representativeness errors of  $X$  and  $Y$ . The choice for  $t$  to only resolve the coarsest scale measurement allows the approximation  $\langle \mathbf{d}_X t \rangle = \langle \mathbf{d}_Y t \rangle = \langle \mathbf{d}_Z t \rangle = 0$ , that is, the observation errors are assumed uncorrelated with  $tEE$ . Furthermore, since  $zFF$  does not include the smaller scales, the observation error of system  $Z$  is independent of the errors of  $X$  and  $Y$ , that is,  $\langle \mathbf{d}_X \mathbf{d}_Z \rangle = \langle \mathbf{d}_Z \mathbf{d}_Y \rangle = 0$ . The assumption that the wind component errors of the different observation systems are uncorrelated, except for the representativeness error, is essential to determine the calibration. Now the calibration coefficients can be derived from the different covariances

$$\begin{aligned} s_Y &= \langle yz \rangle \langle zx \rangle^{-1} \\ s_Z &= \langle yz \rangle (\langle xy \rangle - r^2 s_Y)^{-1} \end{aligned} \quad (2)$$

These coefficients can be used to create

$$\begin{aligned} GG^{y*} &= s_Y^{-1} y \\ z^* &= s_Z^{-1} z \end{aligned} \quad (3)$$

HHwhich are the calibrated data. Subsequently, all random error parameters of the observation systems  $X$ ,  $Y$ , and  $Z$  can be resolved pairwise from the different covariances, as illustrated in Appendix A by (A5)II. Here we used observation system  $XJJ$  as a reference system. This preference can be easily altered by scaling all parameters to one of the other systems.

So under the premise that we find an estimate for  $r^2KK$  we have found a way to perform a first-order calibration. In work by *Stoffelen* [1996] the spatial representativeness error of the scatterometer with respect to the ECMWF model is estimated to be  $r^2 = 0.75 \text{ m}^2 \text{ s}^{-2}LL$ . We use this as a baseline assumption here as well. The sensitivity of the results to this choice is discussed later on and shown to be small (section 6).

## 5. Higher-Order Calibration

After the first-order calibration the three systems should be largely unbiased. However, in this section we consider a more detailed calibration of the systems by pairwise comparison. For the triple-located data the procedure is run comparing  $X$  and  $Y$ ,  $Y$  and  $Z$ , and  $Z$  and  $X$  so that consistency can be checked between the results.

Now first consider  $X$  and  $Y$ . After obtaining  $\mathbf{e}_X$  and  $\mathbf{e}_Y$  we decide which system is the least noisy; for example, suppose  $\mathbf{e}_X > \mathbf{e}_Y$ . Then system  $Y$  may be convoluted with a Gaussian distribution with width  $\sqrt{\mathbf{e}_X^2 - \mathbf{e}_Y^2}$  to obtain a distribution (and a system  $Y'$ ) that has the same error properties as that of system  $X$ , i.e.,  $\mathbf{e}_{Y'} = \mathbf{e}_X$ . In fact, since they represent the same true distribution, the resulting distributions of  $X$  and  $Y'$  should be identical in case of a large sample size. When dealing with winds, the errors of  $X$  and  $Y$  may be matched for both components, such that either components or speed and direction distributions should be identical. By comparing the cumulative distributions of these two systems,  $f(x)$  and  $g(y')$ , that are monotonically increasing functions, we can easily compute a mapping  $y^m = \mathbf{m}(y')$  that results in identical distributions  $f(x)$  and  $g(y^m)$ . The higher-order correction would then be  $\mathbf{m}(y) - y$ , which may be plotted versus  $y$ .

The higher-order calibration is only reliable when the errors of system  $X$  and  $Y$  are well characterized by a normal distribution. However, if substantial errors of order higher than 2 would be present in either system  $X$  or  $Y$ , then the detailed bias computation method set out above may provide large pseudobias. When more than two systems are involved, such as in our triple collocation data set, a consistency check between the different comparisons may reveal such problems. In the extreme parts of the domain, where the error distributions of either system are insufficiently sampled, further pseudobias effects may occur. To gain confidence, the computed corrections may be verified by Monte Carlo simulation to test such sampling problems.

## 6. Calibration and Error Model Results

In this section we describe the implementation of the method given earlier and show the results of the calibration of scatterometer and forecast winds relative to the anemometer winds. A 1-month data set kindly provided by NCEP from March 1995 with off-line anemometer winds from the NOAA buoys corrected to 10-m height [Wilkerson and Earle, 1990] was used collocated with the ESA-processed ERS-1 scatterometer and NCEP forecast model winds. The NCEP forecast wind is valid at the time and location of the buoy measurement. All scatterometer data within 200 km and 3 hours of a buoy were selected and as a result 40,091 triple collocations were available resulting from 1465 independent buoy measurements.

The average wind components of the in situ, scatterometer, and forecast winds are very close (within a few tenths of a  $\text{m s}^{-1}$ ). As such, the assumption just below (1) that the systems have no absolute bias, i.e.,  $\langle \mathbf{d}_i \rangle = 0$  for  $i = (X, Y, Z)$  proves valid.

A quality control procedure is applied to exclude gross errors. An iterative scheme is followed, where in each trial a calibrated (equation (3)) collocation triplet is rejected when



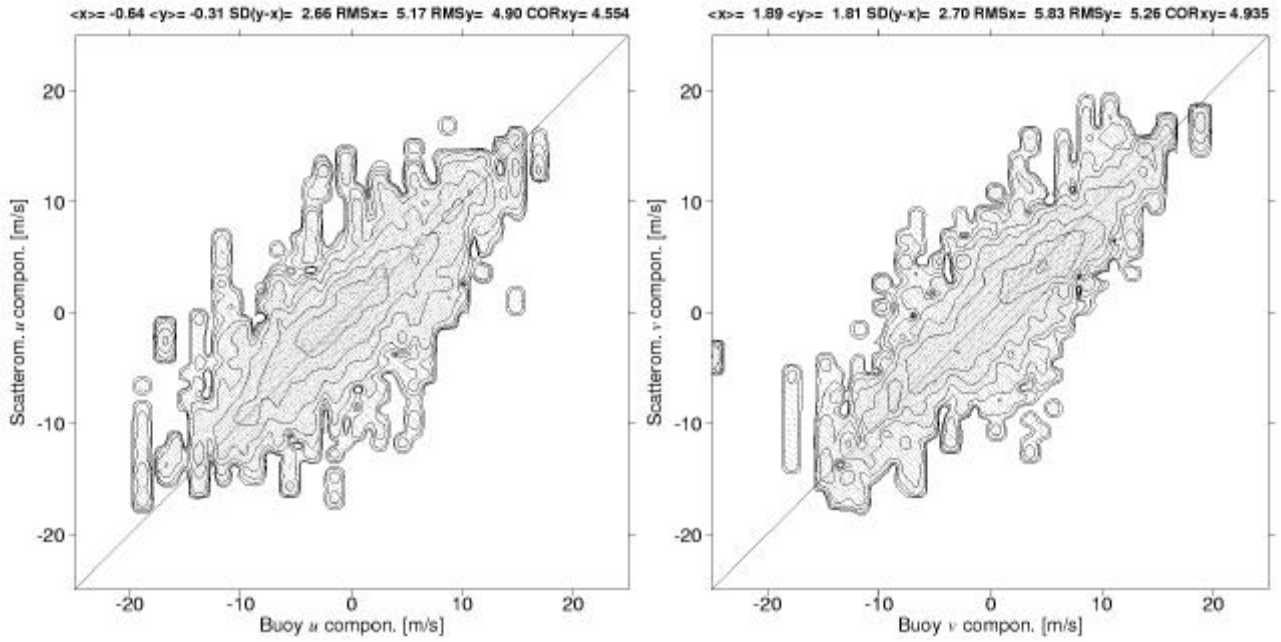


**Figure 3.** Joint distributions for the along-track ( $u$ ) and across-track ( $v$ ) ERS-1 wind components, respectively, for the (a, b) NOAA buoy anemometer and ERS-1 scatterometer, (c, d) scatterometer and NCEP forecast model, and (e, f) forecast model and anemometer winds. Statistics of the mean, RMS, SD, and correlation of the data are shown at the top. These plots show the full characteristics of the triple collocation database in the wind domain.

for any pair the following condition holds, illustrated here for pair  $(x, y^*)$

$$|x - y^*| > 3 \sqrt{\mathbf{e}_x^2 + \mathbf{e}_y^2} \quad (4)$$

where the calibrations and the errors are taken from the previous trial. In the first trial we start with calibration factors equal to 1 and errors equal to  $2 \text{ m s}^{-1}$ . The calibration factors are within a percent of their final value after one iteration, and also, the rejection rates remain constant (at  $\sim 1\%$ ) after 1 or 2 trials; 6 trials were used. A wind direction bias correction is repeated after every trial, and the resulting corrections are  $4^\circ$ - $5^\circ$  for the scatterometer and  $1^\circ$ - $2^\circ$  for the forecast model, where the incremental correction in the sixth trial was very small ( $< 0.01^\circ$ ). Wind direction corrections of this size do not substantially impact the wind component statistics, but the scatterometer bias may need further attention. *Stoffelen* [1996] shows that the bias reverses in the southern hemisphere and is difficult to explain from existing theories on air-sea interaction.

### 6.1. First-Order Calibration

The calibration factors resulting from the above procedure are shown in Table 1. The NCEP forecast model appears biased high by roughly 6%. The representativeness error

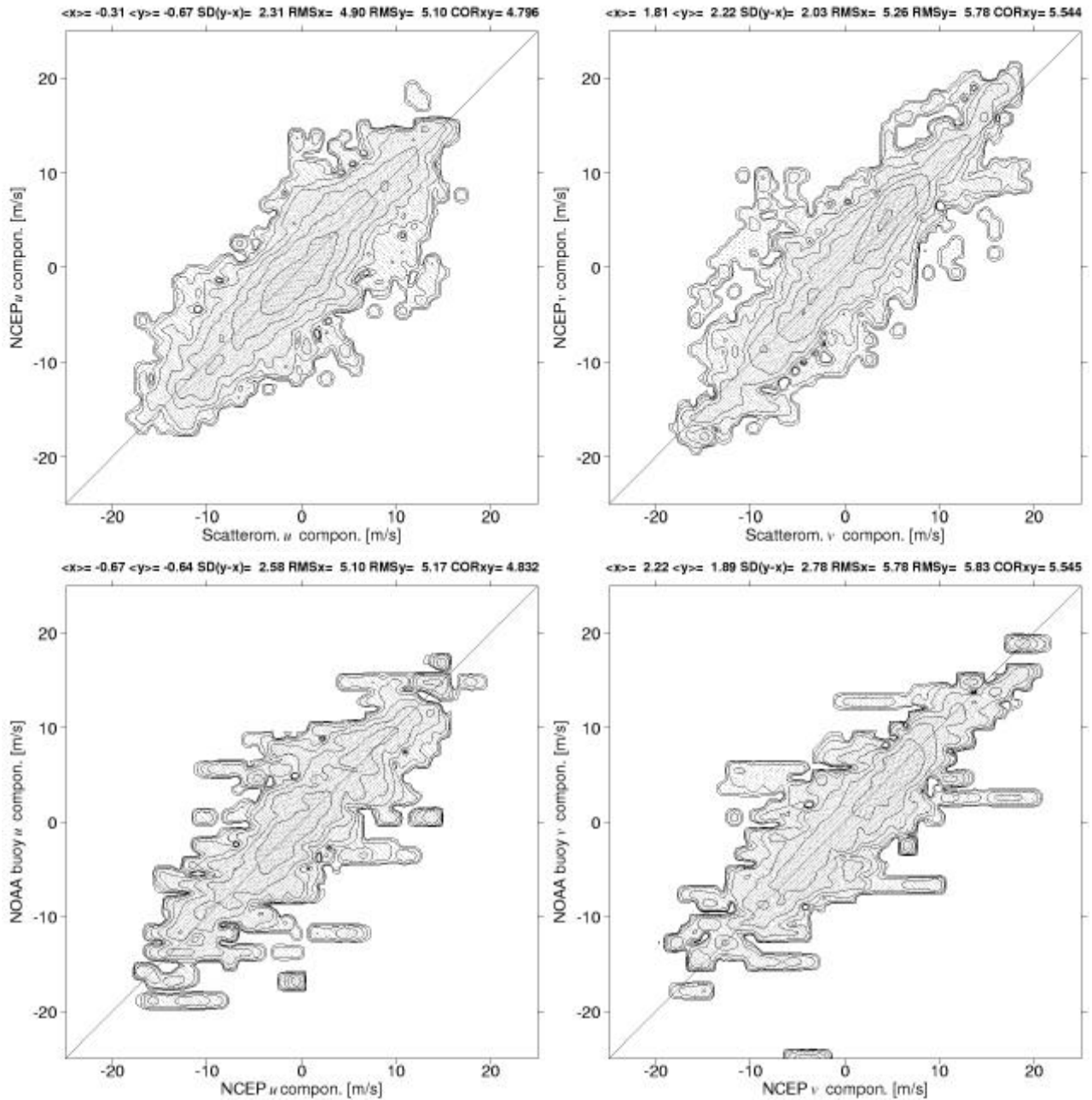


**Figure 3.** (continued)

estimate modestly influences the calibration coefficient of the forecast model as we would expect from (2). In contrast, the scatterometer calibration enforces the winds. Remarkably, the scatterometer along-track component is biased less than the across-track component. This difference, however, may be explained by the relatively small number of independent collocations used.

Figure 3 shows the joint distributions of the wind components of in situ and scatterometer, scatterometer and NCEP, and NCEP and in situ data. It is evident that the scatter in the scatterometer and NCEP plot is smallest. This means that the in situ winds have the

**Table 1.** Calibration Scaling Factors Against Buoy Winds for Wind Components From the Scatterometer and Forecast Model for Different Representativeness Errors.

	Component Scaling		$r^2, \text{m}^2 \text{s}^{-2}$
	$u$	$v$	
Scatterometer	0.97	0.95	all
NCEP model	1.06	1.06	0.50
NCEP model	1.06	1.07	0.75
NCEP model	1.07	1.08	1.00

Here  $u$  is the along-track, and  $v$  is the across-track wind component;  $r^2$  is the representativeness error (due to scatterometer and model spatial resolution difference).

largest error. The in situ and scatterometer plot shows the largest scatter, which indicates

that the NCEP winds are the most accurate. Table 2 shows the results of our random error estimates from (A5) in Appendix A, which confirm our subjective analysis. The error estimates for the  $u$  and  $v$  components are quite similar for NCEP and conventional winds, but for the scatterometer the along-track component seems slightly worse than the across-track component. Given the fact that the wind direction was predominantly across-track in this data set, it may indicate some anisotropy in the scatterometer error distribution.

From a climatological wind spectrum one may estimate the representativeness error variance of the conventional winds with respect to NCEP winds to be  $2.1 \text{ m}^2 \text{ s}^{-2}$  [Stoffelen, 1996]. As such, the (local) error of the in situ winds may be estimated as  $1.41 \text{ m s}^{-1}$  for the  $u$  and  $1.21 \text{ m s}^{-1}$  for the  $v$  component. However, for many applications the local wind is not as relevant as an area-averaged quantity such as provided by the scatterometer.

Since the scatterometer winds are not exactly collocated in space and time with the in

**Table 2.** Estimates of the Wind Component Standard Deviation of the True Distribution and the Standard Errors of the Buoy, Scatterometer, and Forecast Error Distributions.

	Component, $\text{m s}^{-1}$	
	$u$	$v$
True variance	4.68	5.24
In situ error	2.02	1.89
Scatterometer error	1.89	1.62
NCEP error	1.11	1.15

Here  $u$  is the along-track and  $v$  the across-track wind component. The values are computed at the spatial representativeness of the forecast winds with  $r^2 = 0.75 \text{ m s}^{-1}$  (see text).

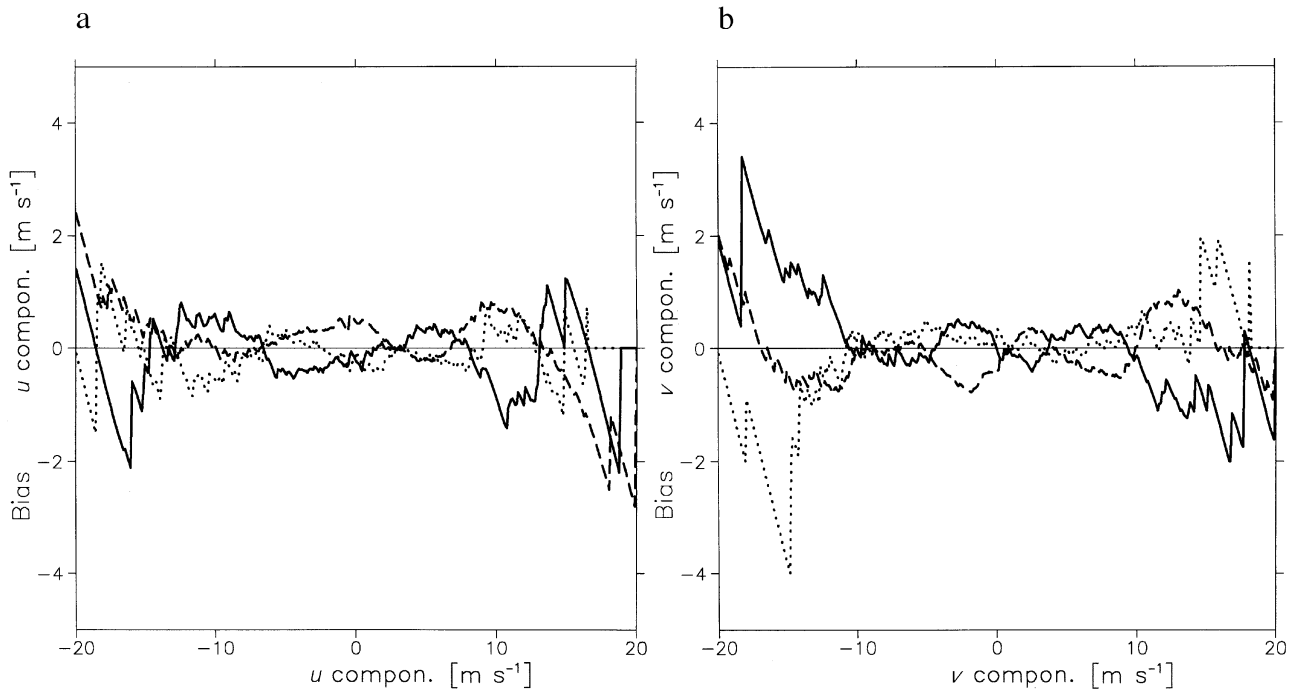


**Figure 4.** Higher-order calibration by cumulative distribution mapping (see text) for (a) the along-track and (b) the across-track ERS-1 wind components. The biases of scatterometer with respect to NOAA buoy anemometer (solid line), NCEP forecast model with respect to scatterometer (dotted line), and anemometer with respect to forecast model (dashed line) winds are shown. Although large biases are present, there is no consistent pattern apparent in the data.

situ and NCEP winds, a collocation error may be subtracted from the former. Wind measurements separated by in between 2 and 3 hours will have an additional error component of  $\sim 1.5 \text{ m}^2 \text{ s}^{-2}$  [Stoffelen and Anderson, 1997c; Chapter V]. When we assume that the collocations are randomly distributed in time (over 6 hours), the average error contribution would be  $\sim 0.75 \text{ m}^2 \text{ s}^{-2}$ . Such a collocation error would reduce the scatterometer error estimates by  $\sim 0.2 \text{ m s}^{-1}$ .

Stoffelen [1996] studied the spatial representation of the ECMWF forecast model and the ERS-1 scatterometer winds on scales between 50 and 250 km. On these scales the scatterometer contained substantially (20-40%) more variance. It was very likely that part of this additional variance verifies with the true wind and that part of it contributes to the scatterometer wind error. From the study it follows that the sum of the scatterometer error on scales between 50 and 250 km and the representativeness error would be  $1.4 \text{ m s}^{-1}$ , which verifies reasonably well with the error estimates obtained in this work. The ECMWF and NCEP model errors would be comparable, since the ECMWF wind error on scales between 50 and 250 km was estimated to be  $1.1 \text{ m s}^{-1}$  in Stoffelen [1996].

## 6.2. Higher-Order Calibration

The higher-order calibration procedure of section 5 requires a convolution of the most accurate system with a Gaussian error distribution with a width determined by the difference in error variance of the two systems. Figure 4 shows the higher-order calibration by the cumulative distribution mapping method. The wind component biases appear to be rather random in nature. The smallest biases are generally present at small wind component values, and the highest are present at high component speeds. This is due to the fact that the largest number of data is present at low component speeds, and the lowest number is present at high speeds. In other words, the higher the speeds the less accurate the results are. In an attempt to fit the bias with a smooth function this would have to be taken into account, and changes at the tail of the distribution should be kept small.

Inconsistency of the wind component biases between the calibration pairs is most noticeable at the tail of the distributions; that is, for example, the bias of the in situ winds with respect to the scatterometer is not equal to the sum of the biases of the conventional winds with respect to NCEP and the bias of NCEP with respect to the scatterometer. Moreover, the plot suggests that the scatterometer has a generally negative bias with respect to the anemometer winds and NCEP for the along-track component. However, this effect is not confirmed by the differences in mean value of the scatterometer along-track component. Closer inspection reveals more (but smaller) inconsistencies. These indicate insufficient sample size or higher-order statistical moments in the error distributions than those accounted for.

The cloud of doubt is assumed to be Gaussian with a fixed standard error. However, in reality, also higher-order moments may be relevant here. Furthermore, the standard error may depend on the geophysical condition, for instance on stability, and we would need a representative sample of all these conditions to perform the higher-order calibration accurately. As such, the number of samples we need to determine the calibration and error model may be quite large. Since there is no mechanism to remove the pseudobiases due to sampling and higher-order moments, we believe that the methodology has to be used with restraint.

Physically, one may expect systematic errors to scale with  $f$  and  $\mathbf{f}$ , rather than with  $u$  and  $v$ . If the errors in  $u$  and  $v$  of systems  $X$  and  $Y$  are identical, then their  $f$  and  $\mathbf{f}$  distributions should ideally also be identical. The wind direction cumulative mapping also does not result in substantial and consistent systematic effects, but for wind speed it does, as shown in Figure 5. The scatterometer is biased high for high and very low wind speed and biased low for moderate speeds with respect to the buoys. The NCEP model shows similar differences with respect to the buoys but roughly half in size. However, at the very low

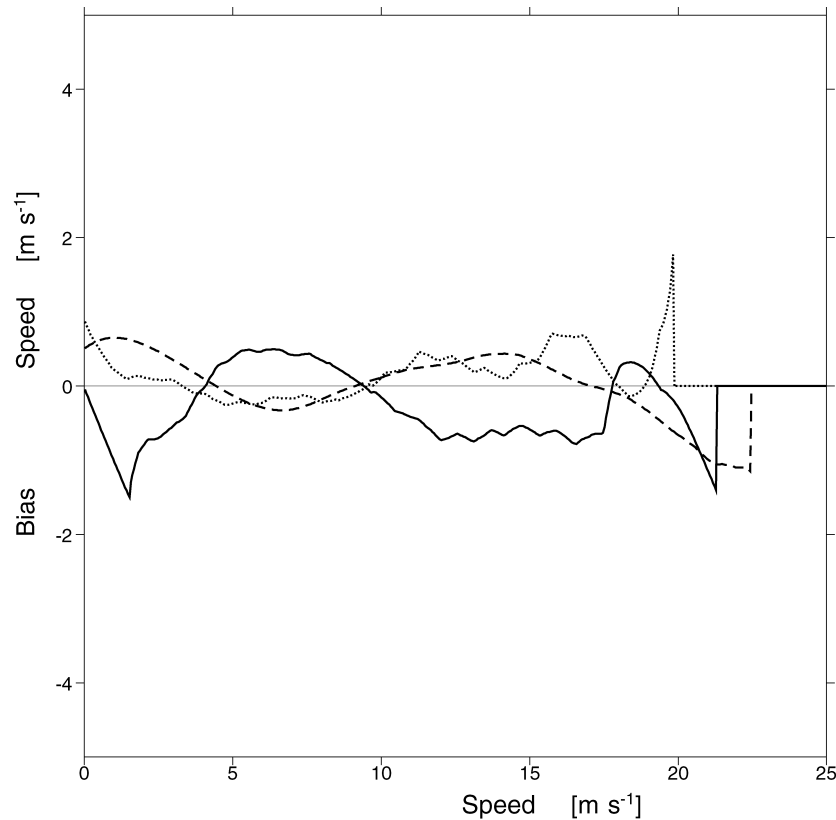


**Figure 5.** As Figure 4, but for wind speed. A consistent speed correction for the NCEP model and scatterometer is present at wind speeds up to  $17 \text{ m s}^{-1}$ . For these speeds the solid line shows the suggested higher-order correction to CMOD4 (in addition to a 4% linear correction).

wind speeds, NCEP and scatterometer are more consistent. The comparison of NCEP and scatterometer winds generally confirms these results, except at the poorly sampled high speeds. After applying to the scatterometer and NCEP winds the first-order corrections and the second-order corrections up to  $17 \text{ m s}^{-1}$ , a repeated application of the calibration method does result in no further substantial corrections and in errors that are very similar to the ones of Table 2. As such, up to  $17 \text{ m s}^{-1}$  the higher-order correction of the scatterometer against the buoys appears sensible, and we suggest it, together with a 4% linear correction, as a modification to CMOD4.

It is worth noting at this point that by taking the buoys as a reference for the scatterometer calibration, we assume that the buoy generally provides an unbiased estimate of the scatterometer footprint area-averaged wind vector. Especially for the very low wind speeds, one may want to further investigate this.

## 7. Conclusions

### 7.1. Résumé

In this paper, calibration and error modeling are discussed, and a methodology is provided to obtain the absolute calibration and accuracy of observing systems. In particular, the focus is put on ocean surface wind speed (or stress) biases that are detrimental for the computation of fluxes of momentum, humidity, and energy through the air-sea interface. An improved ERS scatterometer wind processing is proposed.

It was demonstrated that the selection of a simple measurement domain where second-order statistics are sufficient to describe the uncertainty of the measurements is preferred. More specifically, we have shown that wind error modeling using component error distributions that are Gaussian and constant represents a simple method to describe the more complex errors in speed and direction. We have shown that substantial pseudowind speed biases can occur through the nonlinear transformation of unbiased wind component errors to the wind speed and direction domain. In a direct wind speed calibration, where usually unjustly symmetric error distributions are assumed, the pseudobiases would be taken out, leading to biased wind components [see also *Hinton and Wylie, 1985*]. Wind component error modeling as proposed here elegantly solves this problem.

In order to calibrate one observing system with respect to the other, one may use, either explicitly or implicitly, a simplifying assumption on the errors of the two systems. For instance, it is common practice to assume that the errors of two systems that are compared are equal or to assume that one system is much more accurate (i.e., is “truth”) than the other. Given our results in Table 2 and Figure 3, it is obvious that both of these choices would have been crude for any of the observation systems dealt with in this paper. We have shown that such assumptions may lead to substantial pseudobias effects. Furthermore, in Appendix A it is shown that it is impossible to calibrate one noisy system against another without such assumptions or other prior knowledge on the error characteristics of one or both systems.

For a proper calibration of an observing system a reference system is necessary and at least one other observation system. Using triple collocations, a method to calibrate noisy systems has been developed. Subsequently, in a pairwise comparison of the calibrated observation systems the covariances were used to estimate the true variance resolved by both systems and the error variance of the observations. To complement the linear calibration, a more refined bias estimation procedure was adopted.

We used the NOAA buoy anemometer winds as a reference, although they turned out to be the least accurate amongst the scatterometer and NCEP forecast model winds. The spatial representativeness error is the main reason for the low accuracy of the buoys in our

triple comparison. One would expect this error to be of a random nature and not lead to biases in the results. We found that the CMOD4-derived scatterometer wind components are biased low by 4%. The NCEP forecast model appears to be very accurate but biased high by 6% for the period we examined (March 1995). In another study, using triple collocations of the ECMWF forecast model, ERS scatterometer winds, and real-time available anemometer winds, similar results were obtained [Stoffelen, 1996]. The higher-order scatterometer calibration with respect to the buoys resulted in a correction additional to the 4% mentioned above. The total correction is recommended for operational implementation in the ESA fast delivery processing chain.

## 7.2. Application

Our statistical analysis on surface winds has direct implications in the area of data assimilation in numerical weather prediction (NWP) models and in ocean circulation and wave model forcing. However, the methodology may be applied for the interpretation of any geophysical variable with a high variability on the smaller scales or high signal-to-noise ratio. It provides a way to compare data with different amounts of noise or different spatial and/or temporal resolution.

It is essential that NWP models assimilate unbiased data. It has been observed by ECMWF that the scatterometer bias with respect to their forecast model (~10 %) had the tendency to slow down the forecast winds in the analysis and subsequently fill in low-pressure systems. This effect can be circumvented by a model wind correction to match the mean observed wind [Roquet and Gaffard, 1995]. The 6% bias we found between the buoys and the NCEP model may result from physical parameterizations that also control atmospheric boundary layer humidity, depth, and temperature and that require careful tuning. Such biases, when detected, are therefore not easily corrected, and a short-term solution such as adopted by Roquet and Gaffard will be beneficial. However, in the long term the forecast model bias correction should be replaced by forecast model improvements.

Roquet and Gaffard [1995] computed a bias correction in the wind speed domain, rather than in the wind components. The wind components, however, are used for data assimilation and should be unbiased. Figure 2 clearly shows that because of the nonlinear transformation, unbiased component errors will lead to biased speeds and vice versa. It is therefore essential to compute biases in the domain of the analysis variables, i.e., the wind components [see also Le Meur *et al.*, 1997]. For other analysis variables the same strategy may be applied; that is, observations and forecast data are compared in that domain where the errors are best described, and bias corrections are computed after the transformation of the random errors to the analysis variable domain. For noisy data a careful statistical error analysis as described in this work will be essential to arrive at an optimal bias correction and



assimilation.

Wave models directly rely on NWP model winds. Here it was shown that NWP forecast model winds are very accurate in describing the synoptic scale flow but may be biased. However, since we quantified the bias, it is easily corrected for when the winds are used in wave models. We note that it is more problematic to take account of the error in the forcing since this error is nonlinearly related to the random wind error. Also, it is relevant to be aware of the fact that a NWP model provides an area-averaged vector wind and that the additional forcing due to the wind on the unresolved scales needs be parameterized.

Tropical wind analysis is very important for ocean circulation models and as such for the study of the Earth's climate. In ocean circulation experiments, similar arguments apply as in wave forecasting concerning the forcing problem. *Stoffelen* [1996] and *Bryan et al.* [1995] noted a large directional inconsistency between scatterometer and ECMWF wind direction at the equator. The tropical array of (TAO) buoys may provide a relevant data set to enhance our knowledge on the utility of scatterometer and forecast winds in this area using the methodology described here.

## Appendix A: Necessity of Error Modeling Before Calibration or Validation

In this appendix the problem of calibration and validation of one noisy system with respect to another one will be discussed. Usually, scatter plots are used to compare the data followed by a regression analysis to compute a calibration coefficient or to validate the system(s). First, the interpretation of scatter plots and associated regression and bin average (BA) analyses are discussed, and it is illustrated that calibration or validation, without knowing the error characteristics of one or both systems, can easily lead to pseudobiases. In the second part it is shown that calibration or validation of one noisy system against another, without knowing the error characteristics of the observing systems, is generally not possible.

### A1. Scatter Plots and Regression

Usually, a scatter plot is used to determine the error characteristics of a measurement system (see, for example, Figure 4). In this section we quantify the properties of the scatter plot. If enough collocation data are available, then the density of points in the scatter plot is proportional to the joint probability density of  $x$  and  $y$ , given by

$$p(x, y) = \int p(x/t) p(y/t) p(t) dt \quad (A1)$$

The integration is over the distribution of true states  $p(t)$  and over the distributions of error. Here  $p(x|t)$  is the conditional probability density of  $x$  given  $t$ , which includes all measurement and error characteristics of the measurements  $x$ . (It is closely

related to what was introduced as the cloud of doubt around observation  $x$ , DDD which formally reads  $p(t|x)$  EEEFFF and where  $p(t|x)GGGHHH = p(x|t)IIJJJ p(t)$ . ) We can see that the joint distribution of  $x$  KKK and  $y$  LLL is not only determined by the error characteristics of both systems but also by the distribution of true states MMM. In the simple case of unbiased Gaussian errors with standard error (SE) equal to  $e_x$  or  $e_y$  and a Gaussian true distribution with zero mean and RMS  $s$  NNN, the joint probability of  $x$  OOO and  $y$  PPP can be written as

$$p(x, y) \propto \exp\left[-\frac{(s^2 + e_y^2)x^2 + (s^2 + e_x^2)y^2 - s^2xy}{2(s^2 e_x^2 + s^2 e_y^2 + e_x^2 e_y^2)}\right] \tag{A2}$$

For given  $x$  QQQ the mean  $y$  value of this distribution does not lie at  $y = x$  RRR but at  $y = s^2 (s^2 + e_x^2)^{-1} x$ . SSSSo, even for unbiased Gaussian error distributions, computing the mean of  $y$  TTT for a fixed subrange or bin of  $x$  UUU (bin average) does, in general, reveal a pseudobias that depends on the error characteristics of  $x$  VVV. This needs to be accounted for in the interpretation, and therefore, when correcting for bin-average biases with respect to a reference system, the error characteristics of that system, in this case  $e_x$ , need to be known well.

For calibration or validation, often linear regression is used as a tool. For a well-calibrated system and in the case of  $e_x = e_y$  a geometric mean linear regression on the joint distribution would indeed result in the line  $y = x$ , but in the more general case of  $e_x \neq e_y$  it would result in  $y = (s^2 + e_y^2) (s^2 + e_x^2)^{-1} x$ , where it would again result in a pseudo-bias. When the error characteristics of  $x$  and  $y$  are known, a weighted fit may result in a proper calibration. However, most often the errors are unknown.

**A2. Necessity of Error Modeling Before Calibration**

Then the question emerges; Is it possible to perform a calibration or validation of one noisy system against the other without prior information on the error characteristics of one or both of the systems? Below we illustrate that this is generally not possible.

Suppose we have a set of true states, indicated by variable  $t$ , measured by systems  $X$  and  $Y$  resulting in measurements  $x$  and  $y$ . We define  $s^2 = \langle t^2 \rangle$ , where  $\langle \rangle$  denotes the expected mean, WWW and introduce the error model

$$\begin{aligned} x &= t + d_x & e_x^2 &= \langle d_x^2 \rangle \\ y &= t + d_y & e_y^2 &= \langle d_y^2 \rangle \end{aligned} \tag{A3}$$

where  $x$ ,  $y$ , and  $t$  XXX are as defined before and  $d_x$  and  $d_y$  YYY are the independent observation errors on  $x$  and  $y$  respectively ZZZ, i.e.,  $\langle d_x d_y \rangle \approx 0$  BBBB. The observation errors are random and uncorrelated with  $t$  CCCC, i.e.,  $\langle d_x t \rangle \approx 0$  DDDD and  $\langle$

$\mathbf{d}_Y$  EEEE  $t > \approx$  0FFFF. For simplicity we have removed the true distribution's mean and the systematic errors, i.e.,  $\langle t \text{ GGGG} \rangle = 0$ ,  $\langle \mathbf{d}_X \text{ HHHH} \rangle = 0$ , and  $\langle \mathbf{d}_Y \text{ IIII} \rangle = 0$ . We now find

$$\begin{aligned} \langle x^2 \rangle &= \mathbf{s}^2 + \mathbf{e}_X^2 \\ \langle y^2 \rangle &= \mathbf{s}^2 + \mathbf{e}_Y^2 \\ \langle xy \rangle &= \mathbf{s}^2 \end{aligned} \quad (\text{A4})$$

which are three equations with three unknowns that are easily resolved

$$\begin{aligned} \mathbf{e}_X^2 &= \langle x^2 \rangle - \langle xy \rangle \\ \mathbf{e}_Y^2 &= \langle y^2 \rangle - \langle xy \rangle \\ \mathbf{s}^2 &= \langle xy \rangle \end{aligned} \quad (\text{A5})$$

Thus from the covariances we can resolve the true variance and the standard errors of systems  $X$  and  $Y$ .

Now suppose that one system is not calibrated, for example, we change (A3) to

$$\begin{aligned} x &= t + \mathbf{d}_X & \mathbf{e}_X^2 &= \langle \mathbf{d}_X^2 \rangle \\ y &= s_Y(t + \mathbf{d}_Y) & \mathbf{e}_Y^2 &= \langle \mathbf{d}_Y^2 \rangle \end{aligned} \quad (\text{A6})$$

where  $s_Y$  is the calibration (scaling) constant. We now find

$$\begin{aligned} \mathbf{e}_X^{*2} &= \langle x^2 \rangle - \langle xy \rangle = \mathbf{e}_X^2 + (1 - s_Y)\mathbf{s}^2 \\ \mathbf{e}_Y^{*2} &= \langle y^2 \rangle - \langle xy \rangle = s_Y^2 \mathbf{e}_Y^2 + s_Y(s_Y - 1)\mathbf{s}^2 \\ \mathbf{s}^{*2} &= \langle xy \rangle = s_Y \mathbf{s}^2 \end{aligned} \quad (\text{A7})$$

such that for  $\mathbf{e}_X^{*2} \text{ JJJJ} \geq 0 \text{ KKKK}$  and  $\mathbf{e}_Y^{*2} \text{ LLLL} \geq 0 \text{ MMMMNNNN}$  the transformed distribution of  $t^* = \sqrt{s_Y} t \text{ OOOO}$  in combination with error model

$$\begin{aligned} x^* &= t^* + \mathbf{d}_X^* & \langle \mathbf{d}_X^{*2} \rangle &= \mathbf{e}_X^{*2} \\ y^* &= t^* + \mathbf{d}_Y^* & \langle \mathbf{d}_Y^{*2} \rangle &= \mathbf{e}_Y^{*2} \end{aligned} \quad (\text{A8})$$

is statistically identical to the system defined in (A3). Consequently, one can show that substituting the transformed quantities defined in (A7-8) into (A2) rather than the real quantities of (A3) leads to an identical joint distribution. As such, the calibration coefficient cannot be resolved unambiguously without further information on the errors in this general case.

This is due to the fact that we have three independent statistical variables, i.e.,  $\langle x^2 \rangle$ ,  $\langle y^2 \rangle$ , and  $\langle xy \rangle$ , and four unknowns that are  $s_Y \text{ PPPP}$ ,  $\mathbf{s}$ ,  $\mathbf{e}_X$ , and  $\mathbf{e}_Y \text{ QQQRRRR}$ , which leaves one degree of freedom. The constraint that error variances are positive gives the following values for the scaling constant  $s_Y^*$  in the case of  $s_Y = 1$ :  $-\mathbf{e}_Y^2 \text{ SSSSTTTT} (\mathbf{s}^2 + \mathbf{e}_Y^2)^{-1} \leq s_Y^* \text{ UUUU} - 1 \leq \mathbf{e}_X^2 \text{ S}^{-2}$ . Only the addition of an independent third system can

help determine the unique and correct value of  $s_Y$ .

**Appendix B: Pseudobias Through Nonlinear Transformation**

A statistical problem that is relevant for considering the optimal error domain may occur through nonlinear transformation. This is easily shown for wind speed  $f$  that depends in a nonlinear manner on the wind components  $(u, v)$ . As an alternative to Hinton and Wylie [1985], we assume normal distributed errors on the wind components  $u$  and  $v$  for measurement systems  $X$  and  $Y$ , i.e.,  $u_X = N(u_t, \mathbf{e}_X)$ ,  $v_X = N(v_t, \mathbf{e}_X)$ ,  $u_Y = N(u_t, \mathbf{e}_Y)$ , and  $v_Y = N(v_t, \mathbf{e}_Y)$  and, in addition, normal distributed true components,  $u_t = N(0, \mathbf{s})$  and  $v_t = N(0, \mathbf{s})$ , where  $N(0, \mathbf{s})$  indicates the normal distribution with zero mean and standard deviation  $\mathbf{s}$ . The wind speed distribution of system  $X$ ,  $p(f_X) df_X$ , then becomes

$$p(f_X) df_X = \frac{f_X}{\mathbf{s}_X^2} \exp[-\frac{f_X^2}{2\mathbf{s}_X^2}] df_X \tag{B1}$$

where  $\mathbf{s}_X^2 = \mathbf{s}^2 + \mathbf{e}_X^2$ . A similar expression can be derived for system  $Y$ . The expected mean value of  $f_X$  will be  $\langle f_X \rangle = \sqrt{\pi/2} \mathbf{s}_X$ , and  $\langle f_X - f_Y \rangle = \sqrt{\pi/2} (\mathbf{s}_X - \mathbf{s}_Y) \approx \sqrt{\pi/2} (\mathbf{e}_X^2 - \mathbf{e}_Y^2) \mathbf{s}^{-1}$ . Thus the difference in mean wind speed is generally nonzero, and a pseudobias occurs, since the component error distributions were not biased. More detailed analysis shows that the pseudobias results from the fact that the wind speed error distribution is asymmetric in the case of symmetric wind component error distributions, especially for low wind speeds. The magnitude of the pseudobias depends on wind speed (see, e.g., Figure 2).

**Acknowledgments.** This work has been greatly stimulated by discussions in the ESA ASCAT Science Advisory Group and in particular by discussions with Didier Le Meur from ECMWF. Tsan Wang Yu from NCEP kindly provided me with the collocation data set and is especially acknowledged.

**References**

Bryan, F. O., I. Wainer, and W. R. Holland, Sensitivity of the tropical Atlantic circulation to specification of wind stress climatology, *J. Geophys. Res.*, 24, 729-744, 1995.  
 Freilich, M. H., Validation of vector magnitude data sets: Effects of random component errors, *J. Atmos. Oceanic Technol.*, 14, 695-703, 1997 .  
 Hinton, B. B., and D. P. Wylie, A correction for the errors in ship reports of light wind, *J. Atmos. Oceanic Technol.*, 2, 353-356, 1985.

- Holton, J. R., An Introduction to Dynamic Meteorology, 2nd ed., *Int. Geophys. Ser.* - vol. 23, Academic, San Diego, Calif., 1979.
- Le Meur, D., L. Isaksen, and A. Stoffelen, Wind calibration of the ERS scatterometer for data assimilation purposes at ECMWF, paper presented at the Wind and Wave Validation Workshop, Comm. on Earth Obs. Satell., Eur. Space Agency, Noordwijk, Netherlands, June 3-5, 1997.
- Lorenc, A. C., Analysis methods for numerical weather prediction, *Q. J. R. Meteorol. Soc.*, 112, 1177-1194, 1986.
- Offiler, D., The calibration of ERS-1 satellite scatterometer winds, *J. Atmos. and Oceanic Technol.*, 11, 1002-1017, 1994.
- Roquet, H. and C. Gaffard, Proposal for a new version of CMOD4, memorandum Forecast Res. Dep., Eur. Centre Medium-range Weather Forecasts, Reading, UK.
- Rufenach, C., A new relationship between radar cross-section and ocean surface wind speed using ERS-1 scatterometer and buoy measurements, *Int. J. Remote Sens.*, 16(18), 3629-3647, 1995.
- Stoffelen, A., Error modelling of scatterometer, in-situ, and ECMWF model winds: A calibration refinement, *Tech. rep. 193*, R. Neth. Meteorol. Inst., de Bilt, Netherlands, 1996.
- Stoffelen, A., A simple method for calibration of a scatterometer over the ocean, *J. Atmos. Oceanic Technol.*, in press, 1998.
- Stoffelen, A., and D. Anderson, Scatterometer data interpretation: Measurement space and inversion, *J. Atmos. Oceanic Technol.*, 14(6), 1298-1313, 1997a.
- Stoffelen, A., and D. Anderson, Scatterometer data interpretation: Estimation and validation of the transfer function CMOD4, *J. Geophys. Res.*, 102(C3), 5767-5780, 1997b.
- Stoffelen, A., and D. Anderson, Ambiguity removal and assimilation of scatterometer data, *Q. J. R. Meteorol. Soc.*, 123, 491-518, 1997c.
- Tolman, H. L., Effects of observation errors in linear regression and bin-average analyses, *Q. J. R. Meteorol. Soc.*, 124, 897-917, 1998.
- Wilkerson, J. C., and M. D. Earle, A study of differences between environmental reports by ships in the voluntary observing program and measurements from buoys, *J. Geophys. Res.*, 95(C3), 3373-3385, 1990.

## CHAPTER V

### Ambiguity Removal and Assimilation of Scatterometer Data\*

**Abstract.** The ERS-1 scatterometer has proved to be a source of high quality ocean surface wind data, but a problem remains, namely the dual directional ambiguity of the solutions. An ambiguity removal scheme, called PRESCAT, is described based on our experience (a) that information on wind direction retrieval skill is an important input to ambiguity removal, (b) that wind-vector filtering is beneficial compared to wind-direction filtering, and (c) that meteorological forecast information already enables us to correctly remove 95% of all ambiguities. The performance of the ambiguity filter is very good compared to other operational ambiguity removal schemes. Furthermore, a statistical interpolation analysis system called ‘buddy’ check is used effectively to identify and remove the few (approx. 0.1%) wrongly selected solutions.

Assimilation of scatterometer winds has a beneficial impact on analyses and short-range forecasts, probably mainly from improvements on the sub-synoptic scales. On the wider temporal and spatial scales, scatterometer winds were also found beneficial, but only in the absence of satellite temperature soundings (SATEMs). In assimilation experiments in which the latter were included, the scatterometer provided a neutral impact on the medium-range forecast. Moreover, the conventional observations, including SATEMs, are shown to have adverse effects on the surface-wind analysis. We believe that both the redundancy and the adverse effects on the surface-wind field are explained by the rigid formulation of the 6-hour-forecast error structure; the forecast error is assumed flow-independent, and information on the special meteorological conditions in the atmospheric planetary boundary layer is lacking. To make observational systems more useful and complementary for numerical weather prediction the effects of the structure functions have to be investigated more precisely. In an adaptive four-dimensional variational assimilation scheme the effect of the assumptions on forecast-error structure will be less. We show that, in a variational framework, scatterometer backscatter measurements are difficult to assimilate directly. Instead, we derive and illustrate an alternative procedure to assimilate retrieved winds rather than backscatter measurements.

---

\*Based on:

Stoffelen, Ad, and David Anderson, Ambiguity Removal and Assimilation of Scatterometer Data, *Q. J. R. Meteorol. Soc.*, 123, 491-518, 1997.

## 1. Introduction

The European Space Agency's remote-sensing satellite, ERS-1, was launched on 17 July 1991, carrying a C-band scatterometer. The satellite flies in a polar orbit at a height of 800 km. The scatterometer instrument (which is also mounted on ERS-2) has three independent antennae pointing in a horizontal plane towards a direction of  $45^\circ$ ,  $90^\circ$ , and  $135^\circ$  with respect to the satellite propagation, thus illuminating a site in the scatterometer's swath three times, by the fore, mid, and aft beam, respectively. The incidence angle of the radar beam varies from  $18^\circ$  to  $47^\circ$  for the mid beam, and from  $24^\circ$  to  $57^\circ$  for the fore and aft beams. The swath, approximately 500 km wide, is sampled every 25 km resulting in 19 measurement nodes across the swath; along the swath the sampling distance is also equal to 25 km. The nodes are not independent, however, and the effective spatial resolution of the instrument on the earth's surface (called the footprint) is approximately 50 km. At the European Centre for Medium-range Weather Forecasts (ECMWF) a quality control procedure has been implemented which can identify and reject anomalous triplets of backscatter measurements [*Stoffelen and Anderson, 1995; Chapter II*]. It was also shown that the scatterometer data can successfully be interpreted as measurements of the 10-m wind vector. Through comparison with the ECMWF numerical weather-prediction (NWP) model, scatterometer winds are found to be more accurate than conventional ocean surface wind data, currently used in operational meteorology [*Stoffelen and Anderson, 1995; Chapter IV*]. However, scatterometer winds have a dual ambiguity because there are two wind solutions at each node on the earth's surface. Several ambiguity removal schemes were evaluated before the launch of ERS-1 [*Graham et al., 1989*], and a scheme called CREO [*Cavanié and Lecomte, 1987*] was selected and implemented by the European Space Agency (ESA). In this scheme two antiparallel fields from the two solutions at each node are built up. For each field the number of cases in which the highest probability solution is chosen is calculated. When this number is significantly higher for one of the fields than for the other, then the field with the higher number is selected. This application of CREO is called 'autonomous' ambiguity removal. If autonomous ambiguity removal fails, or is not applied, then a comparison is made between both antiparallel fields and a forecast of the surface wind field; the field with the higher correlation selected. In section 2 we briefly discuss the performance of this scheme when used with real data, and propose an alternative scheme, based on the United Kingdom Meteorological Office (UKMO) scheme SLICE [*Offiler, 1987*], which improves the ambiguity removal skill.

Given the high quality of the retrieved scatterometer winds, it is important that they be assimilated into numerical weather-prediction (NWP) models. Earlier assimilation experiments with SEASAT scatterometer data in the T106 spectral resolution ECMWF model had a neutral impact in both southern and northern hemispheres [*Anderson et al.,*

1991]. In the case of the rapidly developing QE-2 storm, the KNMI (Koninklijk Nederlands Meteorologisch Instituut) limited area model (LAM) gave a forecast that was better than the ECMWF model's forecast [*Stoffelen and Cats*, 1991], and the use of SEASAT scatterometer data had a further substantial and beneficial effect on the forecast. Preliminary tests with ERS-1 scatterometer data in the ECMWF T106 model showed a neutral impact [*Hoffman*, 1993]. However, the quality of the SEASAT and the preliminary ERS-1 scatterometer data used by Hoffman is substantially less than the current quality of the ERS-1 scatterometer data. Assimilation experiments at the UK Meteorological Office showed that the ERS-1 scatterometer winds had a beneficial impact in a day-5 forecast in the southern hemisphere [*Bell*, 1994]. *Breivik et al.* [1993] obtained a small beneficial effect in the Norwegian 50-km resolution limited-area model.

For many years, ECMWF have been using a statistical interpolation scheme, otherwise known as optimal interpolation or OI, to perform the analysis. To test whether the data can be used to modify the ECMWF analyses using the current OI analysis scheme, various experiments are done in which winds from the ERS scatterometer processing, inversion, and ambiguity removal scheme, called PRESCAT, are assimilated into the ECMWF model analysis. One of the periods selected is from 18 to 28 March; it is chosen so as to coincide with a parallel study being conducted by the UK Meteorological Office [*Bell*, 1994].

Parallel assimilation experiments to assess the 'redundancy' between surface wind data and NOAA/NESDIS (National Oceanographic and Atmospheric Administration/National Environmental Satellite and Data Information System) processed TOVS (TIROS (Television Infra-Red Operational Satellite) Operational Vertical Sounder) vertical temperature soundings [*Smith et al.*, 1979], called SATEM, are also discussed in section 3. Ten-day forecasts from these assimilations were made and are compared with the verifying analyses to test for impact of the scatterometer data on the forecast. Since scatterometer data had not yet been used operationally at ECMWF, they can therefore be used to verify the operational ECMWF surface wind analyses and forecasts, as is demonstrated in section 3.4.

In recent years variational assimilation schemes have become more mature, and at ECMWF a scheme of this kind has been developed but, at the time of writing, has not yet been implemented [*Courtier et al.*, 1993]. It was anticipated that satellite measurements that are indirectly related to NWP model variables, are best assimilated *directly* into such schemes. In section 4, however, it is shown that this is not the case for scatterometer measurements, and that it is more practicable to assimilate the ambiguous winds rather than the scatterometer backscatter measurement values  $S^0$ . The paper ends with a summary and conclusions in section 5.



## 2. Ambiguity Removal

We found that a modified application of CREO at ECMWF worked fairly well in about 65% of cases, but in a relatively large number of cases (approx. 30%) CREO did not provide a solution even when reasonable retrieved winds were present. In a small number of cases (approx. 5%) the solution provided by CREO was wrong. These cases tended to be associated with rapidly changing and/or complex synoptic situations, for which correct scatterometer winds would have been especially valuable. *Stoffelen and Anderson* [1995; Chapter II] have shown that the probability of the two wind-vector solutions is close to 50% and that the rank of the correct solution is horizontally correlated, which implies that autonomous ambiguity removal is not likely to be very successful; a conclusion that indeed was found to be true. Consequently we developed a procedure to use a short-range forecast to select direction at every node, and introduced a revised ambiguity removal procedure within the PRESCAT package.

### 2.1. Description of the Ambiguity Removal Procedure

First a selection of direction is made by choosing that retrieved solution whose direction is closest to the background wind field. This selection is made from the two solutions provided by the previous inversion step [*Stoffelen and Anderson*, 1995; Chapter II]. Experience has shown that the field so produced is reasonable most of the time but there are local regions, i.e., in about 5% of cases, where the solution appears unmeteorological. It is therefore advisable to apply a filter in an attempt to increase meteorological consistency. The choice of selection filter used here was influenced by SLICE [*Offiler*, 1987], but it differs from SLICE in a number of ways, as is discussed below.

The filter consists of a  $5 \times 5$  box which slides over the wind field, up to 114 rows at a time. The box first slides in the direction opposite to that of the satellite, starting at the inside edge of the swath and proceeding as in Figure 1a. When it reaches the end of the sector, the direction is reversed, and it exactly retraces its track. On the third pass it starts at the outside edge of the swath and proceeds as in Figure 1b. On the fourth pass it exactly reverses the trace of the third pass. In SLICE the scheme finishes processing when there are less than a certain number of points changed in a pass. However, it was found that even if there were no changes made on one pass there could be changes on the next pass, and that these changes were, in general, beneficial. In PRESCAT there are always four passes.

Within a  $5 \times 5$  box, the direction at the center of the box is chosen, based on a weighted average of the differences from the  $N$  surrounding points, of which there are usually 24; but there may be less near the edge of the swath if part of the box is over land, or, if some points have been rejected by the quality control on the backscatter measurements. At the central point, a mean likelihood,  $L_i$ , is calculated for each solution  $i$

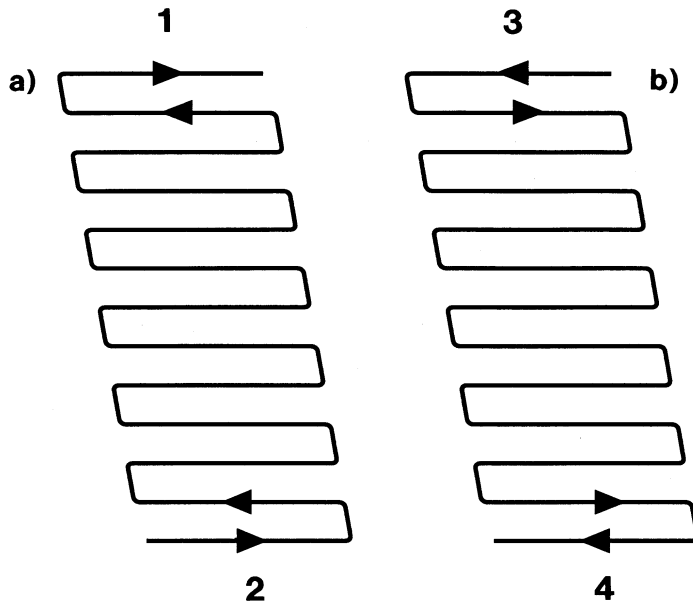


**Figure 1.** Schematic of the way that the ambiguity removal filter slides along an ascending orbit in (a) the first two iterations and (b) the second two iterations.

where

$$L_i = \frac{\sum_{j=1}^N C_j \exp[-0.5\{(u_i - u_j)^2 + (v_i - v_j)^2\}q^{-2}]}{N} \quad (1)$$

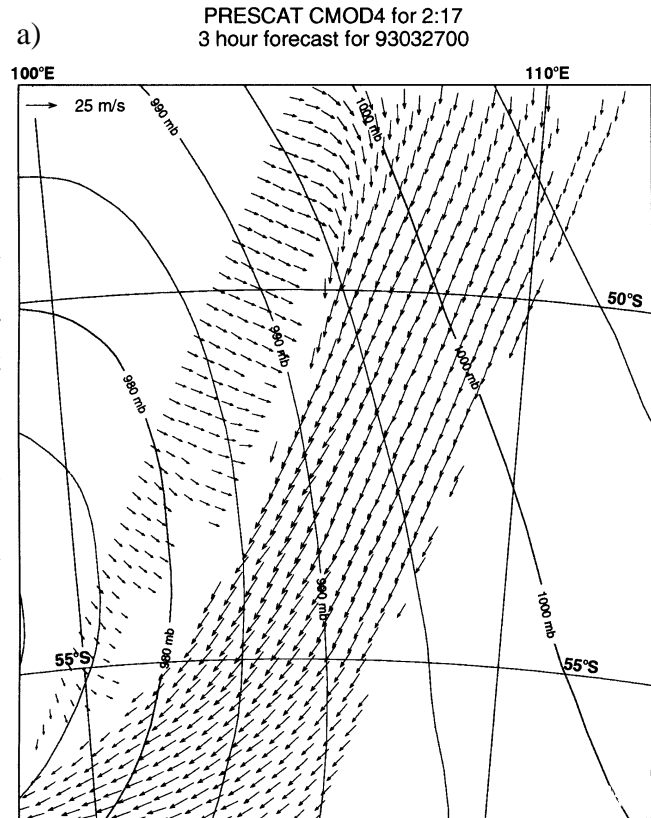
and the summation on  $j$  is over the  $N$  surrounding points in the box. The solution,  $i$ , with the highest probability  $L_i$  is then selected. The parameter  $q^2$  should represent the wind component variability within a box. Currently a value of  $q = 2.5 \text{ m s}^{-1}$  is used. When a lower value,  $2.0 \text{ m s}^{-1}$ , was used, the filter was unable to influence neighboring points sufficiently. In PRESCAT the computed likelihood of a solution depends on the wind vector (Eq. (1)) rather than just direction as in SLICE, since we found several cases (near fronts) where speed as much as direction indicated the consistency between neighboring points.

The parameter  $C_j$  represents the confidence in the solution at node  $j$ . The initial value of  $C$  is

$$C = \frac{P \times A \times NN}{4} \quad (2)$$

where  $P$  is the scaled probability that the wind direction is within, say,  $5^\circ$  of the true direction,  $A$  is the probability that the current solution is the correct one, and  $NN$  is the number of nearest neighbors. A quantity  $I$  indicates the skill with which wind direction can be resolved from the radar back-scatter measurements.  $P$  is derived from  $I$ , which in turn is defined in Eq. (4.4) of *Stoffelen and Anderson [1995; Chapter II]*. As  $I$  can range from zero to quite high values for high speeds and outer nodes, it is necessary to map it to the range 0 to 1 so as to use it as a probability index of skill. The mapping  $P = I'(2 - I')$  where  $I' =$

**Figure 2.** (a) Winds retrieved and with ambiguities removed by PRESCAT for 02 UTC 27 March 1993. Contours are ECMWF 6-hour forecast of mean-sea-level pressure, verifying at 00 UTC. On the right page, (b) FGAT winds, and, (c) winds with ambiguities removed by CREO. In (a) winds with a low confidence rating have not been plotted. These lie mainly along the line of the front, which is very sharp in (a) and (c), but much less so in FGAT. In (c) the winds in area A are in error.



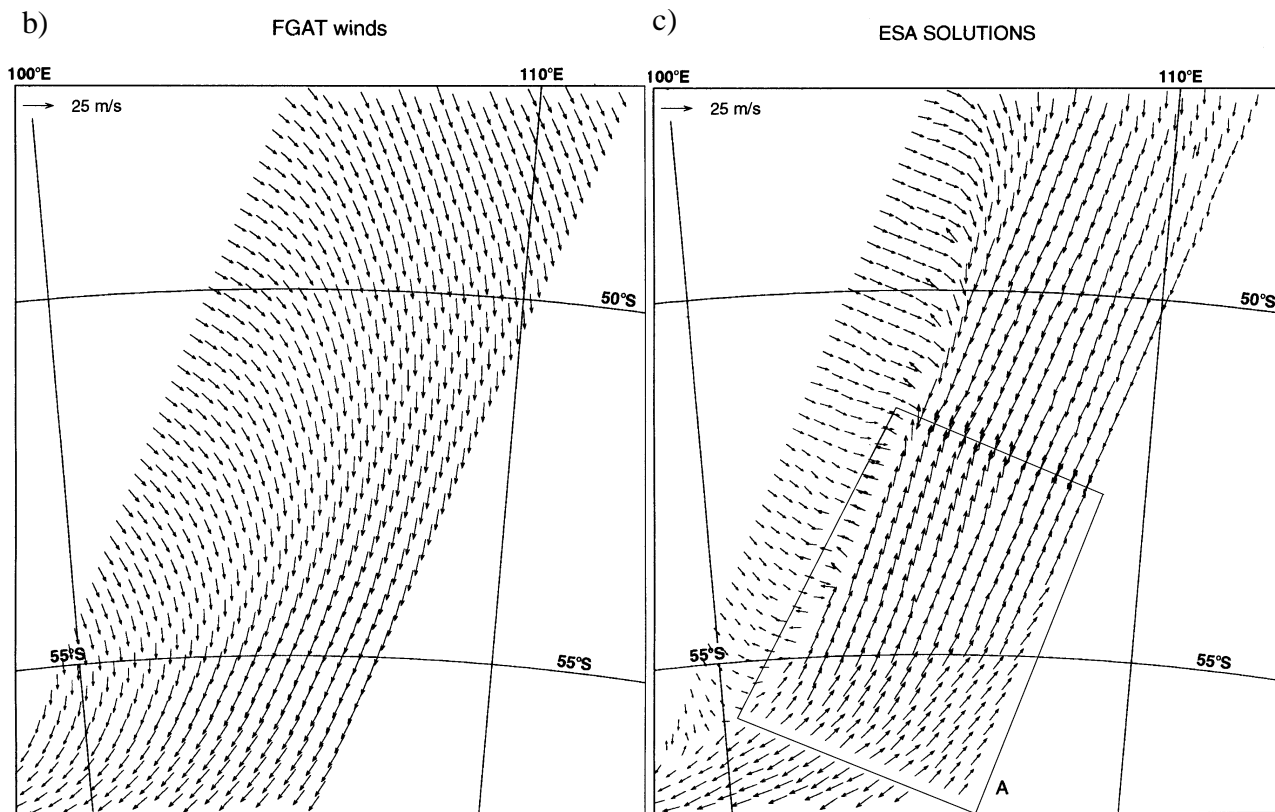
$\min(I/\sqrt{10}, 1)$ , has the property of being 0 for  $I = 0$ , increasing monotonically with increasing  $I$  to a value of 1 at  $I = \sqrt{10}$ , and is constant when  $I > \sqrt{10}$ . In the report by *Stoffelen and Anderson* [1995; Chapter II] it was determined empirically that adequate directional skill exists when  $I > \sqrt{10}$ , as is reflected in the above mapping. The quantity  $A$  is defined by the equation

$$A = \exp[-0.5\{(u - u_B)^2 + (v - v_B)^2\}q^{-2}]$$

where  $A$  determines the probability that the selected solution is the correct one, and  $(u, v)$  is the closest of the two scatterometer wind vectors to the ECMWF model first guess denoted  $(u_B, v_B)$ . We used FGAT (First Guess at Appropriate Time), where the first guess is interpolated to the measurement time from a 3-, 6-, and 9- hour forecast. The factor  $NN$  is the number of nearest neighbors to the node under consideration and therefore has a value between 1 and 4. In Eq. (1) points for which  $C$  is low are given low weight, and will not have a strong influence on the selection of a solution at neighboring points; the opposite is true for points for which  $C \approx 1$ . Thus, the filter propagates information with high confidence to areas where confidence is low.

The confidence of a point is updated on a pass of the filter according to

$$C = C + (1 - C)L$$



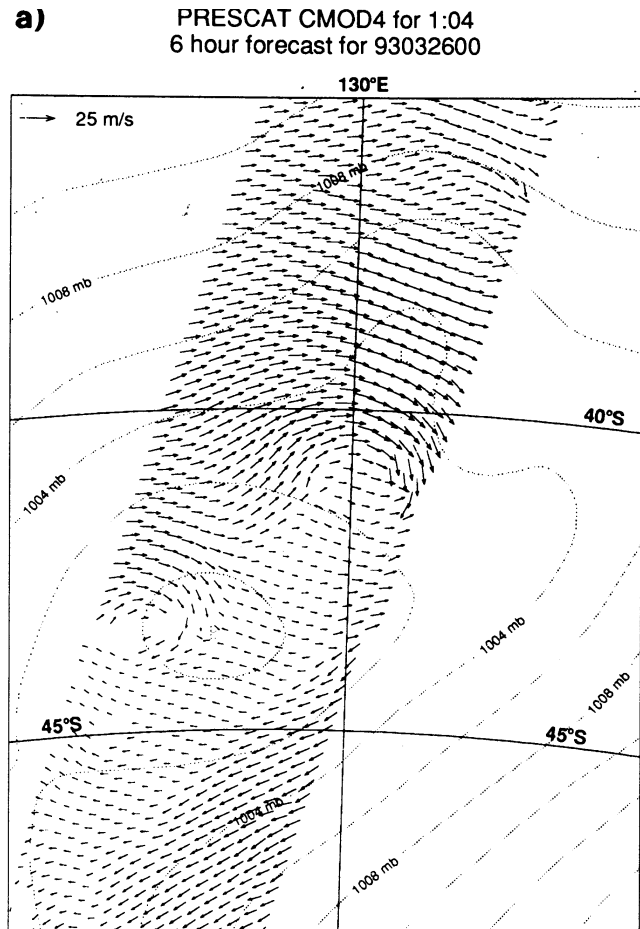
where  $L$  is defined in Eq. (1), i.e., confidence is increased relatively mostly when the wind vector at the neighboring points is consistent, and when we have confidence in the neighboring solutions (see, e.g., Eq. (1)). *Stoffelen and Anderson [1995; Chapter II]* have given the description of a consistency check of the three radar measurements at each location whereby anomalous triplets are rejected (1–2%); these are usually in areas with high variability (i.e., fronts, cyclones, etc.). Because the background information is usually also of lower quality in such areas, and because rejection is often associated with wind shifts, the quality control (QC) benefits the ambiguity removal.

In the next section we give a few examples of PRESCAT to both show its power and also highlight some remaining problems. The examples that have been chosen emphasize important meteorological situations.

## 2.2. Examples of Ambiguity Removal Using PRESCAT

Figure 2a shows a plot of the winds for 02 UTC 27 March 1993 resulting from retrieval and ambiguity removal using PRESCAT. The appropriate FGAT field used in PRESCAT is shown in Figure 2b. The blank areas in the swath in Figure 2a are regions in which data have been rejected by the QC of the inversion procedure. Of most interest is the region close to the front. This is an area in which the winds change rapidly in space and, by implication, also in time, and our hypothesis is that there will be confused sea-state

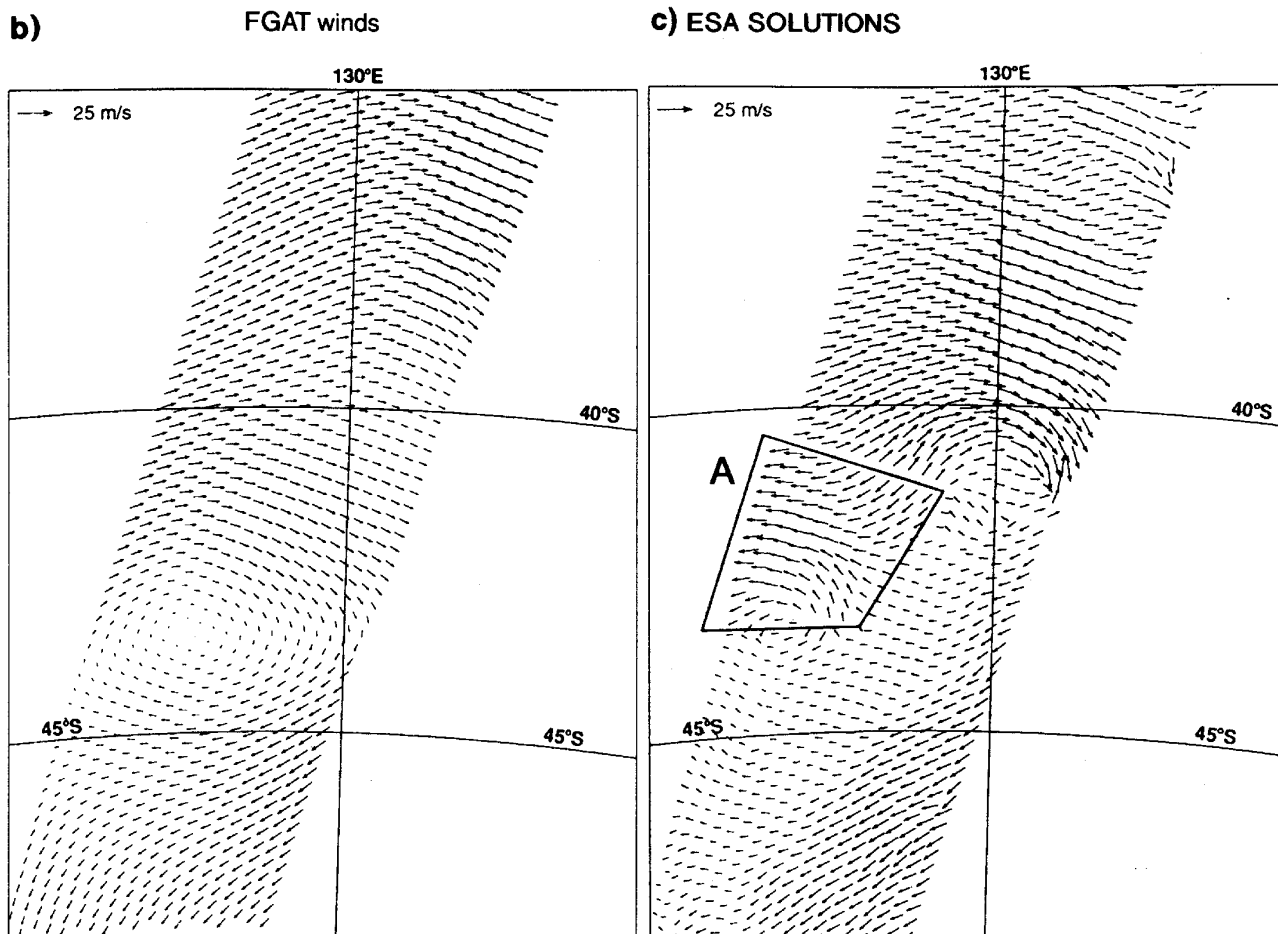
**Figure 3.** Similar to Figure 2, but for 00 UTC 26 March 1993. This figure shows in panel (a) a complex double low structure in the PRESCAT winds, but in (b), on the right page, FGAT depicts only a broad feature. A shear line is needed somewhere. Its position is unclear, but it should probably join the centers of the two lows. Panel (c) shows the ESA solution. Here, the area marked A is obviously wrong.



conditions. However, in some areas rain may also be a disturbing factor on the sea surface. The QC arises from the  $s^0$  measurements themselves, not from a realization that there is a front. Nevertheless, the front is well delineated by this test.

Figure 2a also shows how well the scatterometer can see sharp features. The front is pinpointed to within 50 km with 90° changes in wind direction across it. By contrast FGAT (Figure 2b) shows a much more gentle turning of the wind and no sharp front. A sharp front is present also in the CREO (ESA) solution (Figure 2c), but in one block of winds the direction is wrongly selected. The origin of this error lies in a wrong selection at the location of the front in the south-west of the area. It is obvious from the observed speed gradient that wind-speed information, as used in Eq. (1), rather than just wind direction information, as used in SLICE, is useful for ambiguity removal.

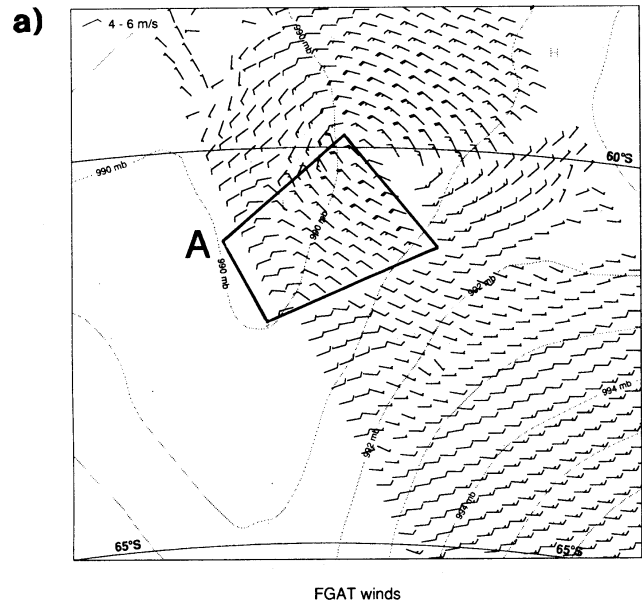
A second example comprises a complex double-centered low-pressure system which developed in the Australian Bight at 00 UTC 26 March 1993. The PRESCAT solution is shown in Figure 3a. Again a region of high residuals is present in and around the southernmost low-pressure system. These points are towards the outside of the swath where wind direction accuracy is generally highest. This figure is selected to show that complex systems exist where it is hard to choose the correct wind pattern. The chosen pattern (Figure



3a) looks unmeteorological in the area east of the southernmost low because there are sharp shear zones with a large shift in direction. A shear line is needed somewhere, probably linking the centers of the two lows, rather than the one selected by PRESCAT. However, in the forecast of surface pressure the southernmost low-pressure system and a wavelike disturbance further to the north-east are present but shifted in position with respect to the scatterometer-measured disturbance.

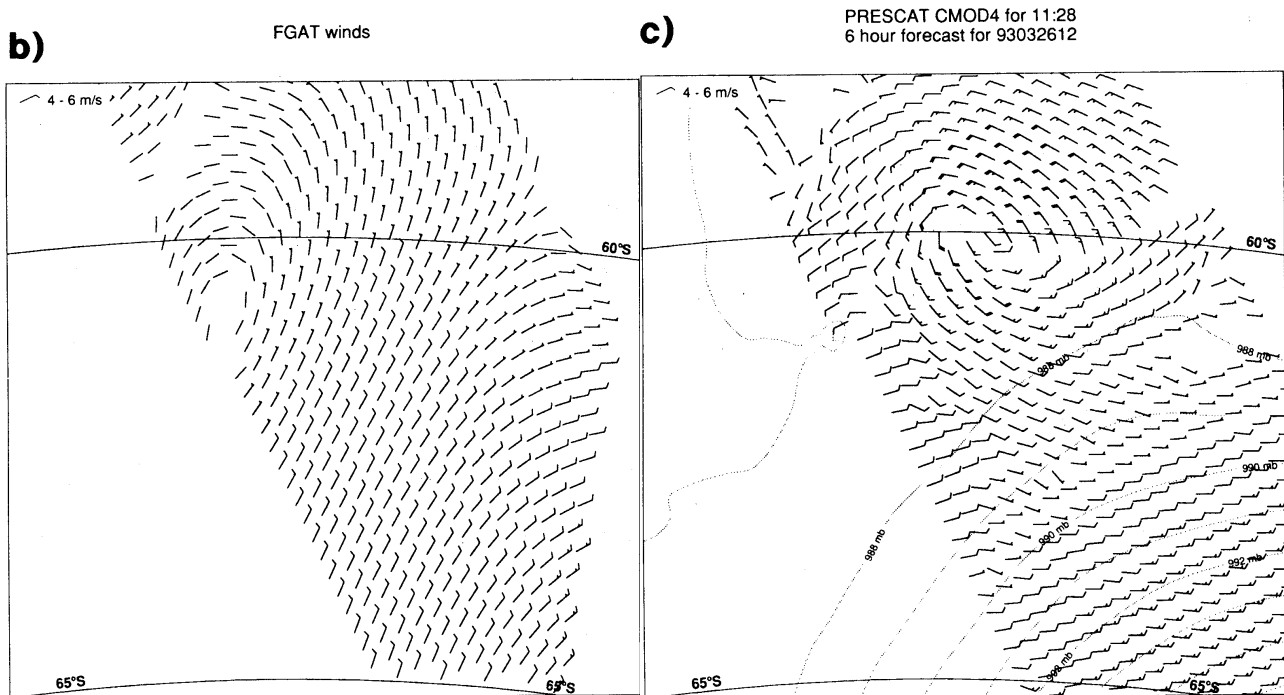
Part of the difficulty in ambiguity removal arises because the scatterometer can see much smaller-scale features than are present in the FGAT winds (Figure 3b), which shows only a smooth wind field. Finally, Figure 3c shows the CREO solution which is clearly wrong in region A. Errors in PRESCAT can arise when the FGAT directions are roughly along the direction of the wrong solution. In these cases the initially wrongly selected solutions compare relatively well with FGAT and are assigned high confidence (Eq. (2)). If the FGAT is close to 180° wrong for only a few isolated points, then the filter can correct for this. If, however, the area of wrong solutions is large, then the filter is unable to make a satisfactory correction. Errors also arise if the FGAT directions are nearly orthogonal to the pseudo-streamline defined by the scatterometer. (The term pseudo-streamline is used rather than streamline since the rank-1 and rank-2 directions are not exactly antiparallel.) Such

**Figure 4.** Plots of a low pressure system for 12 UTC 26 March 1993. In (a), ambiguities are removed using the FGAT from the ECMWF operational analysis system shown in (b), while in (c) ambiguities are removed by using FGAT obtained from an experiment in which scatterometer data were assimilated. The latter FGAT was visually close to (b) but just marginally different, leading to improved winds in the sector south-west of the depression. The pseudo streamline is nearly orthogonal to FGAT directions at many nodes in this example. This means that the solutions are very sensitive to small changes in FGAT, and prone to error as in area A in panel (a).



points would be given low confidence and would be corrected by PRESCAT provided they are surrounded by areas of higher confidence. However, if higher confidence areas are not present then errors can occur. The above directional errors can arise when the FGAT winds are light and the wind direction therefore not very important, or when there is a mispositioning of a meteorological system in the first guess. The next two examples provide illustrations.

Figure 4a shows the retrieved winds in an intense polar low at 12 UTC on 26 March 1993, and Figure 4b the corresponding FGAT winds, in which the low is virtually absent. Although PRESCAT has delineated this structure very well in general, there is a patch to the south-west of the depression in which the winds are obviously wrong. The main cause of error in Figure 4a arises because FGAT winds over a significant part of the area are nearly orthogonal to the pseudo-streamline defined by the scatterometer, thus making the direction selected very sensitive to errors in FGAT. There is also a smaller area in which FGAT is closest to the wrong solution. A small difference in FGAT could tip the selected winds by almost  $180^\circ$ , as is illustrated in Figure 4c. In this case FGAT is taken from an experiment in which scatterometer data have been assimilated (see next section). This FGAT is very similar to Figure 4b (not shown), but compares slightly better with the circulation indicated by the scatterometer in the south-west sector of the low. This is just enough to tip the initial selection at a few nodes; subsequently the filter is then able to bring about convergence to the correct solution. This example illustrates the sensitivity that the ambiguity removal has to the quality of the input forecast data. It is also a very good example showing mesoscale features which can be seen by the scatterometer but have not been detected by the ECMWF



analysis/forecast system, because there were no other useful observations available in this area of the southern hemisphere.

In Figure 5 we show an example of a tropical storm. In this case the FGAT shows a tropical feature with wrong position and weak winds near the center, while the scatterometer shows an active tropical storm. The reason for including this example is two-fold: first to show that PRESCAT can represent tropical storms not present in the FGAT, but secondly there can still be correlated error resulting from large phase errors in FGAT. The batch of winds labeled A is almost certainly in error. In the next section we describe a quality control procedure, called ‘buddy’ checking, which can effectively remove wrongly selected ambiguities.

When developing PRESCAT, a 6-hour forecast, denoted FG, was used originally as a first guess. However, it was found better to use a first guess which corresponded with the satellite’s measurement time (FGAT). For slow moving, large-scale features, this is not necessary, but for rapidly moving systems it is essential. Figure 6 shows the scatterometer winds to the east of a low-pressure system, the deepest ever recorded (which later hit the Shetland islands and the grounded oil tanker Braer in January 1993). In the case for which FG was used rather than FGAT, the winds in the area marked A and B looked unmeteorological and, very likely, were wrong. By using FGAT, and, therefore, a more appropriate comparison between the background winds and the scatterometer winds, a correct wind selection was obtained. Obviously, the use of a forecast with a lead time of between 18 and 36 hours (as is currently done in ESA operations) will degrade the performance of the PRESCAT scheme (or any other scheme using meteorological forecast



information as background for the ambiguity removal procedure).

PRESCAT uses wind-vector consistency in filtering the data. The use of background-error covariance structures to obtain the most likely wind field structure should lead to a meteorologically more consistent analysis and, thus, ambiguity removal. In a variational analysis procedure these structure-functions together with the information provided by the scatterometer can be used to correct errors in the background field. Thus a meteorologically balanced analysis will result, to be used for the benefit of the ambiguity removal. The three-dimensional and four-dimensional variational (3D- and 4D-Var) data assimilation procedures are a sensible framework for further investigation of the variational approach to ambiguity removal (see section 4).

### **3. Optimum Interpolation (OI) Assimilation**

#### **3.1. The Analysis System**

The analysis uses a statistical filter, called optimum interpolation (OI) in which the observations and the model forecast are combined into a coherent, balanced analysis. Differences between the model and observations are used to alter the forecast. Although the OI is carried out at discrete 6-hour intervals the correct time of observation (FGAT) is used for the calculation of the difference between observation and model. Data are separated into 6 hour windows.

Since the analysis used is multivariate, measurements of wind will not only influence the wind analysis (as in a univariate scheme where each variable is analyzed separately) but also the mass field (i.e., temperature at a given height or, as in the model, the height of a given pressure surface) through a latitude-dependent application of geostrophy. Near-surface data adjust not only the surface layers but have an influence in the vertical also. Differences between the PRESCAT winds and the FGAT are projected vertically as in Figure 7. This projection is strictly vertical. This is good for mature systems, but probably not so for young developing baroclinic systems.

Since the background error is assumed to have a horizontal structure, the difference between a datum and the FGAT influences an area around the observation with an influence that decreases with increasing distance from the observation. This is defined by the horizontal weighting functions shown in Figure 8. As shown in Section 2, the scatterometer can see mesoscale features very well. In order that we might allow the best possible use of this data in the current analysis system, we used the highest possible model spectral sampling of the ECMWF model, viz. T213, which corresponds to about 60 km spatial sampling, i.e., comparable with the resolution of the scatterometer. However, the effective analysis resolution is likely to be considerably poorer than this, being governed by the

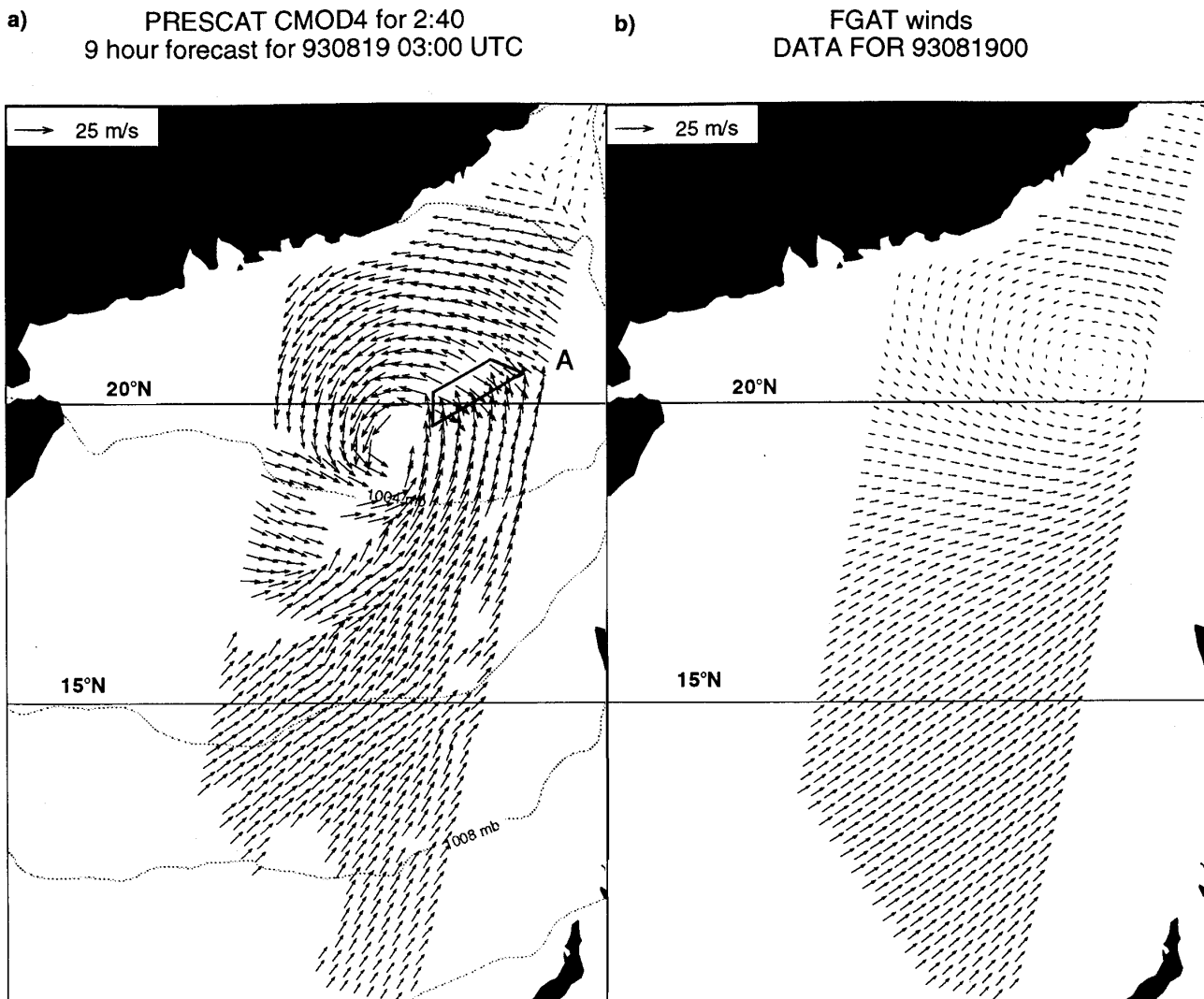


**Figure 5.** a) Plot of winds with ambiguity removed using PRESCAT. (b) Plot of the FGAT field used in the ambiguity removal. An important tropical cyclone is shown for 19 August 1993. The system is present in (a), but only a weak feature can be seen in (b).

weighting functions shown in Figure 8. Analysis is a costly procedure, so some assimilation experiments were carried out at the reduced model spectral sampling of T106 (approx. 125 km spatial model grid).

Although there are typically 40 000 scatterometer measurements in a 6-hour period, the data presented to the analysis are thinned to 100 km resolution. This is done because the resolution of the analysis is lower than that of the scatterometer and so cannot resolve the structure seen by the scatterometer. To avoid horizontal correlation in the data used for assimilation we performed thinning rather than averaging to achieve 100 km resolution. In retrospect, averaging over  $3 \times 3$  nodes and thinning to 100 km would have been sufficient, since horizontal wind error correlation is small for scales larger than 50 km [Stoffelen and Anderson, 1995; Chapter IV].

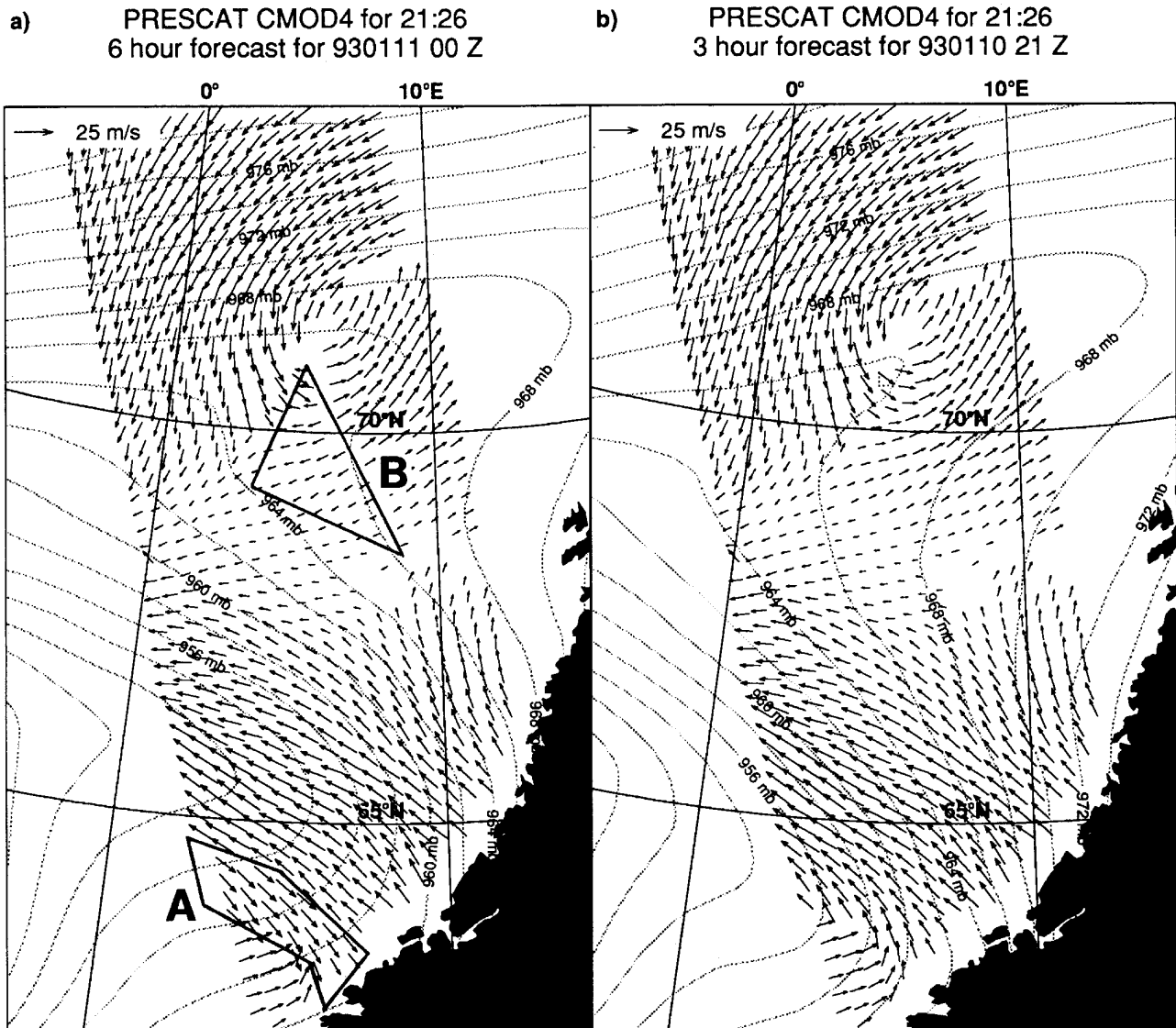


**Figure 6.** (a) Plot of winds close to the ‘storm of the century’, with the lowest ever recorded pressure. In this application of PRESCAT, the winds are selected using a forecast valid for the central time (FG), i.e., 00 UTC 12 January 1993. The winds are probably wrong in the areas marked A and B. (b) Winds after ambiguity removal using FGAT at 21 UTC, showing improvement in these areas.

One stage in the analysis procedure consists of a buddy-check. For every datum, an analysis is done without that datum and the value of the analysis is then compared with the measurement. If the difference is large, the datum is rejected. Typically about four PRESCAT winds are rejected every analysis from about 3000 presented to the analysis. Thus, the most serious ambiguity-removal errors are removed.

**Table 1.** Analysis Experiments

Experiment	Dates (1993)	Grid	Levels	PRESCAT	SATEM/ SATOB
SCAT	18 to 28 March	T213	31	YES	YES
NoSCAT	18 to 28 March	T213	31	NO	YES
SCAT/SATEM	26 April to 1 May	T106	19	YES	YES
NoSCAT/SATEM	26 April to 1 May	T106	19	NO	YES
SCAT/NoSATEM	26 April to 1 May	T106	19	YES	NO
NoSCAT/NoSATEM	26 April to 1 May	T106	19	NO	NO

YES means that the data are assimilated.

### 3.2. Analysis and Short-Range Impact

Several analysis periods have been considered and forecasts done from these analyses. We consider here only the periods from 12 UTC 18 March 1993 to 12 UTC 28 March 1993 and from 12 UTC 26 April 1993 to 00 UTC 2 May 1993 (see Table 1). Figure 9a shows the differences in the control and assimilated analyses for 12 UTC 18 March, i.e., after a single 6-hour assimilation of scatterometer winds from PRESCAT. Differences in the 1000-mb height are, typically, of order 10 m (approximately 1 mb in surface pressure) although, in the southern hemisphere, larger differences occur of approximately 30 m (i.e., 4 mb). Speed differences at the 10-m level can be up to  $10 \text{ m s}^{-1}$ . From other experiments, not shown, we found these numbers to be representative. These differences now evolve with time to the next analysis, six hours later, when new data are assimilated and, consequently, changes are made. After a few days of scatterometer data assimilation, differences grow in magnitude and need not be confined to the satellite swath, but in the southern hemisphere cover the storm track belt around Antarctica. However, the differences do not grow indefinitely. Figure 9b shows the differences between the control (NoSCAT) and SCAT assimilation after 10 days of assimilation. Typical differences are a few tens of meters (a few mb) and maximum differences are approximately 140 m, i.e., about 18 mb.

An important question is whether these changes are beneficial. This is not easy to determine. Possible methods of assessment are (a) to compare the fit of the FGAT from the SCAT and NoSCAT runs to the scatterometer data, (b) to compare the fit of other data to the FGAT from the SCAT and NoSCAT runs, or (c) to compare meteorological or wave-model forecasts started from the analyses. The latter approach has been tried using meteorological forecasts (see below) but wave forecasts have not been attempted in this study.

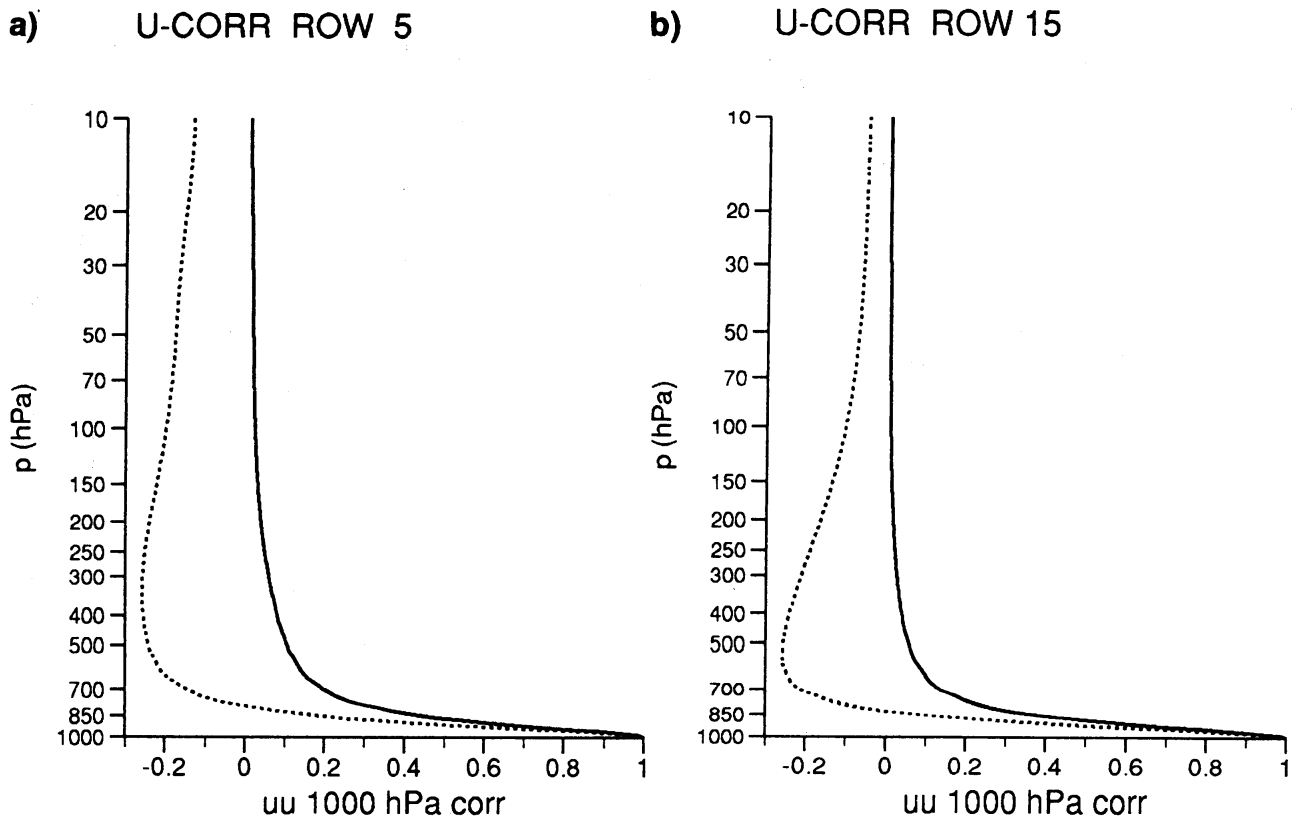


**Figure 7.** Vertical correlation function in the OI system used to extend surface wind increments in the vertical: (a) mid latitudes; (b) tropics. Continuous line: non-divergent wind component covariance. Dotted line: divergent covariance (from *Undén* [1989]).

As illustrated in Figures 2-5, the synoptic detail possessed by scatterometer data is significantly greater than in the ECMWF model fields and, on a 100 km scale, scatterometer errors are random rather than correlated [*Stoffelen and Anderson, 1995; Chapters II and IV*]. We do expect, therefore, an impact from scatterometer data on the smaller spatial scales and, as a consequence, also on the shorter time scales. To measure the improvement on these scales in the ECMWF analysis/forecasting system, the same experiments have been verified by direct comparison with observations. In Table 2 we show a comparison between departure statistics of scatterometer minus FGAT winds for the experiment SCAT and the control NoSCAT, averaged over twelve 6-hour windows near the end of the experiment. Vector root-mean-square (RMS) departures are improved by approximately 5%. Because of the polar orbit each location is generally sampled twice a day, therefore passes 6 hours apart are generally well separated geographically and passes 12 hours apart fall in similar geographical areas. The departure statistics are therefore a verification of information from the scatterometer assimilated at least twelve hours earlier.

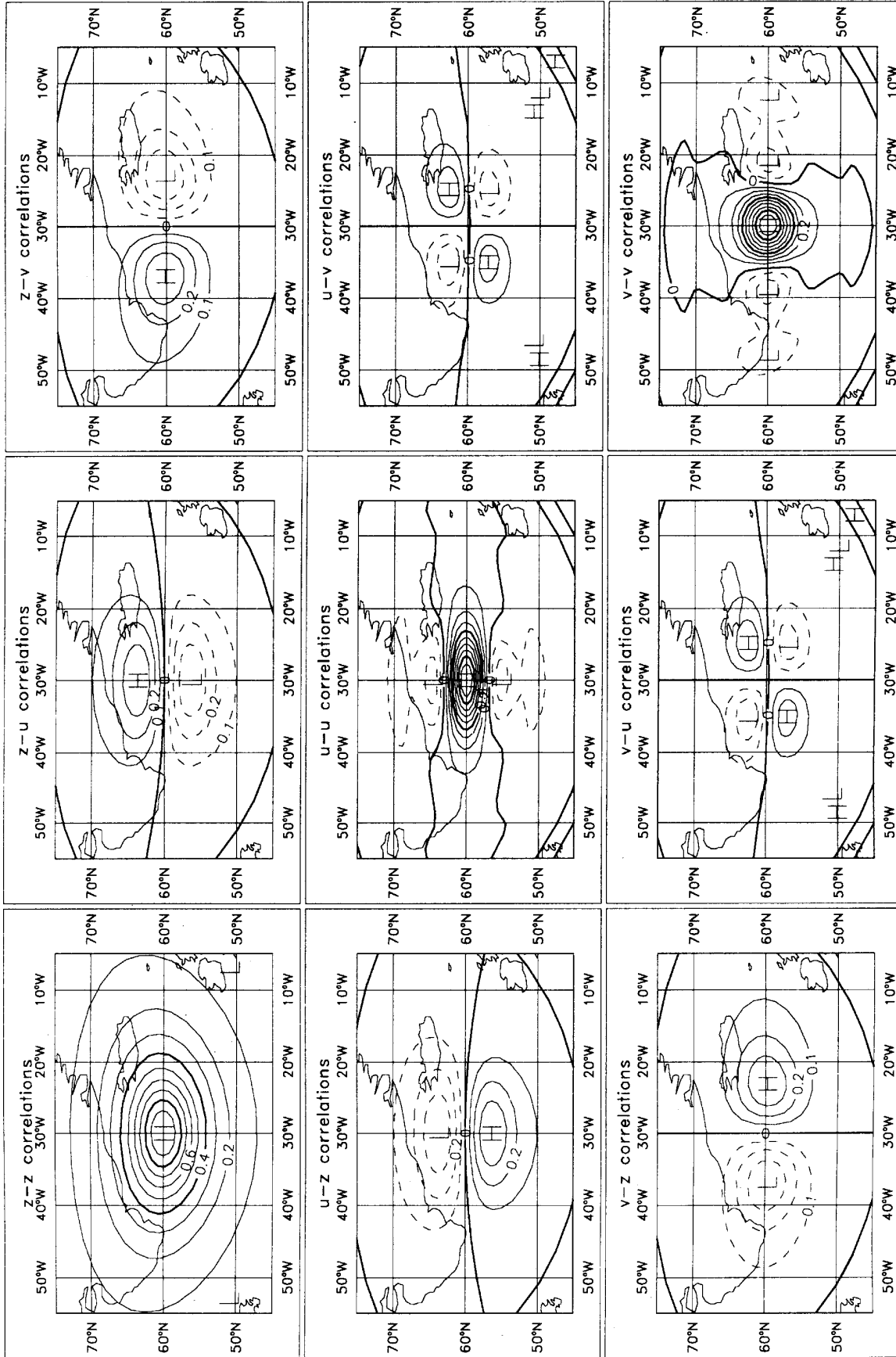


**Figure 8.** The correlation function used to extend forecast error in the horizontal. From the ECMWF Research manual I: Data Assimilation, P. Lönberg and D. Shaw [1987]. Forecast error is computed for both components of the wind ( $u, v$ ). The  $u$ -component error is not only correlated with a  $u$ -component nearby, but also with a  $v$ -component error and height ( $z$ ) error (by geostrophy). The correlation functions depend on latitude by similarity transformation (the spatial scale for the tropics is twice that shown here, and is 1.2 times larger in the southern hemisphere).

**Table 2.** Comparison of PRESCAT Winds With Experiment SCAT and NoSCAT

FGAT SCAT 930324:12, Twelve 6-hour steps							
Node	Number ( $> 4 \text{ m s}^{-1}$ )	Bias (degrees)	SD (degrees)	Number all speeds	Bias ( $\text{m s}^{-1}$ )	SD ( $\text{m s}^{-1}$ )	Vector RMS ( $\text{m s}^{-1}$ )
1	10089	-0.41	31.15	13203	-0.61	1.77	3.92
3	10109	0.42	24.49	13398	-0.59	1.72	3.30
5	10137	0.73	21.90	13560	-0.48	1.72	3.10
7	10008	1.01	20.48	13627	-0.39	1.77	3.04
9	9849	1.13	19.76	13547	-0.30	1.81	3.05
11	9722	1.47	19.10	13462	-0.26	1.83	3.04
13	9546	1.28	18.96	13291	-0.29	1.83	3.02
15	9306	1.69	18.65	12986	-0.32	1.84	3.01
17	9118	1.87	18.52	12680	-0.32	1.86	3.02
19	8963	2.37	19.62	12316	-0.33	1.85	3.03
FGAT NoSCAT 930324:12, Twelve 6-hour steps							
Node	Number ( $> 4 \text{ m s}^{-1}$ )	Bias (degrees)	SD (degrees)	Number all speeds	Bias ( $\text{m s}^{-1}$ )	SD ( $\text{m s}^{-1}$ )	Vector RMS ( $\text{m s}^{-1}$ )
1	10040	-0.89	32.14	13203	-0.64	1.88	4.06
3	10054	-0.11	25.75	13398	-0.61	1.83	3.46
5	10097	0.34	22.79	13560	-0.51	1.83	3.24
7	9971	0.80	21.47	13627	-0.42	1.87	3.19
9	9833	0.99	21.06	13547	-0.34	1.91	3.20
11	9743	1.37	20.60	13462	-0.30	1.94	3.20
13	9564	1.40	20.48	13291	-0.33	1.93	3.18
15	9310	1.70	20.08	12986	-0.36	1.93	3.17
17	9078	1.94	19.91	12680	-0.36	1.95	3.19
19	8941	2.33	20.59	12316	-0.37	1.94	3.20

For all nodes, the bias and SD of the FGAT and scatterometer wind differences and the vector RMS differences are smaller in SCAT than in NoSCAT, indicating that the SCAT FGAT has a better quality.

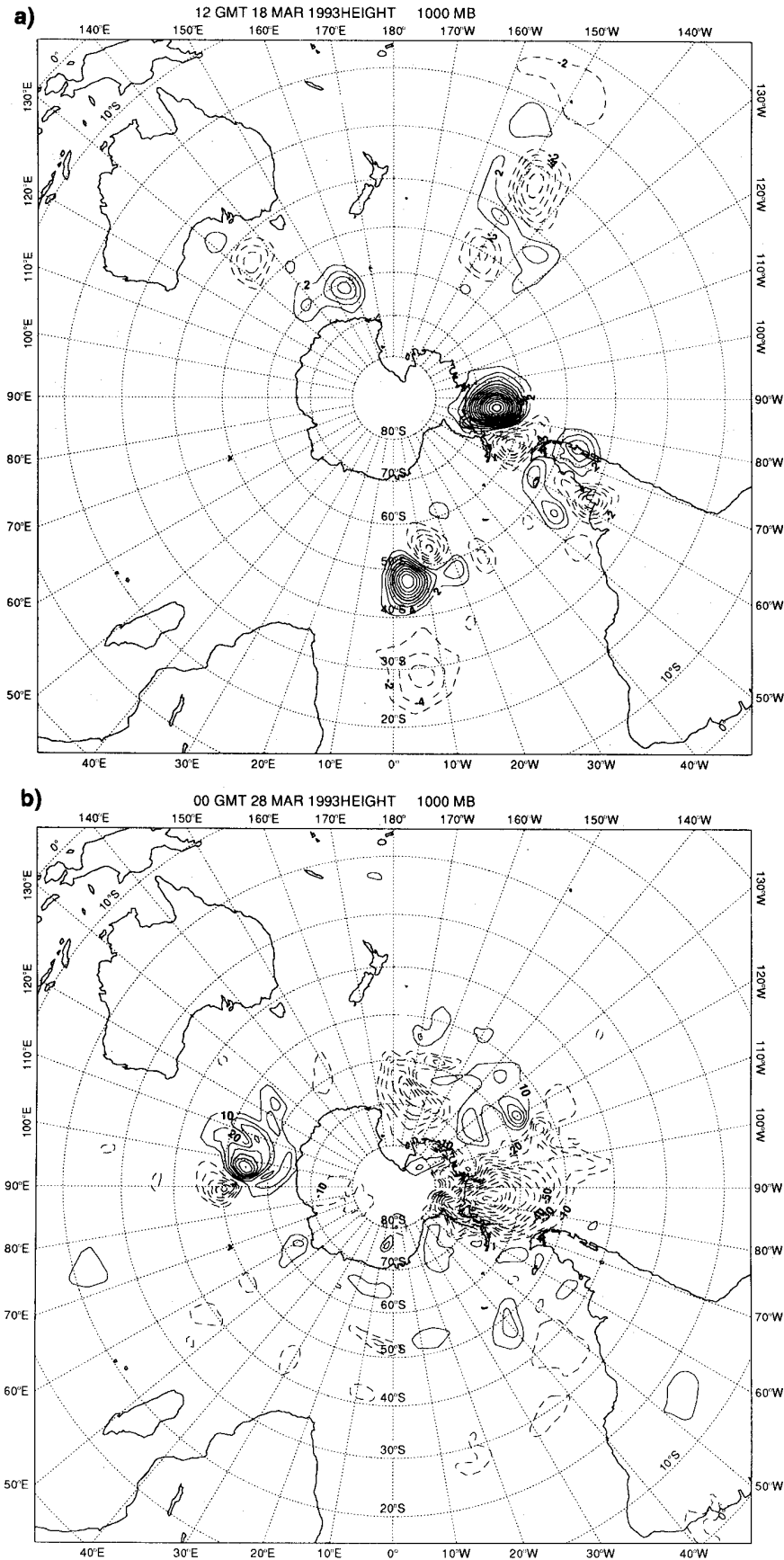


**Figure 9.** Differences between an analysis in which PRESCAT winds are assimilated (SCAT) and a control (NoSCAT) in which they are not used, (a) after the first assimilation, (b) after 10 days of assimilation. Field shown is the height of the 1000-hPa surface. In (a) the contour interval is 2 m; in (b) 10 m. Impact increases with time.



**Table 3.** The Difference Between Vector RMS Departures of SATOB and FGAT Winds for Experiments SCAT and NoSCAT

SCAT	NoSCAT
4.41 m s <sup>-1</sup>	4.46 m s <sup>-1</sup>

†Note the small upper air improvement by inclusion of scatterometer winds.

To verify the improvement in the upper-air first guess we made similar comparisons between SCAT and NoSCAT for SATOB winds (mainly in the subtropics and tropics), as in table 3. Again an improvement in the vector RMS departure was found, greater than 1%. The improvement was greatest in the southern hemisphere, and of similar magnitude both below and above the 700-mb level. Furthermore, we found that using FGAT from experiment SCAT in the ambiguity removal generally gave a better wind field than did FGAT from NoSCAT (one specific example is shown in Figure 4).

To be able to improve short-range forecasts is very important for severe weather prediction, and to improve forecasts of near-surface winds is useful for ocean circulation and wave models.

### 3.3. Medium-Range Forecast Impact

In this section, a height-anomaly-correlation skill index is used for interpretation of the impact of scatterometer data in the ECMWF analysis/forecasting system. Most of the energy in the atmosphere is in the larger spatial scales and it is to these scales that this skill index is most sensitive. The larger spatial scales are important for the medium-range forecast skill.

For the eleven days from 18 to 28 March, 10-day forecasts were made every day and compared with the corresponding operational forecasts (denoted control). All model parameters were the same in these two sets of experiments. The only differences were the analyses from which the forecasts were made: one was the control without scatterometer data (NoSCAT), and the other had assimilated scatterometer data (SCAT). Height anomaly correlations of both forecasts with the operational (i.e., NoSCAT) analyses were then calculated. Anomalies were calculated by subtracting a seasonal climatological height from the forecast and analyzed height fields before the correlation was made. An ensemble average over the 11 forecasts is given in Figure 10, which shows that assimilation of scatterometer data has had no beneficial impact on the forecasts in the sense that the anomaly correlations are, on average, the same in forecasts initiated from NoSCAT and SCAT. On the basis of forecast height anomaly correlations there is no advantage for medium-range forecasts in assimilating scatterometer data. A measure of the scatter of these forecasts is shown in Figure 11 for a forecast lead time of 72 hours. From the 11 forecasts

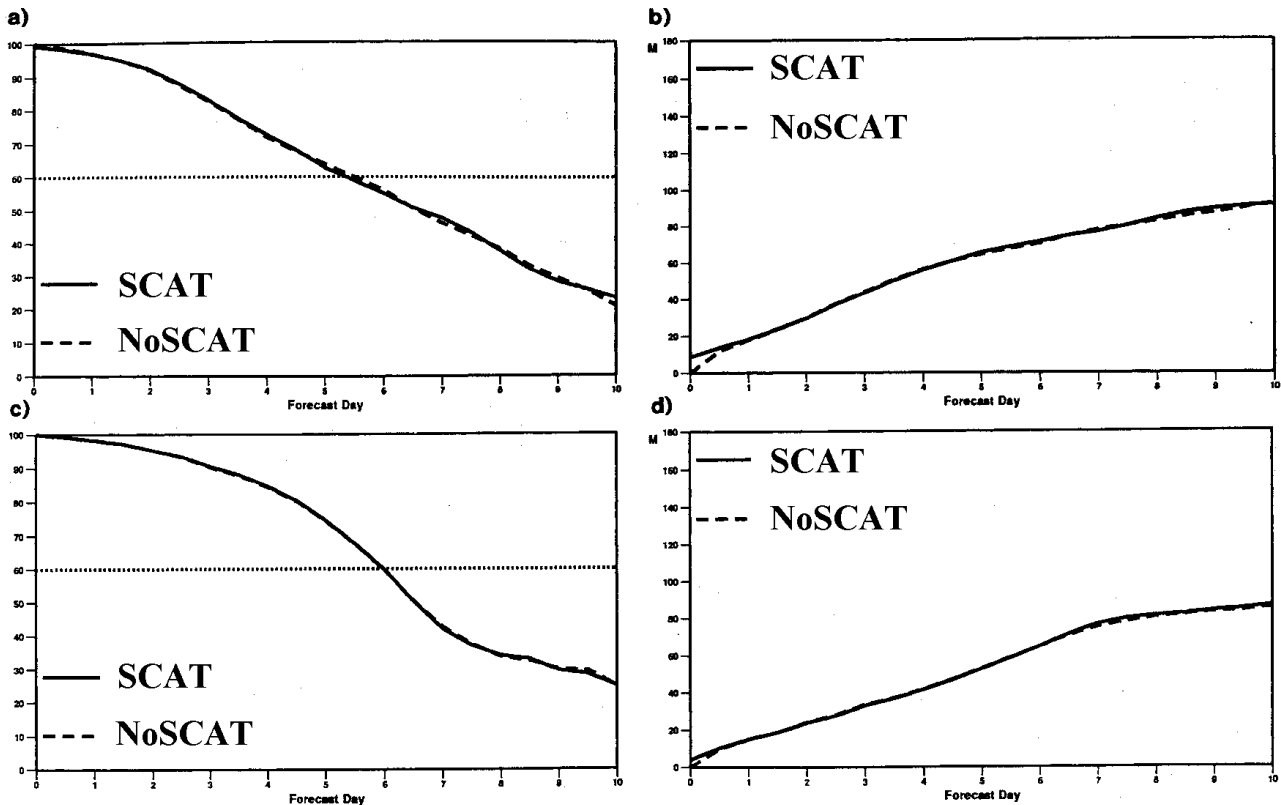


**Figure 10.** (a) Anomaly correlation and (b) RMS errors in the northern hemisphere for an average over the 11 forecasts initiated from SCAT and NoSCAT analyses. Similarly, (c) and (d) are for the southern hemisphere. The statistics are derived from the operational analysis (NoSCAT).

for this period, we found examples when SCAT was slightly better, not much different, or slightly worse. The differences occurred mainly in the southern hemisphere.

The neutral impact of scatterometer data in the ECMWF medium-range forecasts contrasts with the clearly beneficial impact obtained with the UK Meteorological Office’s forecasting system [Bell, 1994]. However, by coincidence, for this particular period in March 1993 the ECMWF 5-day forecasts, without scatterometer data, had approximately 10% better RMS verifications of 500 hPa height against the ECMWF analyses than the UK Meteorological Office’s forecasting system not using the data. The average improvement of 4% in the Meteorological Office 5-day forecasts when using scatterometer data is therefore insufficient to match the quality of the ECMWF 5-day forecasts. It is, therefore, harder to show a positive impact in the ECMWF system over this particular period. From statistics based on daily monitoring of forecast model quality at ECMWF we observed that the 10% difference is atypical and that, usually, the ECMWF and UKMO forecasts are closer. System and situation dependency has occurred frequently in the past in comparative studies of observation system impact.

In a second series of experiments we investigated the impact of scatterometer data in a

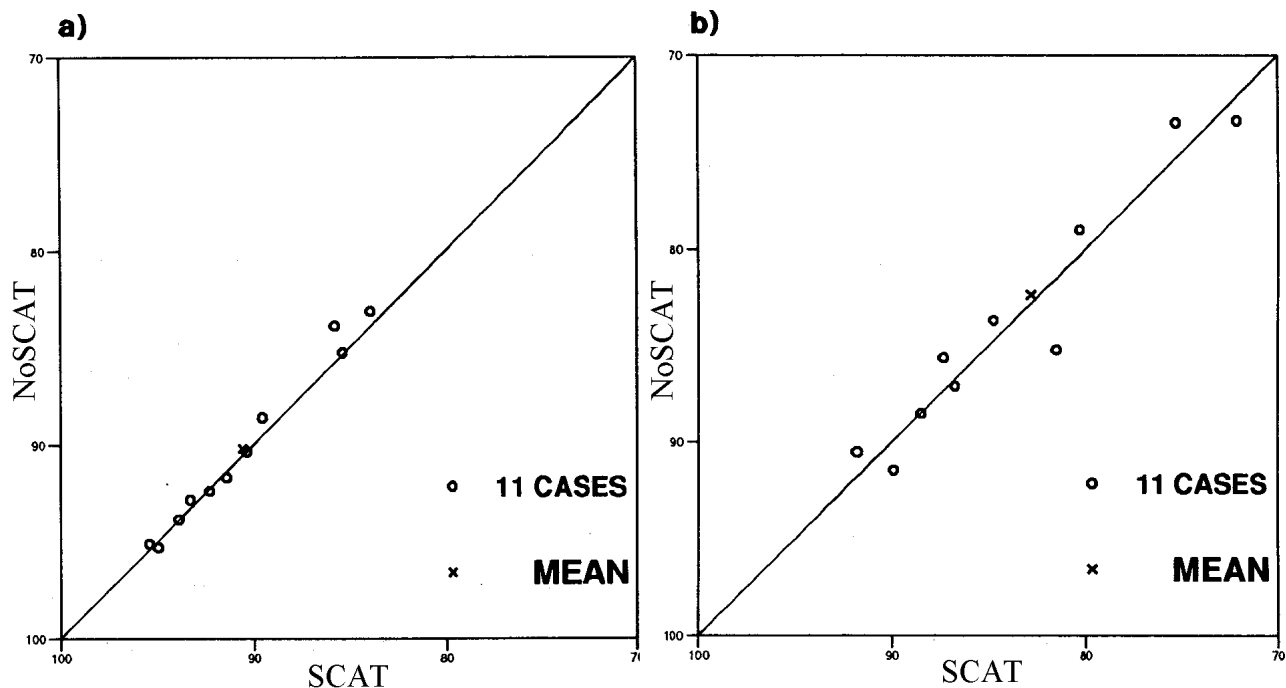


**Figure 11.** (a) Scatter plot of the 11 individual anomaly correlations in the northern hemisphere ( $20^{\circ}\text{N}$ - $90^{\circ}\text{N}$ ) for 72-hour forecasts initiated from SCAT and NoSCAT analyses. (b) As (a), but for the southern hemisphere ( $90^{\circ}\text{S}$ - $20^{\circ}\text{S}$ ).

degraded data assimilation system. Four separate analyses were made and from them forecast experiments were done. The first two analyses are NoSCAT/SATEM, the control without PRESCAT winds, and SCAT/SATEM which assimilated PRESCAT winds. These experiments are similar to those for March discussed above (NoSCAT and SCAT), but for a different time period. Moreover, the horizontal sampling of the model is reduced to T106 spectral truncation (125 km) and it has 19 rather than 31 levels in the vertical. Satellite temperature data, SATEMs, from the TOVS sounder [Smith *et al.*, 1979] contribute positively to the forecast scores for the southern hemisphere. SATEMs mainly define the larger scales of the analysis. SATOBs are made by tracking clouds on the imagery from geostationary satellites. They have much less impact in the southern hemisphere than have SATEMs. Two further analyses were made, removing both SATEMs and SATOBs. In one of them scatterometer winds were assimilated (SCAT/NoSAT), but not in the other (NoSCAT/NoSAT).

Average anomaly correlations in the six forecasts from these analyses, one for each day from 26 April to 1 May, are shown in Figure 12a for SCAT/SATEM and NoSCAT/SATEM, and in Figure 12b for SCAT/NoSATEM and NoSCAT/NoSATEM. Again the figures show comparisons at 1000 hPa, i.e., near the surface, but the results at 500 hPa are similar. In the case when SATEMs were used, the results are consistent with experiments SCAT and NoSCAT in that, on average, the PRESCAT winds do not lead to

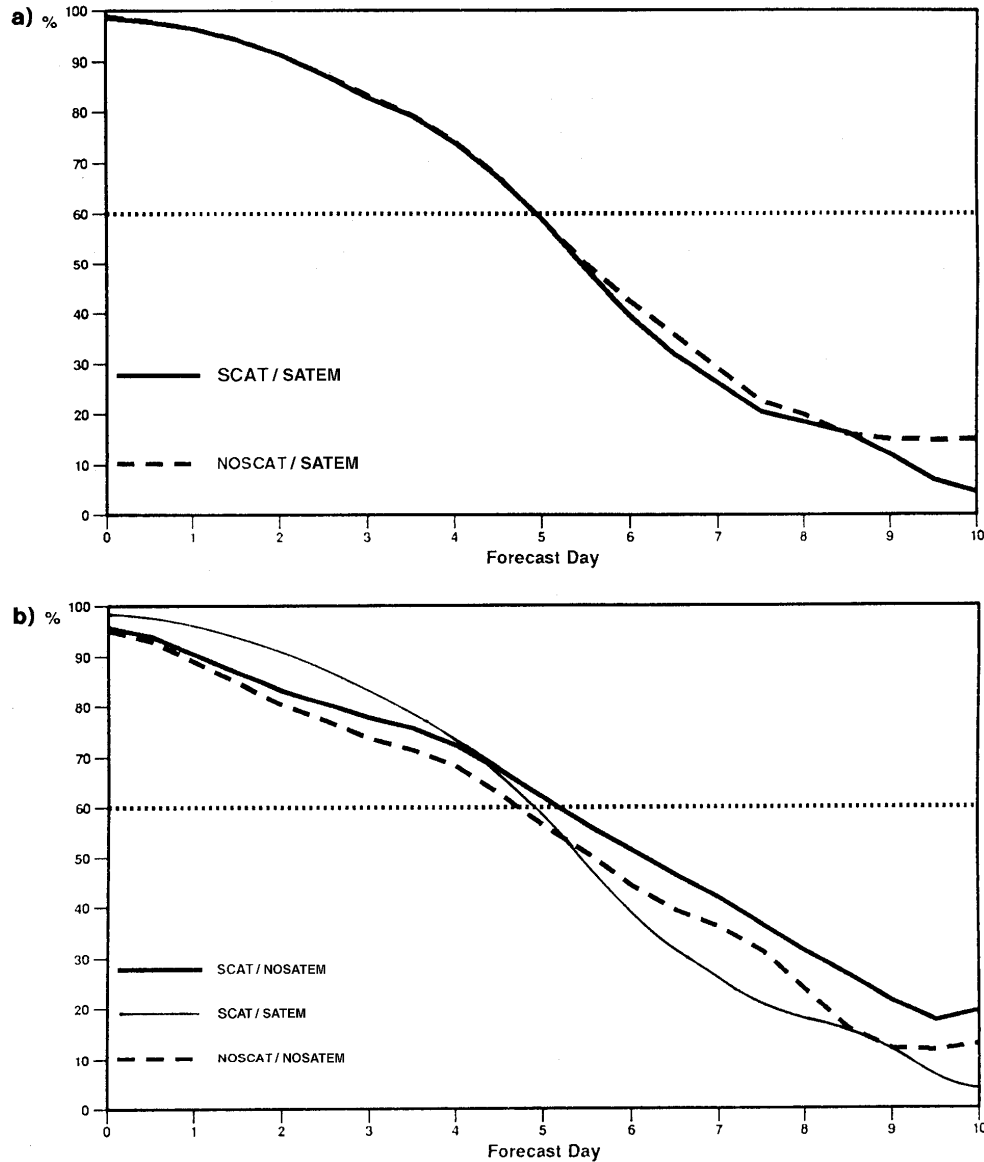


**Figure 12.** (a) As for Figure 10, but the averages are over the six forecasts from 26 April to 1 May, for NoSCAT/SATEM and SCAT/SATEM. The correlations are made with the operational analyses. (b) As for (a), but for experiments SCAT/NoSATEM and NoSCAT/NoSATEM. In this case, assimilation of the scatterometer winds from PRESCAT leads to improved forecasts. For comparison SCAT/SATEM is also shown.

improved forecasts. In the case when SATEMs were not used, however, the assimilation of the PRESCAT winds does lead to a significant improvement in the forecasts for the southern hemisphere. Thus, part of the lack of impact of the scatterometer in SCAT and SCAT/SATEM is because there is significant redundancy between the scatterometer and the other observing systems. If the normal observing system is degraded, for example by the removal of SATEMs (SATOBS are probably not so important), then the scatterometer will have a useful role, although, as might be expected, it will not be able to compensate fully for

the loss of the thermal data provided by SATEMs throughout the atmosphere. Results similar to these have been found by *Baker et al.* [1984] and *Atlas et al.* [1985] for scatterometer data from the 1978 SEASAT mission.

### 3.4. Validation of the OI Data Assimilation System

When data are not used actively in the analysis they can be used to verify the analysis and subsequent forecasts, as is shown in this section for scatterometer winds. Figure 13 shows the variance of the error in the wind vector of the ECMWF model as computed over the oceans using a fixed set of scatterometer data with an estimated wind error variance of  $5 \text{ m}^2 \text{ s}^{-2}$ . The operational ECMWF model (with no scatterometer information included) is verified at different forecast times. After the OI procedure an initialization procedure is run to filter out noise generated by OI (gravity waves). The verification of the initialized analyses (IA) and analysis (AN) are almost identical showing that the initialization filter has little effect.

The first major point to note from Figure 13 is the large increase in variance when a 6-hour forecast is interpreted as being valid at a time 2.5 hours earlier or later, compared to using a forecast at the appropriate time (FGAT). This means that using FGAT is important both for ambiguity removal (as was illustrated in section 2) and for data assimilation. If FGAT is not used for the latter, 15% of the variance of the increments will be due to a timing error and so will be incorrect. The resulting errors made in the analysis will be spatially coherent.

A second important point to note is the fact that the observations used in the analyses adversely affect the first-guess 10-m wind field over the oceans; the vector error variance of the first guess is  $0.5 \text{ m}^2 \text{ s}^{-2}$  (approx. 10%) lower than the vector error variance of the analyses, verified at the same locations. The average analysis minus first-guess difference (increment) over the oceans was computed to be  $2.3 \text{ m}^2 \text{ s}^{-2}$ . So, on average a part,  $0.9 \text{ m}^2 \text{ s}^{-2}$  (approx. 40%), of this increment proves to be correct, and a part,  $1.4 \text{ m}^2 \text{ s}^{-2}$ , proves wrong. In the previous section we demonstrated the positive effect of the assimilation of SATEMs and SATOBs, and scatterometer data. Here we see that the analysis increments are not necessarily beneficial in the full analysis domain, and may even be detrimental. This can be explained by the flow-independent structure functions that spread observational information in the horizontal and vertical, and project mass information on wind and vice versa (see Figures 7 and 8). As a consequence and particularly over the oceans in the southern hemisphere, the ECMWF 10-m wind analysis will be affected mainly by satellite temperature soundings. This vertical mass-to-wind projection, although valid, on average, over many cases, can be detrimental in specific cases. A case-specific and thereby flow-dependent projection would be more appropriate. However, Figure 13 also indicates that

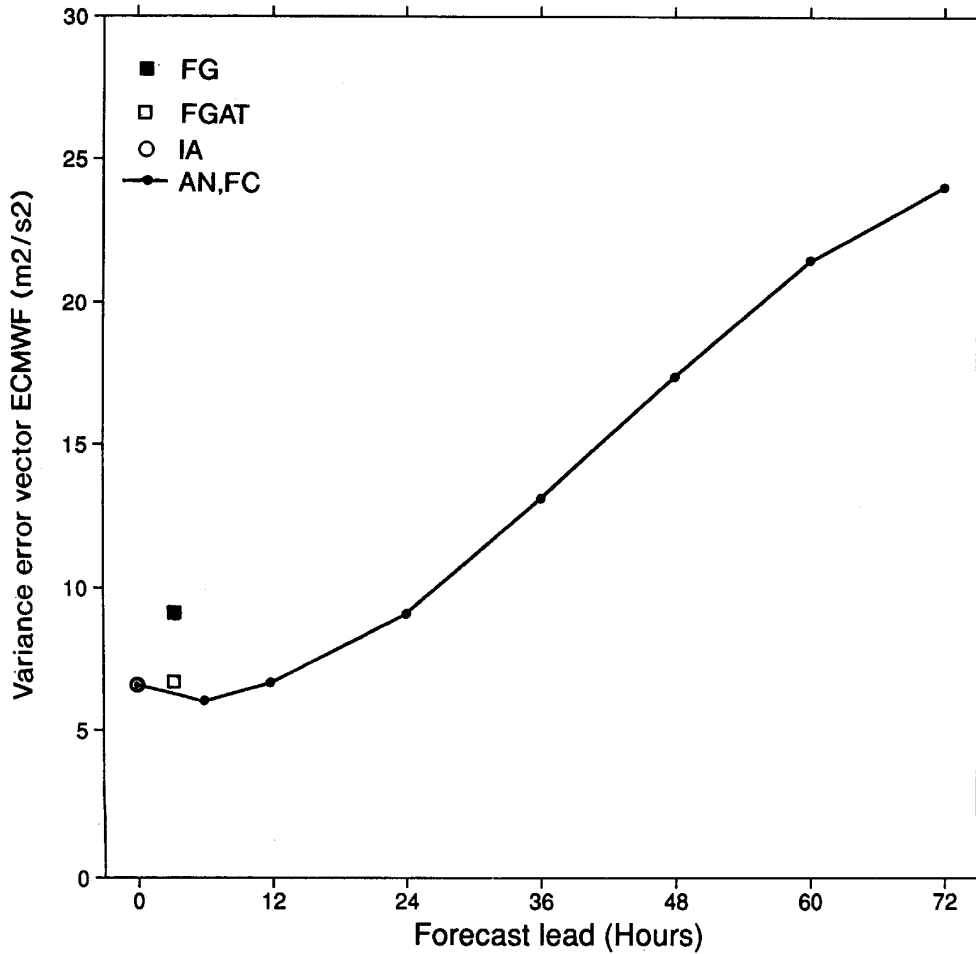


**Figure 13.** Wind vector error variance of the ECMWF model at a fixed set of scatterometer nodes. The wind vector error variance of the scatterometer observations was estimated to be  $5 \text{ m}^2 \text{ s}^{-2}$ . The solid line represents from left to right the analysis, FG, and forecasts with different lead times (lead 0 corresponds to the analysis and a lead time of 6 hours to the FG). The symbol O is the initialized analysis. For this set, the time difference between scatterometer observations and the corresponding field values is less than 1 hour. The squares represent verification against another set of scatterometer winds that are between 2 and 3 hours from the FG verification time; solid squares FG and open squares FGAT.

during the 6-hour forecast the 10-m winds are again properly balanced (baroclinically) with the upper-air dynamics and become more realistic.

In section 3.3, we suggested that the analysis of scatterometer surface winds probably also adversely affects the upper-air mass field for the same reason. As a result, the mass corrections induced by the scatterometer would contradict the SATEM mass analysis-increments. Conversely, surface wind increments induced by SATEMs will contradict scatterometer wind information. It is, therefore, worthwhile that further investigation of these effects be carried out to make observational systems more complementary.

Recent studies show that in a 4D-Var system baroclinic structures can be enforced by assimilating surface (i.e., scatterometer) data [Thépaut *et al.*, 1993], by using the time trajectory of the forecast model. The fact that in a 6-hour forecast the surface balance is restored, indicates that this is a promising technique which, potentially, can overcome a weakness in 3D methods.

#### 4. Variational Methods

A variational assimilation scheme [Le Dimet and Talagrand, 1986] consists in the minimization of a cost function, i.e.,

$$\mathfrak{J} = \mathfrak{J}_O + \mathfrak{J}_B + \mathfrak{J}_C \quad (3)$$

where  $\mathfrak{J}_O$  is a weighted quadratic term which measures the differences between the estimated control variables and the observations, and  $\mathfrak{J}_B$  is a quadratic term measuring the difference between the estimated control variables and the background field.  $\mathfrak{J}_C$  is a small term expressing physical constraints on the atmospheric state. The term  $\mathfrak{J}_O$  describes the observation error characteristics of all observations and is the sum of the contributions of each individual observation. For each node the scatterometer penalty function, denoted  $\mathfrak{J}_O^{\text{SCAT}}$ , will be ambiguous where two penalty minima will exist corresponding to the two solutions resulting from the inversion. Furthermore, it was shown by Stoffelen and Anderson [1995; Chapter IV] that the total observation error of the unambiguous wind is well characterized by a normal distribution around the true wind components with a standard deviation of error of around  $1.7 \text{ m s}^{-1}$ . In this way the observation error characteristics are well defined in the wind domain. We will show in this section that the representation of the total observation error in the  $\mathbf{s}^0$  domain is much more complex due to the highly nonlinear relationship between  $\mathbf{s}^0$  and wind, and conclude that it is therefore more practical to define  $\mathfrak{J}_O^{\text{SCAT}}$  in the wind domain. At the end of the section we discuss the ambiguity in  $\mathfrak{J}_O^{\text{SCAT}}$  and show that the meteorological balance constraints incorporated in the  $\mathfrak{J}_B$  term result implicitly in a beneficial ambiguity removal of scatterometer data in 3D-Var.

Stoffelen and Anderson [1995; Chapter II] showed that  $\mathbf{s}^0$  for each node depends, essentially, on two parameters. Consequently the distribution of  $\mathbf{s}^0$  triplets in the 3D measurement space is located around a 2D surface, which is cone shaped. The scatter of triplets around this cone surface is close to the instrument accuracy (5%). In the wind domain such an error corresponds to a  $0.5 \text{ m s}^{-1}$  vector RMS error, i.e., it is very small.

Following Lorenc [1988], we may specify the contribution of scatterometer data to the cost function in the form

$$\mathfrak{J}_O^{\text{SCAT}} = -2 \ln\{p(\mathbf{s}^0 | \mathbf{V})\} \quad (4)$$

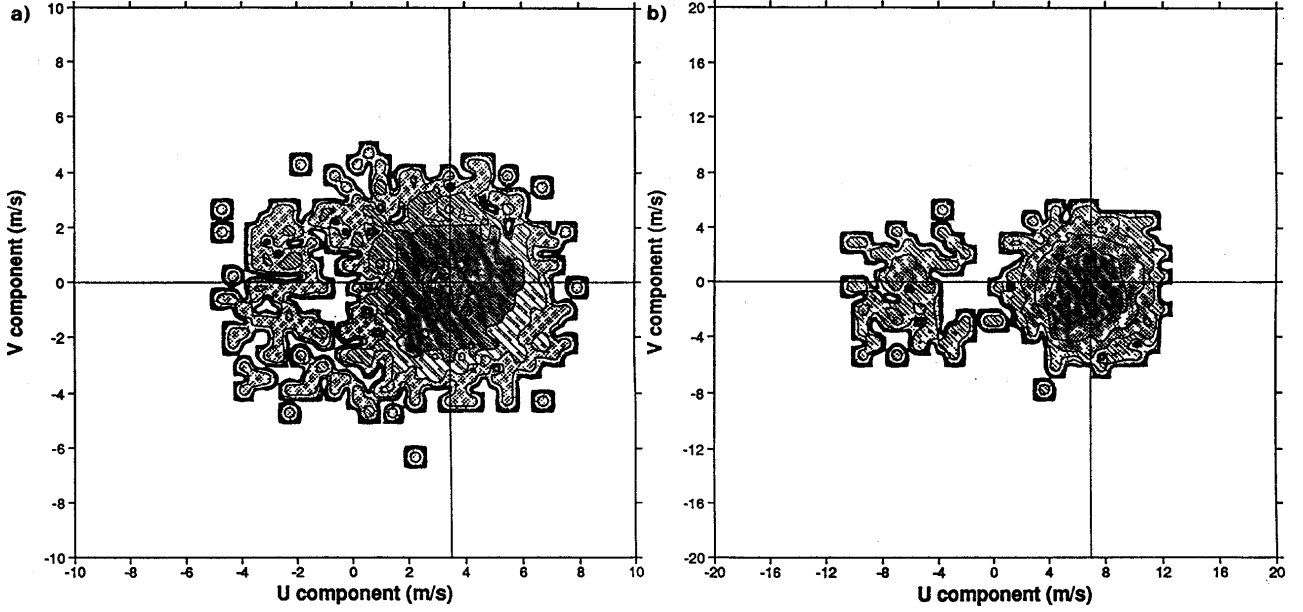


**Figure 14.** Monte Carlo simulations as explained in the text. The solution points are calculated with  $\mathfrak{S}_O^{\text{SCAT}} = \mathfrak{S}_{O,1}^S \mathfrak{S}_{O,2}^S [(\mathfrak{S}_{O,1}^S)^4 + (\mathfrak{S}_{O,2}^S)^4]^{-1/4}$ . In (a) the true wind speed  $V = (3.5, 0)$  in  $\text{m s}^{-1}$ , and noise  $\mathbf{e}_R = 2 \text{ m s}^{-1}$  and  $\mathbf{e}_B = 2 \text{ m s}^{-1}$ . The mean retrieved  $u$ -component in (a) is  $3.25 \text{ m s}^{-1}$ . Panel (b) is for  $V = (7, 0) \text{ m s}^{-1}$ , and the anomalously high noise of  $\mathbf{e}_B = 4 \text{ m s}^{-1}$ . The mean retrieved  $u$  is  $6.44 \text{ m s}^{-1}$  with standard deviations of  $3.29 \text{ m s}^{-1}$  for  $u$  and  $1.84 \text{ m s}^{-1}$  for the  $v$  component. 2000 simulated scatterometer and background winds were used.

where  $\mathbf{V}$  is the estimate for the local wind vector (control variable) and where

$$p(\mathbf{s}_O^0 | \mathbf{V}) = \int_{\mathbf{s}_S^0} p(\mathbf{s}_O^0 | \mathbf{s}_S^0) p(\mathbf{s}_S^0 | \mathbf{V}) d\mathbf{s}_S^0 \quad (5)$$

The integral is over  $\mathbf{s}_S^0$ , i.e., the cone as described by the transfer function, and the expression  $p(\mathbf{a} | \mathbf{b})$  denotes the possibility of  $\mathbf{a}$ , given  $\mathbf{b}$ . The first term in the integral should express the scatter observed at right angles to the cone's surface, which scatter is very small (uncertainty about the cone's location should also be included in this expression). The second term should express knowledge of the errors made when interpreting the two parameters on the surface (speed and direction), corresponding to  $\mathbf{s}_S^0$ , as the 'true' wind vector, and of the representativeness error, i.e., the spatial and temporal scales resolved by the retrieved wind, but not resolved by the NWP model. This error constitutes the main part of the total observational error, which, in the wind domain, was easy to describe.

Now, one could attempt to assimilate  $\mathbf{s}_O^0$  directly into a NWP model, and project the transfer function and representativeness wind errors onto  $\mathbf{s}_S^0$ . Because the  $\mathbf{s}_O^0$  to wind relationship, as represented by the curved surface of the cone, is highly nonlinear the projection of wind errors onto the cone in the 3D measurement space is a complex problem. Certainly plane approximations using only  $\partial \mathbf{s}_O^0 \setminus \partial \mathbf{V}$  will be inappropriate. Using the



curvature, i.e.,  $\partial^2 \mathbf{s}^0 \setminus \partial V^2$ , should be better, although still not perfect, and will certainly result in an algorithm of substantial mathematical complexity and computational cost. Moreover, in an attempt to strive for mathematical elegance, one might forget that the uncertainties regarding our knowledge of  $\partial^2 \mathbf{s}^0 \setminus \partial V^2$  may be a limiting factor.

Alternatively, one could try to formulate the problem in terms of wind. For this purpose, we would have to make some approximations concerning Eq. (5). As mentioned above, we can identify accurately the most likely ‘true’ position of a measured  $\mathbf{s}^0$  triplet on the cone’s surface, and this inversion only results in a small contribution to the overall wind error of scatterometer winds, and so may be neglected. Therefore, replacing  $p(\mathbf{s}^0_{\text{O}} | \mathbf{s}^0_{\text{S}})$  by  $p(\mathbf{s}^0_{\text{R}} | \mathbf{s}^0_{\text{S}})$ , with  $\mathbf{s}^0_{\text{R}}$  as derived from the inversion, we have a valid approximation. The retrieval has multiple solutions  $\mathbf{s}^0_{\text{R},i}$  because of the 180° ambiguity, and therefore the first term in the integral will be a sum of  $p(\mathbf{s}^0_{\text{R},i} | \mathbf{s}^0_{\text{S}}) / n$ , with  $i = 1, \dots, n$ , the solution index where  $n = 2$ . *Stoffelen and Anderson* [1995; Chapter II] found that the two solutions have almost equal probability and therefore we have assumed no skill in the distinction of the different  $\mathbf{s}^0_{\text{R},i}$ , i.e., all solutions have probability  $1/n$ .

The neglect of  $\mathbf{s}^0$  measurement errors in 3D  $\mathbf{s}^0$ -space allows a further replacement of  $p(\mathbf{s}^0_{\text{R},i} | \mathbf{s}^0_{\text{S}})$  with a Kronecker delta function of the form  $\mathbf{d}(\mathbf{s}^0_{\text{R},i} - \mathbf{s}^0_{\text{S}})$ . After integration and using the transfer function to map  $\mathbf{s}^0_{\text{R},i}$  onto the retrieved winds  $\mathbf{V}_{\text{R},i}$ , Eq. (5) reduces to

$$p(\mathbf{s}^0_{\text{O}} | \mathbf{V}) = p(\mathbf{V}_{\text{R},1} | \mathbf{V}) / 2 + p(\mathbf{V}_{\text{R},2} | \mathbf{V}) / 2$$

As such, the formulation of the problem in wind space only needs a proper characterization of the sum of transfer-function error and the representativeness error in wind space. We may assume that

$$p(\mathbf{V}_{\text{A}} | \mathbf{V}) = p(\mathbf{V} | \mathbf{V}_{\text{A}}) = N(\mathbf{V}_{\text{A}}, \mathbf{e}_{\text{R}})$$

for an unambiguous scatterometer wind  $\mathbf{V}_{\text{A}}$ , i.e., normally distributed around the components of  $\mathbf{V}_{\text{A}}$  with error  $\mathbf{e}_{\text{R}}$ . Similarly, for the ambiguous solutions we may write

$$p(\mathbf{s}^0_{\text{O}} | \mathbf{V}) = N(\mathbf{V}_{\text{R},1}, \mathbf{e}_{\text{R}}) / 2 + N(\mathbf{V}_{\text{R},2}, \mathbf{e}_{\text{R}}) / 2$$

From Eq. (4) we can derive the scatterometer cost function, which will not be quadratic, particularly when

$$\|\mathbf{V}_{\text{R},1} - \mathbf{V}_{\text{R},2}\| \leq \|\mathbf{e}_{\text{R}}\|$$

Moreover, in these cases we find only one minimum at  $\mathbf{V} = 0$ .

An alternative analytic formulation can be found, that describes a conditional functionality in terms of the penalty function  $\mathfrak{S}_{\text{O}}^{\text{SCAT}}$

$$\mathfrak{J}_0^{\text{SCAT}} = \left[ \frac{\prod_i^2 K_i}{\sum_i^2 K_i} \right]^{\frac{1}{P}} \quad (6)$$

where  $P = 4$ ;  $K_i = [\mathfrak{J}_{0,i}^S(\mathbf{V}_{R,i})]^P$ , and  $\mathfrak{J}_{0,i}^S$  characterizes the estimated scatterometer wind error for one single solution, and is considered to be quadratic, as before. For low wind speeds this  $\mathfrak{J}_0^{\text{SCAT}}$  cost function also has two minima located at  $\mathbf{V}_{R,1}$  and  $\mathbf{V}_{R,2}$ , and a quadratic dependency on  $\mathbf{V}$  in almost the entire speed domain, except close to  $\mathbf{V} - \mathbf{V}_{R,1} = \mathbf{V} - \mathbf{V}_{R,2}$ . Therefore, this formulation has more symmetry around its minima. For  $P < 4$  we have a weaker gradient towards the minima, or in other words, exact ambiguity removal will be less of a constraint and intermediate solutions will be more likely. This is also the case for the cost function that was derived in the previous paragraph. From our experience with ambiguity removal we believe that a strong constraint for ambiguity removal is more appropriate; but this could be tested further.

To investigate the statistical consequence of the cost-function formulation, we performed Monte Carlo simulations. The terms  $\mathbf{V}_{R,1}$  and  $\mathbf{V}_{R,2}$  ( $= -\mathbf{V}_{R,1}$ ), and a background wind  $\mathbf{V}_B$ , we simulated for a given  $\mathbf{V}$  using respectively a Gaussian wind-component error  $\mathbf{e}_R$  for the scatterometer, and  $\mathbf{e}_B$  for the background wind (in fact  $\mathbf{e}_B$  characterizes the accuracy of all available information, except the observation under investigation). Figure 14a shows a result when minimizing Eq. (3) with the above scatterometer cost function, for 2000 trials. Ambiguity removal is generally successful for a speed as low as  $3.5 \text{ m s}^{-1}$ . Figure 14b shows the distribution of solutions for 2000 simulations, but in this case  $\mathbf{e}_B = 4 \text{ m s}^{-1}$  and  $V = 7 \text{ m s}^{-1}$ . As expected, it can be seen that ambiguity removal is less successful with reduced supporting background information. The statistical difference between the two proposed cost functions is marginal and, therefore, because of its more symmetric and quadratic behavior the functionality in Eq. (6) may be more desirable to use in a minimization. With this equation, we have arrived at a practical and accurate solution for the variational assimilation of scatterometer observations.

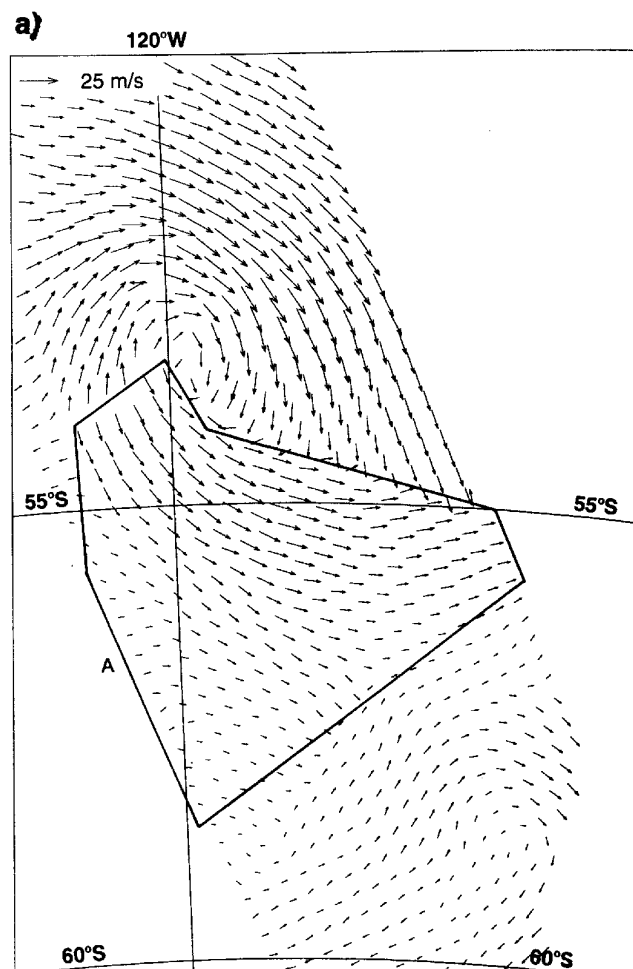
Preliminary results with a 3D-Var analysis system show that ambiguity removal is done accurately, and a large-scale compromise is easily found in complicated situations, as illustrated in Figure 15 (see also *Stoffelen et al [1993]*).

## 5. Summary and Conclusions

We have developed an ambiguity-removal scheme, called PRESCAT, as an alternative to CREO and SLICE, based on the following guidelines,

- (i) that information on wind-direction retrieval skill is an important input to ambiguity removal,

**Figure 15.** (a) ESA winds at 08 UTC 17 August 1993 over the south China Sea. On the opposing page, (b) ECMWF forecast winds, and (c) the 3D-Var analysis using information from PRESCAT and the forecast as shown in (b). The analysis in (c) illustrates, amongst other things, the ambiguity removal capability of 3D-Var.

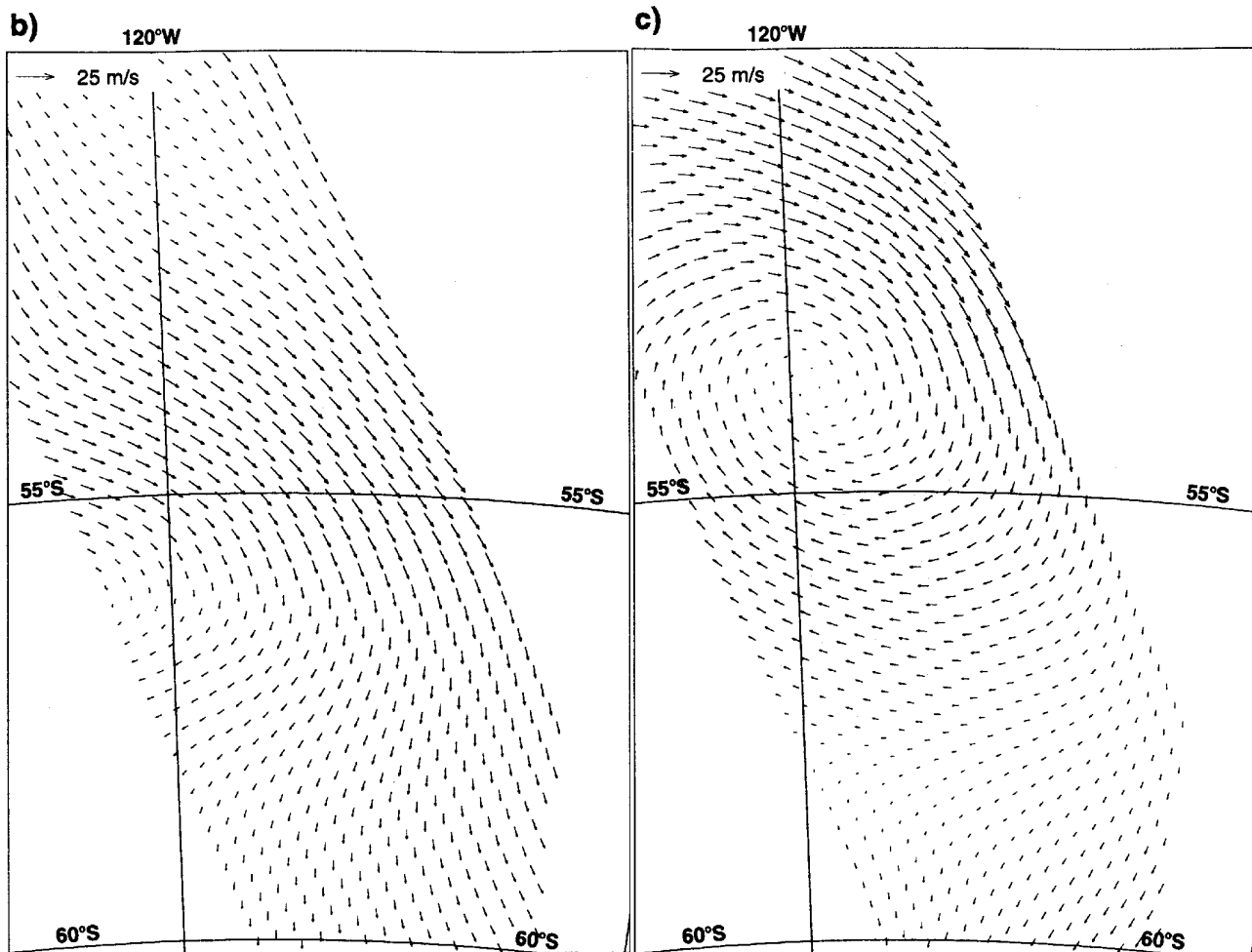


- (ii) that wind-vector filtering is beneficial compared to wind-direction filtering, and
- (i) that meteorological forecast information already enables us to remove correctly about 95% of all ambiguities.

The scheme is able to remove a large percentage of the remaining ambiguities. The performance of the scheme is sensitive to the quality of the forecast wind information that we used, and we found FGAT, based on a 3-hour to 9-hour forecast, to give the best results. PRESCAT was compared with the ESA operational scheme and with SLICE for several cases and was found to be generally beneficial. The OI analysis system ‘buddy’ check is used effectively to identify and remove the few (approx. 0.1%) solutions wrongly selected by PRESCAT.

The PRESCAT ambiguity filter has a purely statistical nature. In meteorological analysis, physical information on the expected structure of forecast errors is also used (e.g. geostrophy). This type of information was shown to be used successfully in a 3D-Var assimilation of ambiguous winds. The development of a simple 2D method, based on the 3D-Var methodology, may be worthwhile.

Assimilation of PRESCAT scatterometer winds has a beneficial impact on the



ECMWF analyses and short-range forecasts (Table 2 and 3), probably mainly from improvements at the subsynoptic scales. Ocean circulation and wave-forecast models will benefit from the improved knowledge of the winds near the surface. Also, high-resolution limited-area models, used for short-range weather forecasting, should benefit from the assimilation of scatterometer winds.

On the larger temporal and spatial scales no significant forecast impact has been found when a ‘full’ observing system is used. We further found that for medium-range forecasts, there is a ‘redundancy’ between scatterometer winds and SATEMs (satellite temperature soundings). If the latter were removed, then the scatterometer could provide beneficial large-scale information. Combining our results with the results obtained by *Bell* [1994], indicates that the impact of scatterometer data depends on assimilation system method and performance: in comparing data impact in two assimilation systems, it is more difficult to show impact in the system which is performing better for that particular period or weather regime.

Surface data are difficult to use in meteorological analysis. In most current data assimilation schemes no account is taken of the special meteorological conditions (Ekman

spiral) in the planetary boundary layer (PBL). Further, the structure functions are defined in a climatological sense and do not take into account the fact that the structure of error in the first guess will depend on meteorological conditions. The spatial structures used to update the background to fit e.g. surface observations will therefore partly be inappropriate to change the upper-air background field and, conversely, upper-air observations may have adverse effects on the surface analysis. In particular, it was shown that the global ECMWF analysis of surface wind is of a quality slightly lower than the first-guess winds, as measured by scatterometer data. When scatterometer data are used they oppose such increment structures that deteriorate the surface wind forecasts. Further investigations are needed to make the different observational systems more complementary and useful.

The above is a weakness also in 3D-Var, but in a 4D-Var assimilation scheme the sensitivity of the time trajectory of the forecast model to external forcing will mainly determine the structure of change in the model owing to an observation at a particular time and location. This will make the 4D-Var analysis meteorologically better balanced than its 3D equivalent and should lead to a more beneficial modification of upper-air fields in response to changes in the PBL.

In addition we showed that scatterometer backscatter measurements are difficult to assimilate directly, and we derived and illustrated a procedure for the assimilation of ambiguous winds.

**Acknowledgments.** It is a pleasure to acknowledge the constructive discussions we have had with members of the ESA analysis team and with ECMWF staff and visitors. Catherine Gaffard implemented the scatterometer processing in IFS under EUMETSAT funding. The other work was carried out at ECMWF under ESA contract 9097/90/NL/BI. Two anonymous reviewers helped by providing useful comments.

## References

- Anderson, D. L. T., A. Hollingsworth, S. Uppala and P. M. Woiceshyn, A study of the use of scatterometer data in the ECMWF operational analysis - forecast model Part II: Data impact, *J. Geophys. Res.*, 96, 2635-2647, 1991.
- Atlas, R. , E. Kalnay and M. Halem, Impact of Satellite Temperature Sounding and Wind Data on Numerical Weather Prediction, *Optical Engineering*, 24(2), 341-346, 1985.
- Baker W. E. , R. Atlas, E. Kalnay, M. Halem, P. M. Woiceshyn, Peteherych S. and D. Edelmann, Large scale analysis and forecasting experiments with wind data from SEASAT-A scatterometer, *J. Geophys Res.*, 89, 4927-4936, 1984.
- Bell, R. S., Operational use of ERS-1 products in the Meteorological Office, *Proc. Second ERS-1 Symp.—Space at the Service of Our Environment, Hamburg, Germany, Eur. Space Agency Special Publ., ESA SP-361(I)*, 195-200, ESA, Noordwijk, the

Netherlands, 1994.

- Breivik, L.-A., Assimilation of ERS-1 scatterometer wind information in a limited area model, *DNMI Technical Report No.104*, DNMI, Oslo, Norway, 1993.
- Cavanié, A. and P. Lecomte, Vol 1 - Study of a method to dealias winds from ERS-1 data. Vol 2 - Wind retrieval and dealiasing subroutines, *ESA contract 6874/87/CP-I(sc) report*, ESA publications division, Noordwijk, the Netherlands, 1987.
- Courtier, P., E. Andersson, W. Heckley, G. Kelly, J. Pailleux, F. Rabier, J.-N. Thépaut, P. Undén, D. Vasiljevic, C. Cardinale, J. Eyre, M. Hamrud, J. Haseler, A. Hollingsworth, A. McNally, and A. Stoffelen, Variational assimilation at ECMWF, *ECMWF Res. Dept. Techn. Memo 194*, ECMWF, Reading, England, 1993.
- Graham, R., D. Anderson, A. Hollingsworth and H. Böttger, Evaluation of ERS-1 wind extraction and ambiguity removal algorithms: meteorological and statistical evaluation, *ECMWF report*, ECMWF, Reading, England, 1989.
- Hoffman, R. N., A preliminary study of the impact of C-band scatterometer wind data on global scale numerical weather prediction, *J. Geophys. Res.*, 98 (C6), 10233-10244, 1993.
- Le Dimet, F-X. and O. Talagrand, Variational algorithms for analysis and assimilation of meteorological observations, *Tellus*, 38A, 97-110, 1986.
- Lönnerberg, P. and D. Shaw, ECMWF data assimilation scientific documentation, *ECMWF Res. Manual 1, 2<sup>nd</sup> revised ed.*, ECMWF, Reading, England, 1987.
- Lorenc, A. C., Optimal non-linear objective analysis, *Q. J. R. Meteorol. Soc.*, 114, 205-240, 1988.
- Offiler, D., ERS-1 wind retrieval algorithms, *U. K. Meteorol. O. 19 Branch Memorandum No 86*, Meteorological Office, Bracknell, England, 1987.
- Smith, W. L., H. M. Woolf, C. M. Hayden, D. Q. Wark and L. M. McMillin, The Tiros-N operational vertical sounder, *Bul. Am. Meteorol. Soc.*, 60, 1177-1187, 1979.
- Stoffelen, A., and D. Anderson, The ECMWF contribution to the characterization, interpretation, calibration and validation of ERS-1 scatterometer backscatter measurements and their use in numerical weather prediction models', *ESA contract 9097/90/NL/BI report*, Eur. Centre for Medium-range Weather Forecasts, Reading, England, 1995.
- Stoffelen, A. C. M. and G. J. Cats, The impact of SEASAT-A scatterometer data on high-resolution analyses and forecasts: The development of the QEII storm, *Mon. Wea. Rev.*, 119, 2794-2802, 1991.
- Stoffelen, A. C. M., C. Gaffard and D. Anderson, ERS-1 scatterometer data assimilation, *Proc. Second ERS-1 Symp.—Space at the Service of Our Environment, Hamburg*,

*Germany, Eur. Space Agency Special Publ., ESA SP-361, ESA, Noordwijk, the Netherlands, 1994.*

Thépaut, J-N., R. N. Hoffman and P. Courtier, Interactions of dynamics and observations in a four-dimensional variational system, *Mon. Weather Rev.*, 121(12), 3393-3414, 1993.

Undén P., Tropical data assimilation and analyses of divergence, *Mon. Weather Rev.*, 117, 2495-2517, 1989.





## CHAPTER VI

### Outlook

During the life time of the ERS scatterometers the usefulness of scatterometry has become established. In the concluding sections of the previous chapters of this thesis many conclusions have already been drawn and prospects been given on scatterometry. In this last chapter a brief and more general outlook is provided, focusing on the applied methodology and the future of scatterometry.

#### **1. Empirical Methodology**

For the interpretation of scatterometer observations, statistical methods are used to take account of the uncertainty in the measurements and to deal with the limited physical knowledge on scatterometry. This thesis concerns these methods, and gives, with the aid of scientific publications, an overview of the state-of-the-art as achieved with ERS scatterometer processing (ERS-1 from 17 July 1991 and later ERS-2 from 22 November 1995). Many aspects of the work may be useful in other disciplines as well; some of these are highlighted below.

##### **1.1. Using NWP fields**

An important asset of this work is the use of output from a Numerical Weather Prediction, NWP, data-assimilation system as the basic material for comparison with the scatterometer measurements and for the development of an empirical transfer function relating radar measurements to wind fields. The use of data-assimilation fields offers many advantages in the validation and calibration of a new data source [Hollingsworth et al, 1986, and Hollingsworth, 1989]. The main point is that for every meteorological observation, there is an equivalent model value. Collocation with other observation data sources often leads to a very serious data reduction. For instance, the ERS scatterometer produces almost a million nodes per 2.5 days, scattered over the worlds oceans. On the other hand, if we put one buoy at the equator for comparison purposes, measuring continuously in time, and allow a collocation radius of 50 km, then it would take on average the same 2.5 days to obtain one collocation with the scatterometer. The accuracy of our tuning, calibration or validation results is proportional to the square root of the number of independent collocations, in principle at least. A striking example of the power of the number of collocations in this

thesis is the backscatter ocean calibration. Within a period of a week the data from the ERS-2 scatterometer could be used, while radar calibration over the rain forest and by transponders took several months. The data abundance furthermore enables that the complete spectrum of possible meteorological conditions may be validated against the model in a relatively short time frame. Moreover, when using data-assimilation fields for validation, the spatial (wavelength) or temporal (frequency) characteristics of the measurements can be easily compared to those of the collocated model equivalents, providing essential information on how these data sources complement each other. At last we note that observations from space often represent a spatial average. NWP model equivalents also represent a spatial average that is usually suitable for comparison, while *in situ* measurements are often taken at a single point in space. Differences in spatial representativeness are often not taken into account in data analysis (e.g., *Rufenach* [1998]), potentially leading to large interpretation errors (Chapter IV).

This does certainly not mean that *in situ* data are useless for the calibration or validation of new observation types. The data-assimilation fields are based on all past and current meteorological observations of many kinds, and represent a best-effort analysis of the meteorological conditions. However, the data-assimilation fields also rely on discretized and filtered equations of motion, interacting with physical processes that are parameterized. As such, the NWP model used in data assimilation has an effect on the data-assimilation fields. To control possible systematic effects, most NWP centers monitor their data-assimilation fields rigorously against *in situ* and other meteorological measurements, both in real time and off line. These observations are thus indispensable to recover in particular the systematic error characteristics of the data-assimilation fields, and help improve NWP models. As a matter of fact, each *in situ* measurement has a NWP model equivalent, and the *in situ* data are used very effectively to characterize the model errors. In the above example of the buoy at the equator, if we compared its measurements hourly to the model, we would obtain **sixty** collocations in 2.5 days. We conclude that data assimilation is a very powerful tool for algorithm tuning, calibration and validation of new observing systems, provided that the data-assimilation fields are in turn validated against reference observations (see also, e.g., *Eyre et al* [1993]).

For instance, as ozone is now being included in NWP models, the new observation systems measuring ozone may be very effectively characterized and exploited through data assimilation (see also *Stoffelen* [1998]).

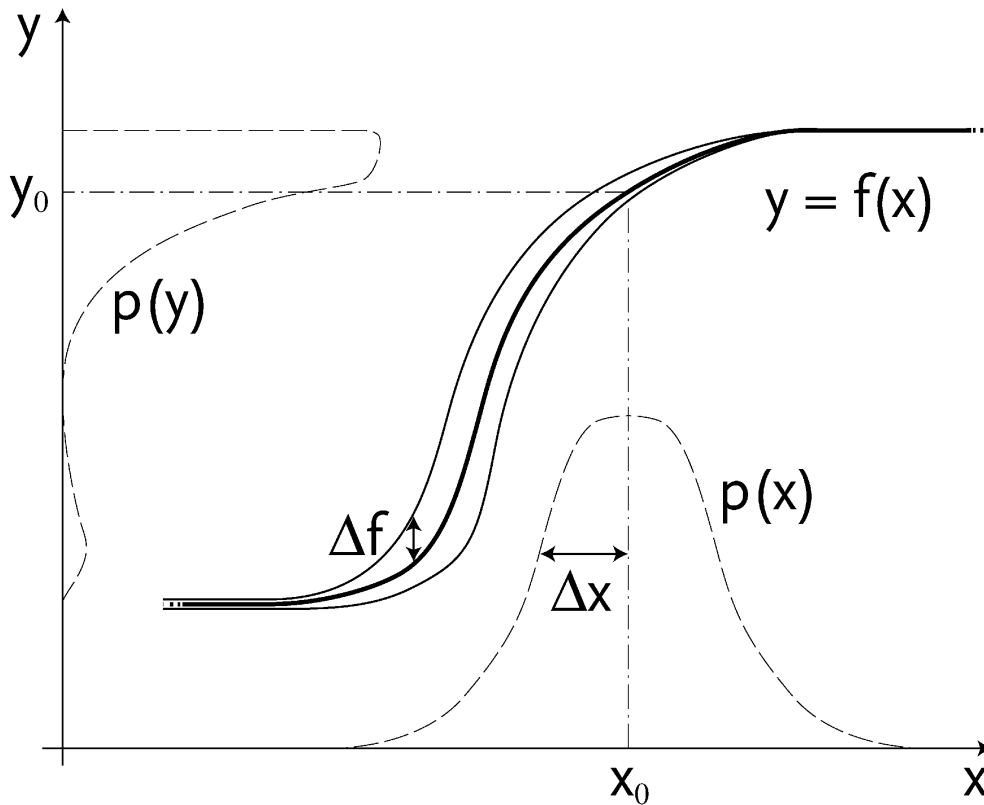


**Figure 1.** Non-linear transformation of a normal distribution  $p(x)$  with mean  $x_0$  and of width  $\Delta x$  to the skew and multi-peaked distribution  $p(y)$  through an equation  $f$  with uncertainty  $\Delta f$ . The projection of the median  $x_0$  of  $p(x)$  to the median  $y_0$  of  $p(y)$  is shown by the dash-dotted line. For  $p(y)$  the median, mean, most likely, and minimum variance values of  $y$  are all different.

### 1.2. Uncertainty and Non-linearity

Uncertainty and non-linearity are relevant to any analysis problem. Almost any equation is approximate, although the amount of uncertainty varies from one equation to the next. Furthermore, the known variables used in equations are often approximate. If the statistical distribution of the uncertainty or error in the equations and the known variables is can be estimated, then the uncertainty in the unknown ones may be computed. This is straightforward when the equations are linear or quasi-linear, but becomes cumbersome when the equations are strongly non-linear. The main problem is that normal error distributions in the known variables may be transformed to skew or multi-peaked error distributions of the unknown variables. Figure 1 provides a simple illustration. After applying the transformation, skewness in the distribution of  $y$  results in a systematic bias of the unknowns. Moreover, multiple peaks indicate multiple solutions of the equations. It may be clear that inversion or analysis schemes dealing with such equations need special

attention when unbiased estimates are required. As a further complication to the transformation depicted, prior knowledge on the probability of occurrence of  $y$  may be useful in the computation of  $y$  from a measurement of  $x$ , in order to reduce the number of unlikely solutions of  $y$ .

For the interpretation of scatterometer data noise and non-linearity are important, and the above problem appears at different stages. In order to avoid systematic wind direction bias in the backscatter inversion, a transformation of variable is carried out, such that skewness of the wind direction error is avoided (Chapter II). In figure 1, this would be similar to transforming  $y$  such that  $f$  becomes linear. Chapter II shows that the backscatter-space transformation corresponds to using additional prior information in a Maximum Likelihood Estimation, i.e., on the non-linearity. In Chapter IV, to avoid the faulty correction of a *pseudo* bias in wind speed, due to the non-linear transformation of Gaussian wind component errors, error modeling and calibration are performed in the wind components. For similar reasons, in the estimation of the transfer function in Chapter III, the input wind data uncertainty is specified in the wind components rather than in wind speed and direction. Also, here a logarithmic backscatter variable is used rather than the physical units, in order to reduce non-linear effects. Even after these precautions have been taken, careful data selection to obtain smooth distributions, and rejection of unsteady winds for noise reduction, were shown to be effective in producing an accurate transfer function.

In the assimilation of scatterometer data, the largest uncertainty is in the wind domain, while the largest non-linearity is in the inversion. The inversion can be fully described in the measurement space (see Chapter II). Given the unfavorable interaction of uncertainty and non-linearity, it is wise to separate the problem of scatterometer data assimilation into an accurate, but non-linear, inversion problem in the backscatter domain and a noisy, but only slightly non-linear, wind assimilation problem. Other measurements, related in a non-linear way to the dynamical variables of NWP or ocean models, for instance through physical parameterizations, will require similar attention before data assimilation (e.g., see *Amato et al* [1996]).

### 1.3. Backscatter Measurement Space

The concept of a measurement space as detailed in Chapter II is very general. It contains all measurement characteristics and different sub-spaces are filled by measurements in different geophysical conditions. It may be defined for any set of collocated measurements. The 3D measurement space for the ERS scatterometers is defined by plotting at all locations each of the three available measurements along a different axes. Due to the high accuracy of the ERS scatterometers the consistency of these triplets is very high, leading to a distinct cone surface in the 3D space. The surface emerges since the triplets

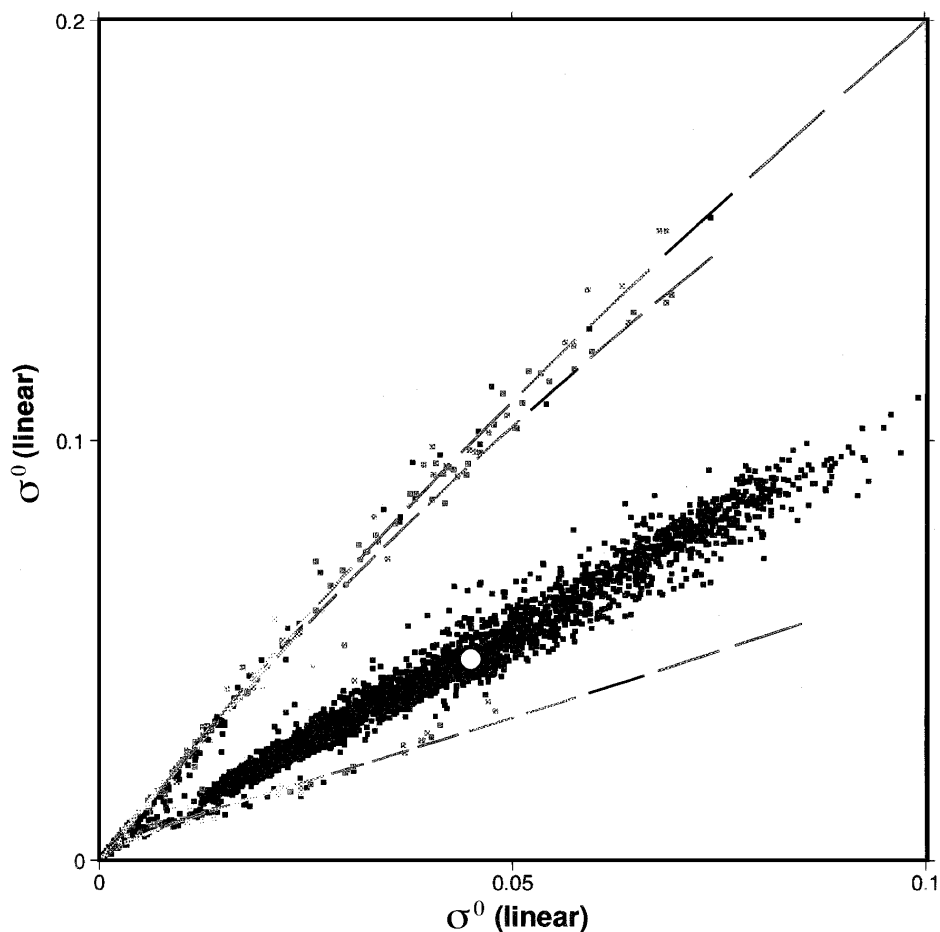


**Figure 2.** Cross section in 3D measurement space for triplets over ice and open water for node 15 and south of 55S. Only triplets for which the ECMWF model sea surface temperature is below 0 °C are black; other triplets are assumed to be over open water and gray-scaled according to wind speed. The gray lines indicate the cross-section with the CMOD4 cone surface (Figure II.5). The white dot depicts a particular local ice type inferred from recent data. Whereas wind triplets lie along a cone, ice triplets are located closely to a line, and locally, if stationary, close to a point.

mainly depend on just two geophysical parameters. Thus, a point on the cone represents a particular wind speed and direction. A main innovation described in this thesis is the visualization of this cone surface, and the systematic exploitation of the geometry and symmetry of it. This plays a role in all aspects of scatterometer data processing, namely, calibration, error characterization, transfer function estimation, inversion, quality control, ambiguity removal, and assimilation of scatterometer winds.

The backscatter measurement space can be exploited for other applications as well. For example, Figure 2 illustrates how ERS backscatter triplets over open water and ice are clearly distinct. It turns out that ice triplets lie generally along a line in the 3D measurement space. A variation along the line indicates a variation in the geophysical condition at the

surface, where several studies document that the aging of ice changes its structure [Gohin, 1995]. Thus, from a measured triplet one could infer the ice age by taking the most likely (closest) point on this line, and from the distance of the measurement to the line, normalized by the usual scatter of triplets around the line, one can infer the ice probability. Subsequently, keeping an ice history over a few days and using the fact that the ice structure is normally stationary over such a period, high probabilities of ice occurrence are limited to a small area around a single point in the 3D measurement space. Then, by using ice likelihood and wind likelihood (Chapter II) one may discriminate ice measurements from wind measurements on a node-by-node basis. This has the practical advantage that scatterometer winds close to the ice edge can be used. It illustrates that the concept of measurement space may prove useful for the application of the ERS scatterometer over sea ice. Sensitivity to swell or rain or the inspection of differences in land surface characteristics may similarly be investigated in the backscatter measurement space.

For the interpretation or Quality Control over the ocean of NSCAT or QuikSCAT/SeaWinds, the concept of a measurement space can be applied also. Chapter II shows that in case of ERS strong changes in curvature of the cone surface as a function of wind direction generate systematic wind direction errors after inversion, and that by a slight transformation of measurement space these effects can be avoided. *Figa and Stoffelen* [1998] show that the NSCAT 4D measurement space can also be transformed in order to reduce the variation of curvature with wind direction, as illustrated in Figure 3. Work is ongoing to demonstrate its effect on the wind retrieval. Also, at Ku-band rain modifies the distribution of backscatter data in the measurement space, and it will be useful to try and find the rain subspace. The rain characteristics may result in a rejection or even improved interpretation of Ku-band backscatter data in case of rain. Taking into account the developments described in this thesis and the similar developments ongoing for NSCAT, an effort should be made to arrive at an accurate interpretation of the QuikSCAT and SeaWinds scatterometers, which will become operational very soon, in order to be ready to assimilate the data in NWP models. Undoubtedly, a measurement space analysis will be of benefit to characterize many other observation systems as well.

## 2. Physics of Scatterometry

The accuracy of the ERS scatterometers (0.2 dB) and the visualization of the 3D measurement space made it possible to learn about the geophysical signature of ocean radar scattering from space and, through CMOD4, provide an accurate description of the cone surface. In laboratory and field experiments with *in situ* and aircraft equipment an accuracy of 1 dB is typical (Chapter II, *Janssen et al* [1998]). 1 dB corresponds to a factor of 1.25. The well-defined cone surface leads to a better definition of the upwind-crosswind

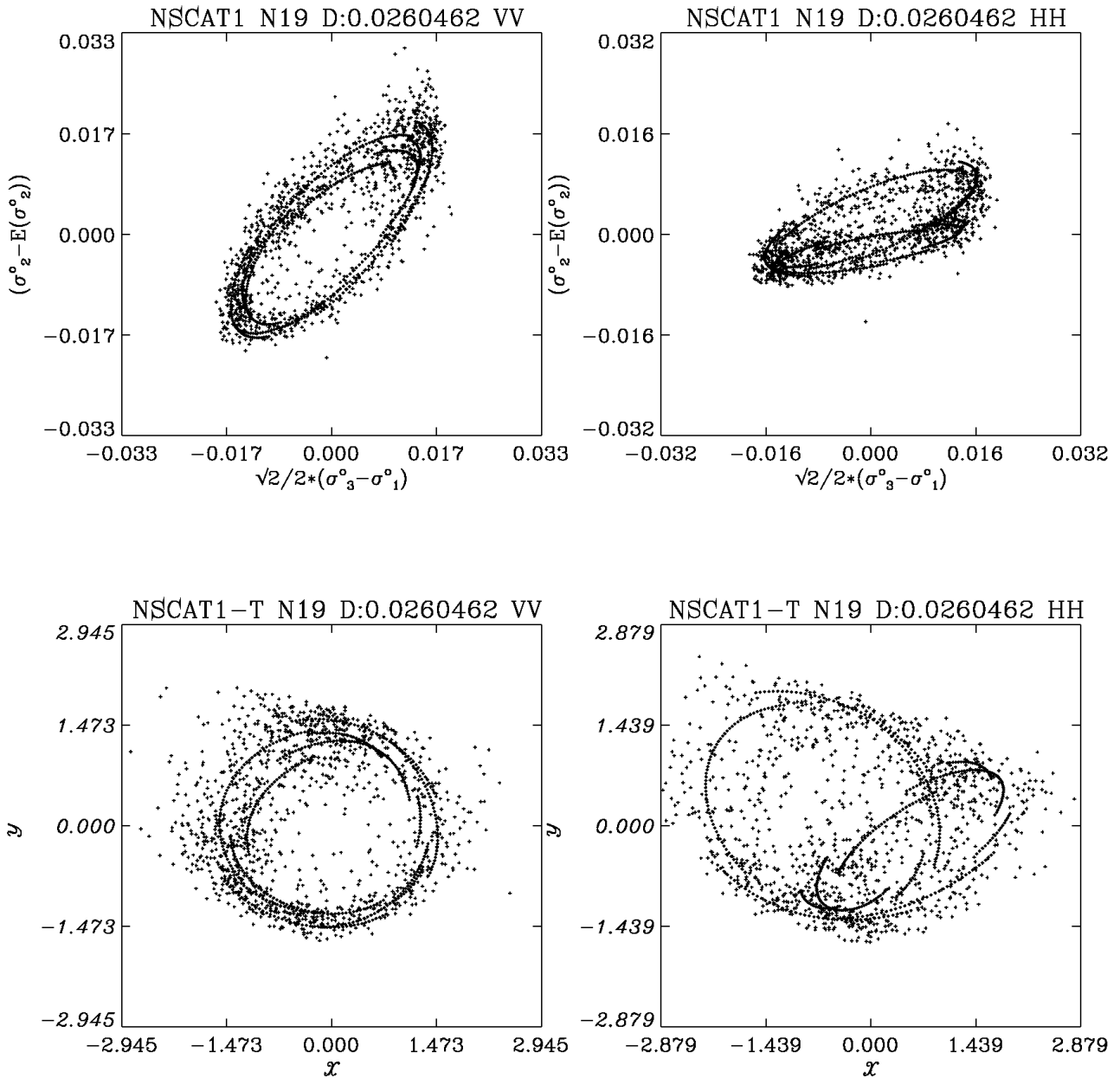


**Figure 3.** Illustration of the transformation of the NSCAT 4D measurement space. On the top the 4D measurement space is depicted by two cross-sections across the cone where the mid beam vertical, VV (left), and horizontal polarization, HH (right), are taken as the vertical axis, and the difference of the fore and aft beam backscatter as the horizontal axis. Only measurements (+) and NSCAT-1 Ku-band model simulations (♦) very close to the plane of section are plotted. The elliptical shape is due to the non-central position of the mid beam (Chapter I, Figure 7). At the bottom many of the same points are shown after transformation (i.e. scaling, 45° rotation and scaling) to a more symmetric space [Figa and Stoffelen, 1998].

backscatter ratio. At low wind speeds this ratio is smaller compared to that found in aircraft campaigns, due to the smoothing effect of the variability of wind direction and speed in the large ERS scatterometer footprint. In this respect, CMOD4 should not be valid for a SAR with a much smaller footprint. The saturation seen at high wind speeds corresponds to the results seen from scatterometers on aircraft [Carswell *et al*, 1998]. What also becomes immediately clear from the cone surface is that higher-order harmonics are required to describe its geometry. That the observed geometric effects are small, is shown by the fact that a fourth-order harmonic of just 4 % is sufficient to describe the asymmetric cone shape (Chapter II). Nonetheless, it is shown in Chapter II that this higher harmonic has a pronounced effect on the wind direction retrieval. Physically-based models are not sufficiently advanced to explain the incidence angle dependence of the upwind-crosswind ratio, nor the behavior of the upwind-downwind ratio, nor the small effects observed in the higher harmonics [Janssen *et al*, 1998].

The upwind-downwind backscatter ratio is more difficult to estimate from the cone surface, but it can be well estimated from NWP model and scatterometer collocation statistics. It turns out that the upwind-downwind coefficient goes up to 15 %, but that its effect on the cone surface geometry is small. Instead, it has a systematic and pronounced effect on the retrieved wind vector, i.e., up to  $1.5 \text{ m s}^{-1}$  in wind speed and a few degrees in wind direction (Chapter II). Physically, one could argue that the increased backscatter when looking upwind may be compensated by a slightly higher wind speed at downwind. This would indicate that the 180 degree ambiguity seen with the ERS scatterometers is basic and independent of, for example, the viewing geometry.

In the inversion, the most likely triplet on the CMOD4 cone surface is sought. Any point on the cone surface corresponds to a particular retrieved wind vector. Ignoring the ambiguity removal problem, one could thus map the retrieved wind vector on a collocated set of calibration wind data. The wind calibration, addressed in Chapter IV, is thus largely independent from the backscatter calibration, as detailed in Appendix A. In Chapter IV we point out that the wind calibration is delicate and can only be properly done in a three-way comparison. An issue of concern is the difficulty to accumulate extreme wind cases. Carswell *et al* [1998] provides evidence of a large underestimation of extreme wind speeds in tropical cyclones due to a large degradation in wind sensitivity of the ERS scatterometer above  $25 \text{ m s}^{-1}$ . A question remains whether the cyclone dynamics cause particular sea state effects, influencing the amount and isotropy of the ocean backscatter. Extreme wind events in the southern hemisphere, usually of larger scale, may provide more evidence, as well as scatterometer measurements in different (parts of) tropical cyclones, subject to different sea states.

There is no doubt that a scatterometer can measure at low wind speeds, but one may



disagree on what it actually measures. For a zero mean vector wind over a footprint of 50 km, it is very unlikely that the ocean surface is flat everywhere. Within the 50 km footprint there will be wind variability, causing ocean surface gravity-capillary waves and backscatter. In fact, in extremely light wind conditions, the scatterometer backscatter will be proportional to the wind variability. By oversampling with backscatter measurements, one may be able to improve their geophysical interpretation and infer both the mean and the variability of the wind vector in such conditions.

Long waves, the presence of slicks, or atmospheric stability may affect the backscatter. However, as stated in Chapter I, these effects partially depend on wind speed and as such are modeled through CMOD4. Furthermore, physical parameterizations that take these effects into account are uncertain and do not mutually agree very well. Thirdly, local measurements of for example stability may not be suitable for a stability correction over the large scatterometer footprint. In order to avoid problems due to these uncertainties, we decided to relate the true 10-m vector wind to the ERS backscatter, rather than the 10-m wind corrected for, e.g., atmospheric stability. This approach has proven to be successful.

In fact, the empirical methodology put forward in this thesis can be naturally extended in order to incorporate the second-order geophysical effects mentioned above. Geophysical conditions that affect the cone geometry are expected to result in an increased distance to the CMOD4 cone. Chapter IV discusses a quality control procedure that rejects 1 % of extreme geophysical conditions when the backscatter triplets are not close to the cone. Here, one may think of more isotropic scattering conditions due to effects of waves or maybe rain. In such cases the measured triplets will be located within the cone. Thus, these physical effects may be easily visualized and identified by the methodology presented in this thesis, provided collocated information indicating such conditions is available. Other second-order geophysical effects, such as stability, do not alter the backscatter anisotropy, but rather the backscatter amplitude through a modification of the surface stress. As such, these effects do not result in an increased distance to the cone, but in a larger wind error. The correlation of the wind error with data containing information on these effects may be empirically investigated. Since these effects are second-order, *pseudo* correlations, due to the statistical processing, need to be taken care of (see also Chapter IV). In summary, the empirical methodology followed in this thesis provides a controlled framework to investigate the physics of radar backscattering.

### 3. Impact of Scatterometers

A wealth of meteorological observations is available daily. However, most of these observations are above land; above the ocean accurate wind observations are sparse. In a strong westerly circulation this poses a main limitation to the weather forecasting capability in western Europe. Especially here the risk of storm and flooding damage is largest. Wind observations are furthermore relevant for the modeling of the atmospheric circulation in the tropics. Near-surface winds determine the forcing of the ocean circulation, which in turn plays a key role in the seasonal forecasting of the weather and in the earth climate system. Scatterometer instruments now deliver many accurate and reliable surface winds with a high spatial consistency, even below cloud, that prove to be useful for weather forecasting and climate applications.

The ERS scatterometer measurements lead to a better analysis and weather forecast over the oceans [*Isaksen, 1998, Andrews and Bell, 1998*] and increased data coverage is shown to further enhance the impact [*Le Meur, 1997, Stoffelen and Beukering, 1997*]. The ERS satellites are polar, which implies that they will pass along most locations twice a day. However, doing so, they still leave large data gaps over the oceans.

The NSCAT scatterometer developed by NASA, that has recently operated for nine months on ADEOS-I, had a three times larger coverage than ERS-1 or ERS-2. For QuikSCAT, planned on a dedicated platform for late 1998, and SeaWinds, planned on ADEOS-II for early 2000, the same applies. However, because of its different microwave wavelength and instrument geometry, development work is necessary to arrive at an accurate interpretation and quality control of the NASA scatterometers. Nonetheless, it is anticipated that in most of the 1800 km broad QuikSCAT or SeaWinds swaths, accurate wind vector data can be retrieved. Then, the methodology of variational ambiguity removal and wind assimilation as presented in Chapter V may be applied for NSCAT, QuikSCAT and SeaWinds as well. In particular the last two instruments will be crucial for providing continuity of scatterometer winds over the first years of the third millennium.

ASCAT, which is planned on METOP/EPSC in 2003 has a coverage similar to NSCAT, with the geometry and microwave wavelength of the ERS scatterometers. With this, the availability of an accurate and reliable scatterometer wind product is ensured on the longer term.

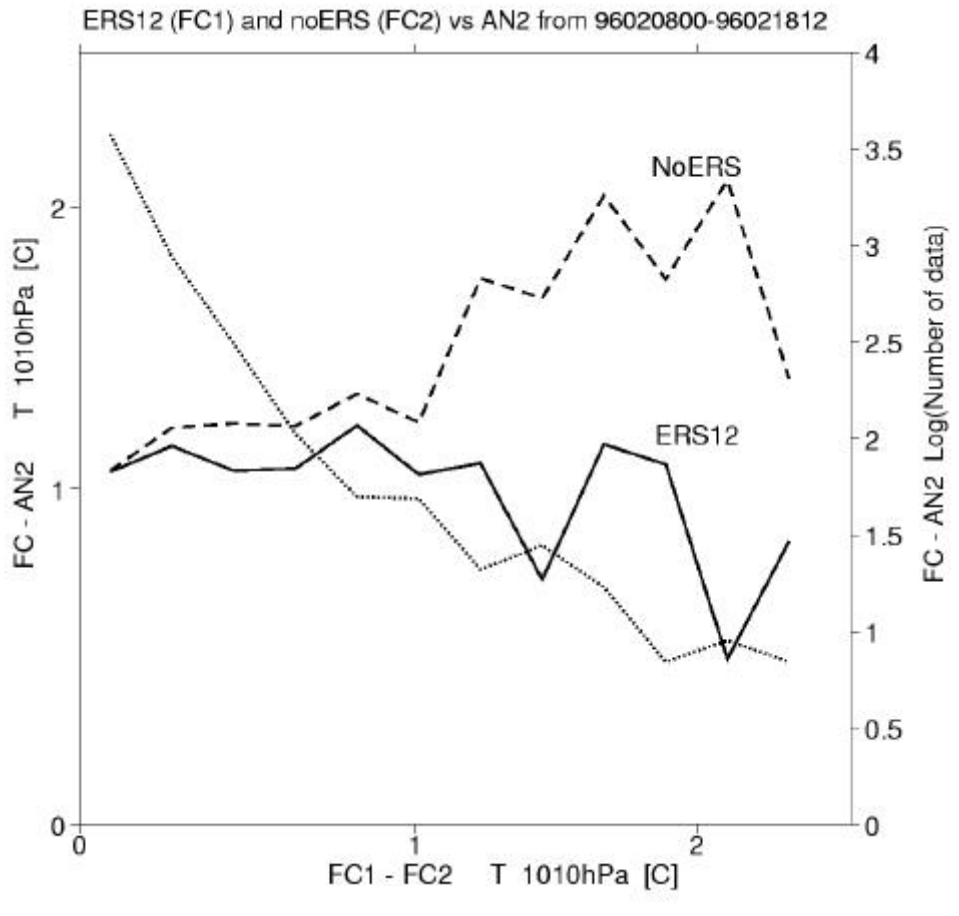


**Figure 4.** The improvement in near surface (2m) temperature of the HIRLAM two-day forecasts due to the use of tandem ERS winds, versus impact threshold. The impact threshold is a classification of the difference between the two-day forecasts based on analyses with (ERS12) and without (NoERS) ERS winds. Over the verification area, which is within roughly 400 km of Amsterdam, the dotted line shows on the right axis that the number of cases decreases with the impact threshold. At the same time, the verification of the ERS12 forecast (solid) with the analysis (NoERS) shows a decreasing trend, while the NoERS forecast (dashed) performs worse at high impact threshold. As such, the plot illustrates that the scatterometer has largest impact in the difficult-to-forecast situations [Stoffelen and Beukering, 1998].

## References

- Amato, U., I de Feis, and C. Serio, Linearization pseudo-noise and its effect on the retrieval of atmospheric state from infra-red spectral radiances, *Geophys. Res. Lett.*, 23, 2565-2568, 1996.
- Andrews, P. L., and R. S. Bell, Optimizing the United Kingdom Meteorological Office data assimilation for ERS-1 scatterometer winds, *Mon. Weath. Rev.*, 126 (3), 736-746, 1998.
- Carswell, J. R., W. J. Donnelly, P.S. Chang, and R.E. McIntosh, Ocean surface winds: satellite and aircraft scatterometer measurements of Hurricane Fran, *Proc. of the Ninth Conference on Satellite Meteorology and Oceanography, Paris, France, 25-29 May 1998*, Eumetsat, Darmstadt, Germany, 1998.
- Eyre, J. R., G. Kelly, A. P. McNally, E. Andersson, Assimilation of TOVS radiances through one-dimensional variational analysis, *Quart. J. Royal Meteor. Soc.*, 119, 1427-1463, 1993.
- Figa, Julia., and Ad Stoffelen, "Towards an improved Ku-band scatterometer wind product", Paper prepared for the Workshop on Emerging Scatterometer Applications - From Research to Operations -, to be held in ESTEC, Noordwijk, The Netherlands, 5-7 October 1998, 1998.
- Gohin, F., Some active and passive microwave signatures of Antarctic sea ice from mid-winter to spring 1991, *Int. J. Remote Sensing*, 16 (11), 2031-2054, 1995.
- Hollingsworth, A., D. B. Shaw, P. Lönnberg, L. Illari, K. Arpe, A. J. Simmons, Monitoring of observation and analysis quality by a data assimilation system, *Mon. Weath. Rev.*, 114, 861-879, 1986.
- Hollingsworth, A., The role of four-dimensional assimilation in the quality control, interpretation, and synthesis of climate data, *Oceanic Circulation Models: Combining*

Data and Dynamics, pp. 303-343, Ed. J. Willebrands and D. Anderson, Kluwer Academic Publishers, 1989.

Isaksen, Lars, Impact of ERS -scatterometer wind data on ECMWF's analysis and forecasts of tropical cyclones, Paper prepared for the Workshop on Emerging Scatterometer Applications - From Research to Operations -, to be held in ESTEC, Noordwijk, The Netherlands, 5-7 October 1998, 1998.

Janssen, P. A. E. M., H. Wallbrink, C. J. Calkoen, D. Van Halsema, W. A. Oost, and P. Snoeij, VIERS-1 scatterometer model, *J. Geophys. Res.*, 103 (C4), 7807-7831, 1998.

Le Meur, Didier, Impact of ERS-1/ERS-2 scatterometer tandem on the ECMWF 3D Var assimilation system, *Proc. of the 3<sup>rd</sup> ERS Symposium - Space at the Service of our Environment, Florence, 17-21 March 1997*, Eur. Space Agency Special Publication, ESA, Noordwijk, the Netherlands, 1997.

Rufenach, Clifford L., ERS-1 scatterometer measurements - Part II: An algorithm for ocean-surface wind retrieval including light winds, *IEEE Transactions on Geoscience and Remote Sensing*, 36 (2), 623-635, 1998.

Stoffelen, Ad, and Paul van Beukering, Improved backscatter processing and impact of tandem ERS winds on HIRLAM, *HIRLAM project report nr 31*, IMET, Dublin, Ireland, 1997.

Stoffelen, Ad (editor), Satellite Ozone Data Assimilation, *1<sup>st</sup> Annual Contract Report to the European Union*, EU 4<sup>th</sup> Framework project by ECMWF, KNMI, Météo France, RAL, UK Meteo. Office, Un. of Cambridge, and DAO, report available from KNMI, de Bilt, the Netherlands, 1998.

## APPENDIX

## A Simple Method for Calibration of a Scatterometer over the Ocean\*

**Abstract.** The absolute calibration of the backscatter signal of a scatterometer is essential for the retrieval of optimum quality geophysical products. The European Space Agency, ESA, targeted a specification of 0.2 dB for the accuracy of the European Remote-sensing Satellite, ERS, scatterometers. A radiometric error of this amount leads to a wind speed error of roughly  $0.25 \text{ m s}^{-1}$ . An interbeam bias of the same amount may lead to notable wind direction effects. In this paper a method is discussed to obtain an accurate calibration of a scatterometer over the ocean using an accurate backscatter-to-wind transfer function and collocated winds from a numerical weather prediction model. The method is estimated to be accurate to a precision of 0.1 dB. It can be used for instrument monitoring and application of the calibration results has a demonstrable and beneficial impact on the wind inversion.

## 1. Introduction

It is not simple to obtain an accurate absolute calibration for a scatterometer. For the calibration of the European Remote-sensing Satellite (ERS) scatterometers [Attema, 1991] the European Space Agency, ESA, planned to perform the absolute calibration by a controlled radar return to the scatterometer from transponders when these are illuminated by one of the three scatterometer radar beams. In addition, an interbeam comparison was planned over the rain forest where the radar cross section is known to be very stable and rather time independent. Furthermore, the incidence angle response is known to be smooth over the rain forest. At first, the two techniques resulted in an inconsistent calibration. It was at this point that the ocean calibration method as described here in section 2 proved very useful. It helped detect an interpretation problem of the results obtained with the transponders. After solving the initial problems the three calibration methods are giving results that lie within the ESA specifications for the radiometric accuracy of the ERS scatterometers, which is 0.2 dB [Guignard *et al.*, 1992, Stoffelen and Anderson, 1995, p. 8].

The ocean calibration method is still used for instrument monitoring purposes. The main advantage of the ocean calibration with respect to the other two methods is the much

---

\* Based on:

Stoffelen, A., A simple method for calibration of a scatterometer over the ocean, *J. Atmos. Ocean. Technol.*, in press, 1998, © American Meteorological Society.

shorter time period over which accurate results can be obtained. Within a period of 6 hours the method can detect sudden instrument anomalies, and consequently it could be decided to reject the data for real time use in for example a meteorological analysis. For instance, switching of instrument hardware modules may change the absolute calibration to a small amount. With the ocean calibration method these can be corrected for in the processing within a few weeks. So far, several cases of such anomalies have been found during the life time of ERS-1 and ERS-2. The timely detection of these is of the utmost importance to render the data useful for near real time application.

To perform an ocean calibration we divide the average of the measured backscatter measurements, denoted  $\mathbf{s}_M^0$ , by the mean simulated backscatter  $\mathbf{s}_S^0$ . For the computation of the latter, collocated wind data and a transfer function are needed. *Stoffelen and Anderson* [1997b; Chapter III] derived an accurate transfer function, denoted CMOD4, that has been adopted by ESA for operational use. Its formulation is

$$z(\mathbf{q}, V, \mathbf{f}) = B_0(\mathbf{q}, V) [1 + B_1(\mathbf{q}, V) \cos(\mathbf{f}) + B_2(\mathbf{q}, V) \cos(2\mathbf{f})] \quad (1)$$

where  $z = (\mathbf{s}^0)^{0.625}$ ,  $\mathbf{f}$  is wind direction with respect to the pointing of the radar beam,  $V$  is wind speed, and  $\mathbf{q}$  is the incidence angle of the radar beam at the earth's surface.  $B_0$  is usually referred to as the bias term and is by rough approximation proportional to  $V^g$ , where  $g$  depends on incidence angle and varies between 0.35 and 1.0 for incidence angles between 18 and 57 degrees.  $B_1$  and  $B_2$  are respectively the upwind/downwind and upwind-crosswind amplitudes. From (1) it can be seen that wind direction modulates  $z$  through the  $B_1$  and  $B_2$  terms, and that the bias term is only dependent on wind speed and incidence angle. It is shown later that the computations to arrive at a calibration of sigma naught can best be done in  $z$  space rather than in  $\mathbf{s}^0$  space.

The transfer function derived at the European Centre for Medium Range Weather Forecasts (ECMWF) was tuned using ERS data for the month of November 1991, which is before the last engineering calibration performed by ESA. By performing an ocean calibration for the months of March 1992, which is after the last engineering calibration, and November 1991, by taking the ratio of both months, and fitting this as a function of incidence angle, a beam independent multiplication factor to the transfer function had been derived such that it represents the mean backscatter values after the last engineering calibration. The evolving transfer function, which is CMOD4, has been implemented by ESA after comparing its performance against some other transfer function proposals [*Offiler*, 1994]. Furthermore, ECMWF kept a beam dependent sigma naught calibration in addition to CMOD4 in its scatterometer processing (called PRESCAT; *Stoffelen and Anderson* [1997a, b, c; Chapters II, III and V]), since this marginally improved the quality of

the retrieved winds. Although a beam independent transfer function is preferred, in this paper we denote, for convenience of notation, the combination of CMOD4 and March '92 ocean calibration as CMODEC. By using CMODEC, the "ocean" calibration procedure has for long been an integral part of the PRESCAT ERS scatterometer data processing. In the ESA processing CMOD4 is used, not CMODEC.

The calibration consists in a multiplication of the bias term with a beam and incidence angle dependent constant. The ERS scatterometer backscatter measurements are organized in 19 nodes across the swath. For each of these 19 nodes the triplet of incidence angles for the fore, mid and aft beam is more or less fixed along the track. We use for each node and beam the average value of the incidence angle. As such a calibration results in  $19 \times 3 = 51$  calibration constants.

$V$  and  $f$  need be available at any location where the scatterometer makes a measurement in order to obtain a quick procedure. Such a widely available wind data source is provided by a global Numerical Weather Prediction (NWP) model and we used the ECMWF model winds in our study. As such, changes in the mean ECMWF wind speed will change the mean sigma naught simulated using CMOD4 and ECMWF winds, since wind speed is the prime geophysical sensitivity of the backscatter signal over the ocean. Fortunately, forecast model wind error characteristics are monitored routinely by e.g. ECMWF and are also documented in special studies (e.g., *Stoffelen* [1998; Chapter IV]).

For each of the 19 nodes the triplet distribution of measurements from the fore, mid and aft beams can be plotted in a three dimensional measurement space, where each beam is represented by one axes. *Stoffelen and Anderson* [1997a; Chapter II] explored the coherence of the ERS triplet backscatter measurements by visualization of the 3D measurement space, and found that the data are generally distributed along a well-defined and conical (2D) surface. The two parameters describing the surface most likely express the mean amplitude and direction of the relevant gravity capillary waves at the water surface. Using this concept, the sigma naught calibration procedure should seek for a bias correction that moves the CMOD4 cone surface towards that surface in the measurement domain at which the density of measured ERS-1 (or ERS-2) scatterometer triplets is largest, in order to bring model and measurements as close together as possible, and thereby improve the wind inversion.

In section 2 the ocean calibration method is described in detail and both the effects of errors in the transfer function and the wind data are addressed. Section 3 presents the results of our method, whereas in section 4 a summary and conclusions are given. It is estimated that the method is accurate to a radiometric precision of 0.1 dB when the precise calibration of the transfer function and forecast model winds are given. It can be used for instrument



monitoring and application of the “ocean” calibration has a demonstrable and beneficial impact on the wind inversion.

## 2. Method

In this section the ocean calibration procedure is described. For the method to work accurately, the result should be independent of the geophysical conditions sampled by the collocation data set used for the calibration. Using Bayes theorem, for the joint probability density of the wind one may write

$$p(V, \mathbf{f}) = p(\mathbf{f}|V) p(V) \quad (2)$$

where  $p(V)$  and  $p(\mathbf{f}|V)$  are the probability density function (pdf) of respectively wind speed and, at a given speed, wind direction. When combining (1) and (2) we see that for a uniform wind direction pdf, i.e.,  $p(\mathbf{f}|V) = (2\pi)^{-1}$ , the harmonic terms disappear when integrated over  $\mathbf{f}$ . So, if we are able to achieve for the ocean calibration a collocation wind data set with uniform wind direction distribution, then our results are independent of errors in the harmonic terms of the transfer function, and insensitive to uncertainty in wind direction.

When we now also integrate over  $V$ , the expected average backscatter becomes

$$\langle z(\mathbf{q}) \rangle = \overline{B_0(\mathbf{q}, V)} \quad (3)$$

i.e., identical to the average value of the bias term. By computing the right-hand-side from CMOD4 and the collocated model winds we would have a reference to compare the mean measured backscatter against. As such, at each across-track node the application of Equation (3) for the three beams defines the center of gravity of the cone in  $z$  space. When this center of gravity matches for the measured and simulated triplets, then the inversion should work best [*Stoffelen and Anderson, 1997a; Chapter II*].

Computation in  $\mathbf{s}^0 = z^{1.6}$  (for Equation (1) we defined  $z = (\mathbf{s}^0)^{0.625}$ ), using Taylor expansion, causes an additional term to be added to the mean backscatter [*Stoffelen and Anderson, 1997a; Chapter II*]

$$\langle \mathbf{s}^0(\mathbf{q}) \rangle = \overline{B_0^{1.6}(\mathbf{q}, V)} + 0.24 \overline{B_0^{1.6}(\mathbf{q}, V) B_2^2(\mathbf{q}, V)} + 0.24 \overline{B_0^{1.6}(\mathbf{q}, V) B_1^2(\mathbf{q}, V)} \quad (4)$$

The right-most term is very small, since in this notation  $B_1 \leq 0.1$ . Since  $B_2 \leq 0.4$ , the mid term on the right-hand-side may contribute up to 4%, but dependent on wind speed.  $B_0$  also depends on wind speed, and as such the term with  $B_2$  may to a small extent interfere with systematic changes in mean  $B_0$  due to changes in the wind speed level of the ECMWF model. It may be clear to the reader that the interference of the harmonic terms in the ocean

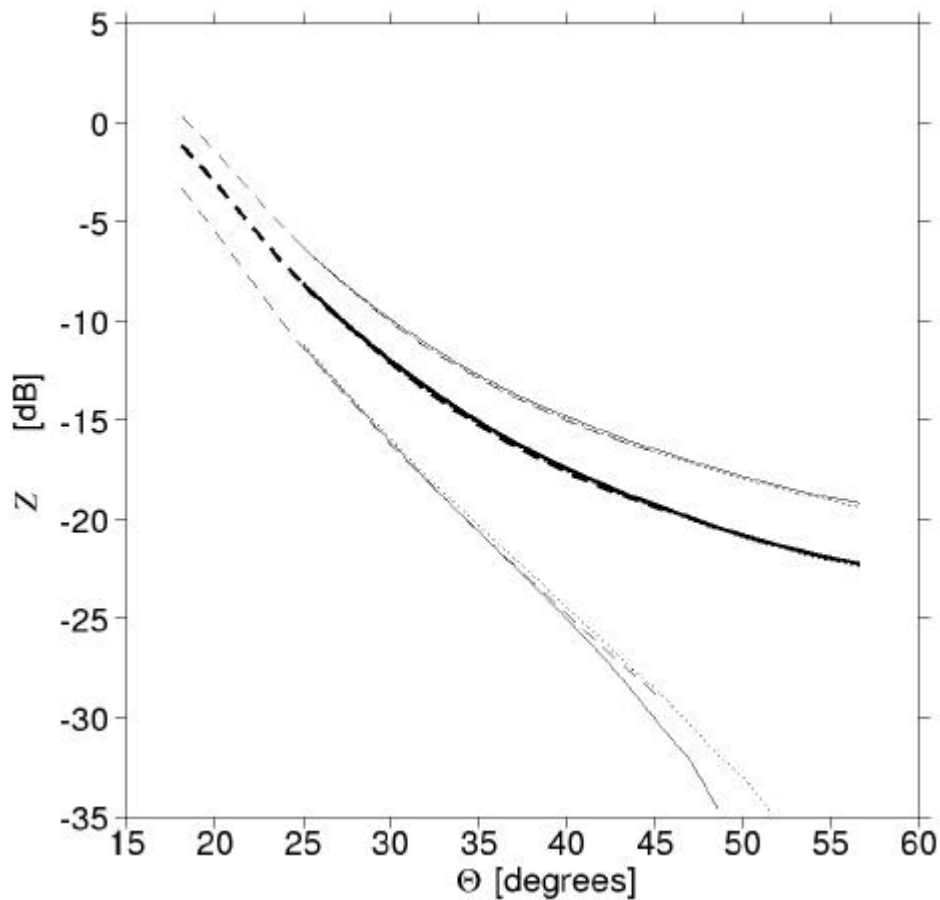


**Figure 1.** Example of the logarithm of the average transformed measured ERS-1 backscatter ( $z$ ) versus incidence angle for the fore, mid and aft antennae in respectively solid, dashed and dotted for March 1996. The thin lines show the logarithm of the average transformed backscatter signal plus or minus one standard deviation (SD) of the transformed backscatter. One may note that the mean and SD do not exactly overlap for the three beams, suggesting an interbeam bias and thus a remaining calibration problem.

calibration is undesirable.

*Stoffelen* [1998; Chapter IV] finds the random wind component error of a forecast model to be normal distributed with a standard deviation of roughly  $1 \text{ m s}^{-1}$ . In case of unbiased component errors and a true wind component variance of  $25 \text{ m}^2 \text{ s}^{-2}$ , he computed that model wind speeds would systematically overestimate the true wind speed by 2% (i.e., a *pseudo* bias would occur). The non-linear transformation of random wind component errors also causes a bias in the computation of the backscatter bias. For a wind speed sensitivity of  $g = 0.5$  in  $B_0$  as defined in  $z$  space, it follows that this may cause  $B_0$  to be overestimated by roughly 1% or 0.04 dB, i.e. a very small amount. Although straightforward, we did not correct for this *pseudo* bias in the computations.

The scatter of measured triplets around the cone is roughly 5% and is assumed to have a normal distribution around the true  $\mathbf{s}^0$  with zero mean. In  $z$  space the distribution is therefore slightly skew and it is relevant to estimate the effect of this on the ocean calibration. Taylor expansion of  $\mathbf{s}^0 [1 + \mathbf{d}]$  in  $z$  space shows that

$$\langle z \rangle = \overline{(\mathbf{s}^0)^{0.625}} [1 - 0.12 \overline{\mathbf{d}^2} + O(\overline{\mathbf{d}^4})] \quad (5)$$

Based on this result we conclude that the measurement noise is not a motivation for either computation in  $z$  or  $\mathbf{s}^0$  space, since for an expected standard deviation  $\mathbf{d}$  of 5% the  $\mathbf{d}$  terms between square brackets only amount to roughly 0.0003.

Polar satellites sample the trades and the westerlies in a systematic manner. This results in a modulation by more than a factor of two of  $p(\mathbf{f}|V)$  over the worlds oceans for medium and high wind speeds. For low wind speeds the modulation is much less, as is shown later. *Freilich et al.* [1998] assume  $p(\mathbf{f}|V)$  to be independent of wind speed, which to our experience is not valid. The wind direction distribution becomes increasingly uniform going from high to moderate, to low wind speed. The assumption of an invariant  $p(\mathbf{f}|V)$  for varying  $V$ , introduces additional uncertainty in the results. A way to remove the wind direction modulation for all wind speeds without this approximation, is to first determine  $p(\mathbf{f}|V)$  for a given data set, and subsequently in a second pass remove randomly a fraction of the data such that the resulting  $p(\mathbf{f}|V)$  becomes as uniform as possible. Then Equations (3) and (4) can be used for the ocean calibration, without unnecessary assumptions on  $p(\mathbf{f}|V)$  as in *Freilich et al.*

In *Freilich et al.* [1998] the wind direction distribution of the collocated winds is used to compute the mean contribution from the harmonic terms of the transfer function. However, this direction distribution is affected by the error in the wind direction of the collocated data, and thereby somewhat smoothed. As a consequence, the estimated contribution from the harmonic terms will be underestimated. We filtered wind directions by using collocated ECMWF winds. We assume here that a uniform ECMWF wind direction distribution corresponds to a uniform “true” wind direction distribution, and verify this later. After the filtering to a uniform  $p(\mathbf{f}|V)$  as proposed here, the contribution of the harmonic terms to the mean backscatter becomes negligible and its uncertainty unimportant.

After some testing, speeds were binned in  $4 \text{ m s}^{-1}$  intervals, i.e.  $0-4 \text{ m s}^{-1}$ ,  $4-8 \text{ m s}^{-1}$ , up to  $36-40 \text{ m s}^{-1}$ , and directions in 5 degree intervals. After the first pass over the data, for each speed interval the direction bin with the least points is searched for and in each bin the fraction to keep is computed as the ratio of this minimum and the actual number of points in the bin. In order to keep some points in the most data sparse areas of the wind domain, the minimum is bound to values higher than 5 in case of a month of data.

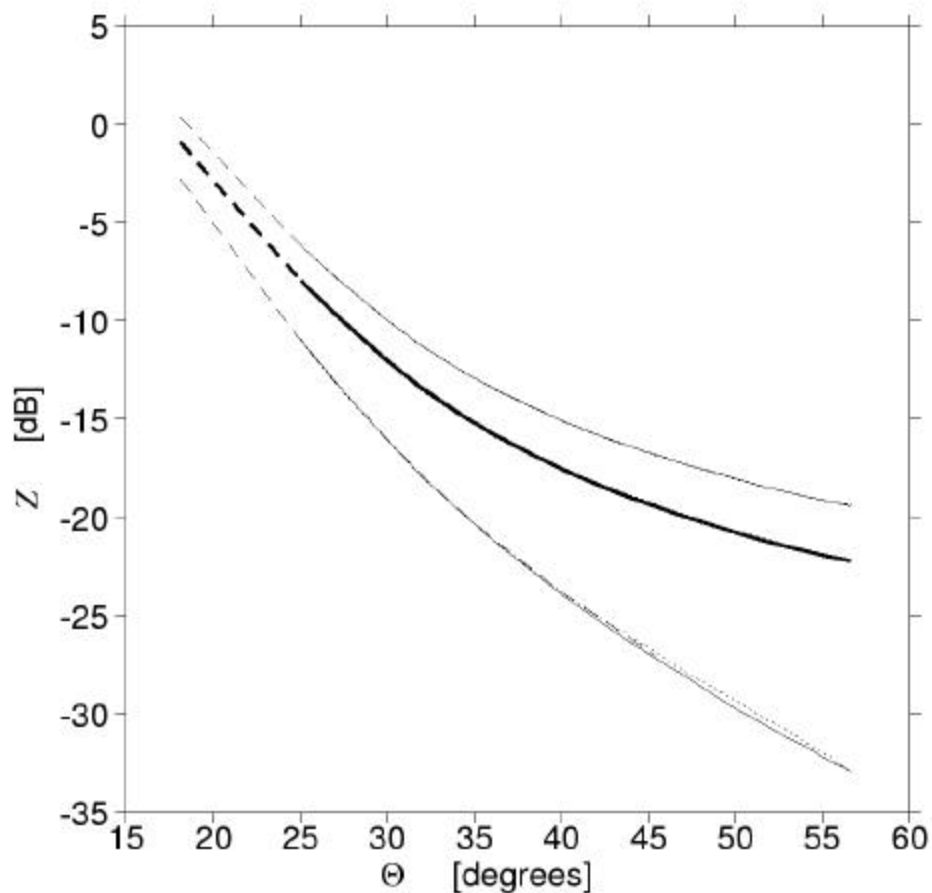


**Figure 2.** As Figure 1, but now the modified backscatter is simulated from the ECMWF winds using CMOD4. For the three antennae, the average modified backscatter and the SD overlap to a large degree.

Some quality control is necessary on the backscatter data used. In particular, we found the calibration results to be very sensitive to ice contamination. We use Sea Surface Temperature (SST) fields, obtained from the National Center for Environmental Prediction, NCEP, and operationally used at ECMWF, with a temporal resolution of a few days and a spatial resolution of 100 km to reject potentially ice contaminated backscatter measurements. We found that in some cases a threshold as high as 279 K was only sufficient to exclude all ice areas. This threshold is used in this study. Furthermore, the big lakes in the US and Canada have been removed as target areas. For security, we also reject points where the forecast model wind is interpolated from one or more land points. We did not apply quality control in the wind domain.

### 3. Results

#### 3.1. Ocean Calibration

In this section we demonstrate the accuracy of the ocean calibration method. The ratio of measured and simulated backscatter was computed over periods of different length, from 6 hours to two months. Over a month, the wind direction filter rejects typically 50% of the collocation points, from about 25% at the lowest speeds up to over 60% at the highest speeds. No sensitivity was found to the sample of randomly selected points from the full data set. For different geographical areas and/or seasons the biases remain the same within the expected accuracy. In subsection 3.4 we check whether the ocean calibration is beneficial for the scatterometer wind inversion.

Figure 1 shows an example of the logarithm of the average measured backscatter versus incidence angle for the three antennae. After careful inspection, one may note that the mean does not exactly overlap for the three beams, suggesting an interbeam bias and thus a remaining calibration problem. We further analyze this here.

The thin lines show the logarithm of the average backscatter signal plus or minus one standard deviation. The standard deviation is computed as

$$SD = \sqrt{\overline{z^2} - \bar{z}^2} \quad (6)$$

and is determined by both the bias term and the harmonic terms, which means that the actual wind direction distribution affects  $SD$ . However, a wrong calibration should affect the  $SD$  in the same way as it affects the mean of  $z$ . Note that the wind direction distribution relative to north is similar for all nodes, but that the average and  $SD$  of the backscatter are determined by the “true” direction distribution relative to the respective beam pointing, which is different for each antenna. A similar value of  $SD$  for the three beams (after calibration) would thus indicate that the “true” wind direction distribution is indeed uniform.

Figure 2 is similar to Figure 1, but now the backscatter is simulated from the ECMWF winds using CMOD4. The average backscatter and the  $SD$  for the three antenna overlap to a large extent, as expected for simulated data and from a uniform input wind direction distribution. The  $SD$  of backscatter is similar to Figure 1, which indicates that the dynamic range of the transfer function, determined by  $B_0$ ,  $B_2$  and  $B_1$ , matches well the dynamic range of the measurements for each incidence angle. We further verified this, and the true wind direction uniformity, by plotting the ratio of the  $SD$ s as plotted in Figures 1 and 2 (not shown), which is generally smaller than 0.2 dB.

To further check the random wind direction filtering, wind direction can be retrieved

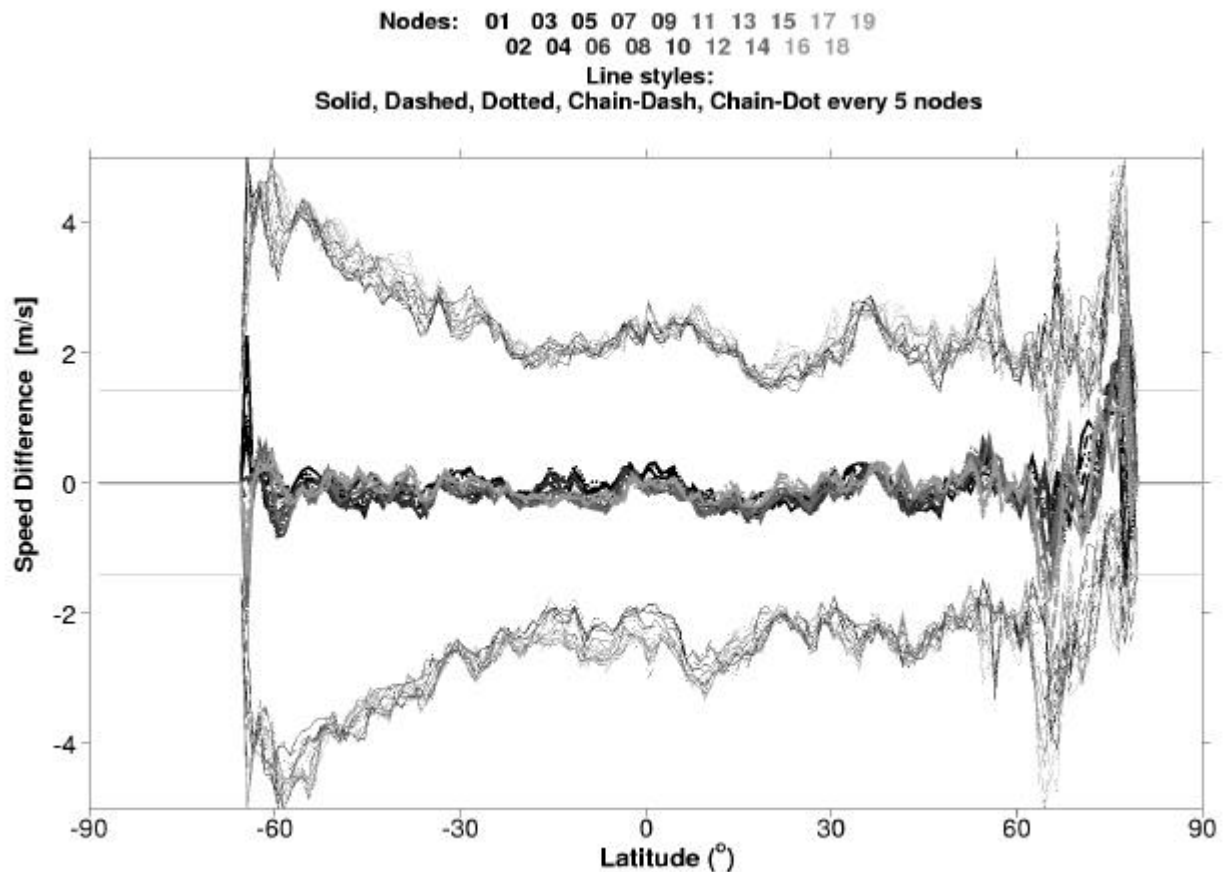


**Figure 3.** The average difference between ascending and descending tracks of ERS-1 scatterometer (PRESCAT) minus ECMWF model wind speed versus latitude, for data from June 10 to July 1 1995. Each node is plotted with a different style and gray scale. The thin lines are the average differences plus or minus one SD of that difference. An eclipse effect does not appear.

from each measured backscatter triplet. The distribution of retrieved winds is determined by the distribution of “true” wind directions and the wind direction retrieval error. We used PRESCAT to retrieve direction [Stoffelen and Anderson, 1997a, b, c; Chapters II, III and V], and it has been shown that its wind direction inversion has no large systematic error tendencies. Therefore, ideally one would expect that a data set with uniform “true” wind direction, would result in a uniform retrieved wind direction distribution.

We find that the retrieved wind direction distribution varies moderately with direction, with a standard deviation of less than 10% around the mean. If we assumed that this variation was equally caused by variations in the ECMWF and scatterometer direction error distributions then we may compute the error in the estimate of the calibration constant using (1). Ignoring the smaller  $B_1$  and using the value of  $B_2 = 0.4$  (which corresponds to its maximum [Stoffelen and Anderson, 1997a; Chapter II]), we find an uncertainty in the calibration of roughly 0.05 dB, which is very small indeed. Therefore, we conclude that

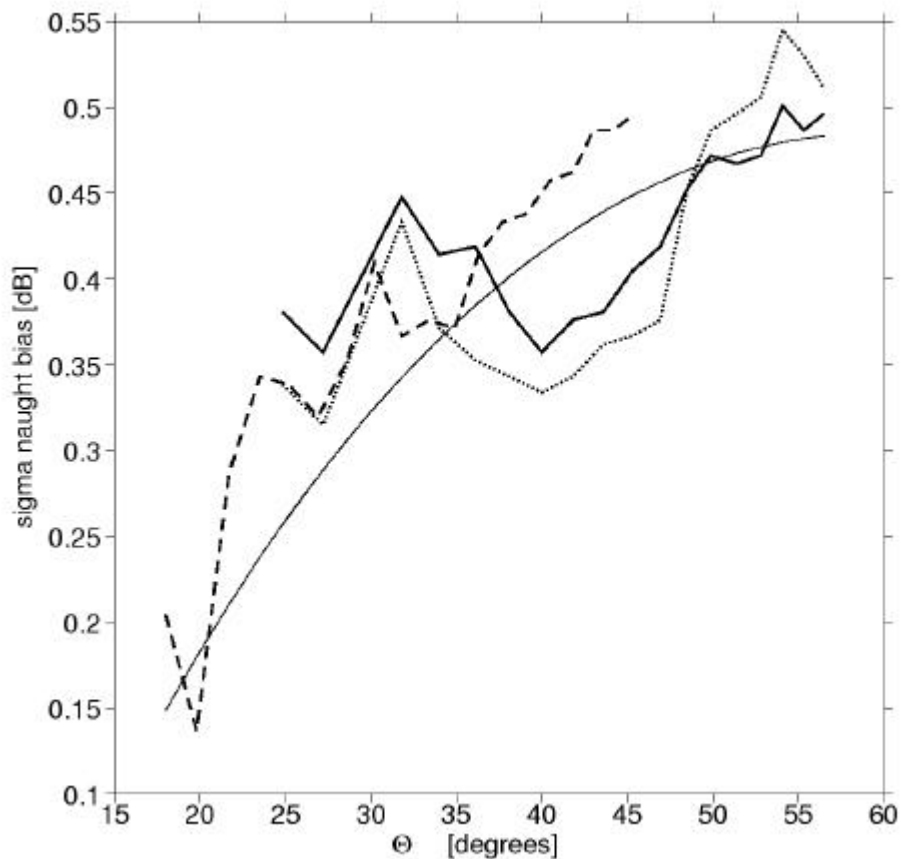


**Figure 4.** Bias of ocean calibrated ERS-1 with respect to CMODEC in dB for March 1996, computed using  $s^0$ , for the fore (solid), mid (dashed), and aft (dotted) beam. The thin solid lines illustrates the effect of a 7% increase in ECMWF wind speed. It is clear that this bias is non-zero and significant compared to ESA requirement of 0.2 dB.

after the wind direction filtering using ECMWF winds, the non-uniformity of the “true” wind is small and the error this introduces in the ocean calibration small.

### 3.2. Antenna Gain Variations

For ascending passes the antennae are moving from light to dark and dark to light again, whereas for descending passes they are always in sunlight. Temperature variations may deform the antenna and affect the antenna gain. Ascending and descending backscatter biases are marginally different, indicating the relative unimportance of antenna gain variations due to temperature changes.

A more detailed way of checking the effect of temperature on the antenna gain, is to plot the difference of the inverted scatterometer wind speed and the ECMWF wind speed versus latitude. The wind speed bias is particularly sensitive to simultaneous gain variations

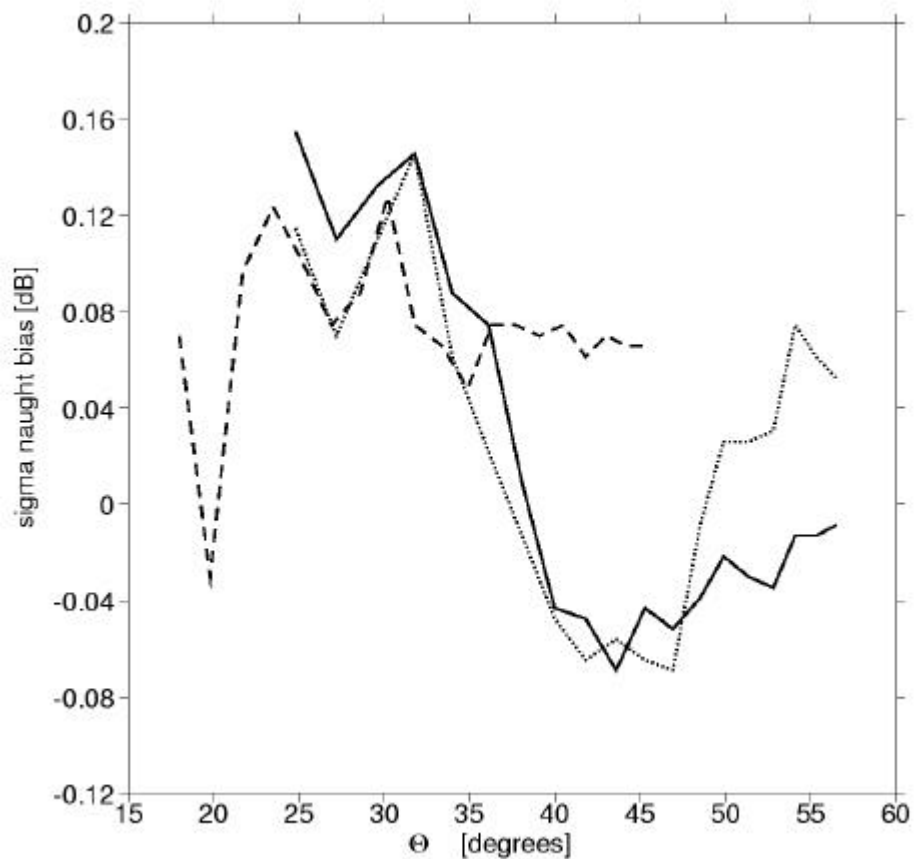


**Figure 5.** As Figure 4, but here the ECMWF wind speed was multiplied by a factor 0.93 before the backscatter simulation. Now the backscatter ratio varies around -0.04 dB, and is small everywhere.

on the fore and aft antenna, and relatively insensitive to changes of the mid antenna gain [Stoffelen and Anderson, 1997a; Chapter II]. Geophysical changes at the earth surface associated with sunset or sunrise, that affect the 10m wind speed do occur not at the same latitude than where the antennae see sunrise or sunset. Furthermore, as a function of latitude the geophysical changes are expected to be smoother than the antenna gain effects.

For all data from 10-30 December 1995 and for all 19 nodes individually, the wind speed bias versus latitude was computed, separately for ascending and descending orbits. Subsequently, the difference of the bias at ascending and descending passes was computed in order to highlight the eclipse effect and eliminate latitude-dependent statistical and ECMWF model bias effects. The computations were repeated for the last 20 days of June 1995. It was found that the ascending minus descending wind speed bias difference versus latitude does not vary much (Figure 3). This confirms in more detail the relative unimportance of antenna gain variations along the orbit.



### 3.3. Application

When PRESCAT was implemented at ECMWF, it was decided to implement the beam dependent ocean calibration (from March '92) as in CMODEC, because it resulted in a slightly better wind retrieval. However, the calibration coefficients were derived using Equation (4) rather than (3).

Figure 4 shows the bias in dB of ocean calibrated ERS-1 backscatter with respect to CMODEC for March '96, using Equation (3). It is clear that this bias is non-zero. No engineering changes have been detected from March '92 to March '96 in the backscatter data, but the mean ECMWF wind speed has been increased. The increased ECMWF wind speeds will give rise to increased backscatter as simulated by CMODEC. As a consequence, the ratio of the mean measured and simulated  $\sigma^0$ 's for March '96 will be smaller than for March '92 (zero) as verified in Figure 4. The thin solid curve gives the sensitivity of the backscatter (in  $B_0$ ) to a 7% increase of wind speed at  $8 \text{ m s}^{-1}$ , which corresponds very well with the general trend observed in the calibration curves of the three beams.

The ECMWF model near surface wind speed is sensitive to the boundary layer parameterization scheme. Latter is subject to re-evaluation, for instance to solve problems with boundary layer humidity or cloud, and as such the level of ECMWF wind speed may change from one forecast model software cycle to the next. *Stoffelen* [1996] estimates the average speed level of ECMWF in 1996 to be roughly 10% larger than the average ERS scatterometer speed level. The 7% increase of the ECMWF wind speed between March '92 and March '96 is consistent with the scatterometer over model wind speed ratio of 1.10. It may be concluded that in March '92 the same ratio was roughly 1.03, which in retrospect verifies reasonably well with our experience (see, e.g., *Stoffelen and Anderson* [1997b; Chapter III], for departure statistics). Figure 5 is similar to Figure 4, but here the ECMWF wind speed was multiplied by a factor of 0.93 before the backscatter simulation. Now the backscatter ratio varies around -0.04 dB, and is small everywhere. Thus, for a proper use of ECMWF winds for the ocean calibration the wind speed has to be adjusted to the level of the ECMWF model in November (or March) 1992, to which CMOD4 had been tuned.

The (independent) problem of wind calibration of the scatterometer and ECMWF model to for example the buoy network is discussed by *Stoffelen* [1998; Chapter IV]. He compares NCEP model and scatterometer winds to *in situ* wind measurements. Latter are used to calibrate the two former wind data sources. A conclusion from the analysis is that scatterometer wind speeds are biased low by ~4% with respect to the buoys. It is found here that after the ocean calibration the node to node fluctuation of the wind speed bias is less than before (see at the end of this section). However, the effect is small and the backscatter calibration refinement suggested here has little impact on the overall wind calibration (and vice versa).

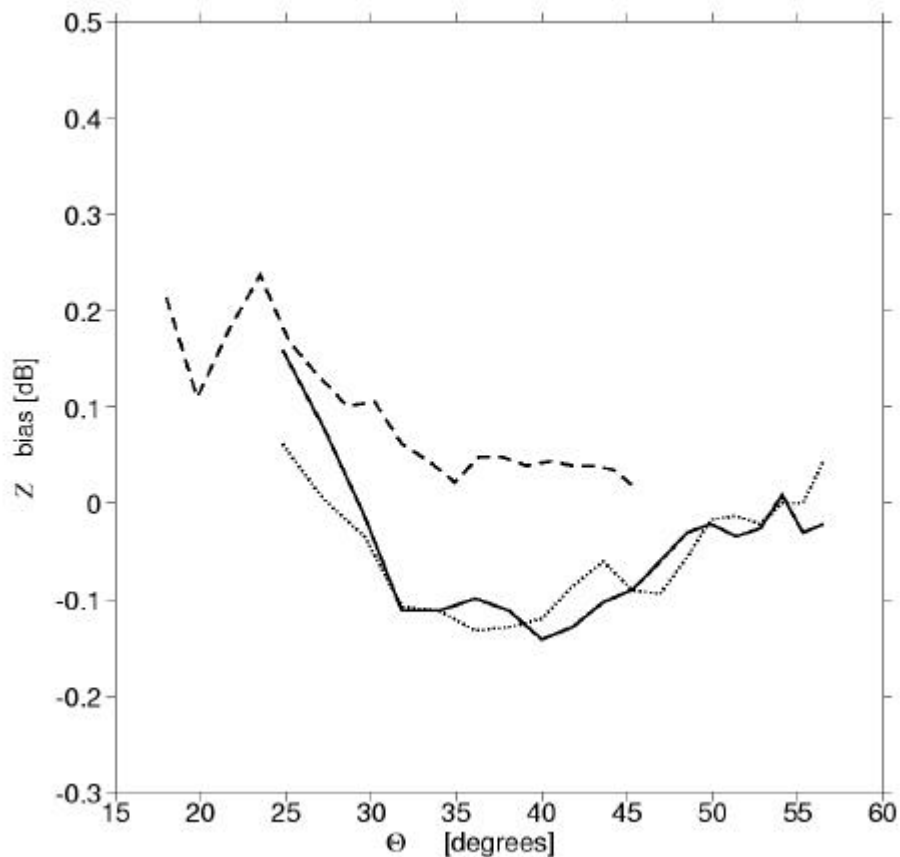


**Figure 6.** Difference between ERS-1 and CMOD4 backscatter (after the 0.93 scaling of the ECMWF velocities) as computed in  $z$  space. The beams are indicated as in Figures 4 and 5. The bias is small and varies with incidence angle and beam.

For verification purposes we computed the ratio as of Figure 5 also in  $z$  space, and found the same curves, but shifted by +0.08 dB, probably showing the small interference of the term  $\overline{B_0^{0.625} B_2^2}$  in (4). Figure 6 shows the difference between ERS-1 and CMOD4 backscatter (after the 0.93 scaling of the ECMWF velocities) as computed in  $z$  space. The bias varies with incidence angle and is different for the mid and fore/aft beams. To check stability, we repeated the computation for February '96 and the ratios are within 0.01 dB of the ones computed for March '96 for each beam and node, as shown in Figure 7. This is in line with our experience over the past years that the ocean calibration over a period of a month is rather independent of the geophysical conditions. In months with frequent tropical storms that are not well resolved by the ECMWF model (often in September) differences may amount to a tenth of a dB. However, these erroneous ECMWF wind cases may be rejected by a gross check on the ERS scatterometer minus ECMWF model speed difference. We did not carry this out.

The difference in Figure 6 is within the ERS scatterometer specifications for radiometric accuracy (0.2 dB), but it is still interesting to evaluate its effect on the wind retrieval. An improvement in the fit of the ERS-1 measurements with the CMOD4 cone should be particularly visible through a decreased average distance to the cone. Because the normalized distance to the cone [Stoffelen and Anderson, 1997a; Chapter II] is reasonably independent of wind speed, the average of it at each node is a good reflection of the overall fit of triplets to the cone. Table 1 shows the normalized distance to the cone after and before the backscatter bias correction. For all nodes the distance to the cone has decreased, even at the outer nodes where the correction is fairly small. On average the distance to the cone has decreased by 7%. As can be seen from Table 1, the correction has little effect on the backscatter triplet quality control, as the number of data is similar with or without bias correction.

A mid beam bias mostly affects the wind direction retrieval accuracy at low and moderate speeds and not so much the speed retrieval. Table 1 shows the *SD* of the ECMWF minus retrieved scatterometer wind direction for all speeds. As expected, the largest improvement is found at the inner nodes where the mid beam bias is largest.

The fore and aft beam have very similar backscatter biases. This combination of fore and aft beam bias will mostly effect wind speed bias, and not so much wind direction. Indeed, the wind speed bias with respect to the ECMWF model winds is less variable from node to node after the bias correction than before.

#### 4. Conclusions

The method of ocean calibration is briefly explained and it is motivated that application of the procedure in  $z$  space rather than  $\mathbf{s}^0$  space gives the most accurate estimate of the difference between the center of gravity of the transfer function cone and the center of gravity of the distribution of measured triplets. As a consequence, application of it in the processing of scatterometer data improves the geophysical product. The method is shown to be stable in time and may be applied for monitoring purposes, as has been done for more than 5 years now at ECMWF.

Land targets are also in use to determine the scatterometer calibration. The ESA rain forest calibration corresponds with the ocean calibration procedure to within the specified instrument precision of 0.2 dB. However, the stability of the land targets to an accuracy of 0.1 dB over all seasons is difficult to be assured of. Also, ESA employed transponders for absolute calibration. However, the relatively infrequent overpass over the transponders and the absolute accuracy of these, makes an absolute calibration on this basis only a tedious procedure. The consistent combination of several methods is probably the best guarantee for a good absolute scatterometer backscatter calibration.

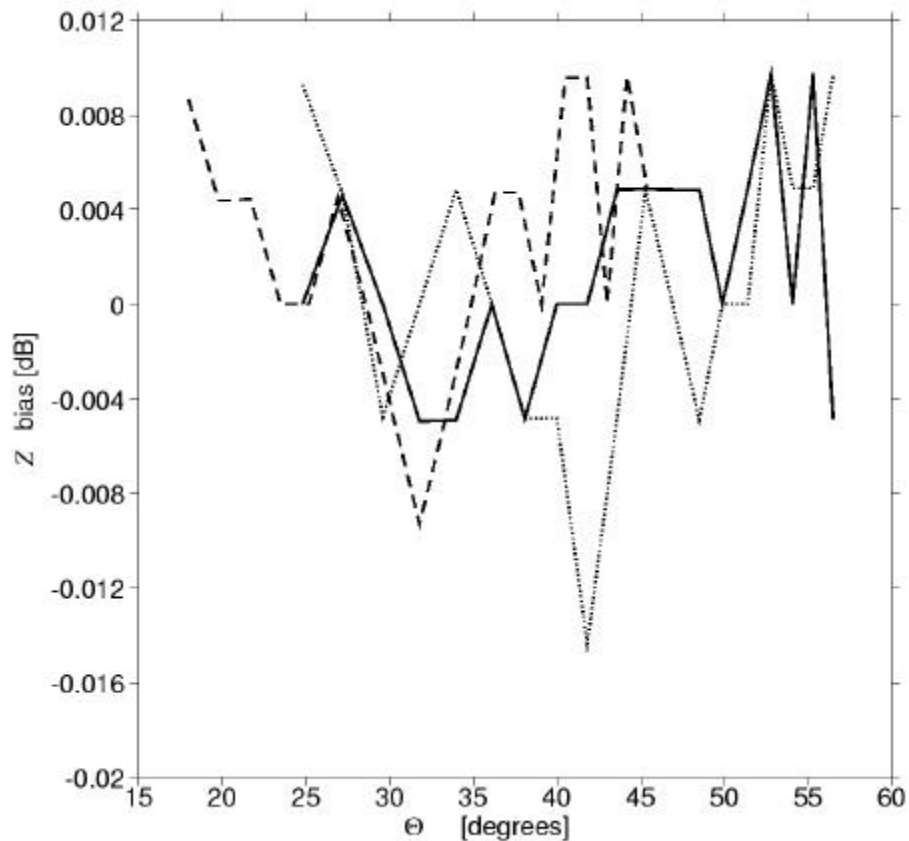


**Figure 7.** As Figure 6, but for the difference in ocean calibration between March and February 1996. The ocean calibration is stable from one month to the next.

In using the ocean calibration procedure we found that the ERS-1 scatterometer has been stable since March '92 until its switch-off in June 1996. Orbit maneuvers, however, occasionally caused temporary changes in the backscatter level due to a mispointing of the beams.

After the launch of the ERS-2 scatterometer, we have been able to compute the backscatter calibration coefficients within two weeks after the data had become routinely available. By measurement space visualization, *Stoffelen and van Beukering* [1997] verified that the calibrated triplets indeed lie closer to the CMOD4 cone surface than before the ocean calibration. As such, a quality assessment of the ERS-2 scatterometer winds could be made well before the engineering calibration was carried out, which provided the evidence that the ERS-2 scatterometer was functioning well.

A mid beam bias mainly causes problems in the wind direction retrieval, whereas a simultaneous and coherent bias in the fore and aft beams mainly causes a wind speed bias. Other bias types will cause combined speed and direction effects. The ocean calibration

**Table 1.** The Effect of Ocean Calibration on Scatterometer Wind Retrieval With PRESCAT

Node	Bias Correction			No Bias Correction		
	Number	Distance [a.u.]	Direction SD [°]	Number	Distance [a.u.]	Direction SD [°]
1	28225	0.39	32.3	28220	0.46	32.6
2	28258	0.43	30.5	28257	0.47	30.5
3	28059	0.45	29.2	28059	0.56	29.6
4	27990	0.50	28.3	27990	0.72	30.1
5	27981	0.56	27.1	27982	0.72	28.2
6	28023	0.65	26.6	28024	0.78	27.1
7	27961	0.77	26.2	27961	0.89	26.4
8	27883	0.91	26.3	27881	1.05	26.4
9	27802	1.08	26.5	27801	1.18	26.3
10	27638	1.26	26.4	27645	1.34	26.3
11	27476	1.43	26.3	27490	1.50	26.2
12	27310	1.59	26.1	27305	1.68	25.9
13	27093	1.79	25.8	27099	1.85	25.7
14	26740	1.95	25.6	26756	2.00	25.5
15	26439	2.16	25.2	26433	2.22	25.1
16	26045	2.39	24.9	26033	2.43	24.8
17	25694	2.66	24.9	25680	2.68	24.8
18	25289	2.91	24.8	25285	2.96	24.7
19	24898	3.19	24.3	24920	3.22	24.3
all	516804	1.39	26.8	516821	1.48	27.0

The first column indicates node number across the swath counted from inner to outer. Columns 2-4 and 5-7 are respectively for bias corrected and no bias corrected retrievals. Each of the three columns indicates from left to right respectively the number of retrievals, the mean normalized distance to the cone, and the standard deviation (SD) of ECMWF model minus scatterometer wind direction for all speeds. The data are from the first three days of February 1996. The bias correction is beneficial for all nodes and improves marginally the wind product.

reduces the average distance of the ERS backscatter triplets to the CMOD4 cone surface by 7% and proved effective in removing remaining backscatter biases.

The ECMWF model near surface wind speed is sensitive to the boundary layer parameterization scheme. Latter is subject to re-evaluation, for instance to solve problems with boundary layer humidity or cloud, and as such the level of ECMWF wind speed may change from one forecast model software cycle to the next. Using the ocean calibration method we found an increase of the ECMWF wind speed between March '92 and March

'96 of 7 %. This is consistent with the results of dedicated wind calibration studies. After the ocean calibration the node to node fluctuation of the wind speed bias is less than before, and for some nodes the wind direction retrieval is improved. However, the backscatter calibration refinement suggested here has little impact on the overall wind calibration.

For the scatterometer processing we recommend correction of the backscatter biases between scatterometer measurements and CMOD4 for e.g. March '96 and thereafter a monitoring of the backscatter bias with respect to this. At the same time, checking of departure statistics of surface wind from one forecast model cycle to the next is necessary as an independent way to check speed level changes.

### Acknowledgments

The work described in this paper profited much from the discussions in the ASCAT SAG and in an earlier stage in the ERS analysis team. The comments of ECMWF staff, and in particular Dave Anderson and Didier Lemeur, motivated me to refine the procedure. The three reviewers of this manuscript are acknowledged for their constructive remarks.

### References

- Attema, E. W. P., The Active Microwave Instrument on board the ERS-1 satellite, *Proc. IEEE.*, 79, pp.791-799, 1991.
- Freilich, M. H., Hongbo Qi and R. S. Dunbar, Scatterometer Beam-Balancing Using Open-Ocean Backscatter Measurements, *J. of Atmos. and Ocean. Technol.*, in press, 1998.
- Guignard, J-P. et al., AMI Performances, *Proc. of the ERS-1 commissioning phase mid-term review* held at ESA/ESTEC from 24-25 September 1991, ESA publishing division, ESTEC, Noordwijk, the Netherlands, 1992.
- Offiler, D., The calibration of ERS-1 satellite scatterometer winds, *J. of Atmos. and Ocean. Technol.*, **11**, 1002-1017, 1994.
- Stoffelen, Ad, Error modeling of scatterometer, in situ, and ECMWF model winds; a calibration refinement, Tech. Rep. 193, KNMI, de Bilt, the Netherlands, 1996.
- Stoffelen, Ad, Error modeling and calibration; towards the true surface wind speed , *J. Geophys. Res.*, 103 (C4), 7755-7766, 1998.
- Stoffelen, Ad and David Anderson, Scatterometer Data Interpretation: Measurement Space and inversion, *J. Atm. and Ocean Techn.*, 14(6), 1298-1313, 1997a.
- Stoffelen, Ad , and David Anderson, Scatterometer Data Interpretation: Derivation of the

Transfer Function CMOD4, *J. Geoph. Res.*, 102(C3), 5767-5780, 1997b.

Stoffelen, Ad, and David Anderson, Ambiguity Removal and Assimilation of Scatterometer Data, *Q. J. R. Meteorol. Soc.*, 123, 491-518, 1997c.

Stoffelen, Ad, and Paul van Beukering, Implementation of Improved ERS Scatterometer Data Processing and its impact on HIRLAM Short Range Weather Forecasts, *Techn. Report No. 31, BCRS project report*, BCRS, Delft, Netherlands, 1997.

**Acronyms**

2D	2-Dimensional
3D	3-Dimensional
4D	4-Dimensional
3D-VAR	3D Variational meteorological spatial data analysis scheme
4D-VAR	4D Variational meteorological spatial and temporal data analysis scheme
ADEOS	Advanced Earth Observation Satellite launched by Japan in 1996
ASCAT	Advanced Scatterometer proposed for METOP/EPS
BCRS	“BeleidsCommissie” Remote Sensing
BUFR	Binary Universal Format Representation; code for meteorological data
CMOD2	Pre-launch transfer function for the C-band ERS scatterometer
CMOD4	Scatterometer transfer function for the C-band ERS scatterometer
CMODEC	CMOD4, including an ocean calibration
CREO	ESA’s ERS scatterometer ambiguity removal
DNMI	The Norwegian Meteorological Institute
DWL	Doppler Wind Lidar
ECMWF	European Centre for Medium-range Weather Forecasts
ESA	European Space Agency
e.m.	electromagnetic
EPS	European Polar System
ERS	European Remote-sensing Satellite
ESA	European Space Agency
EUMETSAT	European Meteorological Satellite agency
FDP	Fast Delivery Product
FG	First Guess
FGAT	First Guess at Appropriate Time
GOS	Global Observing System
GTS	meteorological Global Telecommunication System
HIRLAM	High Resolution Limited Area Model
KNMI	Royal Netherlands Meteorological Institute
LOS	Line of Sight
LUT	Look-Up Table of sigma naught calibration coefficients
MLE	Maximum Likelihood Estimator



METOP	Meteorological Operational Polar satellite series, proposed by EUMETSAT
NASA	National Aeronautics and Space Agency (US)
NASDA	National Aeronautics and Space Development Agency (Japan)
NCEP	National Center for Environmental Prediction (US)
NESDIS	National Environmental Satellite and Data Information System (US)
NOAA	National Oceanographic and Atmospheric Administration (US)
NSCAT	NASA Scatterometer on board ADEOS-I
NWP	Numerical Weather Prediction
OI	Optimal (statistical) Interpolation; meteorological data analysis method
PBL	Planetary Boundary Layer
PRESCAT	Pre-processor of Scatterometer data before meteorological assimilation
QC	Quality Control
QuikSCAT	Scanning scatterometer system to be launched on a dedicated platform in November 1998
RMS	Root-Mean-Squared
RS	Remote Sensing
SAR	Synthetic Aperture Radar
SASS	SEASAT-A Scatterometer System
SATEM	NOAA/NESDIS TOVS vertical sounding
SCAT	Scatterometer on board the ERS-1 and ERS-2 satellites.
SeaSat	Sea state Satellite launched by NASA in 1978
SeaWinds	Scanning scatterometer system on ADEOS-II
SD	Standard Deviation
SLICE	2D modal wind direction filter for ambiguity removal by UKMO
SODA	Studies for Ozone Data Assimilation (EU project)
T106	Truncation of model spectral sampling at wave number 106 (120 km grid)
T213	Truncation of model spectral sampling at wave number 213 (60 km grid)
TAO	Tropical Array Of (buoys)
TIROS	Television Infra-Red Operational Satellite
TOVS	TIROS Operational Vertical Sounder
UKMO	Meteorological Office of the United Kingdom
UTC	Universal Time Coordinate
UU	Universiteit Utrecht
UWI	Acronym for the scatterometer BUFR product disseminated over the GTS

**Acronyms**

2D	2-Dimensional
3D	3-Dimensional
4D	4-Dimensional
3D-VAR	3D Variational meteorological spatial data analysis scheme
4D-VAR	4D Variational meteorological spatial and temporal data analysis scheme
ADEOS	Advanced Earth Observation Satellite launched by Japan in 1996
ASCAT	Advanced Scatterometer proposed for METOP/EPS
BCRS	“BeleidsCommissie” Remote Sensing
BUFR	Binary Universal Format Representation; code for meteorological data
CMOD2	Pre-launch transfer function for the C-band ERS scatterometer
CMOD4	Scatterometer transfer function for the C-band ERS scatterometer
CMODEC	CMOD4, including an ocean calibration
CREO	ESA’s ERS scatterometer ambiguity removal
DNMI	The Norwegian Meteorological Institute
DWL	Doppler Wind Lidar
ECMWF	European Centre for Medium-range Weather Forecasts
ESA	European Space Agency
e.m.	electromagnetic
EPS	European Polar System
ERS	European Remote-sensing Satellite
ESA	European Space Agency
EUMETSAT	European Meteorological Satellite agency
FDP	Fast Delivery Product
FG	First Guess
FGAT	First Guess at Appropriate Time
GOS	Global Observing System
GTS	meteorological Global Telecommunication System
HIRLAM	High Resolution Limited Area Model
KNMI	Royal Netherlands Meteorological Institute
LOS	Line of Sight
LUT	Look-Up Table of sigma naught calibration coefficients
MLE	Maximum Likelihood Estimator

METOP	Meteorological Operational Polar satellite series, proposed by EUMETSAT
NASA	National Aeronautics and Space Agency (US)
NASDA	National Aeronautics and Space Development Agency (Japan)
NCEP	National Center for Environmental Prediction (US)
NESDIS	National Environmental Satellite and Data Information System (US)
NOAA	National Oceanographic and Atmospheric Administration (US)
NSCAT	NASA Scatterometer on board ADEOS-I
NWP	Numerical Weather Prediction
OI	Optimal (statistical) Interpolation; meteorological data analysis method
PBL	Planetary Boundary Layer
PRESCAT	Pre-processor of Scatterometer data before meteorological assimilation
QC	Quality Control
QuikSCAT	Scanning scatterometer system to be launched on a dedicated platform in November 1998
RMS	Root-Mean-Squared
RS	Remote Sensing
SAR	Synthetic Aperture Radar
SASS	SEASAT-A Scatterometer System
SATEM	NOAA/NESDIS TOVS vertical sounding
SCAT	Scatterometer on board the ERS-1 and ERS-2 satellites.
SeaSat	Sea state Satellite launched by NASA in 1978
SeaWinds	Scanning scatterometer system on ADEOS-II
SD	Standard Deviation
SLICE	2D modal wind direction filter for ambiguity removal by UKMO
SODA	Studies for Ozone Data Assimilation (EU project)
T106	Truncation of model spectral sampling at wave number 106 (120 km grid)
T213	Truncation of model spectral sampling at wave number 213 (60 km grid)
TAO	Tropical Array Of (buoys)
TIROS	Television Infra-Red Operational Satellite
TOVS	TIROS Operational Vertical Sounder
UKMO	Meteorological Office of the United Kingdom
UTC	Universal Time Coordinate
UU	Universiteit Utrecht
UWI	Acronym for the scatterometer BUFR product disseminated over the GTS

## Acknowledgments

The work as described in this thesis would not have taken place without the continuing support of my wife Karin. She made it possible for me to spend so much time on science, while she had a busy job managing family life, removals, and birth and breastfeeding counseling. While preparing this literary infant, Kees, Elma, Leon and Rian were the four other infants that took my care and affection.

David Anderson contributed substantially to the quality of the papers produced. His unflinching impetus to question my ideas and improve on the written texts has been invaluable, and I am very grateful for this. Tony Hollingsworth provided great support by fully entrusting me the improvement of the scatterometer processing and by reviewing the material. John Eyre led me to derive the mathematical framework supporting the ideas I had put forward. The valuable time and effort that Bert Holtslag, Arnold Heemink, and the other members of the committee have spend on the thesis is much appreciated. The hand of Rob Hine and Birgit van Diemen in many drawings provides the thesis its current appearance. Wiebe Oost provided the photograph on the cover.

The ESA analysis and experimenters teams bundled the knowledge on microwave-ocean interaction within Europe, and provided a very stimulating atmosphere. In particular Alf Long, who has a long career in the field, helped me with his knowledge, software, and ideas. Evert Attema often joined in our discussions, which I found to be very helpful. Besides the acknowledgments here and in Chapters II-V, many other people contributed by providing a constructive scientific atmosphere.

It is a pleasure to see that the developments on scatterometer data interpretation described here and originally supported by ESA, are now being supported by many other institutes, amongst which the BCRS and EUMETSAT, and active co-operation takes place on an international level, for instance with the NASA on QuikSCAT/SeaWinds. This is of great importance for an optimal use of these costly space-based observations.

Almost four years I shared office and worked with Gerard Cats, whose clear analytical explanations much helped me to understand the meteorological analysis problem. Nowadays, Julia Figa shares my office until it is definitely broken down. At ECMWF my work was often interrupted by Tony McNally, Laurant Phalippou, and Bernd Becker, but in a pleasant and relaxing way. Here, Hervé Roquet, Catherine Gaffard, Didier Le Meur, and more recently Lars Isaksen carried forward the developments initiated by me. During the 11 years of attachment to KNMI and ECMWF, I could easily fill a page with names of people that help, or have helped, to provide a nice social and effective professional atmosphere. All

of you are gratefully honoured. The running, volley, and soccer were appreciated interruptions from a busy job, and the many colleagues at ECMWF and KNMI that joined me in these activities are acknowledged. I must have forgotten many people.

## **Curriculum Vitae**

Born in Alphen en Riel on 25 February 1962 as a farmers son, I have spent many thousands of hours outdoors exposed to the variable Dutch weather. This probably explains my great interest in meteorology. After completing the Atheneum B education at the St. Odulphuslyceum in Tilburg, I studied from 1980 to 1987 at the Technical University of Eindhoven, where I became Ir in Physics. Fortunately, at the time when I studied in Eindhoven, the curriculum was nominally 5 years and there were many opportunities to train in both practical and theoretical skills. In the last 11 years my scope has been changed from solid states to fluid dynamics and my interest in meteorology has been satisfied during my work at KNMI and ECMWF. Besides scatterometry, I am since 7 years involved in the preparation of an ESA Doppler Wind Lidar mission, and more recently as project leader in ozone data assimilation (SODA European Union project). As a member of the ESA/EUMETSAT ASCAT Science Advisory Group, the ESA Atmospheric Dynamics Mission Advisory Group, the QuikSCAT science team, the ESA Radar Technical Advisory Group and as co-ordinator of the HIRLAM satellite data activities I am well involved in the development of Remote Sensing applications for the benefit of meteorology.

# Stellingen

behorende bij het proefschrift “Scatterometry”

Ad Stoffelen

1 Augustus 1998

## .I

De scatterometer is een nauwkeurige windmeter (dit proefschrift).

## .II

De driedimensionale meetruimte van de ERS scatterometers zoals gedefinieerd in dit proefschrift, én de sterke coherentie van de metingen in deze ruimte, vormen een verfrissend en cruciaal gegeven van belang bij alle facetten in de interpretatie van de radar verstrooiingsmetingen (dit proefschrift).

## .III

Correcties voor o.a. stabiliteit, golftoestand, en oppervlakte-actieve stoffen (z.g. slicks) op de wind-radar transfer functie zijn in het algemeen van secundair belang. Een reden is dat deze effecten in hoge mate correleren met de windsnelheid en als zodanig impliciet zijn opgenomen in het empirische CMOD4. Bovendien is in de meeste gevallen en voor enkele van deze parameters geen adequate a priori informatie voorhanden, zodat dan een eventueel windonafhankelijk effect niet gecorrigeerd kan worden (dit proefschrift).

## .V

Gegevensassimilatie in een mondiaal weermodel is een krachtig middel voor de calibratie en validatie van in situ, satelliet-, en weermodel-gegevens (dit proefschrift).

## .V

Niet alleen een notie van het verband tussen meting en relevante geofysische grootheden is van belang bij de interpretatie van metingen, maar ook een goede notie van de nauwkeurigheid van de meting, de nauwkeurigheid van het geofysische verband, en de ruimte- en tijdschalen die de meting én de geofysische parameters beschrijven (dit proefschrift).



#### **.V**

Elke natuurwetenschappelijke uitspraak zou gepaard moeten gaan met een analyse van zijn nauwkeurigheid. Een recursieve toepassing van deze stelling is echter heilloos.

#### **.IV**

De inhomogeniteit van en schaarste in het wereldwijde meteorologische waarnemingsnetwerk zijn de belangrijkste beperkingen voor een nauwkeurige voorspelling van het weer. Met name windwaarnemingen in de troposfeer zijn nodig voor een verbeterde beschrijving van de atmosferische circulatie (dit proefschrift).

#### **.III**

Een prijspolitiek voor aardobservatiegegevens ondermijnt het potentiële gebruik ervan in de maatschappij, en is daarom niet kosten besparend.

#### **.X**

De illusie van kennis is schadelijker dan onwetendheid.

#### **X**

In tegenstelling tot dat wat gepropageerd wordt door veel media, is de functie van de vrouwelijke borst voornamelijk gericht op het pasgeboren kind.

#### **.X**

Het ouderschap is ook een respectabele baan.